Peter Adel

Pulsed fiber lasers

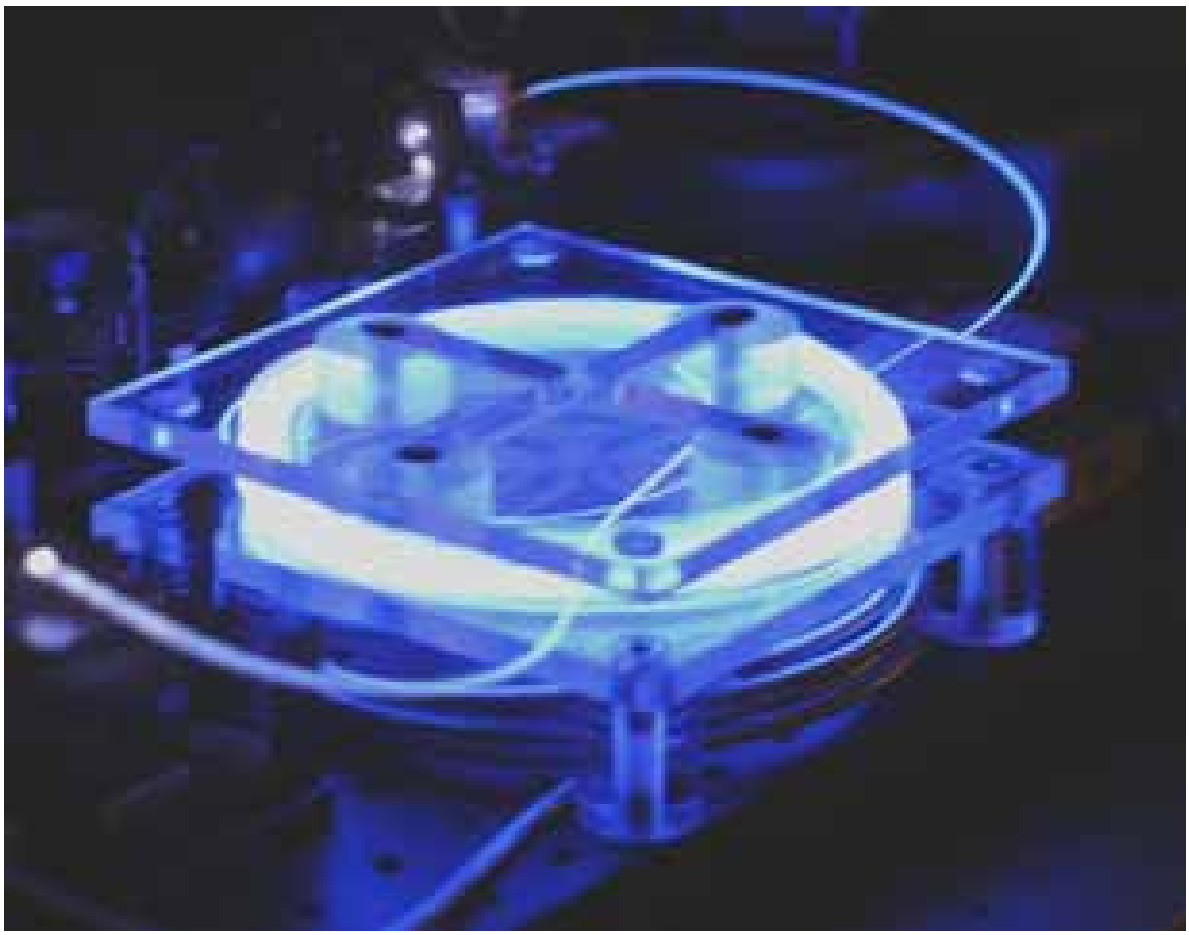

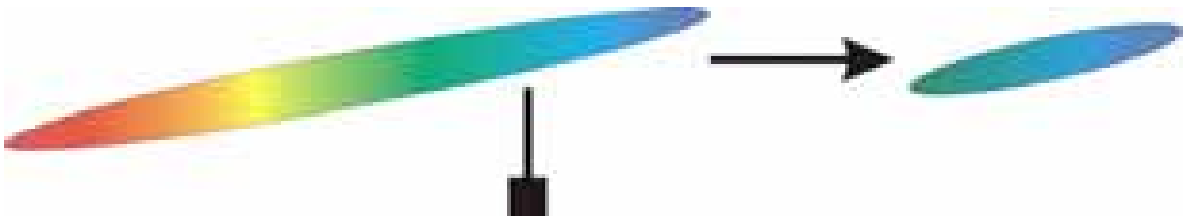

Cuvillier Verlag Göttingen

Pulsed fiber lasers

Vom Fachbereich Physik der Universität Hannover
zur Erlangung des Grades

Doktor der Naturwissenschaften
- Dr. rer. nat. –

genehmigte Dissertation

von

Dipl. Phys. Peter Adel
geboren am 25. Juli 1969 in Nürnberg

2004

Bibliografische Information Der Deutschen Bibliothek
Die Deutsche Bibliothek verzeichnet diese Publikation in der Deutschen Nationalbibliografie; detaillierte bibliografische Daten sind im Internet über http://dnb.ddb.de abrufbar.
1. Aufl. - Göttingen : Cuvillier, 2004
Zugl.: Hannover, Univ., Diss., 2004
ISBN 3-86537-146-9

Referent:	Prof. Dr. Herbert Welling, Universität Hannover
Koreferent:	Prof. Dr. Andreas Tünnermann, Friedrich-Schiller Universität Jena
Tag der Promotion:	27. Mai 2004

⊕ CUVILLIER VERLAG, Göttingen 2004
Nonnenstieg 8, 37075 Göttingen
Telefon: 0551-54724-0
Telefax: 0551-54724-21
www.cuvillier.de

Alle Rechte vorbehalten. Ohne ausdrückliche Genehmigung des Verlages ist es nicht gestattet, das Buch oder Teile daraus auf fotomechanischem Weg (Fotokopie, Mikrokopie) zu vervielfältigen.
1. Auflage, 2004
Gedruckt auf säurefreiem Papier

ISBN 3-86537-146-9

Abstract

Peter Adel

Pulsed fiber lasers

Laser systems based on rare-earth-doped silica fibers have many advantages, since these fibers offer a high beam quality, a high amplification and a broad amplification bandwidth. The latter enables tunable laser operation and the generation of ultrashort pulses with large spectral bandwidths. In order to demonstrate the various laser parameters, which can be realized by pulsed fiber laser systems, different fiber laser set-ups were developed and investigated during this work.

Passive Q-switching of an Ytterbium fiber by a Thulium codoping was demonstrated for the first time. By this way, wavelength tunable laser operation with a minimum pulse duration of 1.1 µs, pulse energies of up to 21.8 µJ and a maximum linewidth of 4 GHz were shown. The passive Q-switching mechanism was analyzed and the strong interaction of the saturable absorption with relaxation oscillations identified. Furthermore, four-wave-mixing was identified for the first time as the dominating spectral broadening mechanism in narrow linewidth fiber ring-lasers.

Passive mode-locking of a fiber ring-laser by nonlinear polarization rotation was realized for the first time in combination with a long cladding pumped Ytterbium fiber. In this super-stretched fiber-laser, dispersion was compensated by a dispersive grating line. The pulsed output signal showed up to 40 nm spectral bandwidth and 9.5 nJ pulse energy. It was observed, that the maximum pulse energy was limited by nonlinear effects and that several closely spaced pulses were circulating in the cavity at higher pump powers. Investigations of the cavity dispersion and the output pulse chirp pointed out, that the highly uncompensated third order cavity dispersion strongly restricted chirp compensation of the output pulses. Furthermore, a suppression of the long wavelength spectral components by intra-cavity spectral filtering resulted in spectral bandwidths, which were several times larger than in previous Ytterbium fiber laser systems. This spectral broadening was due to nonlinear effects in the gain fiber and enabled bandwidths of up to 118 nm at 1.3 W output power from such a modified laser set-up.

For generation of femtosecond pulses with microjoule pulse energies, a chirped-pulse Erbium-fiber oscillator-amplifier system was developed. This modular system was seeded by a passively mode-locked Erbium-fiber laser and enabled at a center wavelength of 1.56 µm pulse energies of more than 4 µJ and a pulse duration of 810 fs. The repetition rate was quasi-continuously tunable, at least between 50 kHz and 1 MHz, while the system design enabled a synchronization of the pulse emission to an external electrical trigger signal. Detailed investigations of the system operation showed that the influence of four-wave-mixing effects on the signal depended strongly on the amplifier pump direction. Furthermore, strong nonlinear dispersion in the amplifier-chain was observed, which must be caused by the gain material. Furthermore, the maximum pulse energy was limited by gain saturation effects.

Key words: fiber laser, mode-locked; fiber laser, Q-switched; fiber laser tunable; fiber laser, narrow linewidth; fiber laser, broad bandwidth; fiber-amplifier, chirped-pulse amplification; nonlinear effects.

Zusammenfassung

Peter Adel

Gepulste Faserlaser

Die hohe und breitbandige Verstärkung von Seltenerd-dotierten Quarzglasfasern unterstützt sowohl die Erzeugung von ultrakurzen Pulsen mit hohen Bandbreiten als auch einen spektral weit abstimmbaren Laserbetrieb. Um die sich daraus ergebenden vielfältigen Möglichkeiten aufzuzeigen, wurden im Rahmen dieser Arbeit verschiedene gepulste Faserlasersysteme entwickelt und untersucht.

Erstmalig wurde dabei eine passive Güteschaltung eines Ytterbiumfaserringlasers durch eine Thulium-Kodotierung realisiert. Ein spektral abstimmbarer Laserbetrieb mit einer minimalen Pulsdauer von 1,1 µs, mit bis zu 21,8 µJ Pulsenergie und einer maximalen Linienbreite von 4 GHz wurde damit demonstriert. Die passive Güteschaltung wurde analysiert und eine starke Wechselwirkung zwischen der sättigbaren Absorption und Relaxationsoszillationen festgestellt. Weiterhin wurde erstmalig die Vier-Wellen-Mischung als der dominierende spektrale Verbreiterungsmechanismus identifiziert.

Passive Modenkopplung eines Faserringlasers durch nichtlineare Polarisationsdrehung wurde erstmalig in Kombination mit einer langen Ytterbium-Doppelkernfaser demonstriert. In diesem „super-stretched“-Faserlaser erfolgte die Dispersionskompensation durch ein Gitterpaar. Pulsenergien von bis zu 9.5 nJ und spektrale Bandbreiten von bis zu 40 nm wurden damit erzielt. Bei höheren Pumpleistungen wurden mehrere zeitlich dicht benachbarte Pulse im Resonator beobachtet, da nichtlineare Effekte die maximale Pulsenergie begrenzten. Die zeitliche Komprimierbarkeit des Ausgangssignals wurde durch die hohe unkompensierte Dispersion dritter Ordnung im Resonator begrenzt. Eine Unterdrückung der langwelligen Signalanteile im Resonator führte zu einer starken spektralen Verbreiterung des Ausgangssignals durch nichtlineare Effekte in der aktiven Faser. Die mit diesem modifizierten Laseraufbau erzielte Signalbandbreite von 118 nm übertraf bisherige Ytterbium-Faserlaser um ein Mehrfaches und wurde bei einer Ausgangsleitung von 1.3 W gemessen.

Für die Erzeugung von Femtosekundenpulsen mit Pulsenergien im Mikrojoule-Bereich wurde ein Erbium-Faser Oszillator-Verstärkersystem mit dispersiver Pulsstreckung entwickelt. In diesem modularen System wurden die Pulse in einem modengekoppelten Faserlaser erzeugt und nach der Verstärkung Pulsdauern von 810 fs und Pulsenergien von bis zu 4 µJ bei einer Wellengänge von 1.56 µm erreicht. Die Pulswiederholrate wurde zwischen 50 kHz und 1 MHz variiert und war quasi-stufenlos abstimmbar. Dabei erlaubte das Systemdesign eine Synchronisation der Pulsemission auf ein externes Steuersignal. Weiterhin wurde festgestellt, dass der Einfluss von Vier-Wellen-Mischungs-Effekten auf das Signal stark von der Pumprichtung der Faserverstärker abhängig war. Zusätzlich wurden starke nichtlineare Dispersionseffekte der aktiven Fasern im Verstärkersystem festgestellt. Sättigungseffekte in den Faserverstärkern begrenzten die Pulsenergie.

Schlagwörter: Faserlaser modengekoppelt; Faserlaser, gütegeschaltet; Faserlaser, abstimmbar; Faserlaser, schmalbandig; Faserlaser, breitbandig; Faserverstärker; Pulsverstärkung, gechirped; Nichtlineare Effekte.

CONTENTS

1 INTRODUCTION 1

2 BASICS OF PULSED FIBER LASER SYSTEMS 5

2.1 BASICS OF FIBER OPTICS 5
2.1.1 Fiber modes 6
2.1.2 Chromatic dispersion 8
2.1.3 Modal birefringence 9
2.2 NONLINEAR EFFECTS IN FIBERS 10
2.2.1 Kerr-Effect 11
2.2.2 Self- and cross-phase-modulation 12
2.2.3 Stimulated Raman scattering 13
2.2.4 Stimulated Brillouin scattering 15
2.2.5 Four-wave-mixing 15
2.3 PULSES IN OPTICAL FIBERS 16
2.3.1 Dispersion pulse broadening 17
2.3.2 Polarization mode dispersion 19
2.3.3 Interaction of GVD and SPM 19
2.3.4 Stimulated Raman scattering of pulsed signals 21
2.4 FIBER LASER AND AMPLIFIER 22
2.4.1 Ytterbium gain fibers 24
2.4.2 Erbium gain fibers 27
2.5 GENERATION OF LASER PULSES 31
2.5.1 Passive Q-switching and relaxation oscillations 32
2.5.2 Mode-locking 32
2.6 STRETCHING AND COMPRESSION OF OPTICAL PULSES 35

3 PASSIVE Q-SWITCHED YB^{3+}-FIBER LASER 39

3.1 EXPERIMENTAL SET-UP 40
3.2 Q-SWITCHED LASER OPERATION 41
3.2.1 Influence of output coupling 43
3.2.2 Influence of fiber length 44
3.2.3 Signal linewidth 45
3.2.4 Wavelength tuning 48
3.2.5 Laser operation without spectral selective elements 49
3.3 PHYSICAL MECHANISM OF PASSIVE PULSE GENERATION 51
3.3.1 Effects of Tm^{3+}-codoping 51
3.3.2 Relaxation oscillations 54
3.3.3 Polarization effects 56
3.4 CONCLUSION AND OUTLOOK 57

4 MODE-LOCKED YB^{3+}-FIBER LASER 59

4.1 EXPERIMENTAL SET-UP 59
4.2 MODE-LOCKED LASER OPERATION 61
4.3 PULSE ENERGY QUANTIZATION 64
4.4 CAVITY DISPERSION 66
4.5 SIGNAL CHIRP 68
4.6 INTRA-CAVITY PULSE DYNAMIC 71
4.7 CONCLUSION AND OUTLOOK 73

5 SUPER-BROADBAND YB^{3+}-FIBER LASER 75

5.1 EXPERIMENTAL SETUP 75
5.2 BROADBAND MODE-LOCKED LASER OPERATION 76
5.2.1 Filtering versus spectral broadening 80
5.3 BROADENING MECHANISM 82
5.3.1 Linear effects of the spectral filtering 82
5.3.2 Nonlinear broadening mechanism 84
5.4 CONCLUSION AND OUTLOOK 85

6 FEMTOSECOND ER^{3+}-FIBER OSCILLATOR-AMPLIFIER SYSTEM 87

6.1 EXPERIMENTAL SET-UP OF THE ER^{3+}-OSCILLATOR-AMPLIFIER SYSTEM 88
6.1.1 Femtosecond Er^{3+}-fiber oscillator 88
6.1.2 Fiber-stretcher 91
6.1.3 Pulse picking unit 93
6.1.4 Preamplifier 95
6.1.5 Power-amplifier 97
6.1.6 Grating compressor 100
6.2 EXPERIMENTAL RESULTS FOR THE OSCILLATOR-AMPLIFIER SYSTEM 102
6.2.1 Output signal of the fiber amplifier 102
6.2.2 Transmission properties of the grating compressor 105
6.2.3 Temporal pulse recompression 108
6.3 NONLINEAR EFFECTS IN THE FIBER AMPLIFIER 112
6.3.1 Spectral modulations 112
6.3.2 Nonlinear dispersion 116
6.3.3 Four-wave mixing 117
6.3.4 Gain saturation 120
6.3.5 Fiber surface damages 123
6.4 CONCLUSION AND OUTLOOK 125

7 SUMMARY AND OUTLOOK 127

APPENDIX 131

A CALCULATION OF OPTICAL FIBER PROPERTIES 131
A.1 Numerical approximation of the field distribution in an optical fiber 131
A.2 Calculation of the waveguide dispersion of an optical fiber 135
B UNITS IN FIBER OPTIC TELECOMMUNICATION AND LASER PHYSICS 136
C DOPING CONCENTRATIONS IN SILICA FIBERS 137
D ABBREVIATIONS 139

REFERENCES **141**

PUBLICATIONS **151**

CURRICULUM VITAE **155**

DANKSAGUNG **157**

1 Introduction

Continuous wave and pulsed solid-state lasers have revolutionized many areas like material processing, metrology, medicine, spectroscopy and basic scientific research. One prominent representative of these laser systems, the Ti:sapphire laser, is nowadays commercially available and has become the working horse for many applications. The versatility and the wide use of this laser is attributable to the large gain bandwidth of its laser material, which enables generation of ultrashort pulses as well as tunable laser operation over a broad wavelength range. Additionally, ultrashort pulses with energies of up to several millijoules have been demonstrated from Ti:sapphire based oscillator-amplifier systems. However, this laser material has also several drawbacks, as it must be pumped by gas lasers or frequency-doubled solid-state lasers. This results in a low overall efficiency, a large set-up and high system costs. Furthermore, the laser transition of Ti:sapphire has a lifetime of only about 3.2 microseconds and energy can be stored in this gain material only over a few microseconds. Thus, for repetition rates below several hundred kilohertz, pulsed Ti:sapphire lasers cannot be effectively pumped by continuous wave lasers. Moreover, the pulse repetition rate of oscillator-amplifier systems based on this gain material is usually limited far below 100 kHz, due to the required bulk electrooptic switches.

The broad gain bandwidth of rare-earth doped fibers, which is a result of the amorphous structure of silica glass, allows also tunable laser operation over a broad wavelength range and the generation of ultrashort pulses. However, compared to Ti:sapphire lasers, fiber based laser systems provide several advantages, as they can be efficiently pumped by laser diodes and can be realized in very compact set-ups. Additionally, the light guiding in the fiber results in a well-controlled beam shape, which is insensitive to thermal effects or external disturbances. Furthermore, energy can be stored in these fibers over a much longer time period, as the laser transitions have lifetimes of at least several hundred microseconds. Moreover, fiber-coupled electrooptic switches allow much higher repetition rates in fiber based oscillator-amplifier systems than for Ti:sapphire systems. Thus, potentially the output parameters of fiber based laser systems like wavelength, spectral width, pulse duration, pulse energy and repetition rate can be varied over a large range and adapted to the specific requirements of various applications. The objective of this work was therefore to develop fiber laser systems, which demonstrate the large variety of laser parameters that can be realized. For that reason,

three representative fiber laser set-ups were realized and investigating in detail during this work.

Generation of narrow linewidth laser pulses requires rather long pulse durations due to the Fourier limitation. Passive Q-switching is the preferred pulse generating mechanism for such laser systems, as it permits much longer pulses than mode-locking and it requires no additional control electronics. Commonly, saturable absorbers on the basis of Cr^{4+}-doped crystals or ceramics were used for initiating Q-switched laser operation in the near infrared. However, for fiber-based laser systems the use of such bulk elements results in a larger complexity and therefore the advantages of fiber-based systems cannot fully be exploited. Therefore, during this work a Q-switched fiber laser was developed, in which the saturable absorption was provided to the first time by a Thulium codoping in the gain fiber. By this way, the restrictions due to the previously required additional bulk saturable absorber can be overcome. The advantages of such a fiber-laser system can only be reached directly, if the various laser parameters can be adapted to the specific requirements. Thus, the Q-switching by the saturable absorption of the Thulium ions and the dynamics of the pulse generation were investigated experimentally and theoretically.

Much shorter pulse durations and larger spectral bandwidths can be generated by mode-locked lasers systems. However, most mode-locked fiber laser systems were directly pumped into the active fiber core. Therefore, these systems required high beam quality pump diodes, while the output power was rather limited. In combination with the cladding pumping scheme, fiber lasers can also be pumped by high power laser diodes with low beam quality. An important goal of this work was therefore the realization of a cladding pumped passive mode-locked Ytterbium-fiber laser.

Furthermore, spectral broadband laser sources with single mode-quality were needed for optical measurement techniques, like optical coherence tomography. This request is attributable to the fact, that the spectral bandwidth determines the minimum achievable resolution of such metrology systems. Therefore, an increase of the spectral bandwidth of mode-locked Ytterbium fiber lasers was a further goal of this work.

There is also a strong demand for compact and reliable high beam quality laser systems, which deliver pulse energies in the microjoule range at high repetition rates in combination with femtosecond pulse durations. This demand is driven by applications like fs-Lasik refractive surgery [HML03], writing of waveguides in silica glass [WNC02] [SBG01] or generation

of THz radiation [CLD02]. However, so far, the output pulse energies of femtosecond mode-locked fiber lasers are limited to several nanojoules. In order to overcome this limitation an oscillator-amplifier set-up was chosen, since such a set-up enables a scaling of the pulse energy to higher values, while the temporal pulse properties are still largely determined by the oscillator. Erbium fibers were chosen as gain material, since at the emission wavelength of these fibers at about 1.55 µm, the required fiber optic components are widely used for telecom applications and these components are reliable, relatively cheap and readily available. Furthermore, in combination with a nonlinear crystal, the output wavelength of such an oscillator-amplifier system matches the typical signal wavelength of conventional Ti:sapphire lasers. This strongly simplifies a replacement of Ti:sapphire lasers by this system.

The content of the work is arranged as follows: In chapter 2, the basic properties of pulsed fiber laser lasers are described. This description includes the various linear and nonlinear effects, which influence the pulse generation and propagation in the fibers, the properties of the used gain materials and the employed pulse generating mechanism. Chapter 3 focuses on the properties of a passively Q-switched Ytterbium fiber laser system. Based on the experimental results, the influences of the various physical effects on system operation are discussed. Chapter 4 covers the experimental results and the system properties of the realized mode-locked Ytterbium fiber laser. The extremely broadband operation of such a laser system, which can be achieved by intra-cavity spectral filtering, is then described in chapter 5. A chirped pulse oscillator-amplifier system is covered in chapter 6. The high output pulse energies of this system strongly favor nonlinear effects during signal amplification. Thus, the influences of the various nonlinear effects on system operation are analyzed. Furthermore, the resulting limitations are discussed and various methods to overcome these limitations are described in this chapter. Finally, in chapter 7 the results of this work are summarized.

2 Basics of pulsed fiber laser systems

2.1 Basics of fiber optics

In the geometrical model, wave guiding of optical fibers is due to total reflection of light rays at the boundaries of the dielectric core. Light is trapped as long as the incident angle, at the boundary between fiber core and surrounding cladding, meets the requirement for total reflection. Total reflection of light rays at this boundary can only occur if the light is incident from a denser to a less dense medium. Hence, light guiding in optical fibers requires that the refractive index of the core is higher than the surrounding cladding. This picture gives an intuitive understanding of light guiding in optical fibers. However, it takes not the wave properties of the light into account.

Each refractive index profile where a central part is surrounded with lower refractive index material can act as a waveguide. Since optical fibers have usually cylindrical symmetry, the following discussion is focused on waveguides with such symmetry. However it should be noted, that in general waveguides can also have other shapes or even have a one-dimensional structure (e.g. planar waveguides).

Optical waveguides can be made from various transparent materials like plastic, silica, fluoride or chalcogenide glasses [YEH89][GGZ98]. Nevertheless, silica glass is the material of choice for optical fibers in most cases. This is due to the extremely low optical loss, the good mechanical and chemical properties of this material and that it is non-toxic. The refractive index difference between the core and the cladding is realized during the fabrication process by adding dopants for increasing or decreasing the refractive index. Typically, germanium and phosphor are added for increasing the refractive index while boron and fluorine doping decrease it.

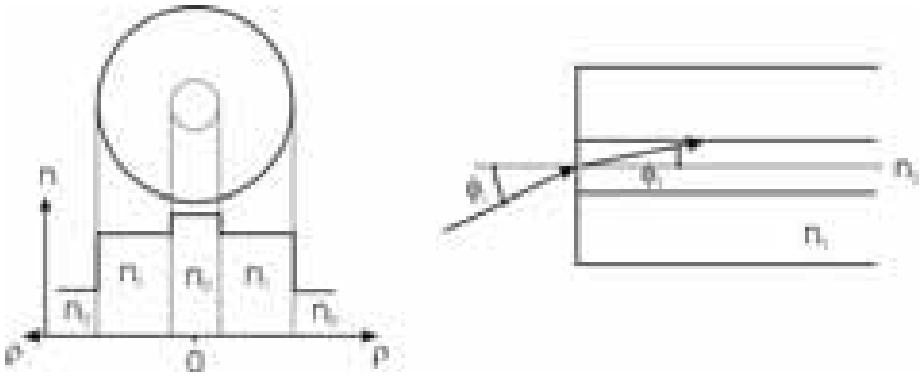

Fig. 2.1.1 *Left side: Index of refraction profile of a step-index fiber. n_0 is the index of the surrounding medium. Right side: Sketch for determining the numerical aperture of a step-index fiber.*

The simplest waveguide structure is a step in index profile, which has a constant refractive index in the core and in the cladding. Step index profiles are commonly used for optical fibers, since such structures are easier to manufacture than complicated index shapes. A schematic picture of the cross section and the refractive index profile of such a fiber is shown in figure 2.1.1. The refractive index difference between core and cladding determines the maximum incident angle θ_t at this boundary for total reflection. This boundary condition determines also the maximum acceptance angle of the fiber at the end facet, which is illustrated on the right side of figure 2.1.1. The sine of this angle is given by equation 2.1.1 and is called the numerical aperture NA of the fiber[1].

$$NA = n_0 \sin(\phi_i) = n_2 \sin(\phi_t) = \sqrt{n_2^2 - n_1^2} \tag{2.1.1}$$

2.1.1 Fiber modes

The previous geometrical approach is a good approximation if the core diameter of the fiber is several orders larger than the wavelength of the guided light. However, typically the wave properties of light must be taken into account, as these highly affects the signal propagation in a fiber. Based on Maxwell equations and the cylindrical symmetry of the fiber, it can be derived that the radial distribution of the transversal electric is determined in each sector by a differential equation for Bessel functions. The differential equations for the three cylindrical coordinates and the corresponding general solutions are shown in equations 2.1.2 – 2.1.6, where J_m, Y_m, K_m and I_m are different kinds of Bessel functions [AGR97]. The constant β in the solution of equation 2.3 shows the physical significance of a phase propagation constant.

$$d^2\Phi / d\phi^2 + m^2\Phi = 0 \tag{2.1.2}$$
$$\Rightarrow \quad \Phi = \exp(im\phi) \qquad m \in Z$$
$$d^2Z / dz^2 + \beta^2 Z = 0 \tag{2.1.3}$$
$$\Rightarrow \quad Z = \exp(i\beta z)$$
$$\frac{d^2F}{d\rho^2} + \frac{1}{\rho}\frac{dF}{d\rho} + \left(n^2 k_0^2 - \beta^2 - \frac{m^2}{\rho^2}\right) = 0 \tag{2.1.4}$$
$$\Rightarrow$$
$$F(\rho) = A\, J_m(\kappa\rho) + B\, Y_m(\kappa\rho) \qquad : \quad n \geq \beta / k_0 \tag{2.1.5}$$
$$\kappa^2 = n^2 k_0^2 - \beta_2$$
$$F(\rho) = C\, K_m(\gamma\rho) + D\, I_m(\gamma\rho) \qquad : \quad n < \beta / k_0 \tag{2.1.6}$$
$$\gamma^2 = \beta_2 - n^2 k_0^2$$

[1] The numerical aperture of a fiber is usually defined according to equation 2.1.1, although it is not very accurate for single-mode fibers. A more accurate description takes into account, that the output is essentially Gaussian in behavior and that the mode field diameter (MFD) in the fiber defines the beam waist for the output beam. Defining the MFD by the 1/e² intensity drop it can be shown that the NA is defined by $NA_{eff} = 2\lambda/(\pi\, MFD)$.

It can be also derived from Maxwell equations, that the tangential electric field and its first derivative must be continuous at the refractive index boundaries of an optical fiber [GUE90]. Furthermore, the field must be finite in the center and for a guided modes it must additionally decay roughly exponential for large ρ. It can be easily derived from the later of these conditions that for a step index fiber the constants B and D must be zero. The boundary condition at the index step results in an eigenvalue equation for the propagation constant β. Each eigenvalue β uniquely determines a field distribution and the corresponding fiber mode. Based on the constant β, an effective index n_{eff} can be defined for each mode (eqs. 2.1.7). This effective or mode index determines the propagation of a mode.

$$n_{eff} = \beta / k_0 = \beta \lambda / 2\pi \tag{2.1.7}$$

In general, the eigenvalue equation for β may have several solutions for each integer value of m. The number of the eigenvalues of β or the fiber modes depends on signal wavelength and the index profile of the fiber. For step index fibers, the two relevant design parameters are the numerical aperture NA and the core radius a. Usually, this relation is described by the normalized frequency V (eqs. 2.1.8).

$$V = k_0 \cdot a \cdot \sqrt{n_2^2 - n_1^2} = k_0 \cdot a \cdot NA \tag{2.1.8}$$

For large V values, a rough estimate for the number of the supported fiber modes is given by $V^2/2$, while for V-values below 2.405 only the fundamental mode is supported [AGR95]. The value of 2.405 is determined by the above mentioned eigenvalue equation and corresponds to the smallest solution for $J_0(V) = 0$. The cut-off wavelength of a fiber can be calculated by setting V = 2.405 and using $k_0 = 2\pi/\lambda$. For wavelengths below this cut-off, a fiber supports several modes and is therefore multi mode (MM) while it is single mode (SM) for longer wavelengths.

For the fundamental mode m = 0 and the field distribution has no zero except for $\rho \rightarrow \infty$. In addition, in a multi-mode fiber this mode has the highest eigenvalue β. The field distribution for this mode is described by the equations 2.1.9 and 2.1.10, where the constant A is determined by the signal power. For arbitrary refractive index profiles the numerical calculation of the propagation constant β and the corresponding field distribution is described in Appendix A.

$$F(\rho) = A\, J_0(\kappa \rho) \qquad \rho \le a \tag{2.1.9}$$

$$F(\rho) = \frac{A\, J_0(\kappa a)}{K_0(\gamma a)} K_0(\gamma \rho) \qquad \rho \ge a \tag{2.1.10}$$

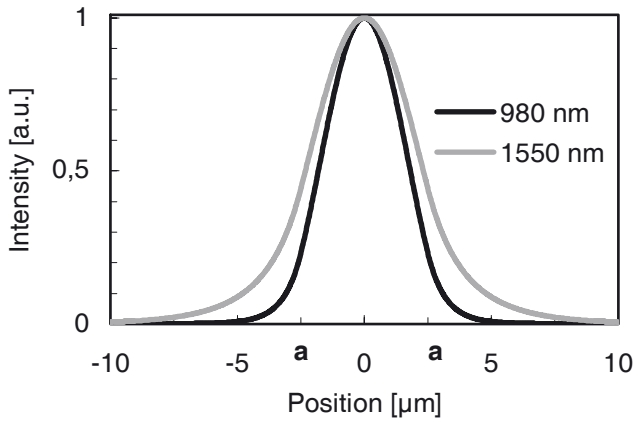

Fig. 2.1.2 *Field distribution for a 980 nm and a 1550 nm signal in step index fiber with a core radius of 2.5 µm and a numerical aperture of 0.13.*

Figure 2.1.2 shows the field distribution of the fundamental mode in a step index fiber for two wavelengths. It can be noticed, that the field extents more into the cladding and that therefore the mode field diameter becomes larger with increasing wavelength.

2.1.2 Chromatic dispersion

For each fiber mode, the propagation speed depends on the signal wavelength. This property, referred as chromatic dispersion, is due to the fiber material and the waveguide. The first effect, which is designated as material dispersion, is fundamentally related to the absorption lines of the material [BSC93], while the waveguide dispersion is due to the dependence of the field distribution on signal wavelength (see Fig. 2.1.2). The latter affects , the effective index of a mode, since the refractive index in the cladding is lower than in the core. Mathematically, the effect of the chromatic dispersion on the signal propagation in fibers can be explained by expanding the constant β in a Taylor series about the center frequency ω_0 [AGR95]. Equations 2.1.11 – 2.1.15 show this expansion and the relation of some of the Taylor-coefficients with the effective refractive index.

Based on this expansion, the group velocity v_g, which determines the propagation of a signal, is the inverse of β_1 and the group refractive index n_g is proportional to β_1. Thus, β_2, the second derivative of the propagation constant, determines the group velocity dispersion (GVD). It should be noted that fiber dispersion is related to the second derivative of the refractive index, while chromatic dispersion in bulk optics, e.g. for lenses and prisms, is related to the fist derivative. If $\beta_2 > 0$, a fiber has normal dispersion and the group velocity increases with increasing wavelength, while for $\beta_2 < 0$ a fiber has anomalous dispersion.

$$\beta(\varpi) = n_{eff}(\varpi)\frac{\varpi}{c} = \beta_0 + \beta_1(\varpi - \varpi_0) + \frac{1}{2}\beta_2(\varpi - \varpi_0)^2 + \frac{1}{6}\beta_3(\varpi - \varpi_0)^3 + \ldots\ldots \qquad (2.1.11)$$

$$\beta_m = \left[\frac{d^m n_{eff}}{d\varpi^m}\right]_{\varpi=\varpi_0} \tag{2.1.12}$$

$$\beta_1 = \frac{1}{c}\left[n_{eff} + \varpi\frac{dn_{eff}}{d\varpi}\right] = \frac{n_g}{c} = \frac{1}{v_g} \tag{2.1.13}$$

$$\beta_2 = \frac{1}{c}\left[2\frac{dn_{eff}}{d\varpi} + \varpi\frac{d^2 n_{eff}}{d\varpi^2}\right] \cong \frac{\varpi}{c}\frac{d^2 n_{eff}}{d\varpi^2} \cong \frac{\lambda^3}{2\pi c^2}\frac{d^2 n_{eff}}{d\lambda^2} \tag{2.1.14}$$

$$\beta_2 = \beta_{2material} + \beta_{2waveguide} = \frac{\lambda^3}{2\pi c^2}\left[\left(\frac{d^2 n_{eff}}{d\lambda^2}\right)_{waveguide=const} + \left(\frac{d^2 n_{eff}}{d\lambda^2}\right)_{n\,material=const}\right] \tag{2.1.15}$$

For pure silica glass the material dispersion is normal for wavelength below 1.27 µm and becomes anomalous above this wavelength. At 1.55 µm, the material dispersion of silica is about $-2.55 \cdot 10^{-26}$ s²/m [AGR95]. The waveguide dispersion it is generally normal, since with increasing wavelength a larger fraction of the signal propagates in the low index cladding, and depends strongly on the refractive index profile of the fiber. At 1.55 µm, standard step-index telecommunication fibers have a waveguide dispersion of about $4 \cdot 10^{-27}$ s²/m. Nevertheless, fibers, which were specially designed for dispersion compensation, can have a waveguide dispersion of up to $1.7 \cdot 10^{-25}$ s²/m [NAS01]. For arbitrary refractive index profiles the numerical calculation of the waveguide dispersion is described in Appendix A.2.

Finally, it should be mentioned that for characterizing the dispersion of a fiber the dispersion parameter D is often used instead of β_2. The relation between these two parameters is described by equation 2.1.16. It should be specially noted, that these two parameters have opposite sign[2].

$$D = -\frac{2\pi c}{\lambda^2}\beta_2 = -\frac{\lambda}{c}\frac{dn_{eff}^2}{d\lambda^2} \tag{2.1.16}$$

2.1.3 Modal birefringence

Previously the polarization of the light was not taken into account, since no polarization axis is preferred in a fiber with cylinder symmetry. As a result, the fiber is degenerate relating to polarization and strictly, each fiber mode consists of two polarized modes. However, in practice small departures from material isotropy and the cylindrical geometry or mechanical tensions inside the fiber breaking the mode degeneracy [AGR95] [URE80]. Because of that,

[2] The parameters β_2 [s²/m] and D [s/m²] describe here the dispersion per unit length. However, it should be noted, that in this work the same symbols were also used for the total dispersion, which is the local dispersion integrated over the corresponding length.

the mode propagation constant becomes slightly different for the two polarization modes, which is referred as modal birefringence. Based on this, a modal birefringence parameter B is defined (eqs. 2.1.17).

$$B = \frac{|\beta_x - \beta_y| \cdot \lambda}{2\pi} = |n_x - n_y| \tag{2.1.17}$$

In standard fibers the degree and the orientation of the birefringence changes randomly along the fiber, because of the fluctuations of the core geometry, fiber bending and external stress. This results in random fluctuations of the signal polarization along the fiber. In addition, variations of the fiber bending or of the external stress modify the polarization at the fiber end. This effect can be suppressed by using fibers where a large amount of birefringence is intentionally introduced, so that this birefringence is much larger than the random fluctuations. Thus, these fluctuations do not affect the signal polarization significantly, if the signal polarization is orientated along one of the fiber axis. Such polarization maintaining (PM) fibers were produced by using an elliptical core or inserting stress elements into the cladding [KJG01].

In addition to the formerly mentioned linear birefringence, fibers can also show circular birefringence. In particular, a fiber twist causes a circular birefringence, which is proportional to the amount of the twist [USI79]. Hence, external pressure in combination with a fiber twist, which result in linear and circular birefringence, can be used for arbitrarily changing the polarization state of a signal inside the fiber.

2.2 Nonlinear effects in fibers

The small core size of single mode fibers results in high signal intensities. Furthermore, this high intensity can be maintained over a long path due to the wave guiding and the low loss of these fibers. Thus, nonlinear effects can significantly affect a signal during propagation in a silica fiber, although the nonlinearity of silica is small compared to most other media [AGR95].

Relevant nonlinear effects in silica are due to the third order susceptibility and to inelastic interactions of the light with the dielectric medium. The optical Kerr-effect and four-wave mixing are attributable to the third order susceptibility, while inelastic interactions are the cause for stimulated Raman- (SRS) and Brillouin-scattering (SBS). All these nonlinear effects are proportional to the signal intensity. Consequently, a detailed analysis of the nonlinear effects must consider the intensity distribution of the fiber mode. For this reason, an effective mode field area A_{eff} was defined (eqs. 2.2.1).

$$A_{eff} = \frac{\left[\oint_{fiber} I(\rho,\phi)d\rho d\phi\right]^2}{\left[\oint_{fiber} I^2(\rho,\phi)d\rho d\phi\right]} \tag{2.2.1}$$

2.2.1 Kerr-Effect

In a dielectric material, a light signal induces electric dipoles, since the electric field of the light interacts with the bound electrons. For extremely high electric fields, this motion is significantly anharmonic and the induced polarization of the electric dipoles in the material shows nonlinear behavior.

The second order susceptibility vanishes in silica glass because of the inversion symmetry of this amorphous material. Hence, the third order susceptibility is the lowest order which results in nonlinear behavior of the induced polarization. The most important effect of this nonlinearity is typically the intensity dependence of the refractive index (Kerr-effect). As a result, the light propagation in waveguides is influenced by the intensity and the time dependence of the signal. This dependence of the refractive index on the intensity is described in equation 2.2.2, where n(ω) is the linear refractive index, n_2 is the nonlinear index coefficient and I is the optical intensity.

$$n(\varpi, I) = n(\varpi) + n_2 \left| E^2 \right| = n(\varpi) + n_2 I \tag{2.2.2}$$

$$n_2 = \frac{3}{8n}\mathrm{Re}\left(\chi^3_{xxx}\right) \tag{2.2.3}$$

The relation between the nonlinear index n_2 and the third-order susceptibility χ^3_{xxx} is shown in equation 2.2.3 for linear polarized light. The tensorial nature of the third-order susceptibility must taken into account, if the nonlinear index change is calculated for other polarization states. For pure silica, the n_2 value due to the Kerr-effect is $2.16 \cdot 10^{-20}$ m²/W. For telecommunication fibers, values between $2.1 \cdot 10^{-20}$ m²/W and $2.3 \cdot 10^{-20}$ m²/W were typically measured, since the core doping slightly modifies the nonlinear index [SPA02][MMF99].

It should be remarked, that in addition to the Kerr-effect, the Raman response and the electro-striction of the material cause also an intensity dependence of the refractive index. Hence, these are additional contributions to the nonlinear index n_2 in equation 2.22. The contribution of the Raman response is about 20% of the nonlinear index that is attributable to the Kerr-effect and has a response time of about 75 fs. Because of this relative fast response, it is commonly included in the nonlinear index, although the polarization dependence is slightly

different [BBU98]. The electrostriction contribution is highly frequency dependant, but polarization independent. The corresponding response time is about 1 ns and depends on fiber geometry. Because of this relatively slow response, it can be neglected for sub-ns pulses. However, due to resonance effects, this contribution can significantly influence the propagation of pulse trains with repetitions rates in the MHz range [FWA98].

Finally, it should be mentioned that the nonlinear refractive index changes slightly the refractive index profile of the fiber. This modification of the refractive index profile causes a slight variation of the mode field distribution. By this way, the intensity influences additionally the propagation constant in the fiber. The above mentioned effect is closely related to the Kerr-lens self-focusing of high intensity signals in bulk optic elements.

Numerical calculations showed that in silica fibers the influence of this effect on the mode distribution is small, as the influence on the propagation constant is typically below 1% of the direct n_2 effect. However, in fibers which are made from materials with much higher nonlinearity this effect can significantly modify the mode field distribution and the propagation constant [MSA98].

2.2.2 Self- and cross-phase-modulation

The refractive index of the fiber and consequently the propagation constant depends on the signal intensity due to the Kerr-effect. By this way, the signal intensity influences signal propagation and phase. The corresponding nonlinear phase shift, which is self-induced by the signal intensity, is called self-phase modulation (SPM). For nonlinear phase shifts, which are attributable to copropagating signals with different wavelength or polarization, the term cross-phase modulation (XPM) is used.

Variations of the refractive index and the corresponding SPM induced phase shift were caused by temporal intensity variations. Hence, an intensity peak travels slower and an intensity tip faster than the adjoining signal. By this nonlinear interaction, an increase of the intensity decreases the instantaneous optical frequency. Consequently, at the leading edge of a pulse, the optical frequency is down, red shifted, while at the tailing edge it is up or blue shifted. Because of this frequency shift, new frequency components were generated during the propagation. This is illustrated in figure 2.2.1. For a particular pulse shape, this effect is proportional to the peak intensity. The absolute nonlinear phase shift ϕ_{NL} caused by SPM is given by equation 2.2.4 where z is the propagation distance, P is the signal power, n_2 the

nonlinear index, γ the fiber specific nonlinear coefficient, λ the signal wavelength and A_{eff} the effective mode field area.

$$\phi_{NL}(z,T) = \gamma P(t) z \qquad \gamma = \frac{2\pi n_2}{A_{eff}\lambda} \tag{2.2.4}$$

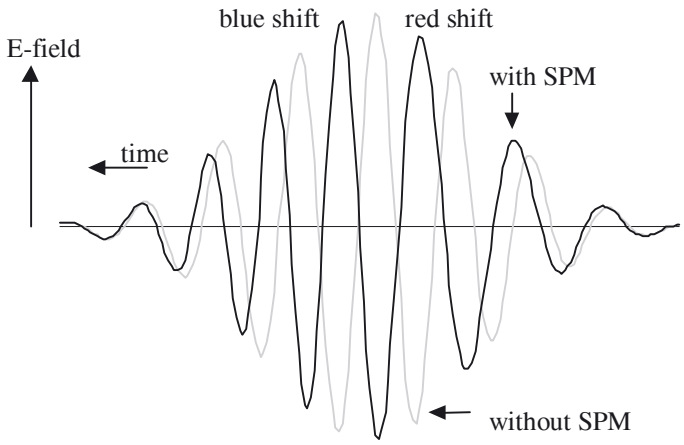

Fig. 2.2.1 *Phase shift due to self phase modulation*

Furthermore, due to SPM the tailing edge of a pulse becomes steeper during propagation, since the propagation velocity decreases with increasing intensity. This effect is called self-steepening and must be taken into account for short peaks of high intensity.

The nonlinear refractive index causes also an interaction between two copropagating waves with different polarizations or frequencies. In addition to the SPM, this XPM introduces a phase shift, which is proportional to the intensity of the copropagating wave. For orthogonal polarized signals, the nonlinear XPM phase shift is only 2/3 of the corresponding SPM phase shift, while for signals with the same polarization and different frequencies the XPM is twice as effective as the SPM.

The different strength of the XPM and the SPM is due to the tensorial nature of the third-order susceptibility. It results in a nonlinear phase shift between the orthogonal polarized components of an elliptically polarized signal. Consequently, the polarization state of an elliptically polarized signal evolves nonlinearly during propagation. This nonlinear polarization evolution can be used for mode-locking of fiber laser systems [HFH91].

2.2.3 Stimulated Raman scattering

Raman scattering in nonlinear media is caused by inelastic scattering of photons. This inelastic scattering converts the incident photons of the pump wave into photons with lower frequency. This is called the Stokes signal. Simultaneously optical phonons were created in

the material. The Raman frequency shift depends on the vibrational modes of the nonlinear medium. Raman scattering shows specific frequency shifts in crystalline materials, while in amorphous materials, like silica glass, the frequency shift is a broad continuum.

Raman scattering can be stimulated by photons at the Stokes wavelength, if they had the same polarization as the Raman pump. The amplification of a forward propagating Stokes signal by stimulated Raman scattering (SRS) is described equation 2.2.5, where I_S is the intensity of the Stokes signal, I_P is the pump intensity and $g_{R(\Delta\omega)}$ is the Raman gain coefficient [AGR95]. A minus sign must be inserted in this equation, if pump and Stoke waves propagate anti-parallel. The equation for the depletion of the pump light can be easily derived from this equation by taking the different quantum energies of the pump and Stokes photons into account.

$$\frac{dI_S}{dz} = g_R(\Delta\varpi)\, I_P\, I_S \qquad (2.2.5)$$

In silica glass the Raman gain coefficient extents up to a frequencies of about 40 THz and has a broad peak of about 5 GHz bandwidth (FWHM) near 13 THz. The maximum gain coefficient of this material is about $1.0 \cdot 10^{-13}$ m/W at 1.0 µm and is inversely proportional to the pump wavelength [STO80]. However, the gain coefficient of silica fibers can be slightly different, as the fiber core is typically doped with dopants like germanium, phosphor or boron. The measured relative Raman gain versus frequency of a standard telecommunication fiber is displayed in figure 2.2.2.

Finally, it is worth to mention that the Raman gain is the same for forward and backward propagating signals, although it was written in reference [AGR95], that SRS dominates in the forward direction. This equality was mentioned in reference [STO80] and was in addition experimentally confirmed to an accuracy of 2% for two different telecommunication fibers.

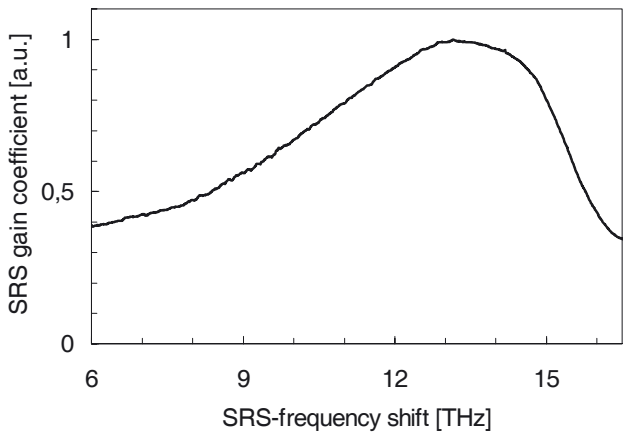

Fig. 2.2.2 *Relative Raman gain versus frequency of a standard telecommunication fiber.*

2.2.4 Stimulated Brillouin scattering

Similar to Raman scattering, Brillouin scattering is caused by inelastic scattering of photons in a nonlinear medium. However, the frequency of the incident photons is downshifted by generation of acoustic phonons, while optical phonons participate in Raman scattering. Because of the interaction with acoustic phonons, Brillouin scattering occurs only in backward direction. In addition, frequency shift and gain bandwidth are much smaller for stimulated Brillouin scattering (SBS) than for stimulated Raman scattering. Typical values for the Brillouin frequency shift and gain bandwidth in a silica fiber at 1.5 µm are 10 GHz and 10 MHz, respectively. The frequency shift increases linear with the pump frequency while the gain bandwidth is proportional to the square of the pump frequency [STO80]. However, Brillouin frequency shift and gain bandwidth depend also on fiber structure parameters like the core radius [YPO02]. The reason for that is that the fiber structure influences acoustic waves in the fiber and that Brillouin scattering is attributable to an interaction between light waves and acoustic waves.

The equation describing the signal amplification by SBS is similar to equation 2.2.5. However, a minus sign must be inserted, since pump and the Brillouin Stokes signal propagate anti-parallel. Furthermore, the Raman gain coefficient must be substituted by the Brillouin gain coefficient.

Brillouin scattering is strongly reduced, if the duration of a pulsed signal becomes much smaller than the lifetime of acoustic phonon. Therefore, due to the short pulses SBS can be usually ignored in mode-locked fiber lasers.

2.2.5 Four-wave-mixing

Third order susceptibility is also the origin for the nonlinear four-wave mixing (FWM). This effect generates a forth field with frequency f_4, if three waves with frequency f_1, f_2 and f_3 propagate simultaneously phase matched in a fiber. The frequency f_4 has a relation to the other frequencies of the form $f_4 = \pm f_1 \pm f_2 \pm f_3$, since the energy is conserved in FWM. Usually phase matching is achieved only for combinations of the form $f_4 = f_1 + f_2 - f_3$. In this expression, the indices 1, 2 and 3 can be interchanged. If $f_1 = f_2$, this process generates two sidebands symmetrically located to the frequency of the input signal. Similar to SRS and SBS, the low and the high frequency sidebands are referred as Stokes and Anti-Stokes sidebands. The generation of these sidebands can be increased, if a signal with one of the sideband frequencies is launched simultaneously with the pump into the fiber. By this way, the signal at

is amplified by the parametric gain of the FWM, while the other sideband is generated simultaneously. The parametric gain factor, which describes the signal amplification similar to equation 2.2.5, is about $2 \cdot 10^{-13}$ m/W at 1 µm, if these waves are perfectly phase matched and is inversely proportional to the signal wavelength. Thus, the parametric gain is about a factor of two larger than the SRS gain at its maximum. The phase matching requirement for the FWM process is given by equation 2.2.6, where n_i are the refractive index for a wave with frequency f_i and Δk is the wave vector mismatch.

$$\Delta k = k_3 + k_4 - k_1 - k_2 = \frac{2\pi}{c}\left(n_3 f_3 + n_4 f_4 - n_1 f_1 - n_2 f_2\right) \cong 0 \qquad (2.2.6)$$

Partially degenerate FWM, in which $f_1 = f_2$ is of particular interest in optical fibers as phase matching becomes easier by this degeneracy. In single mode fibers, this phase matching can be achieved, if the zero dispersion wavelength is close to the signal wavelength or by a modal birefringence [AGR95]. Typically, a small phase vector mismatch is remaining due to fiber dispersion, fiber birefringence and the Kerr-effect. Not to close to the zero dispersion wavelength, the resulting vector mismatch caused by fiber dispersion is given by equation 2.2.7 for the partially degenerate case. For such a vector mismatch, significant FWM occurs only on fiber lengths, which are shorter than the corresponding coherence length L_{coh} (eqs. 2.2.8) [AGR95].

$$\Delta k = \beta_2 \cdot \Omega^2 \qquad \Omega = 2\pi(f_2 - f_1) = 2\pi(f_1 - f_3) \qquad (2.2.7)$$

$$L_{coh} = \frac{2\pi}{\Delta k} = \frac{2\pi}{\beta_2 \cdot \Omega^2} \qquad (2.2.8)$$

Hence, phase matching can be maintained only for short fiber lengths, except for small frequency shifts. Furthermore, even for perfectly phase matched waves, the phase matching is usually disturbed after a short fiber length by fluctuations of fiber birefringence and dispersion. Consequently, the FWM efficiency is especially increased by using short highly nonlinear fibers or high light intensities [AAY00]. Under such circumstances, FWM can make a large contribution to the spectral broadening of a pulsed signal [CCL02].

2.3 Pulses in optical fibers

The previous mentioned linear and nonlinear effects influence the temporal and spectral properties of light pulses during propagation in an optical fiber. At low intensities, the pulse evolution is dominated by the group velocity and polarization mode dispersion. However, for higher signal intensities nonlinear effects and the interaction of the linear and nonlinear effects must also be taken into account.

2.3.1 Dispersion pulse broadening

The duration of a light pulse depends on the pulse spectrum and on the phase relation between the different spectral components. In fibers with non-zero group velocity dispersion the refractive index varies with wavelength. Hence, such a fiber alters the phase relation between of the different spectral components of a pulse. Therefore, generally pulse duration and shape change during propagation.

For Gaussian shaped pulses the GVD influences only the pulse duration, while the pulse shape is maintained. Equation 2.3.1 describes the influence of the fiber dispersion on the pulse duration for a bandwidth limited Gaussian input pulse. In this equation $T_{0\,FWHM}$ denotes the input pulse duration (full width at half maximum), z the fiber position and $T_{1\,FWHM}(z)$ the pulse duration at this position. Equation 2.3.2 describes this temporal pulse broadening in terms of the dispersion parameter D and the spectral pulse bandwidth $\Delta\lambda_{\,FWHM}$. The pulse broadening of effect of the GVD is also illustrated in figure 2.3.1, where the pulse duration is plotted versus applied GVD for Gaussian pulses with bandwidths of 10 nm or 20 nm at 1550 nm. Furthermore, the temporal pulse shapes are shown of the bandwidth limited pulse and for an applied GVD of -127000 fs^2 (= 0.1 ps/nm). It can be seen that the pulse duration decreases with increasing spectral bandwidth if the pulses are nearly bandwidth limited, while it increases with signal bandwidth for large GVD stretching ($D\cdot\Delta\lambda_{FWHM}\cdot z >> T_0$).

$$T_{1\,FWHM}(z) = T_{0\,FWHM}\sqrt{1+\frac{16\ln^2(2)\,\beta_2^{\,2}z^2}{T_{0\,FWHM}^4}} \tag{2.3.1}$$

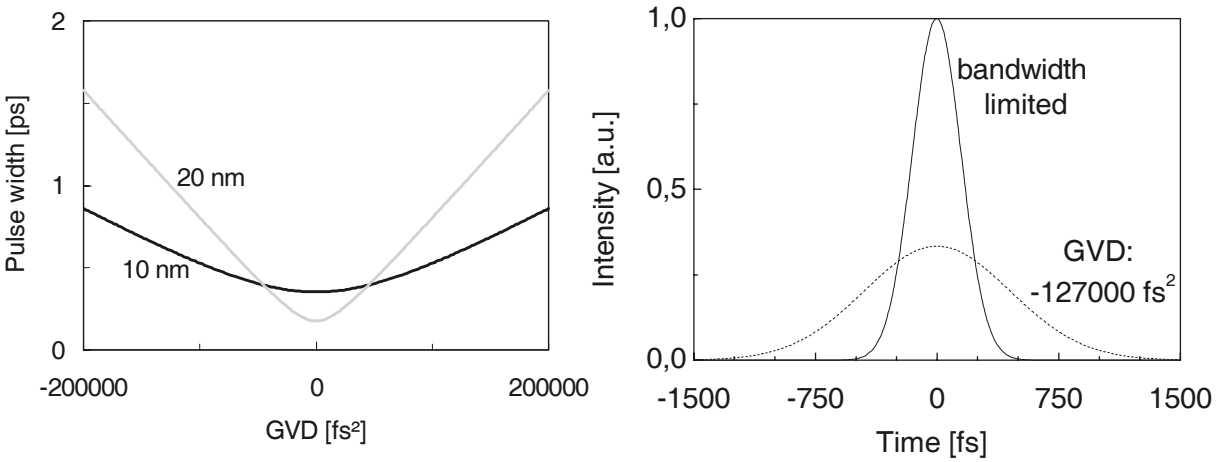

Fig. 2.3.1 *Left diagram: Pulse broadening as a function of the GVD for Gaussian pulses with a center wavelength of 1550 nm and a FWHM spectral bandwidth of 10 nm (black curve) or 20 nm (grey curve). Right diagram: Bandwidth limited pulse shape for a Gaussian pulse width 10 nm bandwidth at 1550 nm (solid line).The dashed line shows the corresponding pulse shape after stretching by -127000 fs². This GVD value corresponds to a propagation distance of about 6 m in a standard telecommunication fiber.*

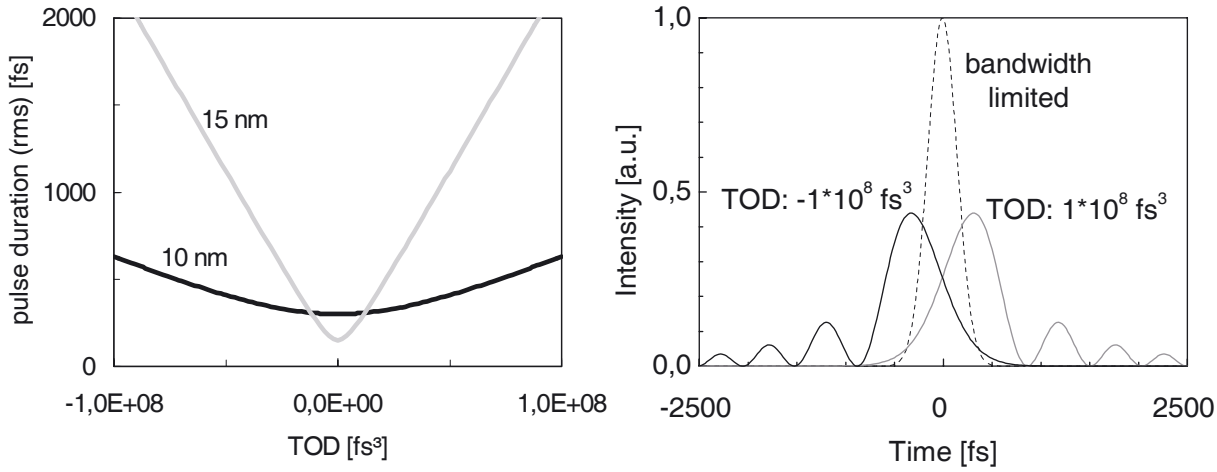

Fig. 2.3.2 *Left diagram: Influence of the TOD on the rms-pulse width for Gaussian pulses with 10 nm (black curve) and 15 nm (gray curve) bandwidth (FWHM) and a center wavelength of 1550 nm. Right diagram: Influence of TOD –1*10⁸ fs³ (black curve) and 1*10⁸ fs³ (gray curve) on pulse shape for a pulse with a Gaussian spectrum of 10 nm bandwidth at 1550 nm. The dashed curve shows the corresponding bandwidth limited pulse shape.*

$$T_{1FWHM}(z) = \sqrt{T_{0FWHM}^2 + \frac{\left(D \cdot \Delta\lambda_{FWHM}\, z\right)^2}{\ln 2}} \cong \frac{D \cdot \Delta\lambda_{FWHM}\, z}{\sqrt{\ln 2}} \quad \left(D\,\Delta\lambda_{FWHM}\, z >> T_{0FWHM}\right) \qquad (2.3.2)$$

Previous discussion included only the dispersive pulse broadening by the GVD. Especially near the zero dispersion wavelength of fiber, or if the GVD of one element is compensated by another element, the third order dispersion (TOD) can become the dominating dispersion term. Consequently, under such circumstances the influence of the TOD on pulse duration and shape must be included. For Gaussian pulses, the combined influence of the GVD and the TOD on pulse duration is described by equation 2.3.3 [AKH92]. As the TOD modifies the pulse shape, the pulse width evolution cannot be suitable described by the FWHM pulse width definition and therefore the root-mean-square pulse width definition was used. In this equation $\tau_{o\,rms}$ denotes the rms pulse-width and Δt_0 the half 1/e width of the bandwidth limited Gaussian pulse. The influence of the TOD on the rms-pulse width is illustrated in the left diagram of figure 2.3.2. Furthermore, it can be seen in the right diagram of this figure, that stretching by TOD results in additional peaks before (or after) the main pulse[3].

$$\tau_{rms} = \tau_{0rms} \cdot \sqrt{1 + \left(\frac{\beta_2}{\Delta t_0^2}\right)^2 + \left(\frac{\beta_3}{2\,\Delta t_0^3}\right)^2} \qquad (2.3.3)$$

For a bandwidth-limited pulse, the carrier frequency is constant along the pulse. However, the carrier frequency varies along the pulse in dispersion-broadened pulses as the different spectral components were separated. This frequency chirp is linear for pulses temporally broadened by GVD, while the TOD introduces a quadratic chirp. Pulses broadened by normal

[3] In figure 2.3.2 pulse intensities are plotted versus time for a specific location along propagation path. Pulse shapes are reversed, if the intensity curves are plotted for a specific time along the propagation axis.

dispersion (D < 0) have a positive chirp, as the carrier frequency increases from the leading to the tailing edge while for anomalous dispersion the chirp is negative.

2.3.2 Polarization mode dispersion

An additional source for pulse broadening is the fiber birefringence. An input pulse, which excites both polarization modes in a birefringence fiber, has different propagation velocities in the two modes and the two orthogonal polarized signal components separate during propagation. The time delay ΔT between these two components is given by equation 2.3.4 as a function of the birefringence B and the propagation distance z.

$$\Delta T = \frac{2\pi}{\lambda} B \cdot z \tag{2.3.4}$$

By this way, the birefringence of a polarization maintaining fiber leads to the evolution of two separate pulses, if the input polarization is not parallel to one of the polarization axis. However, in standard fibers the amount and the orientation of the birefringence vary randomly along the fiber, which results in a coupling between the polarization modes. Thus, an input pulse is spread out by the polarization mode dispersion (PMD). This broadening scales with the square root of the fiber length, if the fiber is much longer than the fluctuation length. For standard telecommunication fibers, the PMD broadening is typically between 0.1 $ps/\sqrt{km}$ and 1 $ps/\sqrt{km}$. Consequently, even for short fiber length the polarization mode dispersion can significantly increase the duration of femtosecond pulses.

2.3.3 Interaction of GVD and SPM

The group velocity dispersion changes pulse duration and shape during propagation in the fiber. Hence, the GVD influences also the SPM, since the SPM depends on signal intensity and pulse shape. Furthermore, an interaction between these two effects is due to the fact, that the GVD as well as SPM influence the signal chirp during propagation. The GVD separates (or unites) the different spectral components of a pulse, while the SPM causes a red shift at the leading edge and a blue shift at the tailing edge of a pulse (fig. 2.2.1).

In order to compare the influence of GVD and SPM on a propagating pulse, the dispersion length L_D and the nonlinear length L_{NL} is defined (eqs. 2.3.5 – 2.3.6). The dispersion length corresponds to the propagation distance after which the pulse duration of a bandwidth limited Gaussian pulse has doubled due to the GVD. In equation 2.3.5 T_0 denotes the half 1/e pulse

width for a Gaussian pulse or the half sech(1) pulse width for a hyperbolic-secant pulse. The nonlinear length corresponds to the propagation distance after which the SPM had introduced a phase shift of 1 at the pulse maximum with peak power P_0 (eqs. 2.3.6) [AGR95].

$$L_D = \frac{\Delta t_0^2}{|\beta_2|} \tag{2.3.5}$$

$$L_{NL} = \frac{A_{eff}\,\lambda_0}{2\pi\, n_2\, P_0} \tag{2.3.6}$$

If the nonlinear length is much larger than the dispersion length, fiber dispersion dominates over SPM, the influence of the SPM on pulse evolution is small and the interaction between GVD and SPM can usually be neglected.

Both effects have initially the same strength, if the nonlinear length is equal to the dispersive length. In a fiber with normal dispersion, GVD and SPM generate a positive pulse chirp. Thus, the pulse broadens more rapidly than without significant SPM. Finally, after several dispersion lengths, the pulse evolution is dominated by GVD as the pulse broadening reduces the intensity.

If the nonlinear length is equal to the dispersive length in a fiber with anomalous dispersion, the chirp induced by SPM and GVD nearly cancels each other along the central part of a Gaussian pulse. It can be mathematically shown, that under these circumstances a complete cancellation occurs for hyperbolic-secant-pulses. These pulses were called optical solitons, since the shape of these pulses remains constant during propagation in the fiber. The energy of these pulses is determined by the fiber dispersion β_2 and the pulse duration T_0 (ΔT_{FWHM} = 1.763 T_0) (eqs. 2.3.7). [AGR95].

$$W_{sol} = \frac{2c\, A_{eff}\, \beta_2}{n_2\, \varpi_0\, T_0} \tag{2.3.7}$$

Solitons are the only solutions of the propagation equation, which are stable against small perturbations in anomalous dispersive fibers. For this reason, solitons evolve during pulse propagation in an anomalous dispersive fiber, even if the input signal deviates slightly from a soliton.

SPM dominates over GVD, if the nonlinear length becomes much shorter than the dispersive length. SPM therefore introduces a chirp onto the pulse and new frequency components were generated by SPM. Nevertheless, the GVD cannot be treated as a small perturbation, since dispersive effects have a significant influence on pulse shaping. The reason for that is the large SPM induced frequency chirp.

For a Gaussian pulse, the SPM induced chirp is linear and positive over a large central region and approaches zero in the outer pulse wings. In anomalous dispersive fibers, the interaction

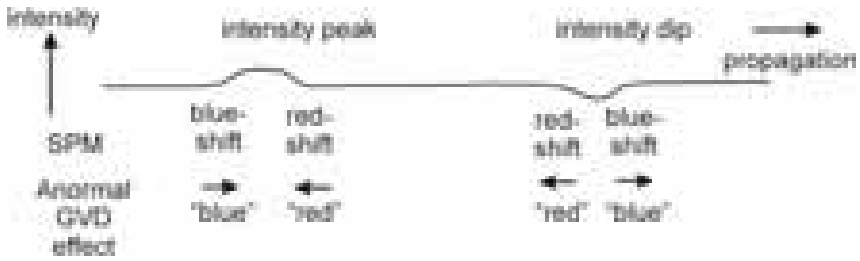

Fig 2.3.3 *Effects of SPM and GVD on a cw-signal with intensity fluctuation in an anomalous dispersion fiber.*

of this central chirp with fiber dispersion results in a pulse compression and the pulse evolves into one or several solitons [MEN93][ATT97]. On the other hand, in normal dispersive fibers the GVD induced chirp has the same sign as the SPM induced chirp in the central pulse region. Therefore, the stretching caused by GVD is stronger for the central part than for the outer wings and the pulse becomes more rectangular with sharp leading and tailing edges. This is accomplished by a linear chirp nearly across the entire pulse width. In addition, during this pulse stretching SPM generates typically multi peaks in the central part of the spectrum, which were modified and reduced by the additional effect of the GVD [AGR95].

Another effect of the interaction of SPM and GVD is that continuous wave signals or highly chirped pulses are inherently unstable against perturbations in an anomalous dispersive fiber. In such fibers, the SPM causes a red shift in front and a blue shift at the tail of a small intensity peak. Due to the anomalous GVD, the red shifted and the blue shifted signal components moves to the intensity peak. Thus, the peak is enlarged and SPM is further increased, which results in a roughly exponentially grow. In the same way an intensity dip increases during propagation. This effect is called modulation instability and is illustrated in figure 2.3.2. It strongly limits the signal intensity in fiber amplifiers with anomalous dispersion fibers. On the other hand, in fibers with normal dispersion, the GVD has the opposite effect. Thus, the interaction of SPM and GVD reduces the intensity fluctuations along the signal, except for dark solitons. The later corresponds to an intensity dip in a uniform background. Compared to solitons in anomalous dispersion, the opposite sign of the dispersion parameter is compensated by an inverse intensity distribution [AGR95].

2.3.4 Stimulated Raman scattering of pulsed signals

Compared to continuous wave signals, short pulses have typically higher peak intensities and larger spectral bandwidths. In addition, the pulse energy is concentrated to a short time interval. These features give rise to the following differences in the interaction of the SRS with continuous and pulsed signals.

The higher peak intensity of pulsed signals increases the SRS. However, fiber dispersion results in different propagation velocities for pump and stokes signal. The resulting walk-off limits the interaction length for short pulses in dispersive fibers.
Furthermore, short optical pulses have a large spectral bandwidth, because of the time-bandwidth limit. In an unchirped pulse, these spectral components are equally distributed along the pulse. Hence, the different wavelength components of the pulse can interact by SRS, This causes an energy transfer to longer wavelengths and therefore an increase of the mean wavelength. This is called Raman self-frequency shift [MMO87]. For chirped pulses, this self-frequency shift is strongly reduced, since the different spectral components are distributed along the pulse.

2.4 Fiber laser and amplifier

Light can be amplified by fibers with laser active atoms in the core, if the signal wavelength is inside the gain spectrum. However, this requires a population inversion of these atoms, which is usually realized by optical pumping. Under such circumstances, the amplification increases with fiber length until saturation occurs, since the light is guided by the fiber structure. This is an important advantage compared to bulk amplifiers, were the Gaussian beam propagation limits the interaction length. As a result, the amplification in such fibers can be quite high and is typically limited only by the available pump power or by onset of laser oscillations, if the amplification becomes equal to the optical feedback. Such an optical feedback can be provided by Rayleigh and stimulated Brillouin scattering and by reflections on fiber connections and fiber ends. The high gain potential of such fibers enables laser operation even for low optical feedback simplifies therefore the realization of fiber lasers [ZEN93].
Usually lanthanides like Erbium, Ytterbium, Neodymium or Thulium were used as active dopants in optical fibers. These atoms become triply ionized in silica or other glasses. The optical properties of these ions are determined by the partially filled inner 4f shells. Electric dipole transitions between the different energy levels of the 4f electrons are forbidden because of the even parity of these transitions. However, the spherical symmetry of the ions is disturbed by the host material and electric dipole transitions are therefore nonetheless possible. However, the influence of the host material is reduced by the shielding of the 4f shells by the outer complete 5s and 5p shells. Therefore, the energy levels of rare-earth ions have relative low radiative decay rates.

The nonradiative decay probabilities A_{NR} of the energy levels depend on the energy gap ΔE between the corresponding energy levels and is described by equation 2.4.1. The parameter α is inversely proportional to the highest phonon energy of the host and C depend also on the host material ($C \cong 1.4 \cdot 10^{12} s^{-1}$ and $\alpha \cong 37.9\ eV^{-1}$ for determined for Er^{3+}-ions in silica glass) [VPA00][DES94]. It can be seen from equation 2.4.1 that the nonradiative decay rate decreases exponentially with increasing energy gap. Therefore, the nonradiative decay rate of an exited state is low, if it the energy gap to the energy level below is much larger than the phonon energy of the host (e.g. 0.13 eV for silica glass [DES94]). For such 4f shell energy levels the radiative and nonradiative decay rates are low, which results in long lifetimes and favors the generation of a population inversion.

$$A_{NR} \cong C \exp(-\alpha \Delta E) \qquad \Delta E >> kT \tag{2.4.1}$$

The energy levels are spitted in several sublevels, because of the local crystal field in the host in combination with the Stark effect. Furthermore, the structural disorder of the amorphous glass results in variations of the Stark splitting of the energy levels with ion position. Thus, the amorphous nature of the glass results in a broadening of the optical transitions.

The active ions in these fibers can be pumped by coupling the pump light into the inner core of the fiber. The advantage of this pumping scheme is the good overlap between the pump light and the active doped core since the light is guided in this core. However, coupling the pump light into a single mode core requires a pump light source with single mode beam quality ($M^2 \sim 1$). For that reason, the double-core pumping scheme is commonly used for diode pumped high power fiber lasers and amplifiers [SPH88]. In this scheme, the cladding of the fiber core is surrounded by a second cladding of lower index, creating a second wave guiding structure for the pump light. This wave guiding structure has a relative large diameter and high numerical aperture and supports therefore many fiber modes. For this reason high power laser diodes with relatively low beam quality can be efficiently coupled into this waveguide. Simultaneously a good output beam quality can be maintained, since the signal propagation is determined by the inner core.

Compared to conventional fibers the pump light absorption is reduced due to the smaller overlap between the pump light distribution and the active core in such double core pumping schemes. Hence, a reduction of the pump light absorption coefficient according to the ratio between the area of the outer and the inner core can be expected. However, only meridional light rays, which cross the active core in the center, can be absorbed by the active ions, while there exist also propagation baths were the light in the double core travels around the active core without crossing it. Obviously, this screw rays cannot be absorbed by the active core

(fig. 2.4.1). As a result, the pump light absorption coefficient decreases along the fiber as only the meridional rays were absorbed while the screw rays remain in the pump core [LUE96].
Mode mixing between the different fiber modes, in particular between meridional and screw rays, can be accomplished by a non-cylindrical shape of the pump core, e.g. rectangular or D-shape [BRE98][DLM01]. Alternatively, a efficient mode mixing can be achieved and the pump light absorption can be strongly improved by using a fiber coiling where the amount and direction of the fiber bending varies along the fiber, e.g. a "kidney" or figure "8" shaped coiling [ZTW97][DLM01].
In the following subsections the properties of Ytterbium and Erbium doped gain fibers were described in more detail, since the experiments and set-ups described in this work were based on these fibers.

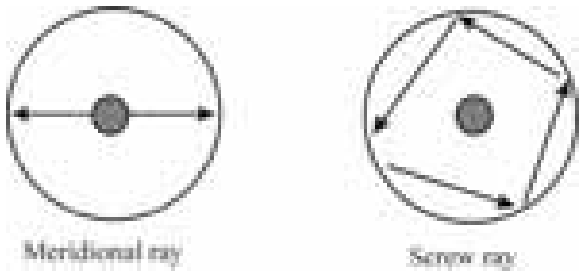

Fig. 2.4.1 *Propagation of merdional and screw rays in a double core fiber. Only the meridional rays cross the active core in the center of the fiber.*

2.4.1 Ytterbium gain fibers

Nowadays, Ytterbium doped fibers were often preferred for fiber lasers and amplifiers. This is attributable to the high efficiency of up to 80% and the broad amplification bandwidth of more than 40 nm [PNT97]. In addition, the pump absorption of Yb^{3+}-ions in silica glass is relatively strong and extents from about 0.85 µm to 1.0 µm. These fibers are therefore well suited for pumping with high power laser diodes in combination with the double clad pumping scheme. Moreover, the large gain bandwidth enables wavelength tuning Yb^{3+}-fiber lasers over a broad tuning range [AAW02] and supports the generation and amplification of ultrashort pulses, which have a broad spectrum, because of the Fourier limitation.
The optical properties of these fibers are determined largely by the energy structure of the Yb^{3+}-ions. It can be seen in figure 2.4.2, that these ions have only two distinct energy levels[4], the $^2F_{7/2}$ ground state and the $^2F_{5/2}$ excited state, which consist of four and three sublevels,

[4] Yb^{3+} has additional energy levels due to partially filled electron shells (e.g. 4d shell). However, the minimum energy difference between these exited sates and the ground state is 10.5 eV. The corresponding transition

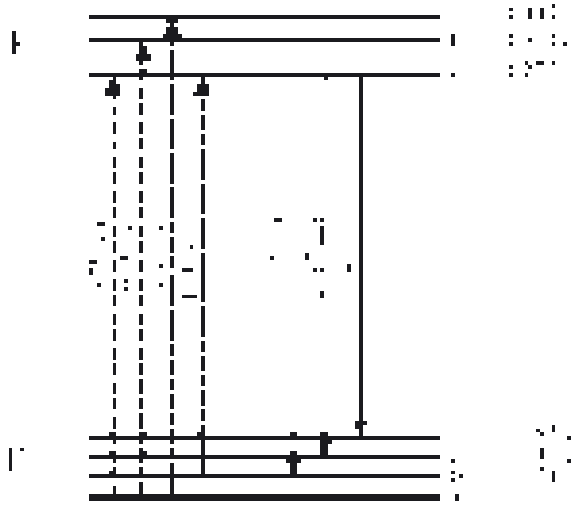

Fig 2.4.2 *Yb^{3+} energy level structure consisting of a ground state and an exited state. The Stark levels of these two manifolds are labeled by (a) – (g). The approximate energies of these levels relative to the ground state are indicated on the right [PCH95]. In addition, some pump and laser transitions are indicated by dashed and solid arrows, respectively.*

respectively [PCH95]. Thus, excited state absorption at the pump or the signal wavelength is excluded.

The lifetime of the exited $^2F_{5/2}$ state is typically 0.8 ms – 1.5 ms and depends on the composition of the silica fibers [PNT97]. The long lifetime is due to the low radiative and nonradiative decay rates between exited and ground state. While the nonradiative decay rate between the two energy levels is extremely low, the nonradiative transitions between the different Stark sublevels are extremely fast. This is attributable to the small energy differences between these levels (eqs. 2.4.1). Hence, thermal equilibrium between the Stark levels of each manifold is achieved nearly instantaneous [DES94][PNT97].

According to Bolzmann distribution, the population of level b is only about 6% of level a at room temperature, while the other levels are nearly unpopulated. Hence, the absorption spectrum of the Yb^{3+} is ions is due to transitions from these two ground state Stark levels to the exited manifold e - g.

The wavelength dependence of the absorption and emission cross section of Yb^{3+}-ions in silica glass fiber are shown in figure 2.4.3. It can be seen from this plot, that the absorption has two maxima at 915 and at 975 nm. The strong and narrow absorption peak at 975 nm is a result of the transition between the lowest Stark levels of the two manifolds. The high absorption at this wavelength is advantageous for diode pumping, since it enables relatively short fiber lengths, even in combination with double clad pumping schemes. An additional benefit of this pump wavelength is the small quantum defect between this pump and the laser wave-

wavelength of 120 nm is outside the transition window of silica glass and is much larger than the pump and signal photon energy. Hence, the influence on optical properties of silica glass can usually neglected [AEA98].

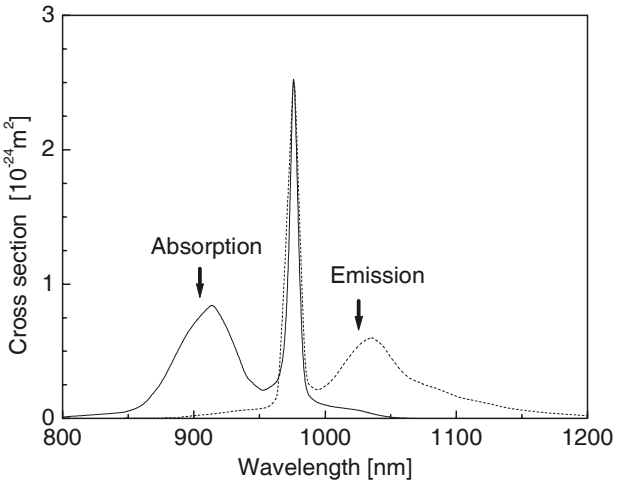

Fig. 2.4.3 *Absorption and emission cross section of Yb^{3+}-ions in silica glass [PCH95].*

length, which increases the efficiency and reduces thermal heating of the gain medium. However, the 975 nm absorption peak has a small bandwidth and is therefore quite sensitive to pump wavelength variations. Furthermore, the maximum upper state population is limited to 50%, since absorption and emission cross section are equal at this wavelength [PNT97].

The 915 nm absorption band is mainly attributable to transitions between the sublevels a and f. It has a much broader bandwidth, which extents to about 850 nm at the short wavelength side, and is therefore relatively insensitive to pump wavelength variations.

The absorption at the long wavelength tail above 975 nm, which extents to about 1100 nm, is caused by transitions from the weakly populated sublevel b to the exited state sublevel e [PNT97]. The most significant role of this transition is signal reabsorption in Yb^{3+}-fibers with low inversion. This reabsorption reduces the gain and shifts in addition the gain maximum to longer wavelengths.

For 975 nm pumping, the Yb^{3+}-ions can show optical gain between about 1000 and 1150 nm, while for shorter pump wavelength (e.g. 915 nm) inversion and optical gain can also be achieved at 975 nm. The gain maximum in Yb^{3+}-glas, strongly pumped at 975 nm, is about 1035 nm. However, with increasing fiber length or doping concentration it is shifted to longer wavelength by the above mentioned reabsorption [PCH95]. Laser action in these fibers is therefore nearly four-level in character at long signal wavelength, while with decreasing wavelength it became more three-level in character.

The relatively smooth gain spectrum of Yb^{3+}-doped silica fibers is attributable to broadening of the individual sublevels and variation of the Stark splitting. The resulting gain is mainly homogeneous broadened, although some inhomogeneous broadening was observed [PNT97] [WFA03].

Especially for short emission wavelengths, the properties of Yb^{3+}-doped fiber lasers and amplifiers were significantly influenced by the fiber temperature, which is due to the small energy difference between the sublevels a and b of the ground state. The population of the sublevel b increases strongly with temperature (e.g. 4% at 0°C; 8% at 100°C), which results in an increased signal reabsorption. Hence, with increasing temperature the gain decreases and shifts to longer wavelengths [BLA01].

Finally it should be noted, that the refractive index of the gain fiber is influenced by the absorption and emission lines of the material. Starting from the short wavelength side the refractive index decreases as the wavelength approaches an absorption. At the center of the absorption, the refractive index increases rapidly and than decreases asymptotically with increasing wavelength. Emission transitions show the inverse variation of the refractive index with wavelength [AEA98]. As a result, the refractive index of Yb^{3+}-doped fibers depends on inversion of the Yb^{3+}-ions. Thus, saturation effects can influence the pulse chirp during amplification of high-energy pulses in Yb^{3+}-doped fibers.

2.4.2 Erbium gain fibers

Erbium doped silica fibers can provide high and broadband gain at the transmission window of optical fibers with the lowest attenuation at 1.55 µm. Furthermore, these fibers can be pumped by semiconductor lasers with high efficiency. Therefore, erbium doped fiber amplifier had revolutionized the field of optical communication. Moreover, due to the broad bandwidth and the high gain, these fibers are well suited for generation and amplification of femtosecond pulses. An additional benefit for this application is the availability of fibers with normal as well as with anomalous dispersion at 1.55µm.

The optical properties of Er^{3+}-ions, which are relevant for these applications, were determined by the energy levels for the 4f electrons. Figure 2.4.4 shows these energy levels and the sublevels attributable to Stark splitting for Er^{3+}-ions in silica glass[5]. The lifetimes of the various exited states are below 7 µs, except for the $^4I_{13/2}$ level. This is attributable to nonradiative decays (see eqs. 2.4.1). Hence, nonradiative decays in silica glass are much faster than radiative decays, expect for the transition between the $I_{13/2}$ level, and the $^4I_{15/2}$ ground state. Moreover, due to the small energy gaps, the nonradiative transitions between the sublevels of each energy band are extremely fast and thermal equilibrium between the sublevels is achieved nearly instantaneous.

[5] Er^{3+}-ions have, like Yb^{3+}-ions, additional energy levels due to the partially filled outer electron shells.

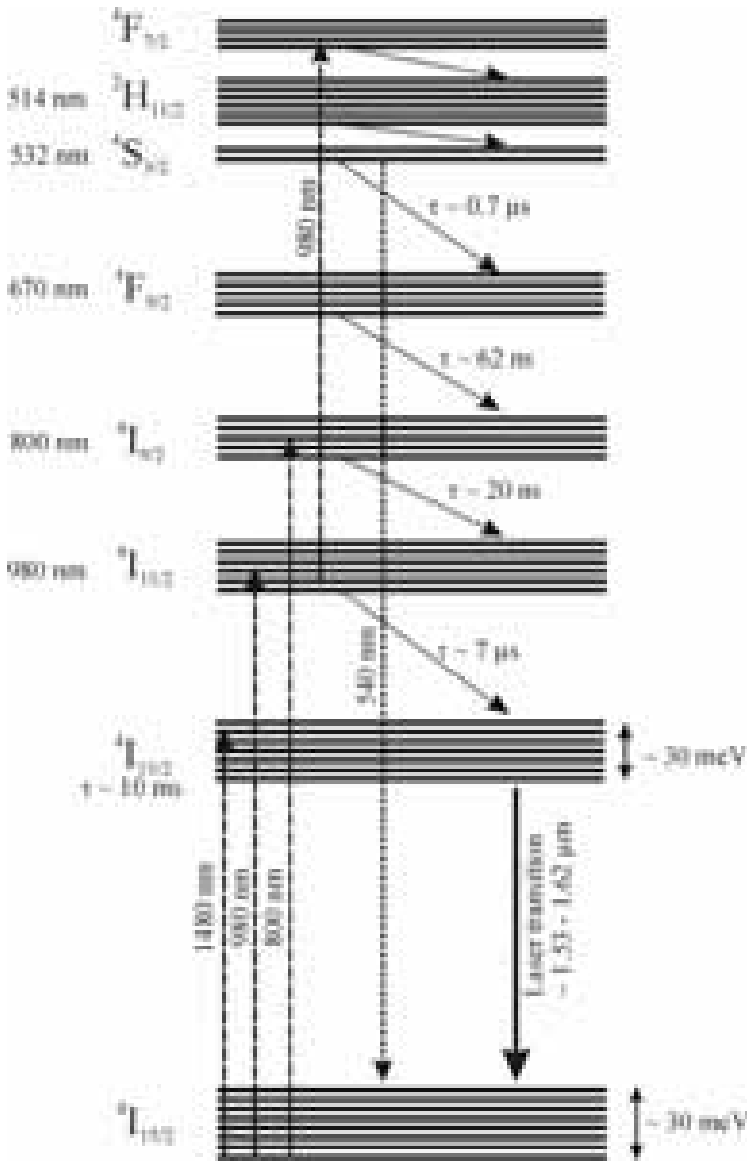

Fig. 2.4.4 *Partial Er^{3+}-energy levels structure. Some pump, excited state and fluorescence transitions are indicated by dashed arrows, while the laser transition is shown by a solid arrow. Diagonal dashed arrows indicate nonradiative transitions. For most of these transitions, the corresponding lifetime is also mentioned. At the left, the transition wavelengths from the ground state to various energy levels are mentioned in nanometers.*

The decay of the $I_{13/2}$ level is essentially radiative, because of the extremely low nonradiative decay rate. In combination with the low radiative transition rate, this results in an extremely long lifetime of about 10 ms for this energy level, which highly favors inversion and therefore optical gain between the $I_{13/2}$ level and the $^4I_{15/2}$ ground state [DES94].

Many transitions can be principally used for pumping of the Er^{3+}-ions. However, 980 nm and 1480 nm are the preferred pump wavelengths, since there is no exited state absorption from the upper laser level for these wavelengths [LFM89][DES94]. Additional benefits are the availability of high power laser diodes and the relative high absorption of the Er^{3+}-ions at these wavelengths.

The 980 nm pump transition terminates in the $^4I_{11/2}$ level, while for the 1480 nm transition the upper pump and the upper laser level lay within the same band. Thus, because of the thermal population distribution in the $^4I_{13/2}$ band, complete inversion can be attained only for 980 nm and not for 1480 nm pumping. For that reason, lower amplifier noise figures are possible for 980 nm than for 1480 nm pumping [SZS97]. The main advantage of the 1480 nm pump band is a low quantum defect between pump and signal photon, which enables high pump efficiencies. A visible side effect of the 980 nm pump wavelength is a green fluorescence of the erbium-doped fiber. This is attributable to excited state absorption from the upper pump level and subsequent spontaneous emission from the $^2S_{3/2}$ level. However, due to the relative low population of the upper pump level, the corresponding energy loss can usually be neglected, if the 980 nm pump intensity is not too high [SZS97].

It can be seen from the left diagram of figure 2.4.5 that the emission spectrum extents roughly from 1.48 µm to 1.62 µm and has a peak at 1.53 µm. This broad emission bandwidth is a result of the broadening of the upper and the lower laser levels. However, there is a large overlap between the emission spectrum and the ground state absorption, as the laser transition terminates into the ground state. This overlap can also be noticed from figure 2.4.5, by comparing the absorption and the amplified spontaneous emission spectra.

The maximum of the absorption and the emission curve is at 1.53µm. As a result, laser operation at this wavelength is strongly three-level in character. With increasing wavelength, the transition terminates in higher sublevels of the ground state with lower population and laser operation becomes more four-level in character. Thus, the gain curve depends strongly on inversion of the Er^{3+}-ions and the dominant gain peak at 1.53 µm is suppressed in weakly pumped fiber sections by signal reabsorption. Therefore, by adjustment of fiber length, the gain maximum can be shifted to the broader gain peak at 1.55µm [SZS97].

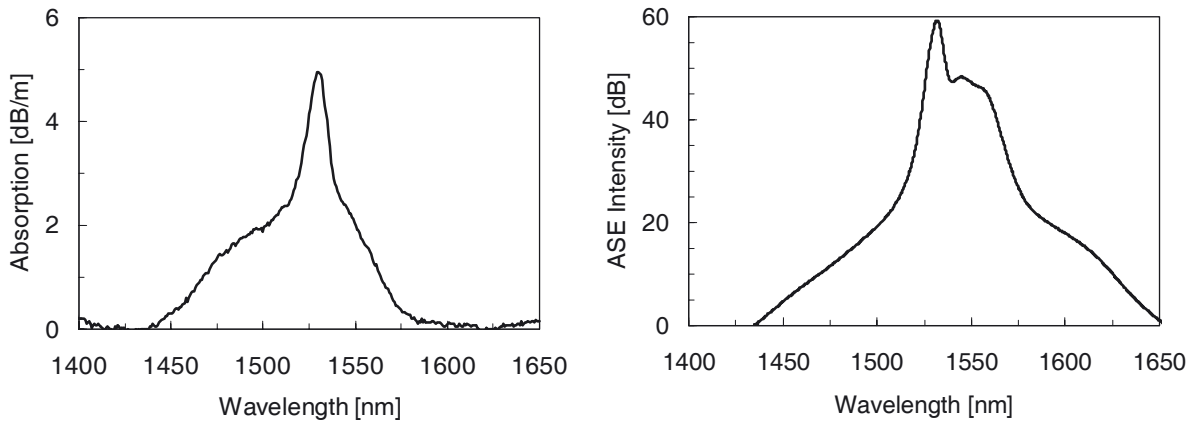

Fig. 2.4.5 *Left diagram: Spectrum of the amplified spontaneous emission (ASE) of an Er^{3+}-doped silica fiber pumped at 980 nm. Right diagram: Absorption spectrum of an Er^{3+}-doped silica fiber.*

The gain curve becomes also smoother with increasing aluminum and to a smaller extent with increasing phosphorus concentration in the fiber [DES94][MIN91][JAL97]. Silica and germanosilicate fibers have homogeneous and inhomogeneous linewidths of 4 nm and 8 nm respectively, while an aluminum codoping can increase these linewidths to about 11.5 nm.

Er^{3+}-doping has the tendency to form ion pairs or even clusters in highly doped silica fibers. The reason for this is that the glass forming silica atoms are typically in tetrahedral sites. However, Er^{3+}-ions prefer a higher coordination number and therefore tend to achieve the preferred six-fold coordination at high doping concentrations by clustering [APL98]. Aluminum or lutetium codoping increases the solubility of Er^{3+}-ions in glass and reduces this clustering effect [MNC97][SDS98].

Clustering in highly Er^{3+}-doped fibers reduces gain and efficiency. This is caused by pair induced upconversion processes. In ion pairs or clusters, with at least two ions in the upper laser level, one ion is exited to the $^4I_{9/2}$ level while the other returns to the ground state. The energy transfer in this upconversion process is attributable to nonradiative electric multi-polar interactions [MNC97]. The upconverted ions relax within microseconds to the upper laser level. Hence, a lower inversion and reduced pump efficiency are consequences of this upconversion process. Experiments showed that this pair induced upconversion is stronger for 1.53 µm than for longer signal wavelengths, which can be attributed to the higher ground state absorption at 1.53 µm [[MNC97].

Ion pairs and clusters act also as a saturable absorber, since the lifetime of the upconversion energy transfer is of the order of microseconds. By this way, Er^{3+} ion clusters favor intensity fluctuations and self-pulsing operation of Er^{3+}-fiber lasers. This is most noticeable if the fiber is pumped at 980 nm, while pumping at 1480 nm should reduce this effect [CCB96].

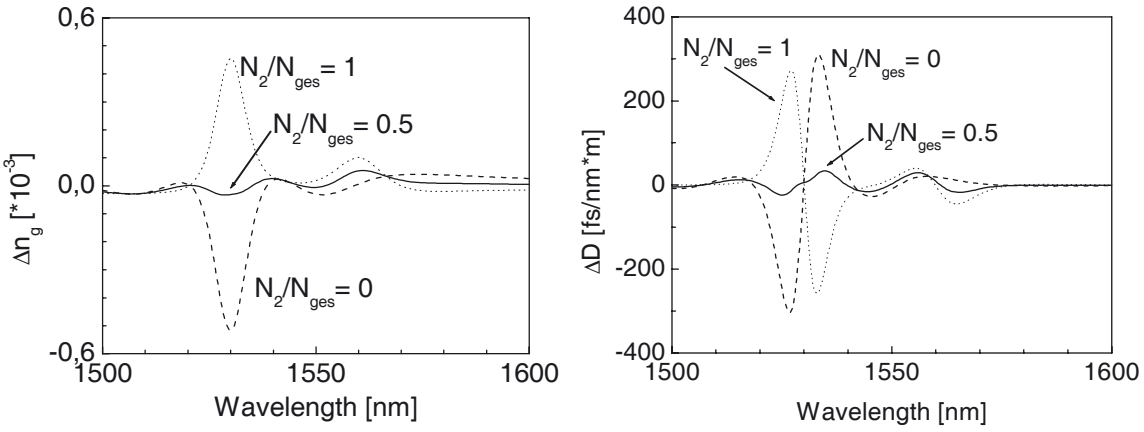

Fig. 2.4.6 *Modification of the group refractive index (left diagram) and dispersion (right diagram) by resonance effects of the Er^{3+}-ions as a function of wavelength and inversion. The plotted curves were calculated according to ref. [HBU96] for a fiber with an Er^{3+}-doping of 2700 mol ppm (Er_2O_3) and an overlap of 0.53 between the fiber mode and the doped core. In this figure, N_2/N_{ges} designates the ratio between the ions in the upper laser level and the total number of Er^{3+}- ions.*

The absorption and emission properties of the Er^{3+}-ions modify also the refractive index of the fiber. As a result, group velocity index and the fiber dispersion vary strongly with wavelength, especially near the strong absorption and emission line at 1.53 µm. In addition, the inversion of the Er^{3+}-ions strongly influences these parameters [HBU96] [KLJ99]. This is illustrated in figure 2.4.6, where the group velocity index and the fiber dispersion are displayed as a function of the wavelength and the inversion. Therefore, the dispersion of fiber amplifiers is modified by variations of the gain and saturation effects can result in variations of the group refractive index during amplification of a high-energy pulse in an Er^{3+}-doped fiber.

2.5 Generation of laser pulses

In order to achieve emission of regular pulse trains from a laser, the corresponding operation mode must be favored against cw-operation or irregular spiking. This can be realized by active control systems or by utilizing passive effects. However, active pulse generation schemes require control systems require an additional control electronic and typically some kind of electro-optical switches. In addition, pulses with sub-picosecond duration cannot be directly generated by active methods, because of the limited switching speed of the control electronics and optical switches. In contrast, passive methods, which are based on nonlinear effects inside the cavity, require no additional control circuits. In addition, only passive effects enable responds times on the femtosecond time-scale. For that reasons, passive methods were exclusively used in this work for pulse generation.

Depending on the ratio between pulse duration and cavity round trip time, pulsed laser operation can be divided into two regimes. If the pulse time scale is much larger than the round trip time, pulse generation is mostly determined by the time evolution of cavity gain and loss and their interaction with the circulating signal. In this regime, which is described in more detail in the following subsection 2.5.1, the interference of the various cavity modes can usually be neglected.

Below the cavity round trip time, the temporal shape of the signal is determined for the most part by the relative amplitude and phase of the cavity modes. Consequently, generation of shorter pulses requires a coupling of the various resonator modes in amplitude and phase. This operation mode and the used mode-locking mechanism are described in subsection 2.5.2.

2.5.1 Passive Q-switching and relaxation oscillations

In a laser cavity, at and above laser threshold the loss is compensated by the gain. Consequently, gain, inversion and therefore the energy stored in the gain material become larger at the threshold, if the cavity loss is increased. For that reason, pulsed laser operation can be achieved by modulation of the cavity loss (Q-switching). Such a loss modulation can be generated by a nonlinear element in the cavity, which loss decreases with increasing intensity. By this way, the intra-cavity signal modulates the intra-cavity loss and vice versa in such passive Q-switched systems. Hence, laser inversion is build up until the gain achieves the lasing threshold corresponding to the high cavity loss. Thereafter, the cavity loss decreases and a laser pulse is rapidly built up until the second threshold, corresponding to the reduced cavity loss. By this way, the stored energy is emitted in a laser pulse.

For passively Q-switched operation, loss modulation is typically quite large relative to the gain of the laser medium. However, even small disturbances of gain or loss can result in much larger oscillations of the laser amplitude. Such relaxation oscillations were typically observed in solid-state lasers, where the lifetime of the upper laser level is substantially longer than the photon lifetime in the cavity. The influence of the upper laser level decay rate γ_A, the cavity photon decay rate γ_C and the pumping rate r (relative to the laser threshold) on the frequency f_{RO} and the decay rate α_{RO} of these oscillations are described by equations 2.5.1 and 2.5.2 [SIG86].

$$f_{ro} = \frac{1}{2\pi}\sqrt{(r-1)\gamma_A\gamma_C - 0.25\,r^2\gamma_A^2} \tag{2.5.1}$$

$$\alpha_{ro} = 0.5\,r\,\gamma_A \tag{2.5.2}$$

2.5.2 Mode-locking

A laser cavity supports only discrete modes, as the circulating signal must be in resonance with the cavity. The frequency spacing Δf between these modes is given by $\Delta f = 1/T = c/L$ where T is the cavity round trip time, L is the cavity round trip length and c is the velocity of light. Furthermore, the temporal and spectral characteristics of pulsed signals are related to each other by a Fourier transform. Thus, the required spectral bandwidth increases as the pulse duration decreases and the pulse spectrum must extent over several resonator modes if the pulse duration approaches the resonator round trip time.

The detailed signal structure inside the cavity depends on amplitude and phase of the resonator modes. The circulating signal becomes periodic with the cavity round trip time, if

the amplitude and phase of the various resonator modes become locked by a coupling mechanism. The interference of the these modes result in a bandwidth limited pulse, if they are in phase, while phase disturbances increase the pulse width.

Generation of ultra-short pulses requires therefore an effect, which favors such mode-locking against other laser operation modes. This can be accomplished by active or passive modulation of amplitude or phase of the circulating signal [SIG86]. During this work, mode-locking was exclusively realized by passive amplitude modulation based on the intensity dependant polarization evolution in optical fibers. The exclusive use of this mechanism was due to the facts, that this scheme is well adapted to fiber-optic laser systems, that the response time of the Kerr-effect is extremely fast and that no special wavelength adoption was required.

Mode-locking by nonlinear polarization rotation (NLPR) is based on the nonlinear phase shift which is generated in an optical fiber by SPM and XPM between two copropagating orthogonal polarized signals with different intensity. Due to this nonlinear phase shift, the polarization evolution of an elliptically polarized signal in a fiber is intensity dependant. In the NLPR mode-locking scheme, this nonlinear polarization evolution is used in combination with a polarizing element for discrimination of lower signal intensities relative to the desired pulsed operation. In an alternative description of this scheme the two polarization modes of the fiber correspond to the two arms of an interferometer, where the resulting interference signal is intensity dependant due to SPM and XPM. Compared to a classical interferometer, the influence of external disturbances is greatly reduced and the adjustment is greatly simplified in such a set-up, as the linear phase difference between the two interferometer arms depends only on the birefringence of the fiber.

The basic operation principle of NLPR mode-locking is illustrated in figure 2.5.1. For sim-

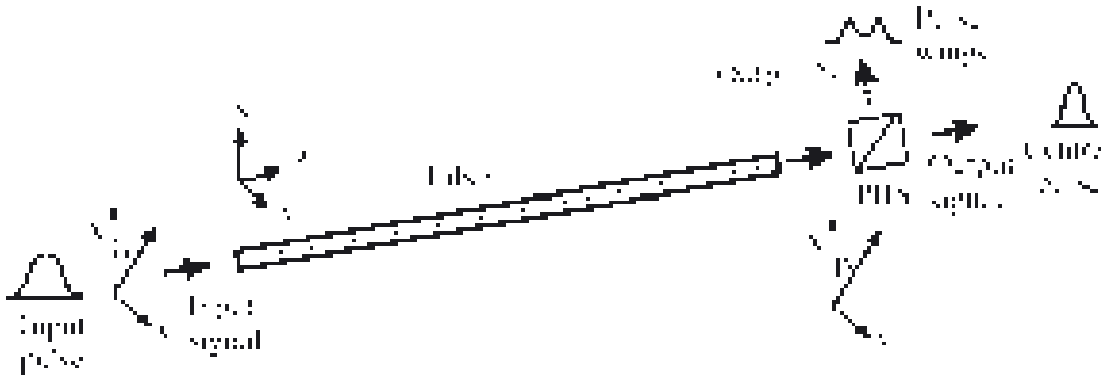

Fig. 2.5.1 *Basic principle of nonlinear polarization rotation mode-locking. The angle between the input polarization and the x-axis is denoted by α while β denotes the angle between the x-axis and the transmission axis of the polarization beam splitter (PBS) at the output. The polarization eigenmodes of the linearly birefringent fiber are orientated along the x- and the y- axes. For proper adjustment, the duration of an input pulse is reduced by NLPR. This pulse shortening is also illustrated in this figure.*

plicity, it is assumed in the corresponding equations, that the eigenmodes of the fiber are linear polarized along the x and the y-axes and that the input signal is linearly polarized. The angle between input polarization and the x-axis is denoted by α. Behind the fiber, interference between the two polarization modes is achieved by a polarization beam splitter (PBS), which transmission axis is rotated by an angle β relative to the x-axis. The total phase delay for each polarization mode Φ_x and Φ_y is the sum of the linear, the self-phase and the cross-phase modulation phase terms (eqs. 2.5.3 - 2.5.4) [HFH91][HSI97]. In these equations, n_x and n_y are the propagation constants for light polarized along the x- and the y-axis, n_2 is the nonlinear refractive index, L is the fiber length and A_0 is the electric field amplitude of the input signal. The phase difference between these two modes is given by equation 2.5.5, where B denotes the modal birefringence of the fiber. Finally, the resulting transmission at the PBS is shown in equation 2.5.6. The phase of the transmission curve depends on the linear phase terms and can therefore be adjusted by waveplates or by introducing an additional birefringence in the fiber.

$$\Phi_x = \frac{2\pi}{\lambda} L \left(n_x + n_2 A_0^2 \cos^2\alpha + \frac{2}{3} n_2 A_0^2 \sin^2\alpha \right) \tag{2.5.3}$$

$$\Phi_y = \frac{2\pi}{\lambda} L \left(n_y + n_2 A_0^2 \sin^2\alpha + \frac{2}{3} n_2 A_0^2 \cos^2\alpha \right) \tag{2.5.4}$$

$$\Delta\Phi = \Phi_x - \Phi_y = \frac{2\pi}{\lambda} L \left(B + \frac{1}{3} A_0^2 \left(\cos^2\alpha - \sin^2\alpha \right) \right) \tag{2.5.5}$$

$$T = \cos^2\alpha \cos^2\beta + \sin^2\alpha \sin^2\beta + 2 \left(\cos\alpha \sin\alpha \cos\beta \sin\beta \right) \cos\Delta\Phi \tag{2.5.6}$$

The nonlinear phase shift decreases as the splitting of the input signal becomes more symmetric and vanishes for a symmetric splitting (α = 45°). While the nonlinear phase shift depends only on the intensity and the splitting of the input signal, modulation amplitude and transmission maximum depend also on the orientation of the PBS. Thus, the transmission curve can be adjusted to some extent by these parameters, which is illustrated in fig. 2.5.2. For an appropriate adjustment of these parameters, the high intensity central part and the low intensity wings of an input pulse can be partially separated. The suppression of the pulse wings at one output port of the PBS corresponds to a reduction of the pulse duration.

In order to make the description more intuitive, the principle of an NLPR was described above for a linearly birefringent fiber. For fibers with other polarization eigenmodes (circular, elliptical) the corresponding calculations must be done for these eigenmodes. Furthermore, in equations 2.5.3 and 2.5.4 it was assumed, that the linear phase delay between the two modes is $\geq 3\pi$ and, therefore, coherence terms for the cross-phase modulation can be neglected. These terms disappear also for a circular polarization basis. Thus, a circular polarization basis is better adapted for isotropic media [TAM94]. However, calculations of the NLPR effects in

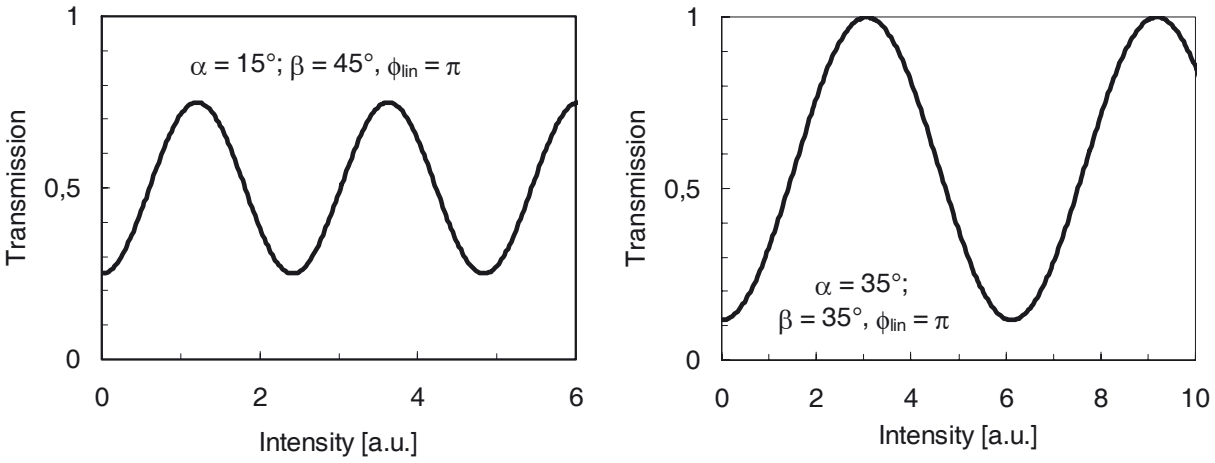

Fig. 2.5.2 *Pulse shape of the input pulse and the output pulses at the transmission and the reflection port of the PBS. This calculation assumed a transmission modulation between 0.1 and 0.7 which corresponds for e.g. to $\alpha = 19°$ and $\beta = 52°$. A linear phase delay of π was chosen so that for zero intensity the transmission curve has a minimum. The peak intensity of the input pulse corresponds to the first transmission maximum.*

real non-polarization maintaining fibers are difficult in practice, because of the random birefringence of these fibers. This birefringence is typically unknown for a specific set-up, as it depends on fiber bending, external pressure and random asymmetries of the fiber core.

The previous discussion showed that NLPR is able to favor and sustain mode-locked operation. However, saturable absorbers, like the NLPR set-up, have usually difficulties in initiating mode-locked operation without an external perturbation [NJT97]. For initiating self-starting mode-locking the built-up of the mode-locking must be faster than the decay of mode-beating fluctuations in the cavity. A decay of these mode-beating fluctuations is caused by an uneven spacing of the resonator modes, which can be caused by spurious reflections in the cavity, spatial hole burning effects and to a smaller extent by intra-cavity dispersion. The decay of mode-beating fluctuations is typically much slower in unidirectional ring cavities than in linear resonator configurations, since spatial hole burning and reflections were largely suppressed by the isolator in the cavity. For that reason, self-starting mode-locking is achieved more easily in unidirectional ring cavities [TAM94].

2.6 Stretching and compression of optical pulses

It was described in section 2.3.1 that the pulse duration can be increased by dispersive elements, which change the phase relation across the spectrum. Such a dispersive pulse stretching reduces the peak power of the pulse and introduces simultaneously a chirp. Furthermore, by compensating this chirp with dispersive elements, pulses can be recompressed up to the bandwidth limit.

Based on these relations, in fiber optic amplification schemes for ultrashort pulses the input pulse duration is usually increased by optical elements with large GVD. Such a stretching reduces peak power and consequently nonlinear effects. By this way, the limitations caused by nonlinear effects were reduced and higher pulse energies can be realized. In order to recompress the amplified pulses, the chirp introduced by the pulse stretcher were compensated after amplification by elements with opposite GVD. Such chirped pulse amplification (CPA) schemes are especially important in combination with single-mode fiber amplifiers, as the small mode field area and the long interaction length of these fibers increases nonlinear effects. By a similar technique the achievable pulse energy is increased in stretched pulse mode-locked fiber lasers. In such fiber laser set-ups, the circulating pulses were periodically stretched and recompressed by dispersive elements (e.g. fiber dispersion). This enables higher pulse energies as it reduces the average peak power of a circulating pulse [JHN98].

Typically, CPA schemes use large stretching ratios, which increase the pulse duration up to several 1000 times above the bandwidth limit [GSB01][LLZ01]. For recompression of the highly stretched pulses, stretcher and compressor must have (nearly) the same dispersion slope, since differences between the dispersion slopes result in an uncompensated TOD. An uncompensated TOD introduces a quadric chirp and increases the pulse duration of the recompressed pulses above the Fourier-limit (eqs. 2.3.3).

Dispersive elements like suitable arrangements of diffraction gratings or prisms [DIE95], chirped fiber Bragg gratings [IDZ00] or fibers with non zero dispersion can be used for pulse stretching and compression. Dispersive fibers or fiber Bragg gratings are especially suited for integration in fiber amplifier systems and can be used for stretching of the input pulses with low energy. However, these elements are not suited for recompression of high-energy pulses, as in these elements high peak powers result in pulse distortions by nonlinear effects. Furthermore, for pulse stretching the used fibers should have normal dispersion, as soliton effects (section 2.3.3) can disturb or cancel out pulse stretching in fibers with anomalous dispersion.

The dispersion slope of fiber stretchers can be influenced by the refractive index structure of the fiber. However, an adaptation of the dispersion slope to the compressor requires eventually complicated refractive index structures or my result in a small mode-field area, which increases nonlinear effects [GKE00][FSG01]. In principle even complicated dispersion curves can be realized for chirped fiber Bragg gratings. However, fabrication technologies with high accuracy are required for a dispersion curve that can be compensated by other dispersive elements.

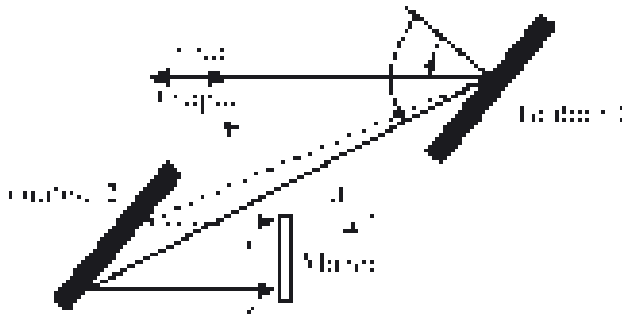

Fig. 2.6.1 *Basic set-up of a diffraction grating pulse compressor.*

Pulse recompression is typically accomplished by reflective diffraction gratings arrangements with anomalous dispersion. The set-up of such a compressor, which basically consists of two parallel gratings, is shown in figure 2.6.1 [TRE69]. Due to the diffraction of the gratings, different wavelengths are transversally displaced after one pass of this arrangement. This transversal displacement can be compensated by a double pass arrangement, where the beam is retro-reflected after the first pass by a plane mirror. By a slight tilt of this mirror (or by use of a 90° retro reflecting prism instead of the mirror), the output beam can be separated in high from the input beam.

For such a double pass grating pair, second and third order dispersion is given by equations 2.6.1 – 2.6.3 [DIE95]. In these equations, λ is the wavelength, ω(λ) the corresponding angular frequency, g the grating constant and d the normal separation between the two gratings. The incident and the diffraction angle at the first grating were denoted by γ and γ'(λ).

$$\gamma'(\lambda) = \arcsin\left(\frac{\lambda}{g} - \sin\gamma\right) \tag{2.6.1}$$

$$\beta_2\big|_{\varpi(\lambda)} = -\frac{\lambda}{\pi c^2}\left(\frac{\lambda}{g}\right)^2 \frac{d}{(\cos\gamma')^3} \tag{2.6.2}$$

$$\frac{\beta_3}{\beta_2}\Big|_{\varpi(\lambda)} = -\frac{1.5\lambda}{\pi c(\cos\gamma')^2}\left[(\cos\gamma')^2 + \frac{\lambda}{g}\sin\gamma'\right] \tag{2.6.3}$$

It can be seen from equation 2.6.2 that the second order dispersion (GVD) is always negative for such a grating arrangement. The ratio between TOD (β_3) and GVD (β_2), is also negative. However, equation 2.6.3 shows that it can be tuned to some extent by the incident or respectively the diffraction angle of the signal. In addition, this ratio depends on the grating constant. This is illustrated in figure 2.6.5 were TOD/GVD ratios are plotted as a function of incident angle for different grating constants.

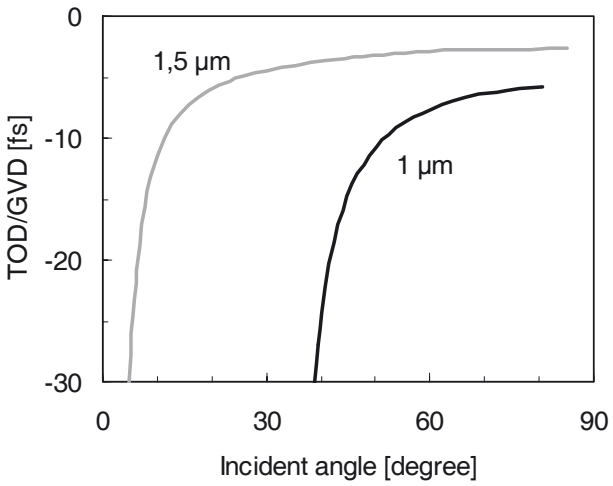

Fig. 2.6.5 *Ratios between third and second order dispersion as a function of the incident angle and the grating constant for a signal wavelength of 1550 nm.*

3 Passive Q-switched Yb^{3+}-fiber laser

Q-switched lasers with pulse durations in the range of a few microseconds have several important advantages over conventional cw or short pulse (ns, ps, fs) laser sources. On the one hand, much higher peak powers were achieved than with cw lasers with the same average output power. By this way, nonlinear optical effects can be enhanced without increasing the thermal load of the corresponding set-up. On the other hand, the Fourier bandwidth-limit for µs pulses is in the MHz range. Such a low bandwidth limit makes µs-pulses more suitable for applications were a high spectral resolution is essential than shorter pulses (ns, ps, fs). Furthermore, the moderate peak powers of µs-laser systems can help to prevent saturation effects. Because of these characteristics, µs-pulses are especially suited for pumping of optical parametric oscillators [KAA03].

By light propagation in single-mode fibers, a good beam quality can be reliably accomplished, which is important for many applications. Moreover, fiber lasers are quite insensitive to thermal effects and require no active cooling due to the large surface-to-volume ratio of the gain fibers. Thus, fiber lasers that generate µs-pulses are very promising, as they combine the advantages of fiber lasers with the benefits of µs-pulses.

In solid-state lasers, the generation of µs- to ns-pulses is usually realized by active or passive Q-switching. Active Q-switching is typically achieved by inserting an acousto-optic or electro-optic modulator into the cavity [CGP98]. However, such a set-up is relatively complicated and expensive, which is attributable to the active optical switch and the related electronics. In contrast to active methods, passive Q-switching by insertion of a bulk saturable absorber is relatively simple and shows a high reliability. Commonly, saturable absorbers on the basis of Cr^{4+}-doped crystals or ceramics were used for Q-switching of Nd^{3+}- or Yb^{3+}-doped infrared lasers with emission wavelengths around 1 µm [TLM02]. However, for fiber-based laser systems the use of such bulk elements results in a larger complexity. This is in contradiction to a needed compact and reliable integrated set-up. Therefore, the advantages of all-fiber laser systems like compact set-up, low adjustment requirements and low sensitivity to thermal effects and mechanical perturbations cannot fully be exploited by such laser systems.

It has been demonstrated, that in bulk lasers, based on Nd^{3+}:YAG, the Cr^{4+}-ions can be co-doped into the Nd^{3+}:YAG crystal instead of inserting an additional Cr^{4+}:YAG saturable absorber into the cavity [HZC01]. This enables a simpler and more compact laser design. It is worth to mention, that until recently it was not possible to produce optical fibers with Cr^{4+}-doping, as Chromium forms usually Cr^{3+}-ions during the production process of glass.

Recently the production of a Cr^{4+}-doped fiber was demonstrated the first time and it was shown that the fiber was suitable for initiating Q-switching. This indicates that the previous mentioned limitations can eventually be overcome [TDD03].

In this section, an Yb^{3+}-fiber laser is presented that is using a Tm^{3+}-codoping in the gain fiber as a saturable absorber. By this way, µs-pulses were generated passively in the fiber laser. The integration of the saturable absorber into the gain fiber overcomes the above mentioned restrictions and enables higher-integrated Q-switched laser set-ups in the future. Moreover, for this diode-pumped laser system wavelength tunability and narrow linewidth operation were demonstrated.

3.1 Experimental set-up

The detailed fiber laser set-up, which enabled simultaneously passive Q-switching and tunable small linewidth operation, is shown in figure 3.1.1. It consists of the following main components: a Yb^{3+}-doped double-clad fiber with Tm^{3+}-codoping that provide the gain and the saturable absorption, quarter- (QWP) and half-wave-plates (HWP) for polarization control, a Faraday rotator (FR) for unidirectional laser operation and a grating pair (1200 lines/mm, gold coated) in Littrow-Littman configuration for tunable narrow linewidth operation. For an improved wavelength resolution of the grating arrangement, the beam diameter was increased to about 4 mm before the gratings by means of a telescope.

The polarization beam splitter (PBS2) at the input of the Faraday rotator acted as a variable output coupler in combination with HWP2. In addition, a polarization beam splitter (PBS1) was placed in front of this HWP2 to fix the polarization state and the output-coupling factor at

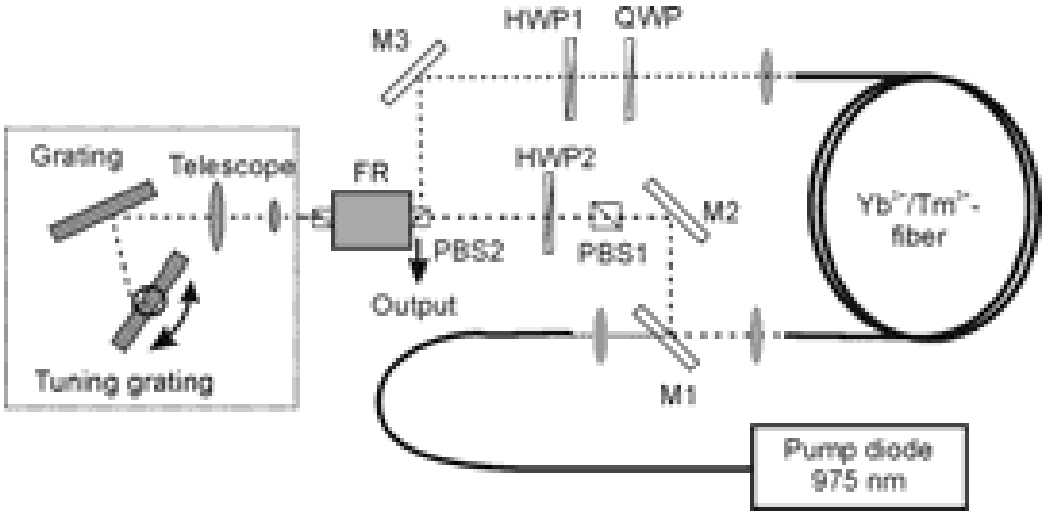

Fig. 3.1.1 *Set-up of the tunable Q-switched fiber laser system.*

PBS2. Otherwise, nonlinear polarization-rotation potentially favors short pulses or even mode-locking for high output-coupling factors (section 2.6.2). This is attributable to the fact, that the polarization state at the fiber output depends on the signal intensity, if the light show elliptical polarization somewhere in the fiber. This effect can reduce output coupling and cavity loss for signal peaks. In order to reduce this effect, PBS1 was inserted into the cavity.

The gain fiber, with a molar dopant concentration of 1500 ppm mol Yb_20_3 and about 5 ppm mol Tm_2O_3, had a pump and laser core diameter of 250 µm and 7 µm, respectively. This fiber had a cut-off wavelength below 1.0 µm and was, therefore, single mode for the laser light. Furthermore, the pump core was D-shaped for improved pump light absorption. Both end facets of the fiber were polished under an angle of about 12° in order to suppress reflection from these facets into the fiber core.

This gain fiber was pumped by a fiber-coupled laser diode module via dichroic mirror M1. A pump wavelength of 975 nm was used, since Yb^{3+} shows maximum absorption at this wavelength. The laser diode case was mounted on a water-cooled heat sink with constant temperature in order to reduce the wavelength drifts caused by temperature variations of the laser emitter (~ 0.3 nm/K). The temperature of the heat sink was adjusted for maximum pump light absorption at maximum pump power.

The light from the fiber was relayed by mirrors M1 and M2 through PBS1 to the variable output coupler, consisting of HWP2 and the PBS2 in front of the Faraday rotator. Behind the Faraday rotator, the signal propagated towards the grating pair. The wavelength of the back reflected signal was determined by adjustment of the incident angle on the Littrow tuning grating. For the back-reflected signal the Faraday rotator acted, in combination with the PBS2, as an optical circulator. By this way, the beam was then coupled into the Yb^{3+}-fiber via mirror M3. The polarization at the fiber input was determined by the settings of the zeroth-order (at 1064 nm) wave-plates (HWP1 + QWP).

An unidirectional ring cavity was chosen, since stimulated Brillouin scattering is suppressed by the optical isolator in such a set-up and random intensity fluctuations were therefore reduced [AAW02]. In addition, this avoids spectral hole burning effects in the gain fiber by standing waves, which potentially increase the spectral bandwidth of the laser.

3.2 Q-switched laser operation

Using a set-up with a 20 m long gain fiber and an output-coupling factor adjusted to 65%, stable pulsed operation started at 5.6 W launched pump power for appropriate waveplate set-

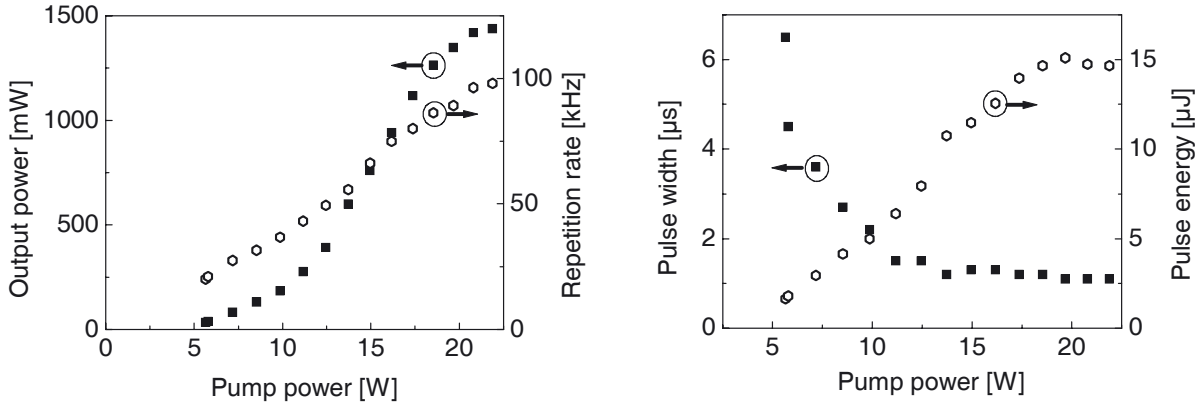

Fig. 3.2.1 *Output data of the laser set-up with a 20 m long Yb^{3+}:Tm^{3+}-fiber. Left figure shows the output power and repetition rate as a function of pump power. In the right figure pulse width and pulse energy as plotted versus pump power.*

tings. At this threshold, the laser showed a repetition rate of 20.1 kHz and an output power of 33 mW. During these measurements, the wavelength was kept fixed to 1065 nm by the tuning grating. At maximum pump power of 21.9 W, an output power of 1.44 W and a repetition rate of 98.1 kHz were measured. Output power and repetition rate are plotted versus pump power in the left diagram of figure 3.2.1. The output power did not increase linearly with pump power but showed a S-shaped curve. This was attributable to a thermally induced increase of the pump diode wavelength with pump power. The increase of the laser emitter temperature with pump power was caused by the increased heat generation, as the laser diode case was mounted on a heat sink with constant temperature. By this way, the pump wavelength moved closer to the relatively narrow absorption peak of Yb^{3+} at 975 nm with increasing pump power, resulting in an improved pump light absorption. This was confirmed by measurements of the transmitted pump power, which showed, that pump light absorption increased with pump power especially at medium power levels.

In the right diagram of figure 3.2.1, the pulse energy is plotted versus pump power. The pulse energy was calculated from the measured output power and the repetition rate. It increased nearly linearly from 1.6 µJ at 5.6 W pump power to a maximum of 15.1 µJ at 19.7 W pump power. A further increase of pump power resulted in a slight decrease of the pulse energy.

Furthermore, figure 3.2.1 (right) shows the pulse width (FWHM) as a function of pump power, which was measured with a 2 GHz photodiode and a 500 MHz oscilloscope. The pulse width decreased asymptotically from 6.5 µs to 1.1 µs with increasing pump power. In the left diagram of figure 3.2.2, a typical oscilloscope trace of the pulsed output is displayed. However, on a shorter time scale the Q-switched pulses showed typically a substructure above the µs pulse pedestal with a periodicity equal to the cavity round trip time. This substructure can

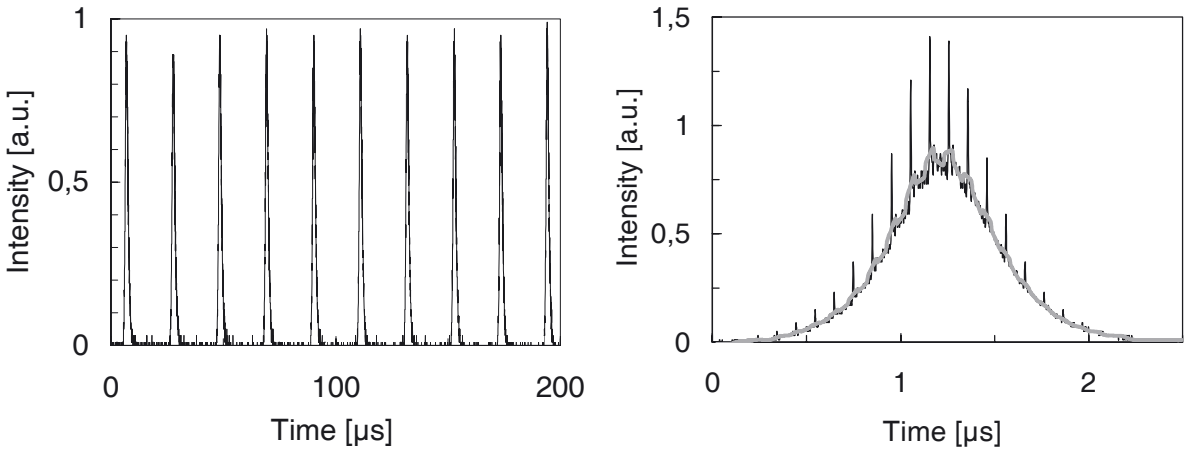

Fig 3.2.2 *Left diagram: Typical photodiode trace of the Q-switched fiber laser output-signal. Variations of the peak height in this figure are attributable to the discrete sampling of the digital oscilloscope. This was confirmed by measurements with an analog oscilloscope. Right diagram: black curve – Typical time signal of a Q-switched pulse, which shows a ns-substructure above the µs pulse pedestal. This curve was recorded with a 500 MHz oscilloscope. Grey curve – corresponding averaged time signal (averaging time 5 ns).*

be seen in the right diagram of figure 3.2.2. The appearance and amplitude of this substructure was influenced by the waveplate settings and the coiling of the fiber.

According to the oscilloscope trace this substructure pulses had a temporal width of about 2 ns. However, this is only an upper limit, since the 2 ns correspond to the resolution limit of the oscilloscope. The pulse width of the µs pulse pedestal was determined by reducing the detection bandwidth electronically to about 20 MHz. By this way, the signal was smoothed. It can be seen from figure 3.2.2 that the area below the ns substructure peaks is only a small fraction (< 5%) of the total area below the pulse trace. Therefore, the contribution of the ns peaks to the total pulse energy of the µs pulses is quite small (< 5%). For this reason, the smoothed 20 MHz trace (gray curve) in figure 3.2.2 nearly coincides with the 500 MHz resolution curve, except for the ns peaks.

It is worth to mention, that during infrared laser operation, the codoped gain fiber shows a blue fluorescence, which was much stronger than for conventional Yb^{3+}-doped fibers. The brightness of this spontaneous emission at about 480 nm was increased with signal intensity, while the pumped fiber showed extremely weak blue fluorescence without laser operation.

3.2.1 Influence of output coupling

Variations of the output-coupling factor showed, that the output power increased roughly linearly with the output coupling up to a factor of about 0.8. It saturated as the output coupling was further increased. The corresponding data are displayed in the left diagram of figure 3.2.3. It can be deduced from this linear relation, that the intra-cavity signal power

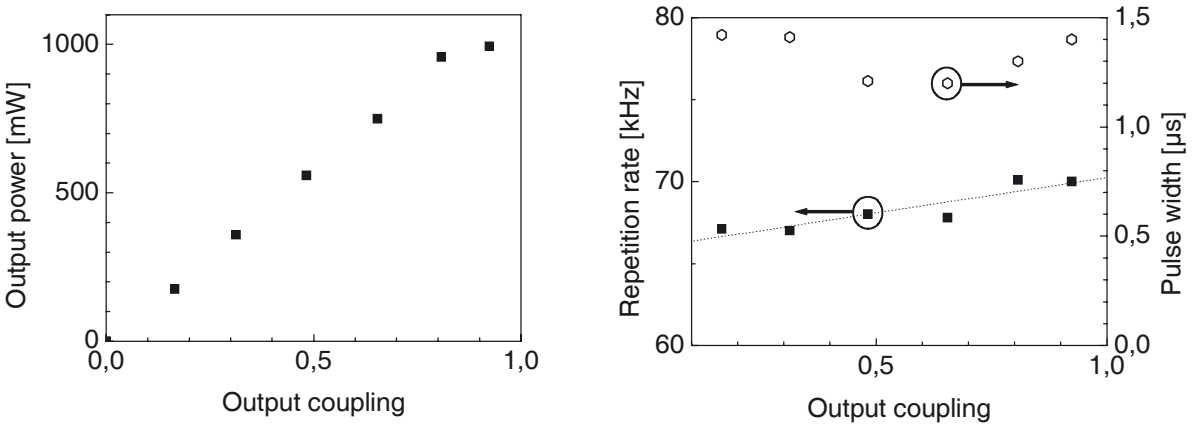

Fig. 3.2.3 *Influence of the output coupling on output power (left diagram), repetition rate and pulse width (right diagram) of the Q-switched laser with a 20 m long Yb^{3+}:Tm^{3+}-fiber at 15 W pump power. The dotted curve in the right diagram is a linear fit function for repetition rate versus output coupling.*

before the output coupler was nearly independent from the output coupling up to a factor of about 0.8. This indicates that in this range the total cavity loss was larger than the output coupling. The high total cavity loss was mainly attributed to the grating line, which had a loss factor of about 0.65, the fiber coupling and the loss caused by the Tm^{3+}-codoping.

The influence of the output-coupling factor on the repetition rate and the pulse width is displayed in the right diagram of figure 3.2.3. It can be seen from this diagram that the repetition rate increases slightly with increasing output coupling. The minimum pulse width was observed for an output coupling of about 0.5 – 0.65, while lower and higher output coupling resulted in a pulse width increase of up to 20%. Finally it should be noted, that for extremely high output-coupling factors (i.e. > 90% at 15 W pump power) only unstable Q-switching was observed.

3.2.2 Influence of fiber length

In order to investigate the influence of a larger fiber length on laser performance a second set-up with a 32 m long gain fiber was realized. The measured output powers, repetition rates, pulse widths and pulse energies are shown in detail in figure 3.2.4 as a function of the pump power. By comparing this figure with figure 3.2.1, it can be seen that the results for the set-ups with the 32 m and the 20 m gain-fibers were qualitatively the same. Furthermore, it can be seen from table 3.2.1, which shows the main output data of both set-ups, that for the 32 m gain-fiber the lasing threshold was nearly two times lower and slope efficiency was about 60% higher than for the 20 m fiber. This is attributable to an improved pump light absorption. In addition, the maximum output power was 67% and the pulse energy up to 44% higher for the 32 m set-up while the minimum pulse duration was about 20% longer. It should be noted,

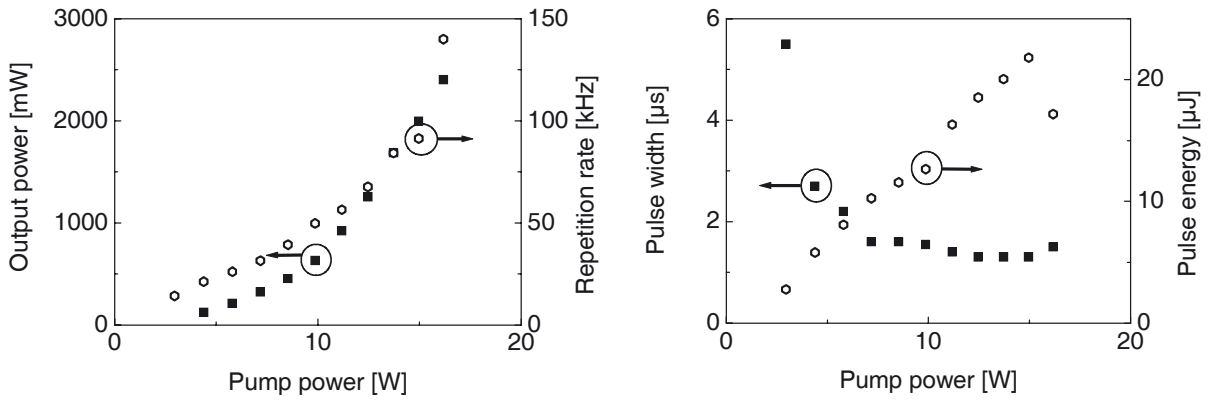

Fig. 3.2.4 *Output data of the laser set-up with a 32 m long Yb^{3+}:Tm^{3+}-fiber. The left figure shows the output power and repetition rate as a function of the pump power. In the right figure the pulse width and pulse energy as plotted as a function of the pump power.*

Fiber Length [m]	Threshold [W]	Max. Pump Power [W]	Max. absorbed Pump P. [W]	Output Power [W]	Rep. Rate [kHz]	Pulse width [µs]	Pulse energy [µJ]
20 m	5.6	19.7	10,8	1.44	20.1 – 98.1	1.1 – 6.5	1.6 – 15.1
32 m	3.0	15.0 16.2	9,8 10,8	2.0 2.4	14.3 – 91.4 140	1.3 – 5.5 1.5	2.7 – 21.8 17.2

Table 3.2.1 *Laser data for set-ups with a 20 m and a 32 m long gain fiber*

that in combination with the 32 m fiber, the maximum pulse energy of 21.8 µJ was observed at a pump power of 15 W. The pulse energy decreased, if pump power was further increased, as this was accomplished by a strong increase of the repetition rate. This can also be seen from the laser data shown in the last row of table 1. For pump powers of more than 16.2 W the Tm^{3+}-codoping caused only a periodic intensity modulation and no on/off Q-switching was observed. This shows that at such high power levels the effect of the Tm^{3+}-codoping on laser operation became too weak for maintaining pulsed laser operation.

3.2.3 Signal linewidth

Measurements with an optical spectrum analysator showed, that the linewidth of the output signal was always below the resolution limit of about 0.05 nm. Therefore, the signal linewidth was determined with a confocal scanning Fabry-Perot interferometer with 10 GHz free spectral range and a finesse of 150. The measured linewidths as a function of the output power are plotted in figure 3.2.5 for both gain-fiber lengths. It can be seen from this diagram, that for the 20 m (32 m) set-up the linewidth increased with output power from 0.17 GHz to 2.3 GHz (from 0.35 GHz to 4 GHz). For a similar set-up with a conventional 20 m long Yb^{3+}-fiber nearly the same linewidth (< 2.5 GHz) was observed as for the 20 m Yb^{3+}-Tm^{3+}-fiber

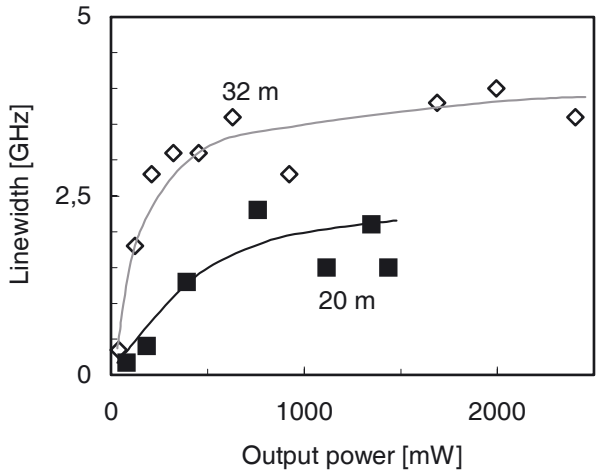

Fig. 3.2.5 *Linewidth of the Q-switched Yb^{3+}:Tm^{3+}-fiber laser as a function of the signal power for the 20 m and the 32 m fiber set-up. The plotted lines are only guides for the eye.*

Q-switched set-up [AAW02]. This shows that the linewidth was not significantly influenced by the Q-switching.

The fluctuations of the linewidth in figure 3.2.5 are attributable to thermal effects on the fiber-positioning set-up. As the pump light was coupled over one end facet into the fiber, the signal coupling efficiency was usually affected by pump power variations. These variations influenced gain and signal intensity distribution along the fiber and by this way the spectral linewidth. This effect can be avoided by transversal pumping schemes.

The actual laser linewidth is a result of an equilibrium between the broadening effects in the resonator and the spectral filtering of the grating pair. The spectral bandwidth (FWHM) $\delta\nu_{Gr}$ of the grating pair is given by equation 3.2.1, where r_B is the radius of the incident beam, α is the incident angle, β_1 is the diffraction angle at the first grating, β_2 is the Littrow angle of the second grating and d_1 and d_2 are the groove spacings of the two gratings [WLT97].

$$\delta\nu_{Gr} = \frac{2c}{\pi r_B \lambda\left(\frac{2}{d_1\cos\beta_1}+\frac{1}{d_2\cos\beta_2}\right)\frac{\cos\beta_1}{\cos\alpha}} \qquad (3.2.1)$$

In the laser set-up, the incident angle and the beam radius were 65° and about 4 mm, respectively. This resulted in a spectral bandwidth of about 5 GHz for the grating pair, as the gratings had 1200 l/mm.

The measured linewidth increased with signal power and fiber length. This shows that the dominant broadening effects in the resonator increase with fiber length and signal power, since the bandwidth of the grating pair is constant. Stimulated Brillouin scattering and standing wave effects are strongly suppressed by the Faraday rotator. Furthermore, the frequency shift for stimulated Raman scattering is much larger than the spectral linewidth. Thus, the broadening of the intra-cavity signal must be due to spectral hole burning or four-

wave mixing between the different resonator modes. However, the homogeneous linewidth of Yb^{3+}-ions is much broader than the measured signal linewidths and the bandwidth of the grating pair. Therefore, the gain must be nearly constant over this bandwidth. Consequently, the broadening caused by spectral hole burning must be small. In addition, there was no spatial hole burning in the gain fiber, because of the unidirectional ring cavity.

Four-wave mixing between resonator modes requires phase matching. This phase matching is disturbed by the fiber dispersion of about $2 \cdot 10^{-26}$ s²/m at 1.1 µm. Calculation of the corresponding coherence length according to equation 2.2.8 showed, that it is about 80 km for a frequency shift of 10 GHz. Hence, for the relevant frequency shifts, phase matching between resonator modes is nearly constant during propagation in the gain fiber and the FWM gain increases with fiber length and signal intensity. Rough calculations of the parametric gain for perfect phase matching gave a value of about 2 dB for the 32 m gain fiber (54 µm² mode field area) and an intra-cavity signal power of 20 W. The latter corresponds roughly to the intra-cavity power of the Q-switched pulses with maximum pulse energy at the fiber output. In order to take the signal amplification in the fiber into account, an effective fiber length of 6.4 m was used for this calculation. This value for the effective length was calculated by approximating the intensity distribution along the fiber for 10 dB Yb^{3+} gain by a quadratic function. However, detailed calculations of the FWM gain must take into account the exact intensity distribution along the fiber, the interactions between the various resonator modes and the phase effect of the grating pair.

The suppression of the resonator modes by the grating pair increases with growing difference between mode frequency and transmission maximum of the grating arrangement. For a detuning by half of the FWHM bandwidth, the mode suppression is by definition 3 dB. Furthermore, a FWM gain of 2dB was calculated for the maximum observed pulse energy for the 32 m set-up. Thus, the measured linewidth of 4 GHz agrees with the spectral broadening effect of FWM. Moreover, the observed increase of the linewidth with fiber length and output power is consistent with the characteristics of FWM. Hence, these results point out that FWM is the dominant broadening mechanism in such small linewidth fiber laser.

The filtering of the grating pair can be approximated by a quadratic function while the FWM gain is proportional to fiber length and signal intensity in such a set-up. As a result, the linewidth is roughly proportional to the square root of the fiber length and the inverse of the mode field diameter. Consequently, the linewidth must become narrower as the fiber length is reduced or the mode field diameter of the fiber is increased. However, shorter fiber lengths require higher doping concentrations for a reasonable pump light absorption and special

adapted refractive index profiles or transverse-mode filtering techniques are required for maintaining a single mode beam quality in combination with large mode field diameters [OBR98][KKG00].

3.2.4 Wavelength tuning

By rotating the tuning grating, the signal wavelength was tunable between 1055 and 1085 nm for the 20 m set-up and between 1059 and 1090 nm in combination with the 32 m long fiber. The applied pump powers of 16.8 W and 13.7 W, respectively were adjusted for similar repetition rates. If the tuning grating position was adjusted for an emission wavelength outside the above mentioned tuning limits, only unstable Q-switching was observed. The observed shift of the tuning range with fiber length corresponds to the change of the Yb^{3+}-gain spectrum (section 2.4.1).

The measured tuning spectra are shown in figure 3.2.6. It can be seen from this figure that the spectral intensity of the amplified spontaneous emission was at least 37 dB lower than the main laser radiation. For these measurements, a spectral resolution of 0.5 nm was used in order to enable simultaneous detection of the amplified spontaneous emission over a sufficient large wavelength span. Additional measurements of the laser lines with higher resolution confirmed, that the spectral linewidth was always below the resolution limit of 0.05 nm.

In the wings of the spectral tuning range, repetition rate and pulse width increased up to a factor of two relative to the minimum in the center of the tuning range. The corresponding data are shown in figure 3.2.7. The maximum output power was measured at about 1065 nm and decreased slightly (< 15%) if the wavelength was detuned, except at the long wavelength limit of the 32 m fiber set-up, were a power drop of up to 35% was observed.

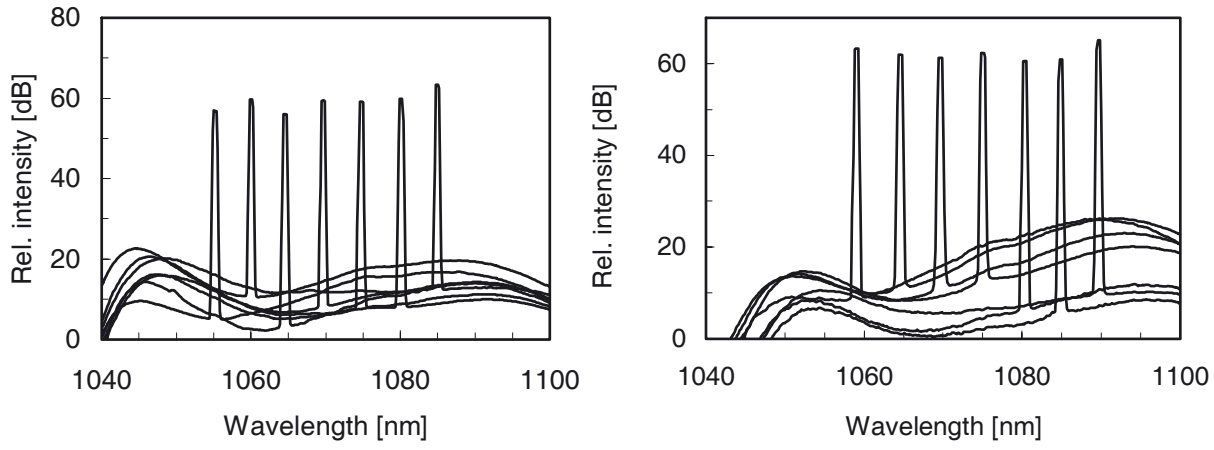

Fig. 3.2.6 *Output spectra of the20 m fiber (left diagram) and the 32 m fiber set-up (right diagram) for different settings of the tuning grating. The resolution of the optical spectrum analysator was 0.5 nm.*

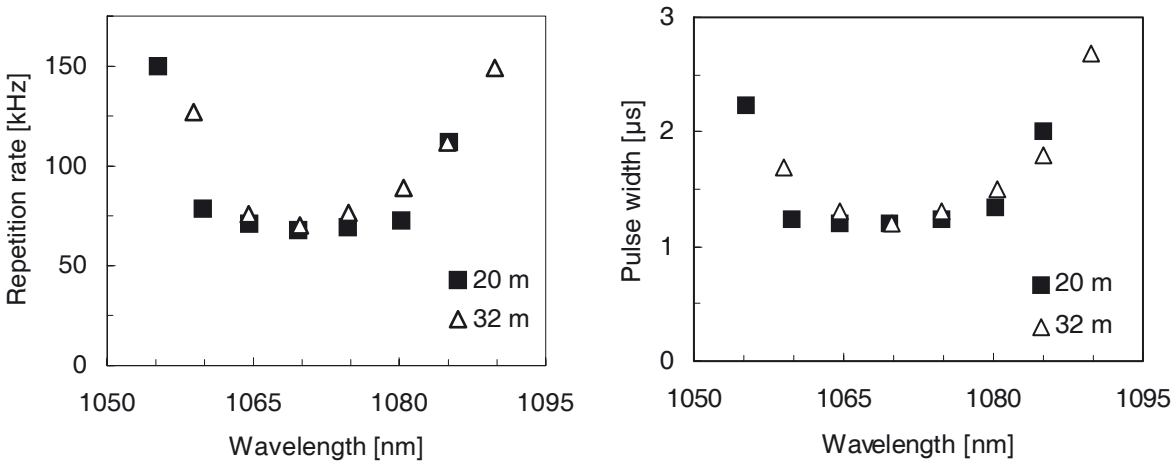

Fig. 3.2.7 *For 20 m and a 32 m Yb^{3+}:Tm^{3+}-gain fiber laser set-ups the measured repetition rate (left diagram) and pulse width (right diagram) as a function of signal wavelength are displayed. The corresponding pump powers were 16.8 W for the 20 m and 13.7 W for the 32 m set-up.*

3.2.5 Laser operation without spectral selective elements

Replacing the grating pair in figure 3.1.1 by a highly reflective mirror, a laser set-up without spectrally selective elements was realized. This "free running" laser set-up with a 20 m Yb^{3+}:Tm^{3+}-fiber showed similar pulsed operation for some waveplate settings as the previously described set-ups. Far above the Q-switching threshold, the pulse duration was typically about 2 µs. However, without the grating pair the signal linewidth increased to about 1 THz (4nm). The corresponding spectrum, which was centered at 1075 nm, is shown in the left diagram of figure 3.2.8.

Moreover, periodic pulse patterns, with up to three different pulse amplitudes in the photodiode signal, were observed for some waveplate settings (see lower trace in fig. 3.2.9). In this operation mode the relative height of the pulse levels depended also on the waveplate settings.

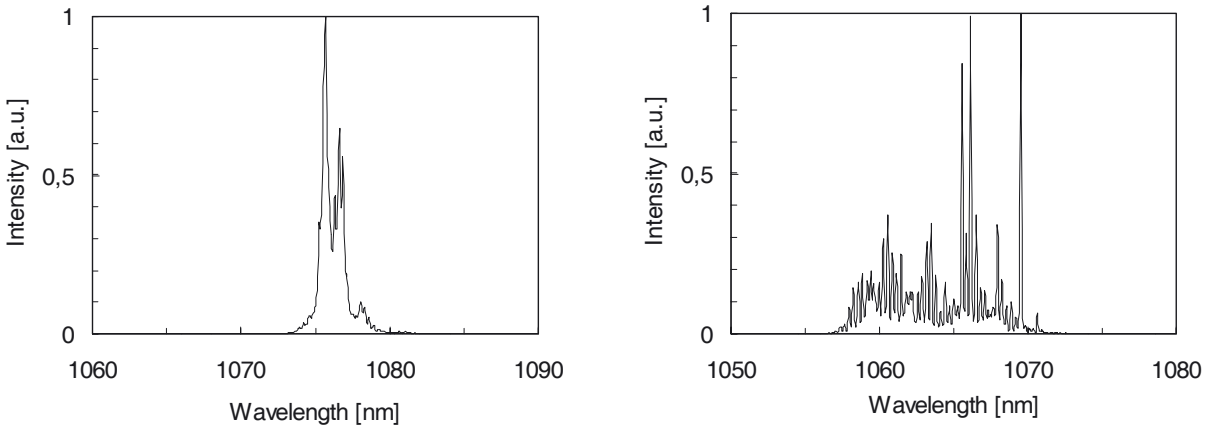

Fig. 3.2.8 *Output spectra of the fiber laser set-up without a grating pair. Left diagram: Typical Q-switched output spectrum for single pulse level operation. Right diagram: Output spectrum for three-pulse level operation mode.*

Measurements of the laser spectrum showed, that the output spectrum extended from 1055 nm to 1070 nm and had several peaks in this range (right diagram in fig. 3.2.8).

In addition to the Q-switching of the fiber laser, the Tm^{3+}-codoping caused also a blue fluorescence of the fiber. Therefore, in order to determine the influence of the Tm^{3+}-ions on laser operation in more detail, the correlation between the pulsed infrared laser emission and this blue fluorescence was investigated. This measurement was accomplished by inserting a dichroic mirror, highly reflective at 480 nm, into the cavity between QWP and the fiber end under an angle (Fig. 3.1.1). This mirror separated the backward traveling blue light from the infrared signal and steered it to a photodiode.

The photodiode signal of the blue fluorescence and the corresponding laser signal for a three level pulse pattern operation are shown in figure 3.2.9. It should be noticed from this figure, that there was no direct correspondence between the infrared pulse amplitude and the blue fluorescence. This shows that the efficiency for the generation of the blue fluorescence is different for the distinct pulses, which correspond to different amplitude levels. Taking the broader spectrum in the pulse pattern mode also into account, this indicate that the pulses with different signal levels in the photodiode signal have different wavelengths. Moreover, the blue emission of the Tm^{3+}-ions is generated by a three-step upconversion process, where the three pump transitions have different absorption peaks and transition probabilities (section 3.3.1) [MSB99]. Thus, the population of the various levels of the Tm^{3+}-ion influences not only the Q-switching properties of the laser but also the emission wavelength. Furthermore, the population distribution of the Tm^{3+}-ions depends also on laser signal wavelength and intensity. Hence, the interaction between laser signal and Tm^{3+}-absorption can generate such pulse patterns, if no spectral selective elements are in the cavity.

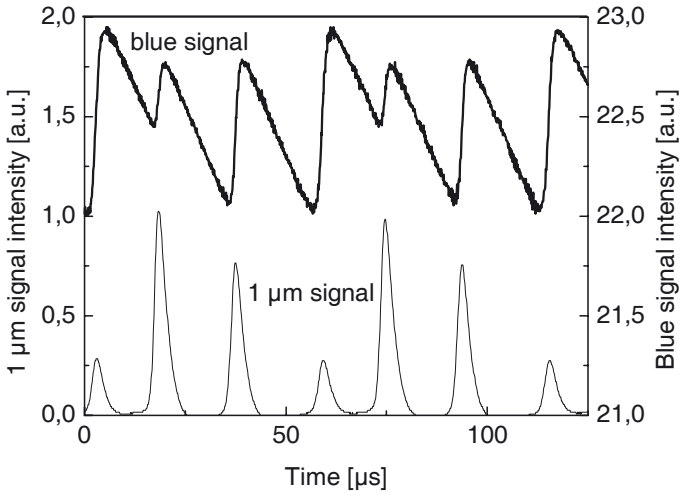

Fig. 3.2.9 *Lower trace: Periodic pulse pattern generated by the laser system. Upper trace: Blue florescence simultaneously emitted by the fiber.*

The waveplate settings influenced the amount and the spectral dependence of the cavity loss, as the polarization evolution in the cavity depends on signal wavelength. The latter is due to fiber birefringence and the limited bandwidth of the waveplates. For that reason, the wave-plate settings influence the transition between cw operation, standard Q-switching and "pulse pattern" Q-switching, especially in set-ups without a spectral selective element.

3.3 Physical mechanism of passive pulse generation

3.3.1 Effects of Tm^{3+}-codoping

Only a cw output or random intensity fluctuations but no stably pulsed operation was achieved, if a Yb^{3+}-doped gain fiber without additional Tm^{3+}-doping was used in the previous described set-up. This indicated that the Tm^{3+}-ions cause the pulsed operation. In addition it was previously mentioned, that the codoped gain fiber emitted blue light during infrared laser operation, which brightness increased with signal intensity. This blue fluorescence showed that the infrared laser signal was partially absorbed by the Tm^{3+}-ions, since a three-step up-conversion process causes blue emission of Tm^{3+}-ions, if they were pumped at about 1.1 µm [MSB99].

The energy structure and the relevant transitions of Tm^{3+}-ions are shown in figure 3.3.1[6]. By assuming a single exponential decay, the lifetime of the $^1G_4$ level was calculated from the measured decay of the blue fluorescence between successive pulses (e.g. fig. 3.2.9). The lifetime of the energy levels $^3F_4$ and $^3H_4$ in a silica glass host were mentioned in the literature [JKI99]. For the remaining energy levels, the lifetimes were calculated according to equation 2.4.1, based on the assumption that the lifetimes are mainly governed by nonradiative decays. Brackets indicate the corresponding data in figure 3.3.1.

Based on the energy diagram and the lifetime data, the absorption dynamics of the Tm^{3+}-ions in combination with a pulsed infrared laser signal was numerical simulated for a laser set-up with a 32 m Yb^{3+}:Tm^{3+}-gain fiber. Figure 2.3.2 shows the time dependence of the assumed laser signal and the calculated absorption curve. From the displayed Tm^{3+}-absorption curve the saturable absorption of the Tm^{3+} -ions on a µs-time scale can be clearly seen. In these calculations a repetition rate of 65 kHz and a circulating signal with 20 µJ pulse energy and 1.5 µs pulse width were assumed.

[6] The nomenclature of the energy levels is according to [MLE02]. However, it should be noted, that [KAM81] used a nomenclature were the manifold $^3H_4$ was changed to $^3F_4$ and vice versa. In the literature, both nomenclatures were frequently used [JKI99][MSB99].

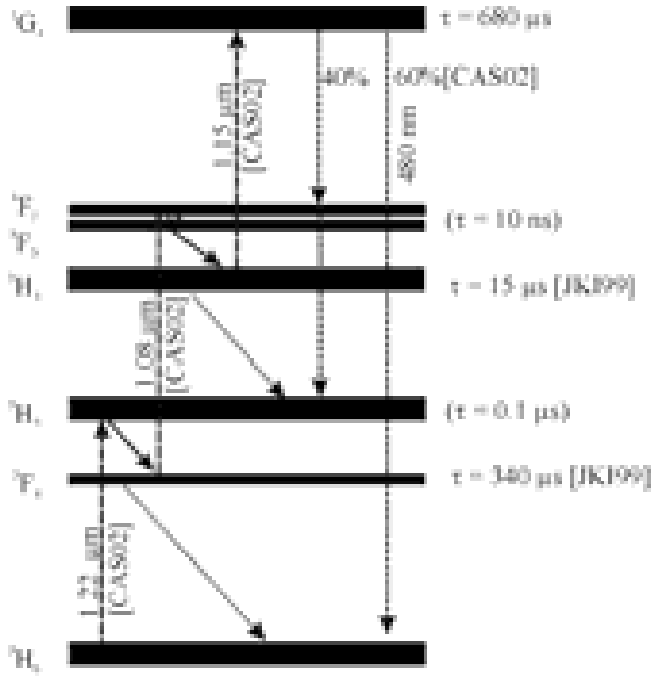

Fig. 3.3.1 *Energy level diagram for Tm^{3+}-ions (left). Vertical dashed arrows indicate pump transitions and fluorescence. Nonradiative decays, which are relevant for the upconversion process (solid), or which are taken into account for the calculations (dashed) are indicated by diagonal arrows. For pump transitions, the wavelength of the absorption peak is shown.*

These simulations also showed, that the saturable absorption is mainly due to the $^3F_4 \rightarrow {}^3F_{2,3}$ transition. This is a result of the strong (compared to the other two transitions) absorption and the long lifetime of the $^3F_4$ level. In addition, the decay time from the upper level of this transition to the $^3F_4$ level is about 15 µs and therefore of the same magnitude as the time interval between subsequent pulses. The main effect of the $^3H_6 \rightarrow {}^3H_5$ transition is the population of the $^3F_4$ level and therefore the activation of the previous mentioned transition. In con-

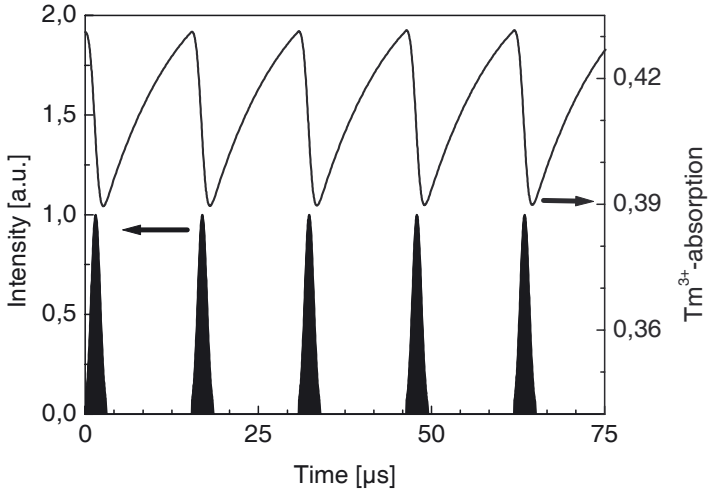

Fig. 3.3.2 *Upper trace shows the calculated Tm^{3+}-absorption at the signal wavelength in a 32 m long Yb^{3+}:Tm^{3+}-fiber. The lower trace shows the corresponding intra-cavity signal (20 µJ, 1.5 µs, 65 kHz).*

trast, the $^3H_4 \rightarrow {}^1G_4$ transition reduces the population of the $^3H_4$ level. Taking the nonradiative decays into account, this decreases also the absorption due to the $^3F_4 \rightarrow {}^3F_{2,3}$ transition.

Furthermore, it can be in figure 2.3.1 that, according to the simulation, the Tm^{3+}-ions absorb about 40% of the circulating signal. Therefore, the relatively low slope efficiency of the laser system is most likely a result of the high absorption loss of the Tm^{3+}-codoping. Moreover, the absorption of the Tm^{3+}-ions increases as the laser system is tuned to longer wavelengths, since the signal wavelength comes closer to the absorption maximum of the ground state absorption. The observed decrease of the output power of up to 35%, which was observed as the laser was tuned to longer wavelengths, strongly agrees with this assumption.

Furthermore, the exited state absorption of the $^3H_4$ level is becoming stronger with increasing signal wavelength. This effect must be even stronger than for the ground state absorption, since the absorption maximum of the corresponding transition is much closer to the signal wavelength than for the ground state absorption. This increased exited state absorption results in a decrease of the absorption by the $^3F_4 \rightarrow {}^3F_{2,3}$ transition. Thus, the saturable absorption decreases if the signal wavelength becomes to long. On the contrary, the ground state absorption decreases if the signal wavelength is tuned to shorter wavelengths. Therefore, the (saturable) exited state absorption by the $^3F_4 \rightarrow {}^3F_{2,3}$ transition is also reduced. These considerations agree with the observation, that Q-switching becomes unstable outside some tuning limits.

The effect of the Tm^{3+}-ions on laser operation of the Yb^{3+}-fiber is somewhat similar to the saturable absorption effect of Er^{3+}-clusters in heavily doped Er^{3+}-fibers. In these fibers the Er^{3+}-clusters favor self-pulsing operation [CCB96]. For both systems the loss modulation of the Tm^{3+}-ions or Er^{3+}-ion clusters, respectively, is relatively weak compared toh the fiber gain. For the Tm^{3+}-system, this can be seen from the simulations shown in figure 3.3.2 (~ 3% modulation).

For the previous mentioned simulations the ground state absorption, the exited state absorptions from the $^3F_4$ and $^3H_4$ levels and the lifetimes of the various energy levels were taken into account. Furthermore, it was assumed that the energy levels decay nonradiative to the level below, except for the $^1G_4$ level. For the $^1G_4$ level, the radiative decay to the ground level was also included and a branching ratio of 60:40 between the decay to the $^3F_2$ level and the ground was used. This branching ratio was mentioned in the literature for Tm^{3+}-ions in ZBLAN glass and was used as a rough approximation for the decay in silica glass [CAS02].

The (unsaturated) ground state absorption at about 1.06 µm was estimated to about 0.5 dB in the 32 m fiber, based on absorption measurements on a Tm^{3+}-doped silica fiber. Furthermore, it was roughly estimated, that the oscillator strength of the $^3F_4 \rightarrow {}^3F_{2,3}$ transition is about

30 times higher than the ground state absorption. This estimation is based on the absorption spectrum of the Tm^{3+}-fiber and the information from the literature that (in ZBLAN fibers) the excited state $^3F_4 \rightarrow {}^3F_{2,3}$ transition has a similar oscillator strength as the $^3H_6 \rightarrow {}^3H_4$ transition [CAS02]. For the $^3H_4 \rightarrow {}^1G_4$ transition it was assumed that it is about three times higher than the ground state absorption, since the mismatch between the absorption peak and the signal wavelength is smaller than for the ground state absorption. Variations of these ratios showed, that the qualitative behavior of the absorption curve was quite insensitive to these ratios. Therefore, these simulations confirm a saturable absorption effect of the Tm^{3+}-ions, despite of the uncertainties for the absorption cross sections.

3.3.2 Relaxation oscillations

Previous mentioned simulations have shown that Tm^{3+}-codoping cause saturable absorption. However, the pulse durations in the µs range and the observed high duty cycle are indications that laser operation was also influenced by relaxation oscillations. Calculations of the relaxation frequencies, according to equation 2.5.1, showed a good agreement between the calculated and the observed repetition rates for both set-ups. The calculated and the measured repetition rates are plotted versus output power in figure 3.3.3. The good correspondence between calculated and observed repetition rates show that the repetition rate of this laser system was determined by relaxation oscillations. In the literature a similar behavior was described for Er^{3+}-fiber lasers, where Er^{3+}-clusters or fiber sections which were not pumped above threshold cause some saturable absorption [CCB96][RMO97]. Therefore, a saturable absorption in the fiber favors self-pulsing due to relaxation oscillations in Er^{3+}- as well as in

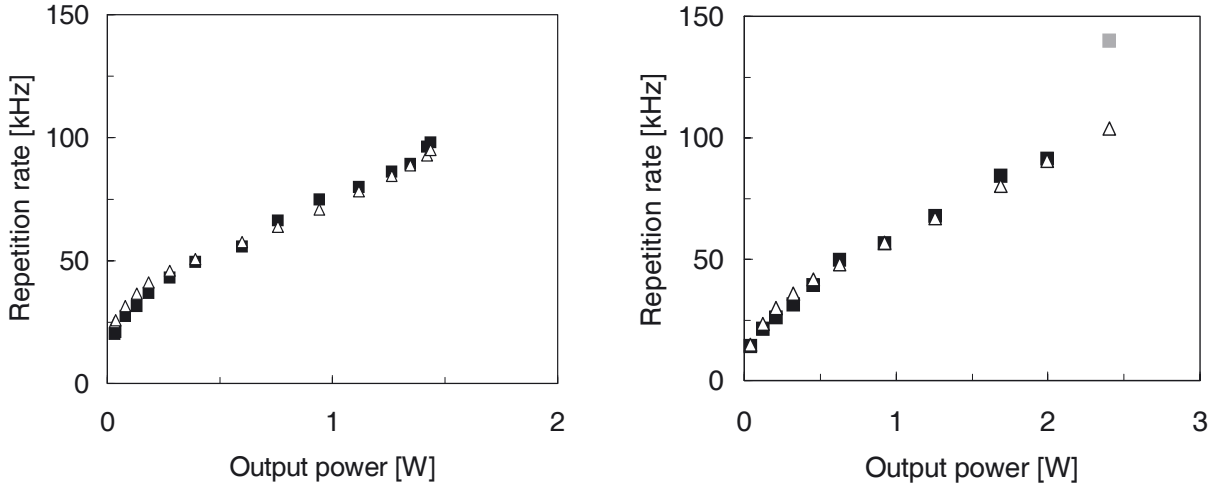

Fig. 3.3.3 *Calculated and observed repetition rates versus output power for the set-up with a 20 m (left diagram) and a 32 m (right diagram) long gain fiber. The calculated repetition rates were indicated by triangles, while the squares correspond to the measured values.*

Yb^{3+}-doped fibers. The saturable absorption causes a positive feedback for relaxation oscillations, which compensate the decay of these oscillations. Hence, the saturable absorption of the Tm^{3+}-ions stimulates and sustains the observed relaxation oscillations.

The decay rates for photons in the cavity γ_C and for excited Yb^{3+}-ions γ_{Yb} were the key parameters for the previous mentioned calculations of the relaxation oscillation frequencies. These parameters were determined according to equations 3.3.1 – 3.3.4. In these equations T_C and L_C are the cavity round trip time and loss, τ_N is the "natural" lifetime of exited Yb^{3+}-ions, R_{out} is the outcoupling factor and P_P and P_{out} are the pump and the output power. Moreover, A_{P_core} and A_{L_core} are the cross sections of pump and laser core. W_{Pump} and W_{Signal} are the absorption and emission cross sections of Yb^{3+}-ions at pump and signal wavelength. N_{Yb} is the total number of Yb^{3+}-ions in the fiber and E_{Photon_S} is the energy of a laser photon. In addition, $\Delta\tau_{abs}$ designates the average time interval between two excitations of a Yb^{3+}-ion which result in stimulated emissions. The pump and the signal power distribution had roughly the same shape along the fiber, as the laser was pumped in backward direction,. Therefore the approximation, that the ratio between pump and signal power was constant along the fiber, was implicitly used in equation 3.3.3. It is worth to mention, that in equation 3.3.4 $\Delta\tau_{abs}$ is calculated from the number of generated laser photons and not from the absorbed pump photons. By this way, the calculated decay rate γ_R is solely due to stimulated emissions. The influence of spontaneous decays on ion lifetime is included by equation 3.3.2.

$$\gamma_C = \frac{-\ln(1-L_C)}{T_C} \tag{3.3.1}$$

$$\gamma_{Yb} = \gamma_R + \frac{1}{\tau_N} \tag{3.3.2}$$

$$\gamma_R = \frac{1+\left(\frac{P_{out}}{P_P \cdot R_{out}}\right)\left(\frac{W_{Signal}}{W_{Pump}}\right)\left(\frac{A_{L_core}}{A_{P_core}}\right)}{\Delta\tau_{abs.}} \tag{3.3.3}$$

$$\Delta\tau_{abs.} = \frac{N_{Yb} \cdot E_{Photon_S}}{P_{out} \cdot L_C \cdot 1/R_{out}} \tag{3.3.4}$$

Furthermore, the repetition rates, which are shown in figure 3.3.3, were calculated by assuming a cavity loss of 90%, a lifetime of 0.9 ms for the Yb^{3+}-ions and a ratio of 5 (see figure 2.4.3) between pump absorption and laser emission cross section. Moreover, the threshold pump powers for both set-ups were used as fit parameters and determined by least square fits for the repetition rates. By this way, threshold pump powers of 3 W and 1.94 W were calculated for the 20 m and the 32 m gain fiber set-ups. These values are relative close to

the measured threshold pump powers of 3.3 W and 1.6 W, respectively. Potential sources for these small deviations are uncertainties about the Yb^{3+}-ion lifetime in the fiber and the total cavity loss. In addition, the loss caused by the intensity dependent absorption of the Tm^{3+}-ions was also not directly included in the previous calculations.

It can be seen from equation 3.3.1 that the cavity decay rate decreases as the outcoupling factor and therefore the cavity loss becomes higher. Consequently, the calculated repetition rate increases with increasing outcoupling factor (eqs. 2.5.1). Such a relation between repetition rate and outcoupling factor was also experimentally observed (fig. 3.2.3).

Furthermore, equations 3.3.2 – 3.3.3 show that the decay of excited Yb^{3+}-ions becomes faster as the output power increases. Moreover, the decay rate of the relaxation oscillations is proportional to the decay of the exited Yb^{3+}-ions (equation 2.5.2). This damping counteracts the stimulation of the oscillations by the saturable absorption. This qualitatively agrees with the observation that for pump powers above 16.2 W no complete on/off modulation was observed for the 32 m set-up (section 3.2.3). Therefore, the Yb^{3+}-lifetime or the modulation amplitude of the saturable absorption must be increased for pulsed operation at higher power levels. A longer lifetime of the exited Yb^{3+}-ions can be accomplished by a higher number of Yb^{3+}-ions in the cavity while the latter requires more Tm^{3+}-ions.

3.3.3 Polarization effects

The following effects can explain the observed influence of the waveplate settings on Q-switched operation: Due to the polarizing elements in the cavity, resonator loss depends on birefringence of the fiber and the waveplates. Furthermore, the polarization evolution in the fiber depends on the signal intensity for an elliptically polarized signal due to the Kerr-effect, which can be used for mode locking (section 2.5.2). Normally, the circulating signal is elliptically polarized somewhere in the fiber as the birefringence of standard gain fibers shows random fluctuations. For this reason, the typically observed ns substructure of the µs pulse is likely due to nonlinear polarization effects in the fiber. This assumption is strongly supported by the fact, that mode-locking was also be achieved for appropriate waveplate settings for the set-up without tuning-gratings.

Both effects can be avoided by a polarization maintaining (PM) gain fiber. For such a fiber, no birefringence compensation by waveplates is required and nonlinear polarization rotation effects can be avoided as a linear polarization is maintained along the fiber if the signal polarization is adjusted to one of the fiber polarization modes.

3.4 Conclusion and outlook

The experiments showed that the repetition rate of such a Yb^{3+}:Tm^{3+} laser system is determined by relaxation oscillations. Therefore, it can be controlled according to the basic relaxation oscillation theory, e.g. by pump power and cavity loss. By this way, it is possible to adjust and to stabilize the repetition rate. Furthermore, an additional fiber amplifier at the output would enable an independent control and adjustment of repetition rate and pulse energy. For such an oscillator-amplifier set-up, even higher pulse energies can be expected, as the cavity set-up does not determine the pulse energy.

The overlap between the laser signal and the Tm^{3+}-ions can be modified by variation of the axial doping distribution of these ions e.g. ring doping [NMP98]. By this way, the power dependence of the absorption can be modified, while the absorption can be simultaneously adjusted by the doping concentration. This would enable a further optimization of such Yb^{3+}:Tm^{3+} fibers for specific operation conditions.

Furthermore, it was shown that the broadening of the laser linewidth is mainly caused by four-wave-mixing in the fiber. This nonlinear effect increases with fiber length and decreasing mode-field area. Hence, laser linewidth can be further reduced by the use of short fibers with high doping concentrations and a large mode field diameter. Alternatively, the linewidth can be minimized by reducing the intra-cavity intensity and using a fiber power-amplifier at the output.

The mechanical complexity of the laser set-up can be further reduced by transversal pump light coupling schemes, as such couplers are now commercially available [OFS03][ITF03]. Hence, a relatively compact pulsed laser system can be realized in combination with a fiber optic circulator, which would be a very promising pump source for small linewidth optical parametric oscillators [KAA03].

4 Mode-locked Yb^{3+}-fiber laser

In the previous section a Q-switched laser system was described, which generated narrow linewidth microsecond pulses. However, a large variety of applications like optical coherence topography [PBH03], multi-photon-microscopy [SKK98] or medical treatments [KKR02] require much shorter pulse durations, higher peak powers or broader signal bandwidths. Such pulse parameter can be realized by mode-locked laser system. Therefore, a mode-locked Ytterbium fiber laser is described in the following section.

Yb^{3+}-doped fibers are extremely suitable for mode-locked laser systems, because of the broad gain bandwidth of more than 80 nm and their high optical conversion efficiency of up to 80% [PNT97]. However, in order to achieve a broad signal and to enable ultrashort mode-locked pulses, the normal dispersion of the silica fibers at the emission wavelength of the Yb^{3+}-ions must be compensated by additional elements.

Cautaerts et al. demonstrated the potential of Yb^{3+} fiber laser for generation of ultrashort pulses [CRP97]. This fiber laser was passively mode-locked by using nonlinear polarization rotation and emitted 100 fs laser pulses. However, this set-up required a large separation of about 75 cm between the external prisms for dispersion compensation, despite of the only 75 cm long active fiber. Because of this short fiber length, the double-clad concept could not be applied, as this pumping scheme requires much longer fibers to absorb sufficient pump energy. Therefore, a high beam quality pump source had to be used. As a further consequence, the pulse energy was rather low and limited to about 100 pJ. In addition, Hofer et al. demonstrated passive mode-locking with a Nd^{3+}-doped double-clad fiber laser at 1065 nm. However, because of the short fiber length of 3.6 m the advantages of the double-clad concept could not be fully exploited in that setup while the dispersion compensation scheme was extremely large [HHR99].

In this section a new Yb^{3+}-fiber laser set-up with a long cladding-pumped active fiber is presented. This laser set-up, pumped by a high power laser diode with low beam quality, achieved self-starting mode-locking as well as a high power broadband output signal simultaneously and therefore overcomes the previous mentioned limitations.

4.1 Experimental set-up

The basic set-up of the mode-locked cladding-pumped fiber laser was similar to the previously described laser set-up for Q-switched operation. However, a dispersive delay line

with two diffraction gratings was integrated into the cavity for dispersion compensation instead of the Littman-Littrow grating pair.

Figure 4.1 shows the set-up in detail, which is comprised of four principal modules: a Yb^{3+}-doped double-clad fiber that provides the gain and the nonlinearity, waveplates for polarization control, an optical isolator for unidirectional laser operation and the dispersive delay line. The first grating of the delay line was also used as an output coupler, since nearly 30% of the laser radiation was reflected into the zeroth diffraction order (port 1). The double-clad fiber was pumped at 940 nm with a 18 W fiber-coupled laser diode.

The gain fiber had a core diameter of 4.2 µm, a Yb_2O_3-doping concentration of 6500 ppm mol and a cut-off wavelength of about 950 nm. Furthermore, an effective mode field area of 20.3 µm² at 1100 nm was calculated from the refractive index structure of the fiber. This fiber with a pump core diameter of 400 µm was coiled in a kidney-shape for improved pump-light absorption. The pump light was coupled into the resonator through the dichroic mirror M1. The signal out of the fiber was reflected by mirrors M1 and M2 to the entrance aperture of the optical isolator. The polarizing beam splitter at the isolator input rejected one polarization and, therefore, acted as an additional output port (port 2). Behind the isolator, the signal propagated below mirror M4 to the dispersive grating pair and the incident angle was about 63° at the first grating. The total dispersion of the two parallel mounted gratings, both with 1200 lines/mm, was adjusted by variation of the grating separation. After passing the second grating, the beam was back reflected by the slightly tilted mirror M3 and then coupled into the fiber via M4 and M5. The total loss of the dispersive grating line was about 83 %. The polarization of the radiation at the fiber input was determined by the settings of the zeroth order waveplates (1.064 µm).

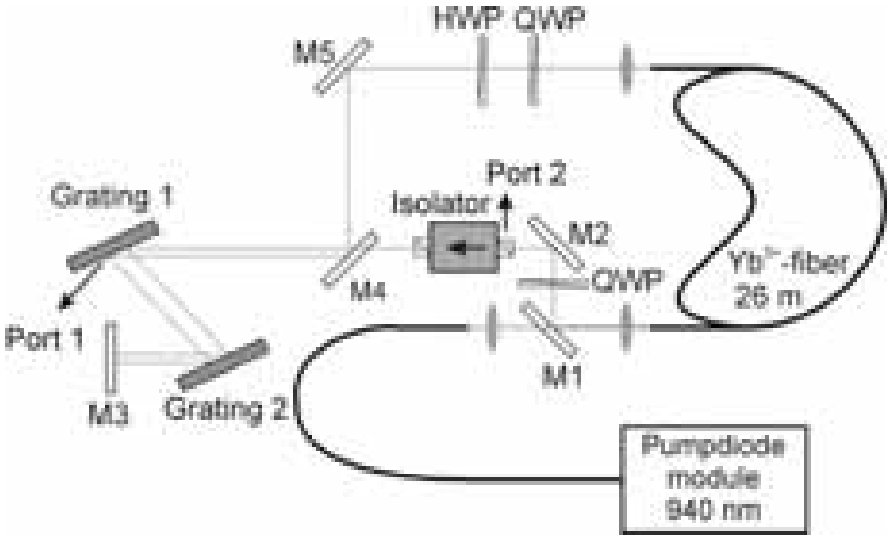

Fig. 4.1.1 *Set-up of the mode-locked Yb^{3+}-fiber laser system.*

4.2 Mode-locked laser operation

For appropriate waveplate settings the polarization beam splitter (port 2) in combination with the nonlinear polarization rotation rejected low intensity signals like a saturable absorber and self-starting mode-locking with a repetition rate of 7.6 MHz was achieved. The measured output powers were plotted versus the pump power in the left diagram of figure 4.2.1. Strong mode-locking hysteresis can be seen in this figure. Mode-locking started at a pump power of 9.5 W and was maintained down to 5.6 W, if the pump power was decreased. During mode-locked operation the output power was higher at port 1 and lower at port 2 compared to cw operation, which is an evidence that the polarization beam splitter is acting like a saturable absorber and is therefore supporting mode-locking. With 17.1 W of pump power a maximum output power of 137 mW at port 1 and 580 mW at port 2 was achieved. The time response of a fast photodiode (100ps rise time), detected by a 500 MHz oscilloscope, was used to identify the pulsed operation of the laser. A typical oscilloscope trace for mode-locked operation is shown in the right diagram of figure 4.2.1.

As spectral bandwidths of about 25 nm can be readily achieved, a maximum bandwidth of 40 nm was only obtained by optimizing the settings of the three waveplates and the grating separation. Such a spectrum is shown in the left diagram of figure 4.2.2. Taking into account only the main peak of this spectrum, a good agreement with a Super-Gaussian fit function, which is described by $I(\lambda)=\exp\left(-(\lambda-\lambda_0)^2/2\sigma^2\right)^{1.5}$ can be obtained. This is in contrast to signal bandwidths of less than 30 nm, where the spectrum was typically consistent with a Gaussian fit function. This can be seen in the right diagram of figure 4.2.2. It is worth to

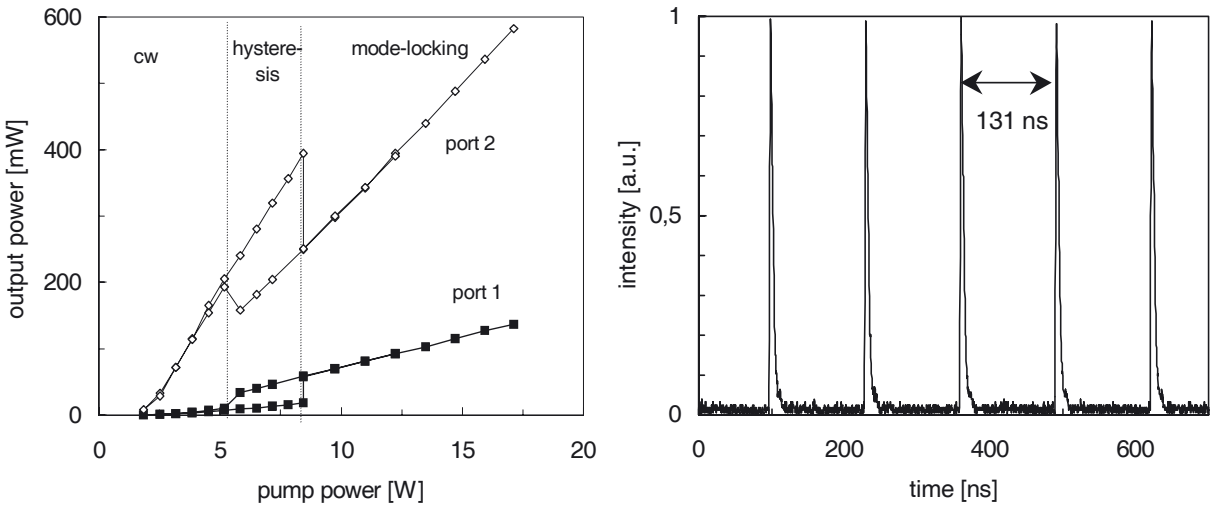

Fig. 4.2.1 *Left diagram: Output power of both output ports versus pump power for a given setting of the waveplates. Right diagram: Photodiode trace of the mode-locked output signal. The pulse to pulse time interval of 131 ns corresponds to the cavity round trip time.*

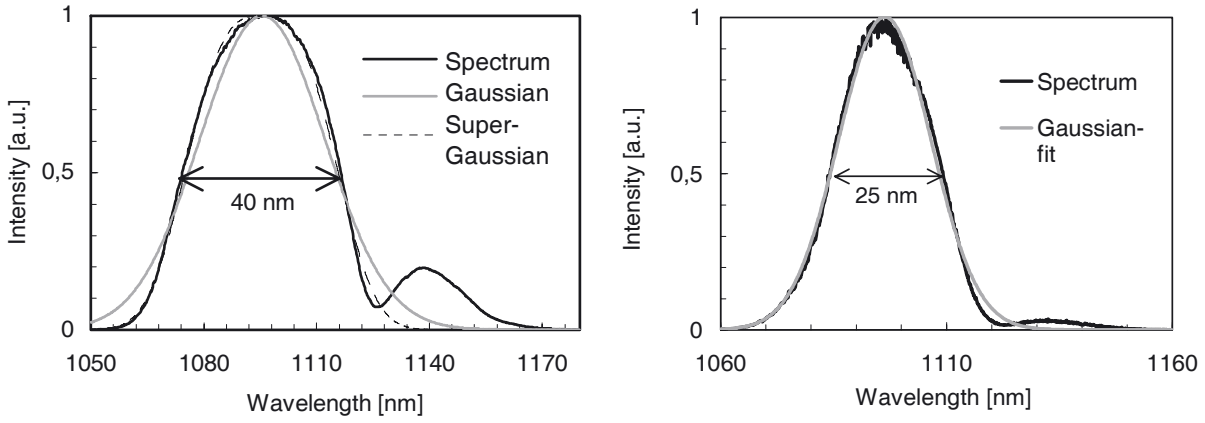

Fig. 4.2.2 *Left diagram: Spectrum with the maximum achieved bandwidth at port 1 (solid curve). Grey curve, Gaussian-fit. Dashed curve, Super-Gaussian fit. Right diagram: Typical output spectrum (black curve) and the corresponding Gaussian fit (grey curve).*

mention that the evolution of the output spectra with pump power indicated a quantization of the pulse energy. This is described in detail in section 4.3.

The long signal wavelength of about 1095 nm was a result of the high Yb^{3+} doping concentration in combination with the large fiber length [PCH95]. Furthermore, with increasing pump power the center wavelength was slightly (< 8 nm) sifted to longer wavelengths. This wavelength shift can be attributed to an increased Raman self-frequency shift of the pulse. During propagation, the sign of the frequency chirp changes somewhere in the fiber due to the fiber GVD (section 4.5). Hence, the different wavelength components of the pulse can interact to some extent despite of the pulse stretching in the resonator (section 4.4 and 4.6) and the Raman self-frequency shift is not completely suppressed.

Figure 4.2.3 shows in detail, that the spectra of the two output ports were similarly shaped with only slight deviations. This suggests that there were only minor pulse quality degenerations at the rejection port (port 2) of the mode-locking scheme. A similar behavior was previ-

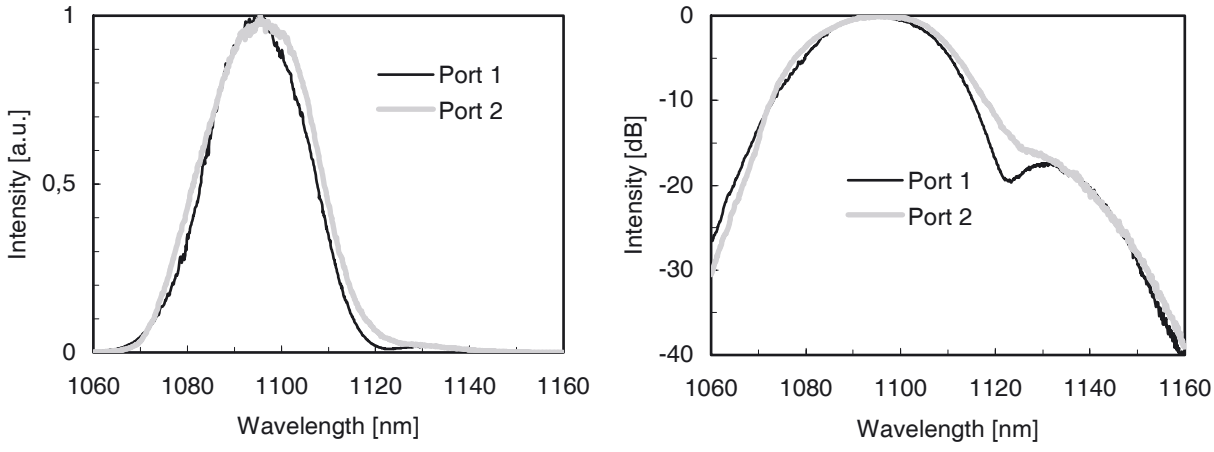

Fig. 4.2.3 *Spectrum at both output ports on a linear (left) and a logarithmic (right) scale. These spectra were measured at a pump power of 9.7 W.*

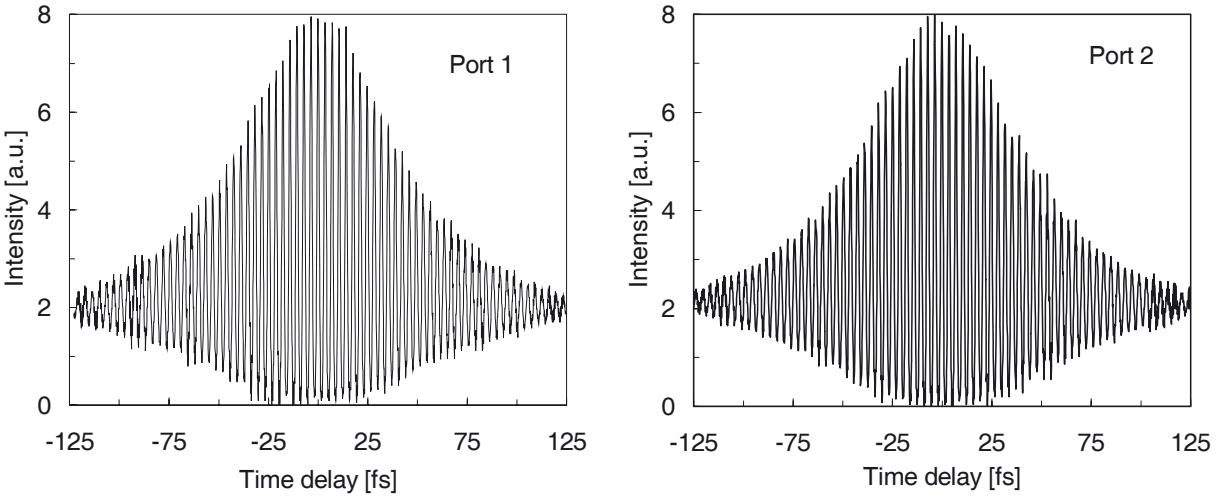

Fig. 4.2.4 *Interferometric autocorrelation function at both output ports. A pump power of 9.7 W was applied to the laser during these measurements.*

ously observed in Er^{3+}-doped fiber lasers using the same mode-locking mechanism [TDN94]. In addition, it can be seen in figure 4.2.4 that the interferometric autocorrelation function at both output ports were similarly shaped, which also implies, that the pulse quality degeneration at port 2 is relatively small. The deviation of the autocorrelation functions from the typical 8:1 ratio at the end of the fringe pattern in figure 4.2.4 is a result of the pulse chirp (section 4.4).

The intensity of the secondary peak at 1140 nm, which is especially noticeable in the left diagram of figure 4.2.2, depended on the waveplate settings, the pump and the output power. The frequency difference between both peaks of about 10.5 THz is within the gain bandwidth of stimulated Raman scattering (SRS) in silica fibers. Furthermore, SRS increases with signal power, as observed in these experiments. Therefore, this peak was most likely supported by SRS. Apart from SRS, the high third order dispersion of the cavity can also cause such a secondary peak in the mode-locked spectrum [SCB94]. Finally, the Yb^{3+} gain curve extents up to 1.2 µm and supports therefore the secondary peak to some extent [PCH95].

The influence of the waveplate settings on this secondary peak is attributable to two effects. First, they affected mode-locking operation and consequently temporal and spectral pulse width as well as the peak intensity in the cavity. By this way, the SRS gain is influenced. Second, because the limited bandwidth of the zero order waveplates, which were designed for 1.064 µm, variations of the waveplate settings had different effects on the polarization evolution for the main peak at about 1095 nm and the secondary peak at about 1140 nm. Consequently, the relative cavity loss and therefore the relative intensity of the main and the secondary spectral peak depend on the waveplate settings.

During laser operation, a slight blue fluorescence was noticeable from the fiber, although the brightness was much lower than for the Yb^{3+}:Tm^{3+}-fiber. This indicated some Tm^{3+}-impurities. These impurities favor intensity fluctuations (section 3.3.1), which probably supports self-starting of the mode-locking. Besides, it should be mentioned, that high cavity losses, e.g. due to misalignment, must be avoided at high pump powers (≥ 7 W), as this would result in a high inversion and gain. Otherwise, stimulated Brillouin scattering can cause the emission of high-energy Q-switched pulses from the long and highly doped fiber [CZT97]. Observations showed that such pulses have even the potential to damage the core region at the end-facets of the fiber.

4.3 Pulse energy quantization

A detailed analysis of the output spectrum showed that with increasing output power the peak spectral intensity made quantization like discrete steps to higher intensity levels at certain thresholds. For the lower and the upper limits of several of these steps, the spectra and the corresponding output powers at port 1 are shown in figure 4.3.1. These spectra show, that between these quantization steps the peak spectral intensity slightly decreased with increasing output power. Simultaneously, the spectral bandwidth increased slightly (< 10%) between the quantization steps. As the output power rose above the threshold for the next quantization step, the spectral bandwidth decreased while the peak intensity increased. The same behavior was observed in reversed order if the output power was decreased by a reduction of the pump power. Starting with an output power of 135 mW at port 1 and 580 mW at port 2 eight different levels in the mode-locked spectrum were observed as the pump power was reduced.

The observed quantization depended on the waveplate settings and indicated that there were multiple pulses circulating inside the cavity. With increasing output power the number of circulating pulses increased, while it decreased with decreasing output power. The quantization steps therefore corresponded to variation of the number of pulses, circulating in the cavity. Assuming that at each quantization step the number of circulating pulses changed by one, the measured output powers corresponded to an individual pulse energy of 2.2 nJ at port 1 and 9.5 nJ at port 2, respectively. As the mode-locking was based on nonlinear polarization rotation in the fiber, such a quantization can be expected, since the transmission at the polarization beam splitter varies periodically with signal intensity (section 2.5.2). This limits the pulse energy and favors the formation of an additional pulse in the cavity, if the pulse energy is becoming too large.

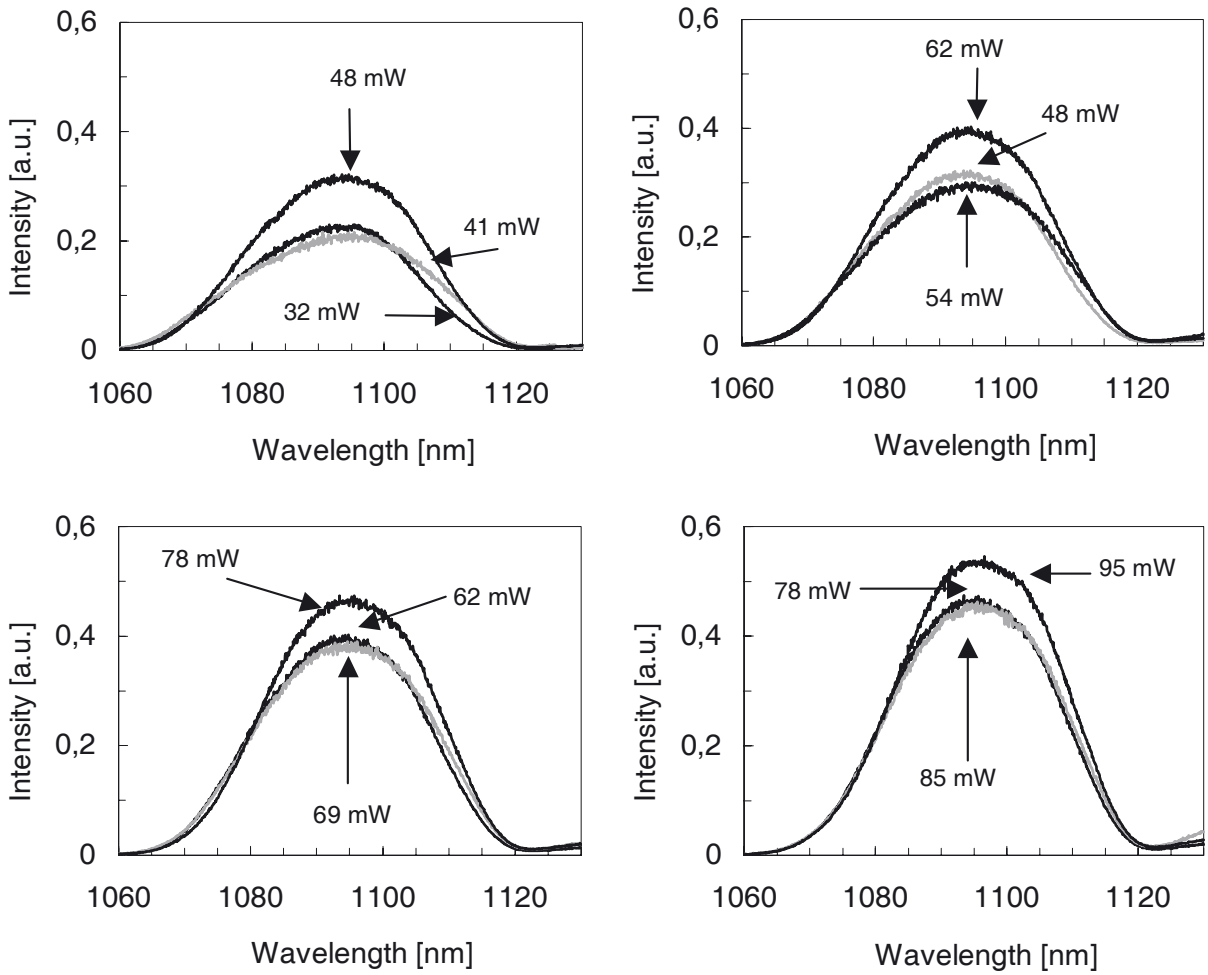

Fig. 4.3.1 *Output spectra at port 1, which were measured for identical set-ups except for the pump power. These spectra show the relative spectral intensities versus wavelength for different output power levels, which correspond to the lower and the upper limits of the observed quantization steps.*

Measurements with a streak camera confirmed this interpretation as they showed several closely spaced pulses at high pump powers. For these measurements the output signal was frequency doubled by a 1 mm thick KDP-crystal, since the spectral sensitivity of the streak-camera extents only from 400 – 900 nm. Figure 4.3.2 shows some of these measurements. It can be seen that the pulses were irregularly spaced and the pulse-to-pulse distance varied from

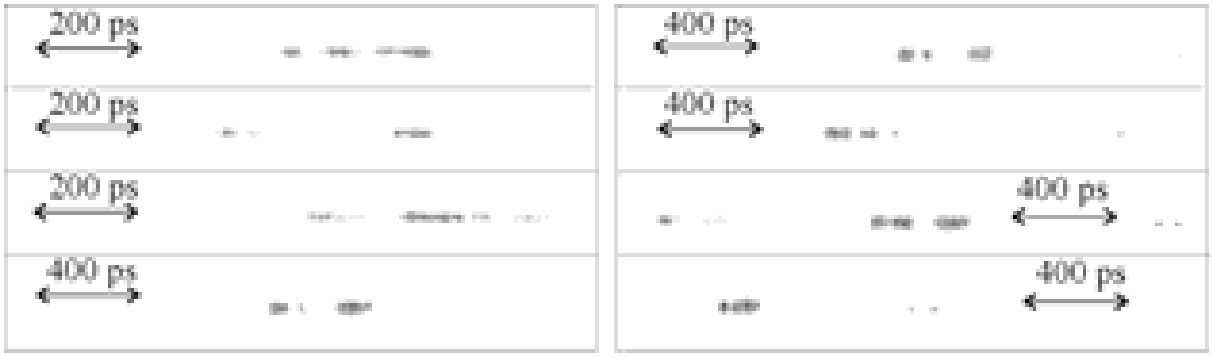

Fig. 4.3.2 *Several streak camera measurements of the frequency doubled output signal from the mode-locked Yb^{3+}-fiber laser.*

about 10 ps to several 100 ps. A systematic analysis of the output signal were limited by the timing jitter of the required electronic trigger signal (~ 20 ns), which was much larger than the measuring time of the streak camera (2.2 ns). Because of the small and irregular pulse-to-pulse spacing, measurements with a fast photodiode in combination with a 500 MHz oscilloscope and interferometric crosscorrelation measurements with path differences up to 100 ps revealed no clear evidence of multiple pulse operation. For some other waveplate settings, the photodiode signal showed clearly detectable multi-pulse operation inside the cavity. However, this operation mode was usually unstable.

4.4 Cavity dispersion

The cavity dispersion is a key parameter for mode-locked lasers, since the dispersion influences the phase relation between the various cavity modes. For that reason, the total cavity dispersion was determined for different grating separations. This was performed by measuring of the repetition rate versus the center wavelength of the signal, as this relation depends on the cavity dispersion [KGO93].

During these experiments, the repetition rate was calculated from the 45. harmonic of the round trip frequency, for an increased frequency resolution. The corresponding measurements were performed by an electrical spectrum analysator in combination with a fast photodiode (2 GHz). Simultaneously, the center wavelength of the output spectrum was determined by means of an optical spectrum analysator. Variations of the center wavelength were introduced by spectral filtering in the grating line with a movable blade in front of mirror M3.

Figure 4.4.1 shows the cavity round trip time versus center wavelength for grating separations

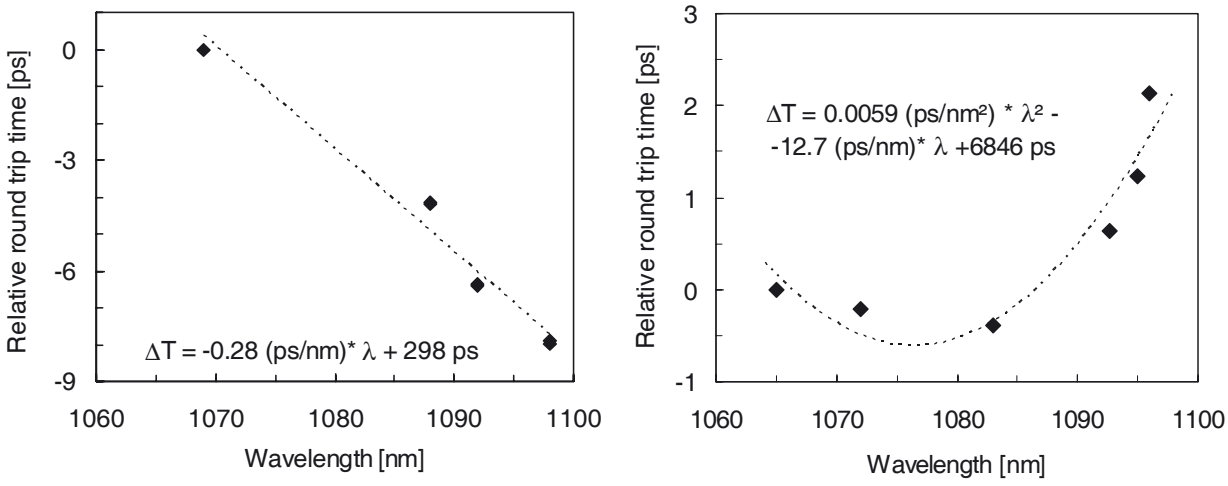

Fig. 4.4.1 *Measured relative cavity round trip time versus wavelength of the mode-locked pulses for grating separations of 5.4 cm (left diagram) and 7.4 cm (right diagram). Furthermore in each diagram a fit function (dashed line) and the corresponding equation is displayed.*

of 5.4 cm (left) and 7.4 cm (right). The relation between round trip time and center wavelength is approximately linear for the set-up with 5.4 cm grating separation, indicating that the GVD is the dominating dispersion term in the cavity (eqs. 2.1.11 -2.1.14). The slope of about –0.28 ps/nm describes the total dispersion in terms of the dispersion parameter D and corresponds to a β_2 value of $1.7 \cdot 10^5$ fs^2 (eqs. 2.1.16).

With the given parameters, the GVD of the grating pair increased by $-8.4 \cdot 10^4$ fs^2/cm with grating separation (eqs. 2.6.2). It was therefore calculated from previous measurements, that the GVD in compensated for a grating separation of 7.4 cm. For such a modified set-up, the relation between cavity round trip time and center wavelength is displayed in the right diagram of figure 4.4.1. It can be seen, that the round trip time had a minimum at about 1080 nm. This shows that the GVD of the cavity was compensated at this wavelength.

For grating separations larger than 7.4 cm, the measured round trip time increased with increasing wavelength, which corresponds to anomalous cavity dispersion. Furthermore, based on previous data, it can be calculated from the corresponding grating separation of 9.2 cm, that the maximum spectral bandwidth was achieved for an anomalous cavity dispersion of $-1.5 \cdot 10^5$ fs^2.

Previous measurements showed that the GVD of the 26 m long fiber was compensated by the grating pair for a grating separation of 7.4 cm. This results in a fiber dispersion of $2.39 \cdot 10^4$ fs^2/m, as this grating separation correspond to a grating GVD of $-6.21 \cdot 10^5$ fs^2. Additionally, the fiber dispersion was calculated from the Sellmeier's equation for silica glass [AGR95] and the waveguide dispersion. The latter was numerically calculated from the fiber structure, which is shown in the left diagram of figure 4.4.2 (Appendix A). The resulting dispersion data are shown in table 4.4.1. The calculated GVD of $2.40 \cdot 10^4$ fs^2/m is in good agreement with the fiber GVD that was determined by previous described measurements. It is worth to mention, that the influence of the Yb^{3+}-doping on material dispersion was not taken into account in these calculations. Therefore, the good agreement between calculated and measured GVD indicate that under the used operation conditions the influence of the Yb^{3+}-doping on fiber dispersion can be neglected.

	material dispersion	waveguide dispersion	fiber dispersion
GVD fs^2/m	$1.53 \cdot 10^4$	$8.7 \cdot 10^3$	$2.40 \cdot 10^4$
TOD fs^3/m	$4.59 \cdot 10^4$	$-2.21 \cdot 10^4$	$2.38 \cdot 10^4$

Table 4.4.1 Calculation of the fiber dispersion for the Ytterbium gain fiber at 1080 nm (eqs. 2.1.15). The material dispersion was calculated from the Sellmeier equation for silica glass, while the waveguide dispersion was computed from the refractive index structure of the fiber.

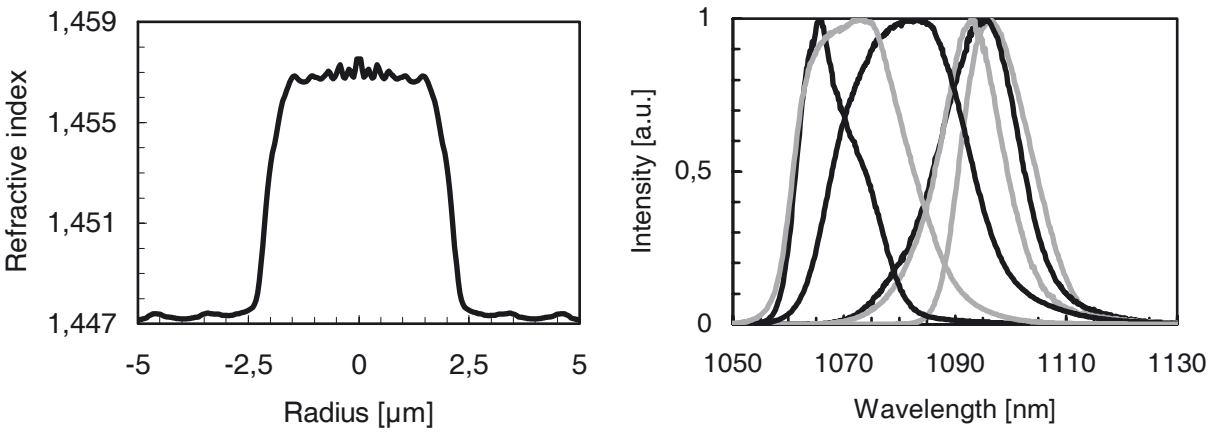

Fig. 4.4.2 *Left diagram: Refractive index profile of the Yb^{3+}-gain fiber [UNG03]. Right diagram: Output spectra of the set-up with 7.4 cm grating distance, adjusted for different center wavelengths*

It can be seen in figure 4.4.1 for the set-up with a grating distance of 7.4 cm, that the relation between relative round trip time and mean wavelength can be described by a quadratic function. Such a quadratic relation can be attributed to the third order dispersion (TOD) (eqs. 2.1.11 – 2.1.14). The quadratic coefficient of the fit function of 0.0059 ps/nm² corresponds to a TOD of $2.27 \cdot 10^6$ fs³.

Further calculations showed that the grating pair was attributable for a TOD of $4.69 \cdot 10^6$ fs³ (eqs. 2.6.2 - 2.6.3) and that the fiber had a TOD of $2.38 \cdot 10^4$ fs³/m (table 4.4.1), which corresponds to a cavity TOD of $4.9 \cdot 10^6$ fs^3. This value pointed out that the TOD was highly uncompensated in the cavity, which is mainly attributable to the high TOD of the grating pair and to the fact that the TOD of the fiber and the grating pair had the same sign.

The above calculated cavity TOD deviates by more than a factor of two from the value that was determined from the measured relation between repetition rate and center wavelength. However due to the quadratic relation, the influence of the TOD on repetition rate depends also on the signal bandwidth [KGO93]. Therefore, this deviation can be put down to the fact that the spectral bandwidth of the signal changed with center wavelength, which can be seen in the right diagram of figure 4.4.2. The averaging effect of the spectral bandwidth of the signal had reduced the effect of the cavity TOD on the repetition rate, since the broadest signal bandwidths were observed in the center of the tuning range.

4.5 Signal chirp

Interferometric autocorrelation measurements showed a fringe pattern for time delays of the order of about 100 fs, however with a ratio of 4:1 between the maximum and the adjoining underground. The typical 8:1 ratio between maximum and underground of the autocorrelation

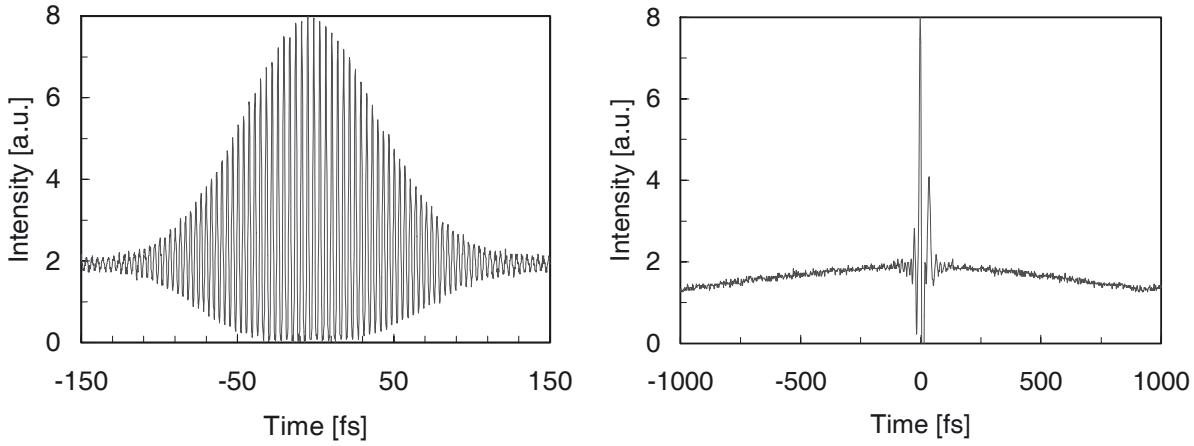

Fig. 4.5.1 *Typical autocorrelation measurement of the output signal. In the right diagram most of the interferometric fringes are not resolved because of the sampling rate of the oscilloscope. These fringes are resolved in the left diagram, which shows the same autocorrelation on a smaller time scale. In the right diagram the maximum delay was determined by the scanning range of the autocorrelator.*

function (ACF) was obtained only for time delays of more than about 1.5 ps, which can be seen in figure 4.5.1. This indicated that the pulses were strongly chirped and extended roughly over about 1.5 ps.

A large pulse chirp can also be expected due to the large GVD of the fiber and the uncompensated TOD. Although the grating pair can compensate the total GVD in the cavity, the lowest pulse chirp is located somewhere in the fiber. This is due the fact that for the applied mode-locking scheme the laser adjusts itself to the operation mode, which maximizes the nonlinear phase shift versus the input pulse energy in combination with the fiber gain curve.

In order to compensate the linear pulse chirp of the output signal, an additional external grating pair was used in double pass configuration. During these measurements, the laser cavity was adjusted for zero overall GVD in the cavity by adjusting the separation of the internal grating pair to 7.4 cm (section 4.4). As the GVD of the external grating pair was varied from

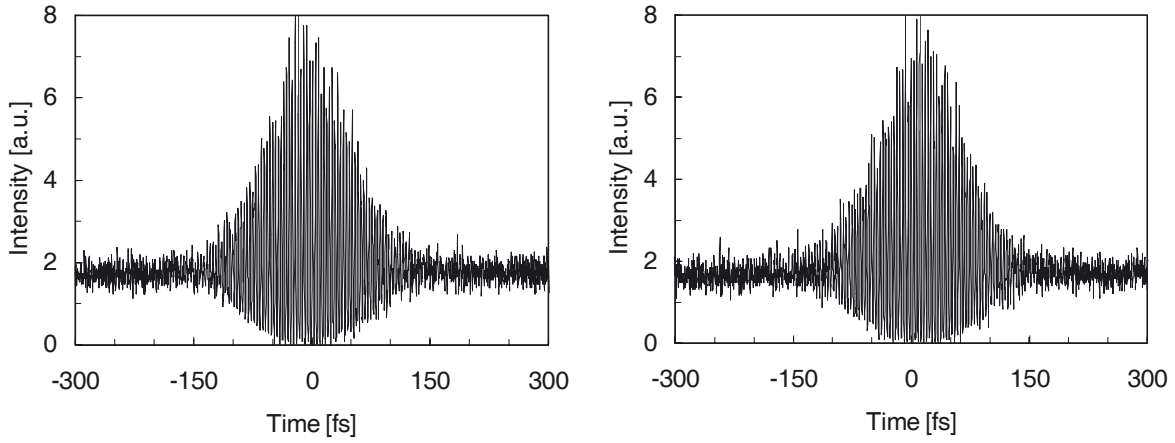

Fig. 4.5.2 *Autocorrelation function of the output signal after passing an external grating pair with a GVD of $-1.5 \cdot 10^5$ fs² (left diagram) or $-4.2 \cdot 10^5$ fs² (right diagram). The time scale was determined from the interference fringes.*

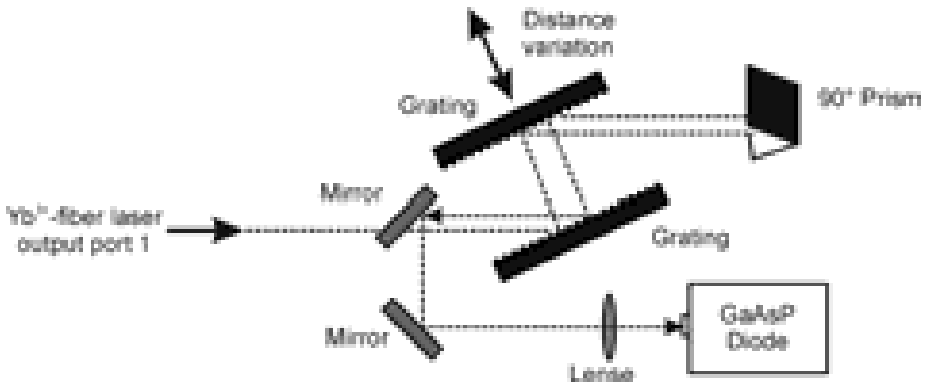

Fig 4.5.3 *External grating arrangement for chirp compensation. The signal was detected by a GaAsP detector, which acted as a two-photon absorber at the signal wavelength.*

$-4.7 \cdot 10^4$ fs² to $-4.7 \cdot 10^5$ fs², slight variations of the absolute signal amplitude of the ACF were observed. However, no influence of the grating distance on the shape of the ACF was observed. Therefore, it was not possible to determine the frequency chirp from these measurements. This is illustrated in figure 4.5.2 by two of the measured ACF, corresponding to grating GVD of $-1.5 \cdot 10^5$ fs² and $-4.2 \cdot 10^5$ fs², respectively.

The influence of the external grating pair on the laser pulses was further investigated by focusing this signal thereafter on a GaAsP-photodiode (fig.4.5.3). The photodiode current of this two-photon absorber is a quadratic function of the laser intensity [RGB97]. Thus, a reduction of the pulse duration results in an increase of the average current.

In the left diagram of figure 4.5.4, the measured photodiode current is plotted versus the GVD of the external grating pair, while the right diagram shows the corresponding laser spectrum. It can be seen that the photodiode current showed a maximum for a grating GVD of $-2.5 \cdot 10^5$ fs², which indicated a minimum for the pulse width and therefore a compensation of the GVD induced chirp. However, theoretical calculations of the photodiode current versus

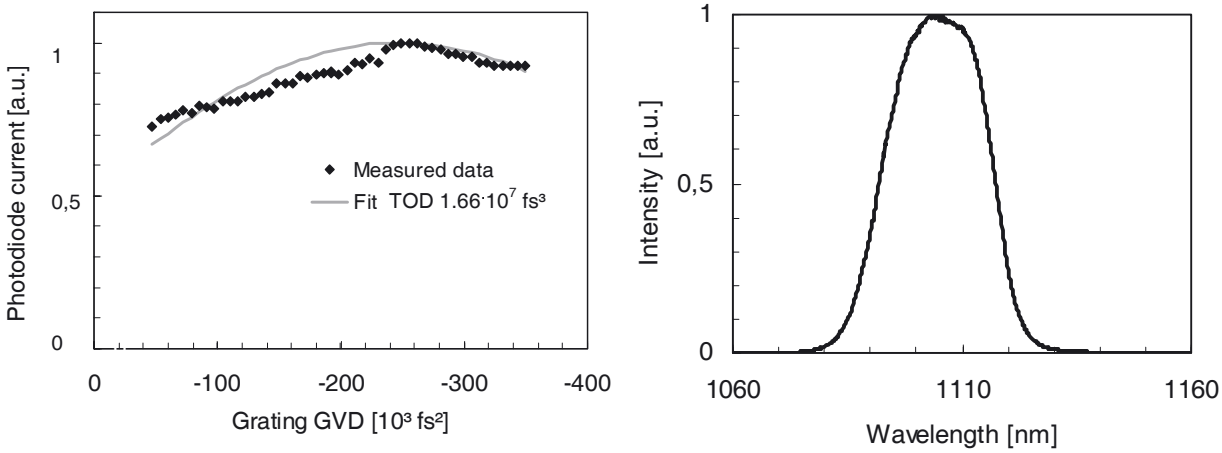

Fig. 4.5.4 *Left diagram: Measured photodiode current of the GaAsP photodiode versus GVD of the external grating pair. In addition, the calculated curve for a laser output with a frequency chirp corresponding to a TOD of $1.66 \cdot 10^7$ fs³ is shown. The TOD value was determined by a least square fit. Right diagram: Laser spectrum during these measurements.*

the GVD showed that the variations of the photodiode current must be much larger if the photodiode maximum corresponds to a bandwidth-limited pulse. This deviation was not a result of saturation effects, as the photodiode operated far below the saturation limit.
Because of the highly uncompensated TOD in the cavity, an additional pulse stretching was expected due to the TOD induced cubic chirp. Therefore, a least square fit function was numerically computed for the measured photodiode current curve by using the TOD induced chirp as fit parameter. The resulting fit function, which is plotted in the left diagram of figure 4.5.3, indicated a TOD chirp of $1.66 \cdot 10^7$ fs³ at the laser output.
This TOD value is about 3.4 times higher than the TOD of the laser cavity. In the cavity, the cubic chirp is increased each round trip by the cavity TOD, while it is reduced by the NLPR mode-locking, which suppresses low intensity wings. Hence, previous result indicates that the equilibrium between both effects result in a cubic chirp 3.4 times higher than the cavity TOD.
However, the interaction of the pulse shortening by NLPR and the stretching by TOD may have resulted in additional higher order chirp terms, as both effects interact in a different way with the signal. Thus, the calculated cubic chirp is only a semi-quantitatively approximation for the actual frequency chirp of the output pulse. A more detailed analysis would require frequency resolved optical gating measurements [AKO03]. However, such a system, suitable for the pulse energies of this laser, was not available during these experiments.

4.6 Intra-cavity pulse dynamic

The described experiments indicated that the output signal at port 1 had a quadratic and a cubic chirp of $2.5 \cdot 10^5$ fs² and $1.66 \cdot 10^7$ fs³, respectively. This output signal is coupled out of the cavity at the first grating. Hence, the chirp of the circulating signal at the fiber input can be calculated by adding the grating pair dispersion. Furthermore, based on these data, the pulse evolution along the fiber can be calculated by taking the fiber dispersion additionally taken into account. Such calculations showed that the pulse width minimum is located about 15.5 m away from the fiber input and that it therefore located closer to the output than to the input fiber end.
The influence of nonlinear effects on a pulse can be better described by a weighted average of the pulse intensity distribution I(t) as by the pulse width, since the TOD causes pulse shape variations and the nonlinear effects (Kerr-effect, SRS) are proportional to the intensity. Such a weighted average M_{NL} is defined by equation 4.6.1.

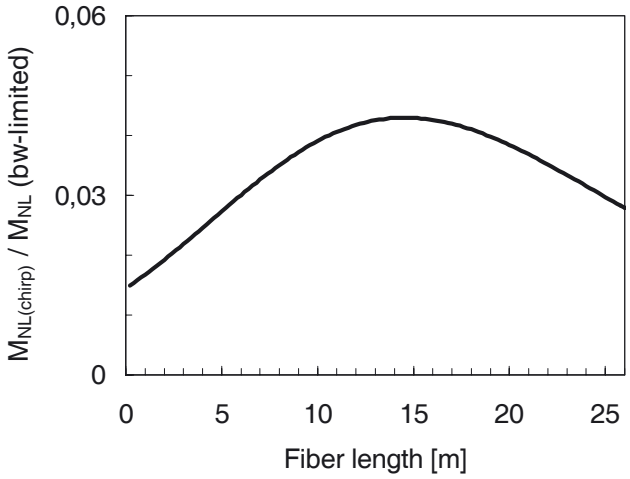

Fig.4.6.1 *Evolution of the strength of nonlinear effects (averaged over the pulse) along the fiber, relative to the bandwidth limited pulse .This was calculated for a Gaussian pulse (1100 nm,25nm FWHM) of constant pulse energy. An input chirp corresponding to a GVD of -3.71·10^5 fs²and a TOD of 2.1·10^7 fs³ was assumed.*

$$M_{NL} \propto \int_{Pulse} I^2(t)\,dt \Big/ \int_{Pulse} I(t)\,dt \qquad (4.6.1)$$

For the above mentioned input chirp parameters, the evolution of M_{NL} along the fiber is displayed in figure 4.6.1 for a Gaussian pulse (1100 nm, 25 nm FWHM) with constant energy. The nonlinearity of the pulse varies along the fiber between 0.015 and 0.043 times the value of the bandwidth-limited pulse. This large pulse stretching, which is about one order in magnitude above previously described laser systems, enables high pulse energies, especially in combination with the relatively low repetition rate of this laser.

Previous description of nonlinear effects had not taken the influence of the pulse amplification along the fiber into account. In order to describe the influence of nonlinear effects on the pulse along the fiber, the curve in the right diagram of figure 4.2.15 must therefore be multiplied with the amplification curve.

Mode-locking by nonlinear polarization rotation depends on the nonlinear phase shift in the fiber. The laser adjusts itself usually to the operation mode with the lowest threshold. For NLPR this corresponds to the operation mode with the highest nonlinear phase shift in the fiber between the two polarization modes (section 2.5.2). The pulse width minimum is therefore shifted from the middle of the fiber closer to the fiber output. As the pulse energy increases along the fiber, this shift increases the nonlinearity for the circulating pulse. This describes qualitatively the observed laser operation.

For an exact quantitative description of the laser operation, the variation of the birefringence along the fiber must be included, as the NLPR depends on signal polarization (eqs. 2.5.5 –2.5.6). Due to the "kidney-shaped" fiber arrangement, strong variations of the fiber birefringence are expected. Furthermore, a more detailed description of the cavity dynamic must include the detailed gain curve along the fiber and the influence of nonlinear effects and on pulse spectrum and pulse shape.

4.7 Conclusion and outlook

The described experiments demonstrated for the first time that passive self-starting mode-locking by NLPR can be realized in combination with a long cladding-pumped Yb^{3+}-gain-fiber [AAF01]. Detailed investigations of this laser system showed that the highly uncompensated TOD in the cavity limited temporal recompression of the output signal. The latter was a result of the high TOD of the grating pair, which has in addition the same sign as the fiber TOD.

However, recently highly doped cladding pumped Yb^{3+}-fibers with large core diameters and low numerical aperture have become available. These fiber had a much higher pump light absorption than previous cladding-pumped fibers (up to 11 dB/m at 975 nm, e.g. [LIE03] [NUF03]). Furthermore, the low numerical aperture of these fibers enables single-mode operation, despite of the large core. Hence, the uncompensated TOD can be strongly reduced by such fibers, since the higher pump light absorption reduces the required fiber length.

In addition, photonic crystal fibers (PCF) with anomalous dispersion at 1 µm are now commercially available [BMK99][THO03]. These fibers enable a compensation of the normal gain fiber dispersion without an additional dispersive grating pair. Theoretical calculations have confirmed, that by such fibers a simultaneous compensation of the gain fiber GVD and the TOD can be achieved [ILI03].

Furthermore, various fibers optic components, which are compatible to the used double clad fibers, e.g. transversal pump light coupling schemes, have become commercial available until recently [OFS03][ITF0]. By this way, the mechanical complexity of the set-up and the sensitivity to external disturbances can be further reduced.

5 Super-broadband Yb^{3+}-fiber laser

Fast and accurate measurements with optical metrology systems, like optical coherence tomography (OCT) [BDG98][WNC03] or optical coherence radar [DHV92], require broad-bandwidth high-power optical sources. Superluminescent diodes, which are the common light sources for OCT systems, show about 40 nm bandwidth, but only a few mW output power. For many non-medical applications, this low output power limits the signal to noise ratio, the probe penetration depth on OCT measurements and increases the required measurement time for large objects.

In the previous section a mode-locked Yb^{3+}-fiber laser was described, which generated up to 40 nm spectral bandwidth in combination with high output powers and a single-mode beam quality. The output power of this system would be sufficient for many of these applications. However, the resolution of OCT and coherence radar measurements would be still limited to about 12.5 µm, as the bandwidth determines the minimum achievable resolution of such metrology systems. For that reason, there is a demand for sources with broader emission bandwidth.

Much broader bandwidths were generated by mode-locked Ti:Sapphire lasers, which are able to provide up to 400 nm bandwidth in combination with output powers of about 200 mW [BKC99] or even higher output powers on the expense of smaller bandwidth. However, these laser systems are too bulky and too expensive for most medical and industrial applications, because they require argon-ion or frequency-doubled solid-state lasers as pump sources.

In this section a modified set-up of the previous described mode-locked Yb^{3+}-fiber is described, which overcomes this restrictions. This laser generated pulses with up to 118 nm bandwidth in combination with an average output power of 1.3 W. This super-broad-bandwidth operation was enabled by spectral filtering inside the laser cavity. For this system, the spectral broadening and the influence of pump power and spectral filtering on pulse bandwidth were investigated.

5.1 Experimental setup

The experimental set-up is shown in detail in figure 5.1.1. Basically, it was the same as for the previous described mode-locked Yb^{3+}-fiber laser (fig.4.1.1). However, the fiber was pumped at 975 nm with a fiber-coupled 25 W laser diode. By this way, the pump light absorption was further improved. Furthermore, gratings with a diffraction efficiency of about 90% were

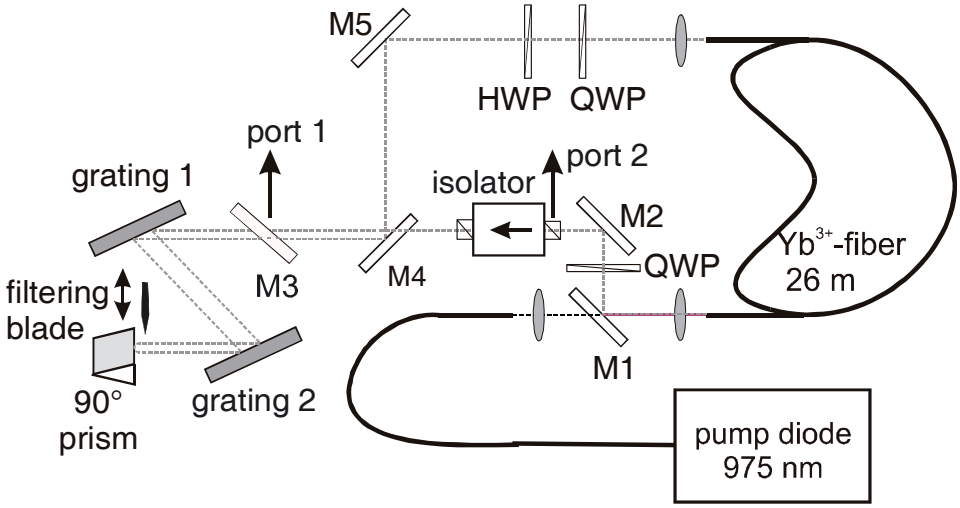

Fig. 5.1.1 *Setup of the broadband fiber laser system.*

available for this set-up. Compared to the previous set-up, these gratings reduced the cavity loss attributable to the dispersive delay line. As a result, the output power from the zeroth order of the first grating was quite low. Therefore, output coupling was realized by insertion of an additional mirror (M3) into the cavity. This mirror reflected about 50% of the signal, which has passed the optical isolator, out of the cavity (output port 1). Moreover, a 90° prism replaced the slightly tilted mirror at the end of the dispersive grating line. Due to this prism, the back reflected light propagated parallel above the incoming light. This simplified the required laser adjustment, compared to the tilted mirror, as this shift was independent from the grating separation. The main difference to the previous set-up was an additional horizontally adjustable (vertical) blade behind the second grating. This blade acted as an adjustable spectral filter, as after the second grating the different wavelengths propagated spatially parallel and were separated laterally.

5.2 Broadband mode-locked laser operation

Without spectral filtering, mode-locking operation was observed, as described in the previous section. Typically, it was self-starting at about 4.5 W pump power. The exact value of the self-starting threshold depended on wave-plate settings and total cavity dispersion.

Moving the blade into the grating line, the long-wavelength components were suppressed. This resulted in a shift of the center wavelength of the circulating pulse to shorter values. Simultaneously, the pump power threshold for self-starting mode-locking increased, because of the increased cavity loss. If the blade was moved further into the beam, the bandwidth of the output signal increased dramatically for appropriate wave-plate settings. At an optimum

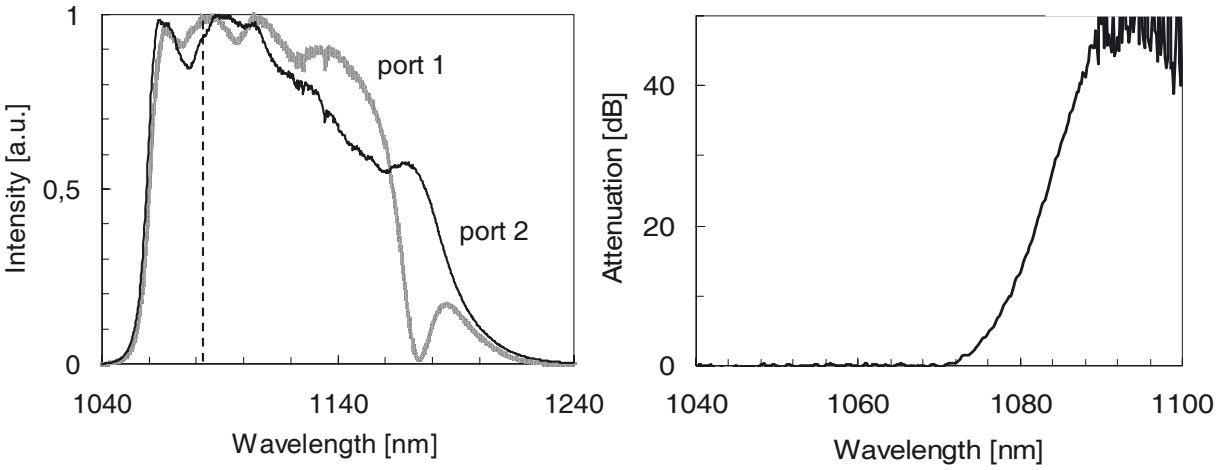

Fig. 5.2.1 *Left diagram: Output spectra of the two ports for maximum bandwidth at port 2. Right of the vertical dashed line the attenuation of the spectral filter was above 40 dB. Right diagram: Corresponding spectral attenuation curve of the filtering plate in the grating line. The fluctuations in this curve above about 1090 nm are due to detector noise.*

position an extremely broadband output signal with up to 118 nm bandwidth (FWHM), extending from 1060 to nearly 1240 nm, was achieved. The signal bandwidth as well as the center wavelength were strongly reduced, if the blade was moved further into the beam.

If the blade was moved from the opposite direction into the beam, the short wavelength components were suppressed. This shifted the pulses to longer wavelength, but no spectral broadening was observed in combination with such a long pass filtering.

The normalized output spectra of the two ports of the laser system, adjusted for maximum bandwidth at port 2, are shown in the left diagram of figure 5.2.1. The bandwidth (FWHM) of the output spectra was 103 nm at port 1 and 118 nm at port 2. This bandwidth is about 3 times larger than for the Yb^{3+}-fiber laser system without spectral filtering. Both curves are similar in shape. However, around 1175 nm the spectral intensity measured at port 1 was negligible, whereas the output of port 2 showed a local maximum. This was most likely caused by the limited bandwidth of the zeroth order (1064 nm) QWP in front of the isolator, as the power distribution between port 1 and port 2 was determined by the signal polarization at the isolator input. These spectra were measured at a pump power of 18.8 W. The corresponding output powers were 0.55 W at port 1 and 1.3 W at port 2, respectively.

At shorter wavelengths, a steep decrease of the spectral intensity was observed around 1060 nm. This behavior was nearly independent of wave-plate settings, pump power and output port. This limited emission of short-wavelength components can be attributed to the reflection characteristics of the dichroic mirror M1, which was highly transmittive for wavelengths below 1055 nm. Furthermore, reabsorption in the Yb^{3+}-fiber is increasing with shorter wavelengths, what may act as an additional long pass filter.

In order to determine the system operation in more detail, the filter cut-off wavelength for that specific blade position was determined. This was accomplished by blocking the fiber input and measuring the ASE-signal of the Yb^{3+}-fiber behind the grating line with and without the blade. The resulting attenuation curve, measured for the blade position for maximum bandwidth, is shown in the right diagram of figure 5.2.1. It can be seen, that only wavelengths below about 1080 nm were transmitted. This is a surprisingly small part of the broad bandwidth signal. The spectral attenuation started at about 1075 nm and increased with a slope of about 3 dB/nm to 45 dB at 1090 nm. Above this wavelength, the detector signal was dominated by the detector noise, as the spectral intensity of the filtered signal was too low.

The influence of the pump power on the measured bandwidth at the two output ports is shown in the left diagram of Figure 5.2.2. For pump powers of up to 15 W, the bandwidths increased nearly linear and similar bandwidths were measured at both ports. This increase can be easily be understood in terms of intensity dependent nonlinear effects, which are broadening the spectral bandwidth. In the pump power range from 15 to 19 W, the maximum signal bandwidth was achieved. At these power levels, the maximum bandwidth at port 2 was at least more than 10 nm broader than at port 1. For pump powers beyond 19 W, the bandwidth of both output signals decreased to values below 100 nm.

In the right diagram of figure 5.2.2 the corresponding output powers of are plotted versus the pump power. An output power of 1.3 W was measured at port 2 in combination with the maximum bandwidth of 118 nm. The output power raised up to 1.0 W at port 1 and 2.1 W at port 2 while the bandwidth decreased, as the pump power was further increased.

Up to about 15 W pump power, the differential slopes increased with pump power. This power characteristic was mainly caused by a power dependant shift of the emission wave-

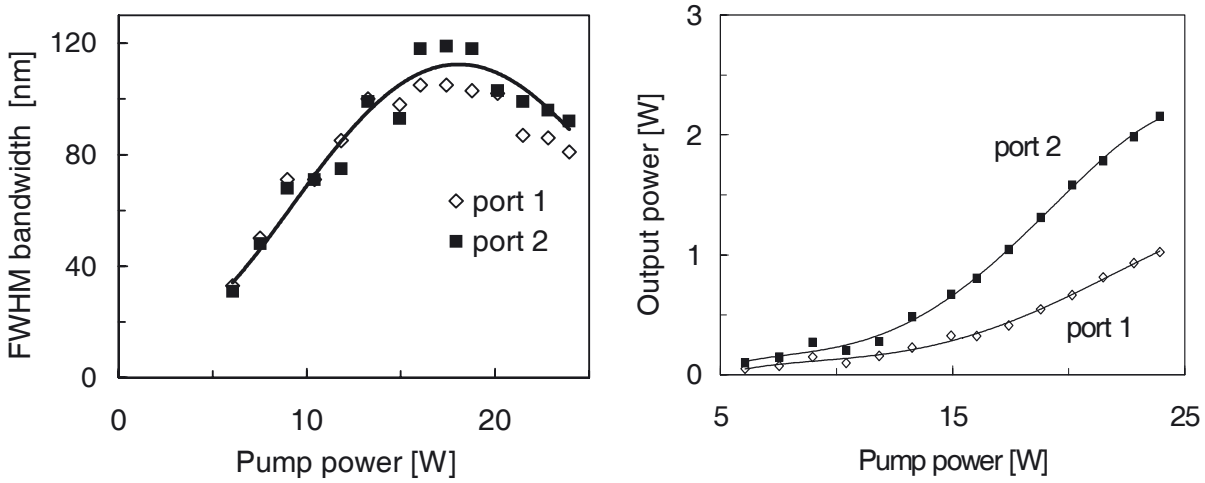

Fig. 5.2.2 *Left diagram: Influence of the pump power on spectral bandwidth at both ports. Right diagram: Corresponding output power at both output ports for this laser set-up.*

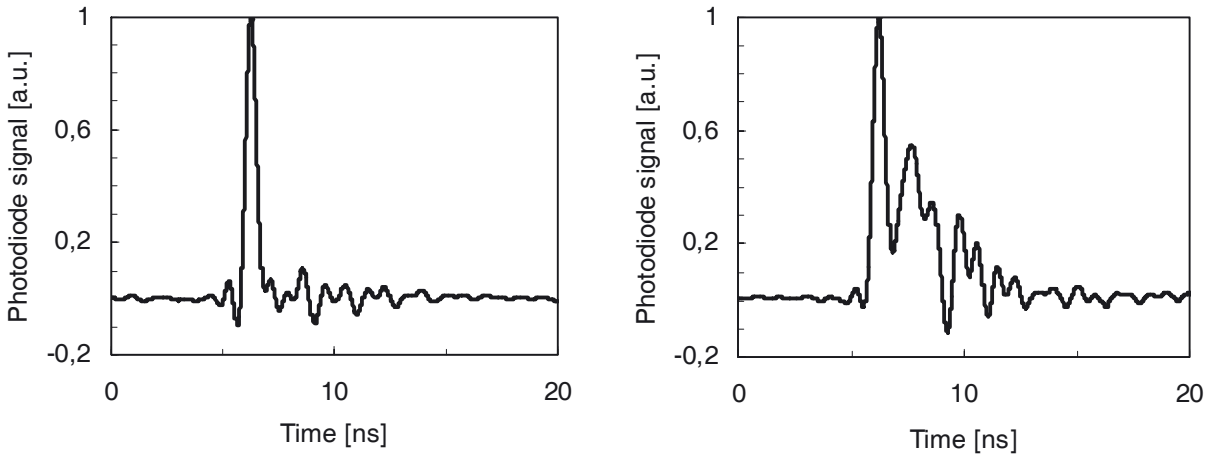

Fig.5.2.3 *Photodiode traces of the output signal. Left diagram: Standard pulse signal. The small second peak was due reflections of the electric signal, as its position depended on the electric set-up of the detector. Right diagram: Photodiode signal which was observed at high pump powers (e.g. ~ 21 W) and indicates multiple closely spaced pulses.*

length of the pump diode. In combination with the relatively narrow absorption peak of Yb^{3+} at 975 nm, this resulted in a variation of the pump light absorption [WAF02].

The time dependence of the output signal was measured by using a fast photodiode (2 GHz) and an oscilloscope (500 MHz). Detailed investigation showed typically only one short pulse with a repetition rate of 7.6 MHz for pump powers below 20 W. For higher pump powers, usually two or more closely spaced short pulses were observed. Figure 5.2.3 shows two photodiode traces, which are typically for these two operation regimes. The multiple pulse operation at high pump power likely reduced the peak intensity inside the fiber. Probably, the decreasing bandwidth with increasing pump power at this power level is attributable to this effect. Besides these details on a short time scale, the photodiode signal has the same shape as described for the conventional mode-locked Yb^{3+}-fiber laser (fig. 4.2.1 right diagram).

In the above-mentioned experiments, the set-up had a total group velocity dispersion (GVD) of $8.9 \cdot 10^4$ fs². In addition, the cavity dispersion was varied between $-1.4 \cdot 10^5$ fs² and $1.6 \cdot 10^5$ fs² in four steps. Measurements of the output spectra for these cavity GVD values revealed always such an extreme spectral broadening with similar signal bandwidths.

Fig. 5.2.4 shows the measured autocorrelation of a 116 nm bandwidth signal from port 2. It is noticeable in the left diagram, that the autocorrelation function has not the typical 8:1 ratio near the interference pattern. Moreover, it can be seen in the right diagram that even for the maximum time delay of 80 ps the autocorrelation signal intensity was still about 1/4 of the interference maximum. Hence, the pulse must extent over a significant longer time interval. To some extent this is attributable to the fiber dispersion, as a pulse width 118 nm bandwidth would be stretched to about 60 ps, even if the linear chirp was compensated in the middle of the gain fiber (see section 4.2.2.). However, additional phase distortions may be attributable to

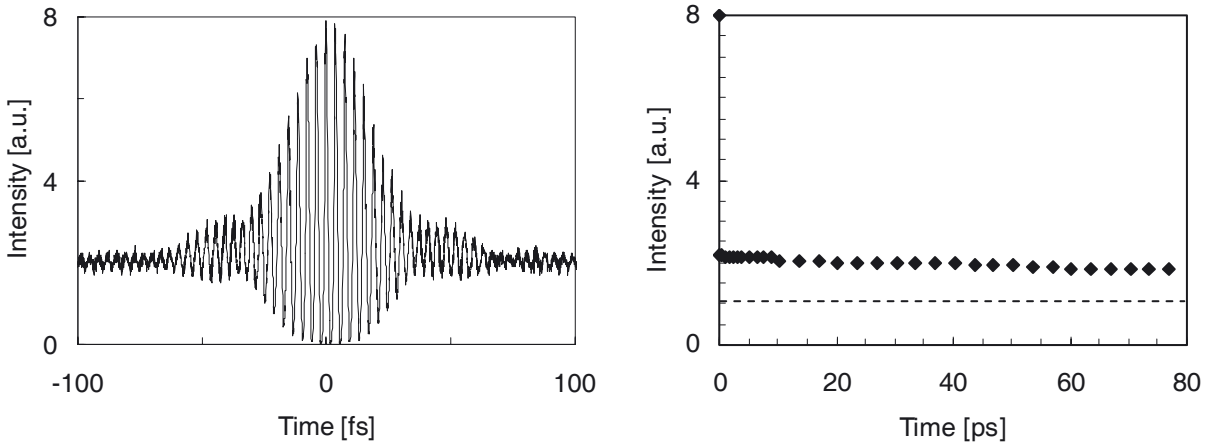

Fig 5.2.4 *Left diagram: Autocorrelation function of the output signal (signal bandwidth 116 nm). Right diagram: Signal of the detector for larger delays of the autocorrelator. As these delays were outside the scanning range, the path difference was manually increased by a micrometer screw. The dashed line indicates the theoretical signal level for no pulse overlap in the autocorrelation.*

the fact, that the phase relation of the generated long wavelength components is determined by the broadening mechanism and not by the input signal.

5.2.1 Filtering versus spectral broadening

The output spectra for different blade positions are shown in figure 5.2.5. For these measurements, the blade position was shifted by 2.0 mm in 0.1 mm steps. Calculations of the signal propagation in the grating line showed, that the filtering curve of the grating line was shifted about 42 nm by the 2.0 mm movement of the filtering blade.

The short wavelength edge of the spectrum shifted to shorter wavelengths as the filtering blade was moved into the resonator. This shift was obviously a result of the short pass spectral filtering in combination with the broadband Yb^{3+}-gain. With increasing filtering a slight sub-peak becomes also noticeable in the spectrum at shorter wavelengths. This peak is attributable to the long wavelength edge of the grating line transmission curve. This can be noticed by comparing the sub-peak positions with the transmission curve of the grating line in combination with the wavelength shift with blade position (fig. 5.2.1). This sub-peak becomes dominating relative to the main spectrum, if the relative blade position approaches 2.0 mm. Hence, the broadening of the signal in the fiber decreases, if the filtering becomes too large. It should be noticed, that no mode-locked operation was observed, if the blade was further moved into the grating line.

The relation between blade position and spectral bandwidth (FWHM) is shown in the left diagram of figure 5.2.6 for the spectra of figure 5.2.5. It can be noticed from this diagram, as well as from the spectra, that the bandwidth increased not continuously but in steps. Between

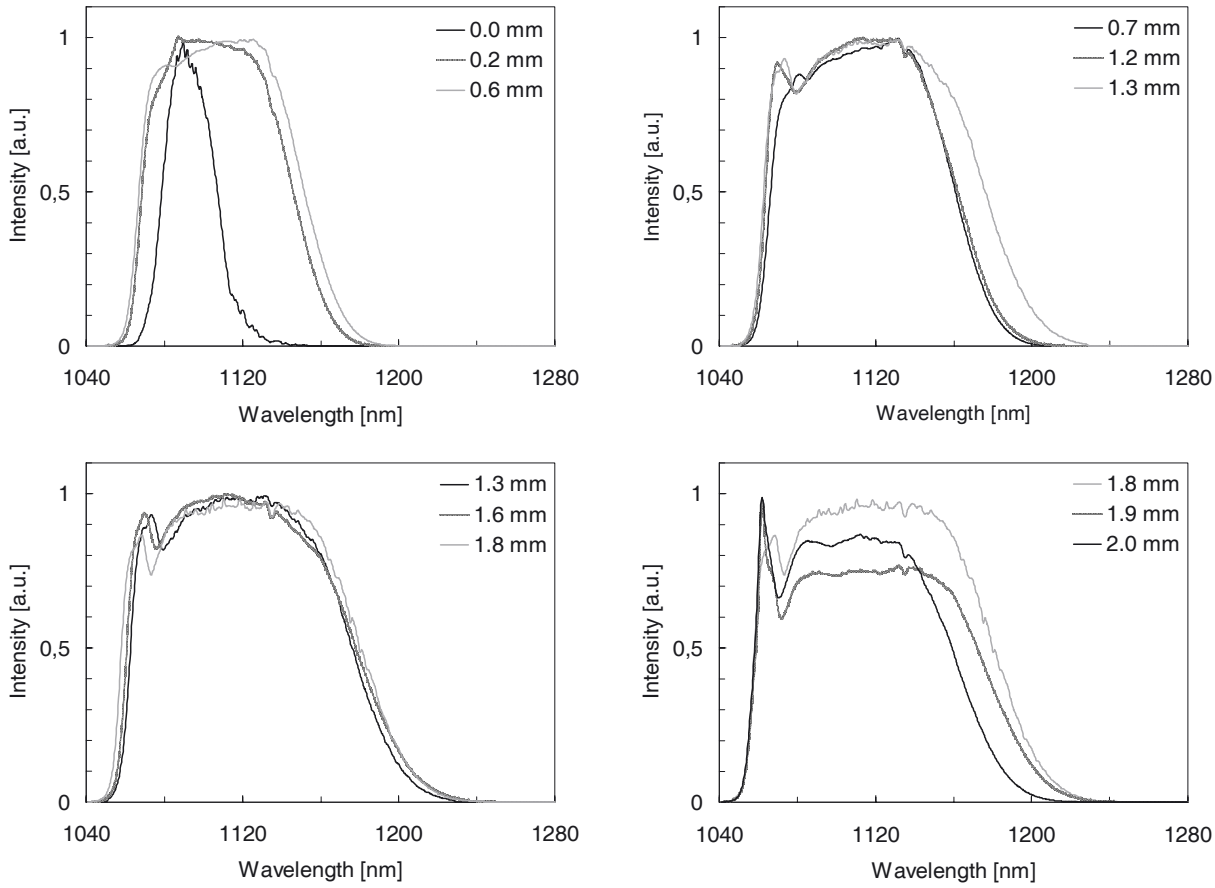

Fig. 5.2.5 *Output spectra of the Yb^{3+}-fiber laser at port 2 as a function of the relative blade position measured at a ump power of 17.5 W. The relative blade position is mentioned for each graph.*

these steps, the bandwidth remained nearly constant. This behavior indicates some kind of quantization.

It should be noticed, that besides of the spectral effects the output power decreased slightly as the filtering blade was shifted into the grating line. This can be seen in the right diagram of figure 5.2.6, where the measured output powers are plotted versus blade position. Such a behavior was expected, since the spectral filtering increase the cavity loss,.

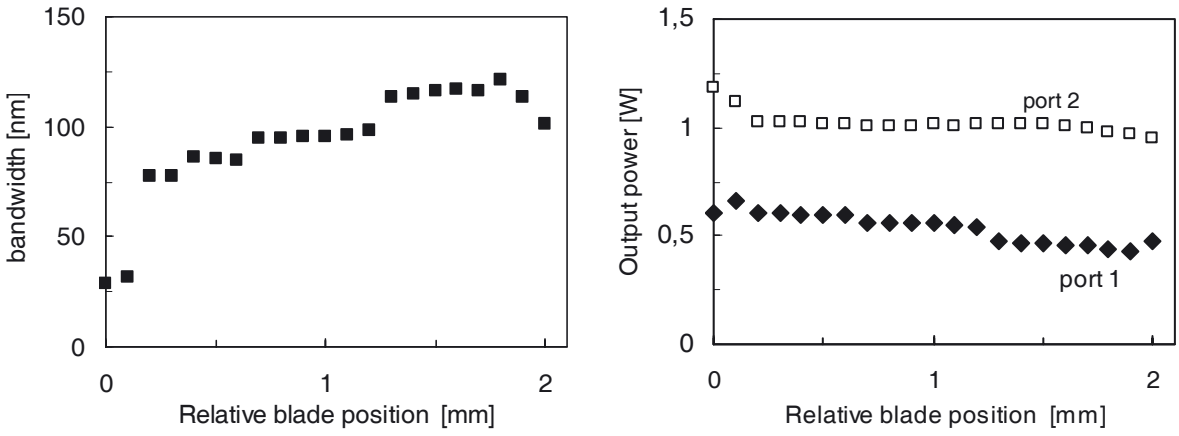

Fig. 5.2.6 *Left diagram: Spectral bandwidth (FWHM) at port 2 versus blade position (spectra shown in figure 5.2.5). Right diagram: Output powers at both output ports versus blade position (pump power 17.5 W).*

5.3 Broadening mechanism

The observed extreme spectral broadening due to a suppression of long wavelength components was unusual and hardly expected. Compared to previous reported Yb^{3+}-fiber laser systems, the spectral bandwidth was increased by nearly a factor of three. Furthermore, the long wavelength components in the broadened output signal must be generated by nonlinear effects in the gain fiber, since they were suppressed before the fiber input. Hence, a description of the spectral broadening must take the interaction between the spectral filtering and the nonlinear effects in the fiber into account.

5.3.1 Linear effects of the spectral filtering

The direct results of the spectral filtering are an increase the cavity loss and a reduction the spectral bandwidth at the fiber input. Calculations, based on the broadband output spectrum and the spectral filtering curve (fig. 5.2.1), showed that the filtering blade suppressed about 85% of the signal power during broadband operation. This increased cavity loss must correspond to an increase of the fiber gain, because of the equilibrium between gain and loss during laser operation. A higher gain results in larger variations of the pulse energy along the fiber. By this way, the increased cavity loss results in a decrease of the nonlinear effects in the fiber sections close to the input, relative to the sections close to the output fiber end. Thus, the pulse width minimum must be shifted closer to the output fiber end, as the mode-locking mechanism prefers the operation mode with the highest nonlinear phase shift (section 4.6). Furthermore, this increases the threshold for pulse formation and enables therefore higher pulse energies, since the mode-locking is based on the accumulated Kerr induced nonlinear phase shift. Consequently, the thresholds for formation of additional pulses are also increased by the higher loss (section 4.3). Most likely, the quantization steps for the pulse broadening indicate that the number of circulating pulses in the cavity decreases and the pulse energy increases with increasing cavity loss (fig. 5.2.6). However, no spectral broadening was observed for laser set-ups, which had a high cavity loss without spectral filtering. Thus, a high cavity loss is not sufficient for an extreme spectral broadening.

Generally, a reduction of the spectral bandwidth increases the pulse duration due to the Fourier limitation [DIE95]. However, in this laser system the pulse duration at the fiber input is far above the Fourier-limit, because of the large quadratic and cubic signal chirp (chapter 4.6). For that reason, the reduction of the spectral bandwidth reduces the dispersive pulse broadening and therefore the pulse duration at the fiber input (eqs. 2.3.2). This pulse width

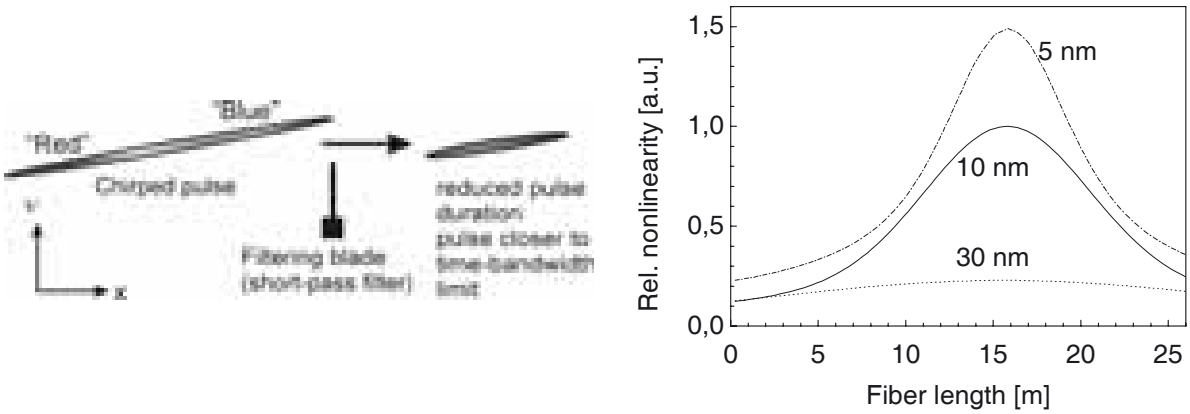

Fig. 5.3.1 *Left graph: Schematic illustration of the pulse width reduction by spectral filtering. As this is illustrated for the output of the grating pair, the pulse has a negative chirp. Right diagram: Evolution of the nonlinearity (eqs. 4.6.1) along the fiber due to the pulse shape evolution for Gaussian pulses with 5 nm, 10 nm and 30 nm bandwidth at 1080 nm. For these pulse an input quadratic and cubic chirp of $-3.71 \cdot 10^2$ fs^2 and $2.1 \cdot 10^7$ fs^3 where assumed (section 4.6). The pulse energy evolution along the fiber was not taken into account.*

reduction, which is in contrast to the common known pulse lengthening with bandwidth reduction, is illustrated o the left side of figure 5.3.1. The bandwidth reduction by the spectral filtering can be driven until the pulse width approaches the Fourier-limit for the remaining signal spectrum.

The dispersive pulse broadening along the fiber is reduced in the same way by the spectral filtering. Consequently, nonlinear effects become more dominant versus the dispersive pulse broadening, especially in the fiber sections close to the output with high pulse energy. This can be seen in the right diagram of figure 5.3.1, which shows the influence of the signal bandwidth on the pulse nonlinearity along the fiber (eqs. 4.6.1). For these calculations, the input pulse chirp parameters were used which were determined for the conventional Yb^{3+}-fiber laser (section 4.6). It can be seen, that the nonlinearity increases due to the reduced dispersive pulse broadening as the spectral bandwidth becomes smaller. The largest increase of the pulse nonlinearity can be observed at the pulse width minimum where the calculated temporal broadening is solely attributable to the cubic chirp, as the quadratic chirp is compensated. It should be noted, that the previous described relation is not longer valid, if the pulse duration approaches the Fourier-limit.

The influence of the spectral bandwidth on the pulse shape at the pulse width minimum is shown in figure 5.3.2 for Gaussian pulses with spectral bandwidths of 5 nm and 10 nm, respectively. It can be noticed, that in combination with such a large cubic chirp, the pulse width decreases and the peak intensity increases as the bandwidth is reduced.

It is worth to mention that in the previous description the spectral broadening in the fiber was not taken into account. Therefore, the previous discussion describes the pulse propagation

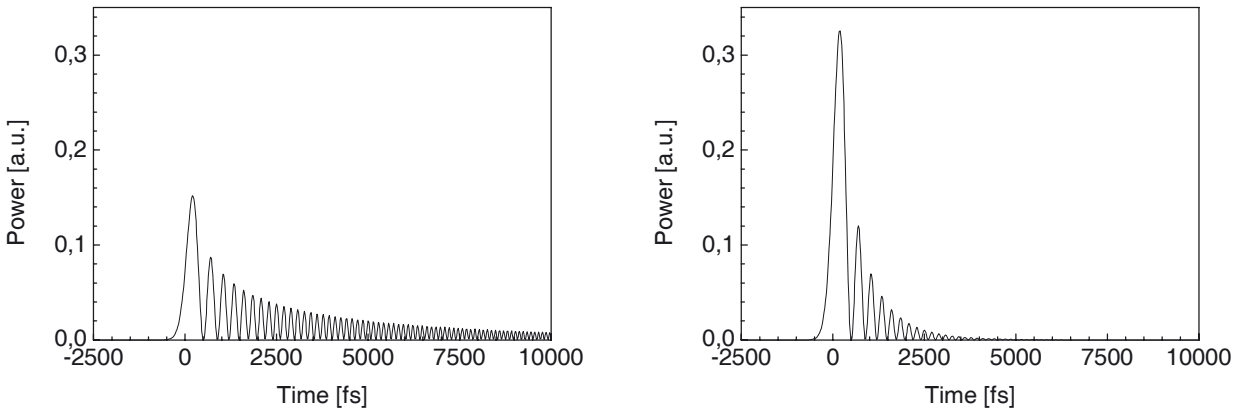

Fig.5.3.2 *Calculated pulse shapes in combination with a cubic chirp o f2.1·10^7 fs³. Left diagram: For a 30 nm (FWHM) Gaussian spectrum at 1080 nm. Right diagram: For a 10 nm (FWHM) Gaussian spectrum at 1080 nm Both signals have the same pulse energy. The power scale was defined by setting the pulse maximum for a 10 nm Gaussian pulse with the same energy equal one.*

along the fiber correctly only from the fiber input to the fiber sections with significant nonlinear pulse broadening.

5.3.2 Nonlinear broadening mechanism

In the previous section, it was described that the spectral filtering reduces the dispersive pulse broadening along the gain fiber and increases the peak intensity. Furthermore, the broad spectrum, which extents up to about 1200 nm, must be generated by nonlinear effects in the fiber, since the spectral components above about 1090 nm were blocked before the fiber input. Hence, in addition to the previous described linear effects, the spectral filtering must initiate a spectral broadening by nonlinear effects in the gain fiber.

Spectral broadening of optical pulses by nonlinear effects was mainly investigated for photonic crystal fibers (PCF), as the high nonlinearity of these fibers favors nonlinear pulse broadening [DPG02][BKR02]. It is known from these experiments, that the broadening mechanism depends especially on fiber dispersion and the pulse duration of the input signal.

Roughly similar shaped broadened output spectra were observed from a normal dispersive PCF, which was seeded by 300 fs pump pulses with 1.25 nJ pulse energy [GLL02]. According to this reference, this spectral broadening was mainly attributable to SPM and additionally influenced by self-steepening.

These PCF had a similar GVD at the input signal wavelength as the gain fiber at the laser wavelength (1.1 µm). Furthermore, in the Yb^{3+}-fiber laser the pulse shape was strongly modulated with a period of 300 fs – 400 fs, due to the high cubic chirp (fig. 5.3.2). Thus, the partial pulses had a similar duration as the signal in the previous mentioned PCF experiment. Furthermore, for the conventional Yb^{3+}-fiber laser an output pulse energy of about 10 nJ was

observed (section 4.3) and a further pulse energy increase a result of the spectral filtering was indicated. Hence, the about 6.5 times higher nonlinearity of the PCF and the reduction of the peak intensity by the pulse chirp were compensated by the higher pulse energy in the Yb^{3+}-fiber laser. Therefore, similar SPM broadening effects as in the PCF can be expected in the Yb^{3+}-fiber. This nonlinear broadening is strongly increased by the spectral filtering, as it shifts the pulse width minimum closer to the output, reduces the dispersive pulse broadening and increases therefore the nonlinear effects (fig. 5.3.1).

Unlike in passive fibers the generated broadband signal is additionally modified by the gain and the absorption of the Yb^{3+}-ions. The gain, which extents to about 1.2 µm, assists the build up of long wavelength components, while shorter wavelength components were absorbed by the Yb^{3+}-ions. Due to this additional interaction with the Yb^{3+}-doping, a detailed analysis of the spectral broadening in the Yb^{3+}-laser is far more complicated than in passive fibers.

Stimulated Raman scattering can also potentially support the observed broadening to longer wavelengths. However, SRS requires a temporal overlap of the different spectral components despite of the fiber dispersion and the pulse chirp. Such an overlap occurs only close to the pulse width minimum, where the input pulse chirp is compensated by the fiber dispersion or, if the broadening by the SPM generates new spectral components inside the chirped pulse.

The contribution of FWM to the observed broadening must be small, as phase matching cannot be achieved, because of the normal fiber dispersion (calculated zero dispersion wavelength 1575 nm). Additionally, the large spectral bandwidth results in a short coherence length (e.g. 5 cm (eqs. 2.2.8) for 50 nm sideband separation). Finally, it should be noted, that stimulated Brillouin scattering cannot contribute to the broadening in the laser, as SBS is only in the backward direction and was therefore was suppressed by the Faraday rotator.

5.4 Conclusion and outlook

The experiments showed, that ultra-broadband spectra (118 nm) in combination with high output powers (1.3 W) can be directly generated by a mode-locked Yb^{3+}-fiber laser. The output had single-mode beam quality, as the fiber was single-mode for the signal. Hence, this light source is well suited for optical measurement techniques, like optical coherence tomography. The broad bandwidth would enable a high resolution, while the high output power would make fast measurements on large objects possible.

During these basic experiments, fiber length, pump wavelength and output coupling were kept constant. However, these parameters influence the laser operation. Therefore, a further in-

crease of the spectral broadening and the output power can be expected, if these parameters were additionally optimized in the future.

Moreover, the active core of this fiber laser system had a cross section of about 20 µm², while nowadays highly doped single-mode double clad Yb^{3+}-fibers with cross sections of more than 100 µm² are available [NUF03][LIE03]. As mode-locking and spectral broadening is attributable to nonlinear effects, these fibers should enable a power scaling by more than a factor of five for broadband operation. It is worth to mention, that the large core of these fibers increases the pump light absorption. Eventually, this supports the broadening as the pulse energy grows faster near the pump light input, because of the higher pump intensity. Otherwise, this can be compensated by shifting the pump wavelength away from the absorption peak at 975 nm (e.g. to 915 nm or 940 nm). Alternatively, the pump core can also be increased, so that the ratio between the active core and pump core diameters remains constant.

The complexity of the fiber-laser set-up can be reduced by using transversal coupling schemes for the pump light [ITF03]. Furthermore, the spectral filtering and the dispersion management can be accomplished by an adapted fiber Bragg grating [LML02][DCH99]. In combination with fiber-coupled circulator, which is suitable for the high signal power levels of this laser system, the bulk dispersive grating pair can therefore also be replaced by fiber optic elements. Besides, fiber optic output couplers and polarization controllers are readily available. Therefore, by using such fiber optic elements, a compact all fiber broadband laser source can be realized.

6 Femtosecond Er^{3+}-fiber oscillator-amplifier system

In the previous sections pulsed fiber laser systems were described, which generated mode-locked pulses with pulse energies of several nJ or much longer Q-switched pulses with pulse energies of several µJ. However, there is a strong demand for compact and reliable high beam quality laser systems, which deliver pulse energies in the µJ range at high repetition rates in combination with femtosecond pulse durations. This demand is driven by applications like fs-Lasik refractive surgery [HML03], writing of waveguides in silica glass [WNC02][SBG01] or generation of THz radiation [CLD02].

Laser systems based on rare-earth-doped fibers are an attractive technology for such applications as light guiding in fibers enables simultaneously a good beam quality and a compact set-up, which is insensitive to external disturbances. Laser and amplifier systems based on Er^{3+}-fibers have the further advantage that the required fiber optic components like pump sources, WDM-couplers, isolators and high-speed amplitude modulators are widely used for telecom applications. Therefore, these components are reliable, relatively cheap and readily available. In addition, in combination with frequency doubling, the signal wavelength of Er^{3+}-fiber laser systems is compatible with conventional Ti:sapphire laser systems [AFF96].

In this section a modular all-fiber diode-pumped Er^{3+} chirped-pulse oscillator-amplifier system is described, which is highly suitable for the above mentioned applications. This system generated pulse energies of more than 4 µJ for repetition rates of up to 200 kHz and enabled pulse energies of more than 1 µJ for repetition rates of up to 987 kHz. After recompression, a pulse duration of up to 810 fs was demonstrated. The repetition rate was quasi-continuously tunable and the timing of the pulses can be controlled by an external electrical trigger signal. FC-APC connectors connected all modules of this system. By this way a simple set-up, service and specific adaptation of the system to applications were accomplished.

The continuously tunable repetition rate and the synchronization of the pulse emission to an external trigger signal is a special advantage of this laser system. Most applications of such a high repetition rate laser system require an exact controlling of the focus position for each pulse by an optical scanner system. Therefore, the mechanical complexity of a scanner system increases with increasing repetition rate, if the positioning for each pulse must be maintained until the pulse emission occurs. However, this laser system enables a control of the pulse emission by the beam-deflecting system. Hence, the targeting of the laser pulses can be done precisely “on the fly”, which highly simplifies high-speed scanner systems.

6.1 Experimental set-up of the Er^{3+}-oscillator-amplifier system

The set-up of this fiber oscillator-amplifier system is shown in figure 6.1.1. It consists of six all-fiber modules: a mode-locked Er^{3+}-fiber oscillator, a fiber based pulse-stretcher, two fiber-coupled modulators, an Er^{3+}-fiber preamplifier and a two-stage Er^{3+}-fiber power-amplifier. The signal amplification was distributed on these three amplification stages, as the gain of a fiber amplifier stage is limited to about 30dB. This limit is attributable to the onset of lasing at high gain, due to Rayleigh scattering and spurious reflections. In addition to these single-mode fiber modules, a diffraction grating compressor was used for temporal recompression of the chirped amplified signal. FC-APC connectors connected all the fiber-optic modules of the laser, in order to accomplish a simple set-up, service and specific adaptation of the system to applications. The set-up and the operation properties of the various modules are described in detail in the following sub-sections.

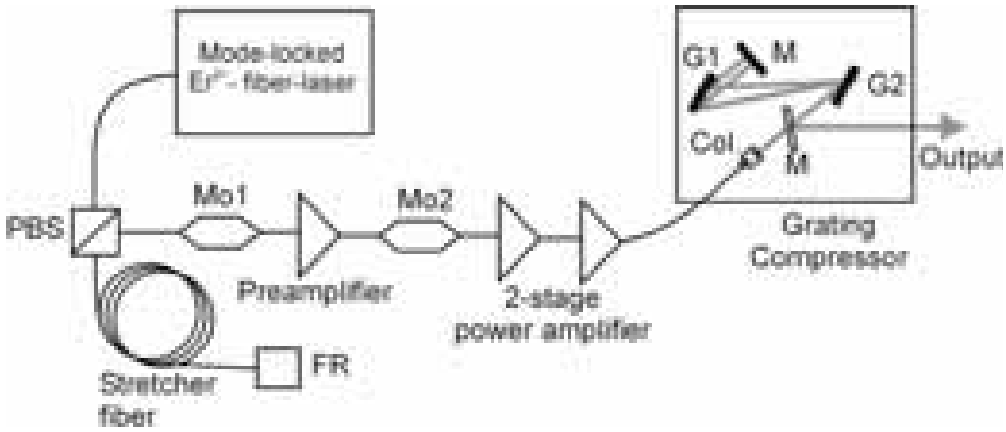

Fig. 6.1.1 *Schematic set-up of the Er^{3+}-fiber oscillator amplifier system. PBS: polarization beam splitter; FR: Faraday rotator; Mo1+Mo2: modulators; G1+G2: diffraction gratings; M: mirror.*

6.1.1 Femtosecond Er^{3+}-fiber oscillator

The detailed set-up of the mode-locked Er^{3+}-fiber oscillator is shown in figure 6.1.2. It consists of five principal fiber optic components: an Er^{3+} gain fiber, a 980/1550 nm wavelength-division-multiplexer (WDM), two fiber-optical polarization controllers (PC), a polarization beam splitter (PBS) and two isolators. The fibers were connected by fusion splices. By this way, a compact and all-fiber set-up was realized.

A fiber-coupled 980 nm laser diode provided the pump light, which was transmitted to the Er^{3+}-fiber via the WDM-coupler. The Er^{3+}-fiber provided the gain, while the intra cavity isolator forced unidirectional operation. For appropriate settings of the PC, the cavity loss at

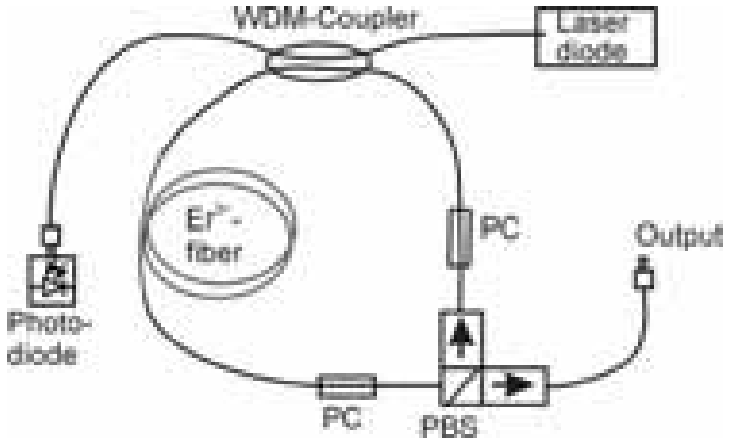

Fig. 6.1.2 *Set-up of the mode-locked Er^{3+}-fiber laser. PBS: polarization beam splitter; PC: polarization controller.*

the PBS decreased with increasing signal intensity because of the nonlinear polarization rotation in the 3.4 m long fiber resonator, which (section 2.5.2). By this way, passive mode-locking was enabled. The rejected signal of the PBS was used as the output signal, since this output signal showed only minor pulse degradation compared to the circulating pulse [TDN94]. Therefore, no additional outcoupling element was required.

The 0.6 m long Er^{3+}-fiber had a doping concentration of 2300 mol ppm Er_2O_3 and a dispersion of -22 fs/(nm·m) at 1550 nm [BOE99]. A mode field area of 16 µm² at 1550 nm was calculated from the refractive index structure of this fiber. As the other fibers in the cavity had a much larger mode field area (> 40 µm²), the nonlinearity in the cavity was mainly generated in the Er^{3+}-fiber. Furthermore, the normal dispersion of the Er^{3+}-fiber compensated largely the anomalous dispersion of the other fiber segments in the cavity. This combination of fibers with opposite dispersion sign resulted in a stretching and recompression of a circulating pulse (eqs. 2.3.2). By this way, the pulse duration, averaged over the cavity round trip, is increased and the peak intensity is decreased. Hence, this periodically stretching enables higher pulse energies, as the longer average pulse duration reduces the nonlinear effects [TDN94].

The set-up was adjusted for anomalous cavity dispersion and the fiber laser operated therefore in the average soliton regime. This dispersion regime was chosen because of the lower mode-locking threshold. The set-up was adjusted to a signal bandwidth of about 20 nm, since this bandwidth was much larger than the gain bandwidth of the Er^{3+}-fiber amplifiers, while still a larger fraction of the pulse energy was within the amplifier gain bandwidth. Furthermore, a low spectral intensity at 1534 nm was preferred for the oscillator output, since Er^{3+}-fibers show a narrow gain peak at 1534 nm, which cannot support femtosecond pulses. Nevertheless, it is worth to mention, that much higher signal bandwidths can be achieved for overall normal cavity dispersion [TNH94][RPN02].

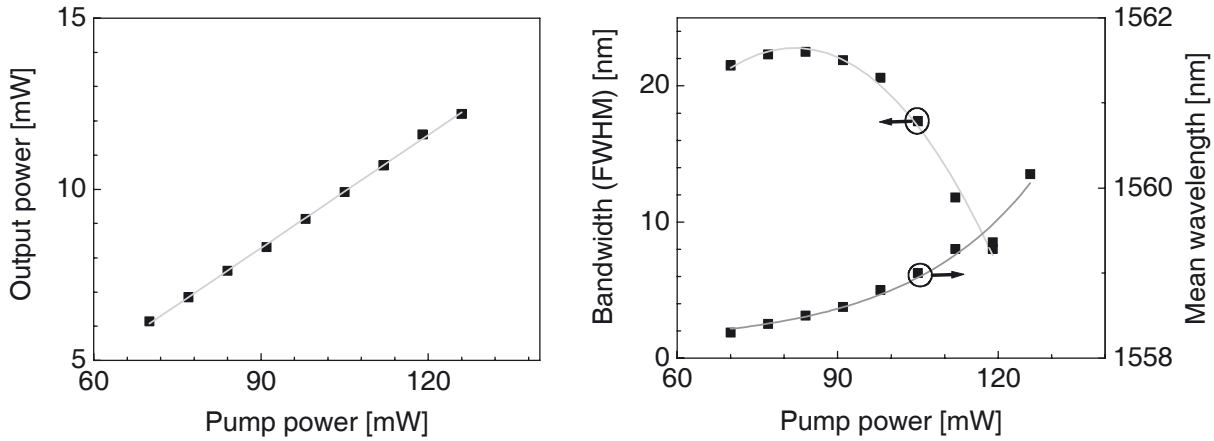

Fig. 6.1.3 *Left diagram: Mode-locked output power of the Er^{3+}-fiber laser versus pump power. Right diagram: Spectral bandwidth of the output signal [FWHM] and average wavelength versus pump power.*

At the output port of the PBS, the signal was coupled into a polarization maintaining fiber with an FC/APC fiber connector at the other end. A isolator behind the PBS blocked back-reflections from the output port into the resonator, which would disturb mode-locked operation. Besides, a small fraction of the circulating signal was coupled out of the resonator by the WDM-coupler. A multimode fiber was spliced to the corresponding fiber end of the WDM-coupler. This multimode fiber suppressed back-reflections from this fiber end into the resonator and transmitted the optical signal to a fast photodiode, which generated an electric trigger signal for synchronization of the modulators to the output pulse train.

For appropriate settings of the polarization controllers (PC), self-starting mode-locked operation with a repetition rate of 60 MHz was observed. The mode-locking threshold depended on the settings of the PC and was typically about 70 mW. The output power, the spectral bandwidth (FWHM) and the average wavelength of the output spectrum are plotted in figure 6.1.3 versus the pump power.

In the pump power range of 70 mW to 126 mW the output power increased linearly from 6.1 mW to 12.2 mW, corresponding to output pulse energies of 0.1 nJ to 0.2 nJ. The spectral bandwidth (FWHM) showed a maximum of 22.5 nm at a pump power of 85 mW and decreased if the pump power was further increased. Moreover, the average signal wavelength rose slightly from 1558.3 nm to 1560.1 nm with increasing pump power or pulse energy. This increase is likely a result of intra-pulse Raman scattering.

The output spectra for 84 mW and 119 mW pump power are shown in figure 6.1.4. It can be seen, that the spectra showed several small local maxima (spectral sidebands) beside the pulse maximum. These sidebands are attributable to a resonance enhancement of the dispersive waves, which are shed from the circulating soliton like pulse by perturbations [DDU94] [KEL92]. As sideband positions depend on the cavity dispersion and the pulse width, a cavity

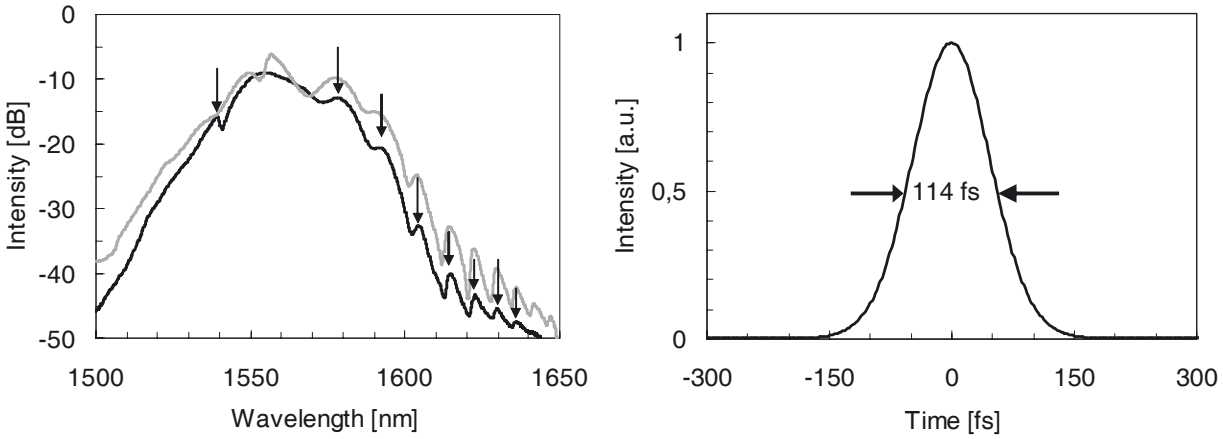

Fig. 6.1.4 *Left diagram: Output spectra of the laser for a pump power of 84 mW (black trace) and 119 mW (grey trace). Arrows indicate the positions of the spectral sidebands for the 84 mW pump power spectrum. Right diagram: Calculated bandwidth limited pulse shape corresponding to the spectrum for 84 mW pump power.*

dispersion of $-2.34 \cdot 10^4$ fs², which is equivalent to an average fiber dispersion of $-6.7 \cdot 10^3$ fs²/m or 5.1 fs/(nm·m) was calculated from the measured spectra and the corresponding relation [DDU94]. For these calculations, the pulse width was determined from the output spectra by assuming a bandwidth-limited pulse shape. For a pump power of 84 mW, the calculated pulse shape, with a FWHM duration of 114 fs, is shown in the right diagram of figure 6.1.4.

The mode-locked Er^{3+}-fiber laser was usually operated at 84 mW pump power level, since this resulted in a smooth spectrum and reliable self-starting mode-locked operation. A smooth spectrum across the amplification bandwidth of the amplifier (~ 1555 – 1565 nm) was preferred, as strong variations of the spectral intensity would have given rise up to phase distortions by SPM in the chirped-pulse amplifier system.

6.1.2 Fiber-stretcher

A dispersive fiber stretcher increased the pulse duration of the oscillator signal, in order to reduce the high signal intensity and thus the nonlinear effects in the fiber elements. The fiber-stretcher consisted of a fiber-coupled PBS and a Faraday mirror. The normal dispersion of the silica fiber was realized by a high waveguide dispersion, which was accomplished by a special adapted refractive index structure (Appendix A). Therefore, the normal waveguide dispersion of the fiber dominated over the anomalous material dispersion at 1550 nm. The stretcher unit was connected to the fiber laser by polarization-maintaining fibers with polarization adjusted FC/APC connectors. Hence, no polarization alignment was required at the PBS. A telecommunication-grade fiber module with a dispersion of -35 ps/nm [COR03], a dispersion slope of 47 nm^{-1} (TOD/GVD = -27 fs) and an effective area of 15 µm² at 1550 nm provided the normal dispersion for pulse stretching. The dispersion slope of this fiber module

enabled simultaneous compensation of the stretcher GVD and TOD by a diffraction grating compressor (section 2.6). Behind this fiber module, a Faraday mirror reflected the signal. Thus, the backward propagating signal was orthogonally polarized to the forward traveling signal. By this way, the polarization mode-dispersion of the fiber module of about 0.1 ps (single pass) was eliminated and variations of the birefringence in the stretcher fiber had no influence on signal polarization or signal power. At the PBS, the backward traveling signal was separated from the propagation path of the input and coupled into a polarization maintaining fiber.

Measurements of the signal power before and behind the fiber stretcher showed, that it caused a loss of about 8.8 dB. The signal spectra behind the stretcher had roughly the same shape as the input spectra from the fiber laser (fig. 6.1.5), however the spectral bandwidth was reduced by about 5%. Probably, this bandwidth reduction is attributable to soliton effects in the 2.5 m long pigtail fibers of the stretcher module and the 2 m long fibers of the pigtailed PBS. As these fibers had most likely anomalous dispersion, the signal bandwidth decreases by soliton effects, if the pulse energy is below the soliton energy for the input pulse shape (eqs. 2.3.7). However, detailed calculations of this effect were not possible, as the dispersion of the packaged pigtail fibers was not specified. The pigtail fibers were not shortened, since on the one hand the spectral bandwidth of the output signal was limited by the gain bandwidth of the amplifier (section 6.1.4) and not by signal bandwidth after the stretcher. On the other hand, such manipulations were avoided due to the high costs of the stretcher module and the damage risk for this element due to the packaging of the pigtail fibers.

Additionally, it can be noticed from the spectra in figure 6.2.3, that the attenuation of the

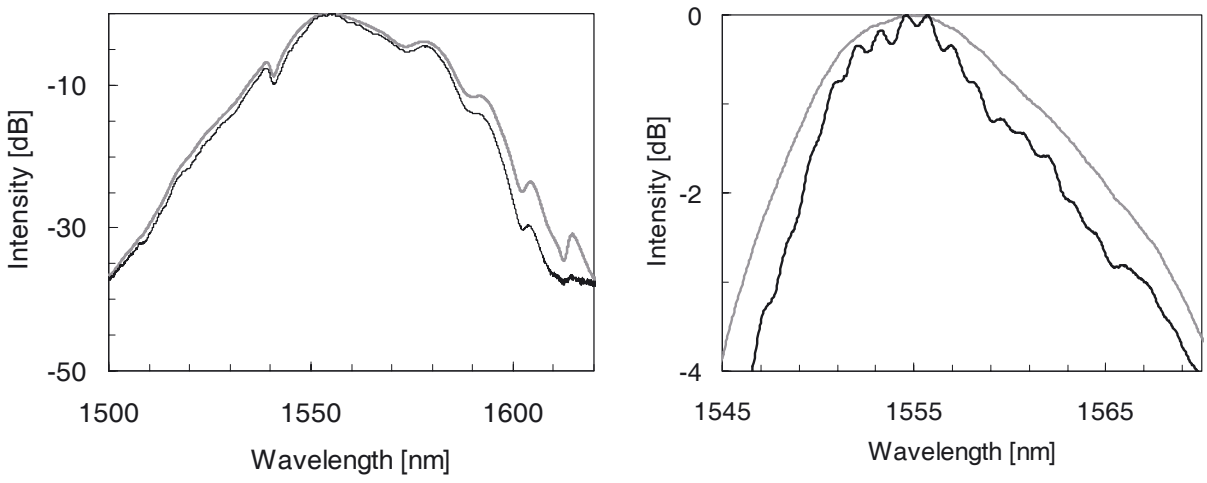

Fig. 6.1.5 *Output spectra the mode-locked fiber laser at 84 mW pump power (grey curve) and the resulting spectrum behind the fiber-stretcher arrangement (black curve). The right diagram shows a magnified view of these spectra.*

stretcher was slightly stronger above about 1580 nm. Most likely, this is attributable to increased bending losses in the stretcher fiber at longer wavelengths [GKE00].
In the right diagram of figure 6.1.5, a slight oscillatory structure with a period of about 1.2 nm was observable on the output spectrum of the fiber stretcher, which was not present in the fiber laser output. These modulations are most likely due to self-phase modulation, since the small effective mode field area of the stretcher fiber resulted in an increased amount of SPM. In addition, it is well known from simulations and experiments, that such an oscillatory structure is created by SPM in normal dispersive fibers [AGR95].

6.1.3 Pulse picking unit

The repetition rate of the fiber laser was reduced by a fiber-coupled telecom-grade amplitude modulator. According to the specifications, this Mach-Zehnder $LiNbO_3$ modulator had a maximum modulation rate of 2.5 GHz, a modulation amplitude of at least 20 dB and a maximum insertion loss of 4 dB [JDS03]. The modulator required a linearly polarized input as only one polarization mode was transmitted and it was therefore connected to the PBS of the fiber-stretcher by polarization-maintaining fibers and connectors.
The phase of the modulator transmission curve was adjusted by a DC voltage (< 6V) for minimum signal transmission without any additional radio-frequency (RF) signal. The picking of the individual pulses from the continuous pulse train was controlled by an electric signal at the RF port of the modulator. According to the modulator specifications, an electrical switching signal with a voltage amplitude of 3.5 – 4 V was required for maximum signal transmission. The pulse-picking signal was generated by specially designed electronics, based on standard high-frequency electronic components (180MHz). The timing of the trigger pulses was determined by a TTL signal, which was supplied by an internal counter or by an external trigger source. Hence, the repetition rate can be quasi-continuously tuned and the pulse timing can be controlled by an external trigger source.
Only the picked pulses were detectable in the oscilloscope trace of the output signal, after adjustment of the DC voltage and the electronic delay (25 dB resolution limit). An insertion loss of 3.4 dB was measured for the modulator, adjusted by the DC voltage for maximum signal transmission and without a pulse-picking signal. Furthermore, the maximum amplitude of the RF signal was slightly too low for maximum modulator transmission, which caused an additional loss of about 0.75 dB for the picked pulses.

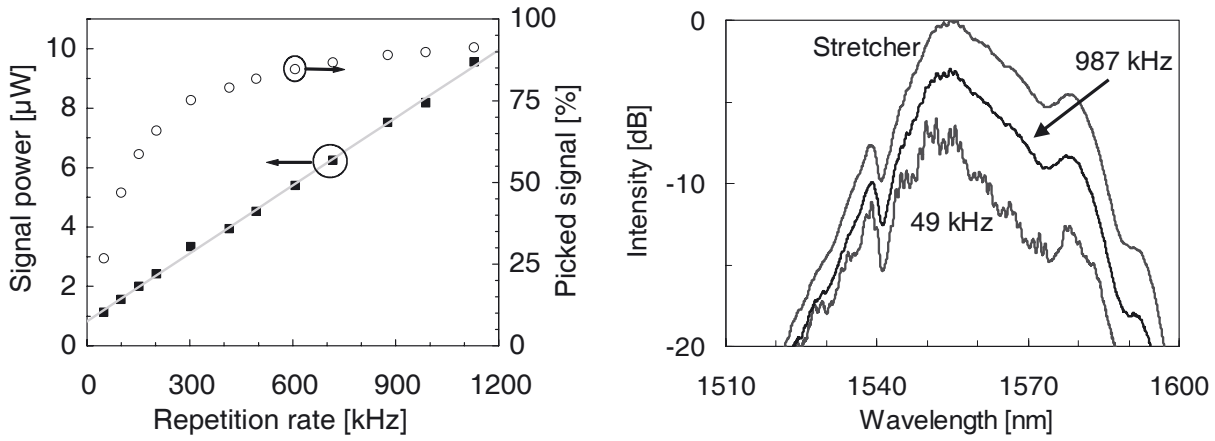

Fig. 6.1.6 *Left diagram: Transmitted signal power at the first modulator versus repetition rate (black squares). The grey line shows a linear fit for these data. The calculated contributions of the picked signal pulses to the transmitted power are indicated by hollow circles in this diagram. Right diagram: Spectra of the input signal from the fiber stretcher and of the transmitted signal for repetition rates of 49 kHz and 987 kHz (An artificial offset is introduced on the intensity of the spectra for an improved visibility).*

The transmitted signal power increased linearly with pulse-picking frequency, as shown in figure 6.1.6. A pulse energy of 7.7 pJ was calculated by fitting those values by a linear function. Furthermore, this linear fit function indicated an offset of 0.82 µJ at zero pulse-picking frequency, which is attributable to the remaining transmission of the modulator for the unpicked pulses and corresponds to a modulation amplitude of 27 dB. Based on these data, it was calculated that the picked pulses contribute between 26% and 91% to the transmitted signal power for repetition rates between 49 kHz and 1128 kHz (fig. 6.1.6).

In the right diagram of figure 6.1.6, the transmitted signal spectra for repetition rates of 49 kHz and 987 kHz and the input signal from the fiber stretcher are displayed. For a repetition rate of 987 kHz the transmitted spectrum was quite similar to the input spectrum, while at a repetition rate of 49 kHz significant deviations between input and transmitted spectrum can be noticed. Variations of the repetition rate confirmed, that this deviations increased with decreasing repetition rate. Due to the high switching speed of the modulator, the spectrum of the transmitted pulses must be independent of the repetition rate. However, as the repetition rate decreased the contribution of the suppressed pulses to the transmitted signal increase. Furthermore, the transmitted spectrum of the suppressed pulses is quite sensitive to small wavelength dependent effects of the modulator (e.g. variations of the splitting ratio, different wavelength dependence of the optical path lengths in the two interferometer arms), as these effects can significantly reduce the signal extinction. Thus, the transmitted spectrum of the suppressed pulses can be quite different to the input spectrum. Taking this into account, the mentioned influence of the repetition rate on the transmitted spectrum is most likely attributable to the remaining contribution of the suppressed pulses to the transmitted signal.

In order to reduce the contribution of the unpicked pulses, a second modulator was inserted behind the preamplifier, which was driven synchronously relative to the first modulator. By this arrangement, the second modulator increased not only the modulation amplitude, but suppressed also the amplified spontaneous emission (ASE) of the preamplifier. As in the preamplifier no polarization maintaining fibers were used, the signal polarization was adjusted after the preamplifier by a fiber optical polarization controller. The increase of the modulation amplitude was confirmed by the oscilloscope trace of the photodiode signal behind the second modulator. It showed that the amplitude was at least 5000 times lower (resolution limit) for the suppressed pulses than for the picked pulses, which corresponds to a modulation amplitude of at least 37 dB.

6.1.4 Preamplifier

After the first modulator, the picked pulses were pre-amplified in an Er^{3+}-doped fiber amplifier (EDFA). This amplifier consisted mainly of an Er^{3+}-doped gain fiber and a fiber optical isolator. A WDM-coupler, placed before the Er^{3+}-fiber, was used for insertion of the pump light from a telecommunication grade 980 nm fiber-coupled laser diode.
The gain fiber was 4 m long and had an absorption of 40 dB/m at 1530 nm [LIE03b]. This commercial Er^{3+}-fiber, which was optimized for telecommunication amplifiers in the C-band, enabled a relatively high efficiency in combination with a relatively short gain fiber length.
The optical isolator after the Er^{3+}-fiber transmitted only one polarization mode. By this way, polarization mode dispersion was avoided, which is normally generated by polarization insensitive optical isolators. The signal polarization was adjusted for maximum transmission at the isolator by a fiber optical polarization controller.
It was shown in the previous section that the suppressed pulses made a relatively large contribution to the output signal of the first modulator. Furthermore, the preamplifier generated some ASE. Due to these facts, the amplified signal was analyzed after the second modulator, since it strongly suppressed the unpicked pulses and the ASE of the preamplifier. By this way, the influence of the preamplifier on the picked pulses was much easier to determine.
The energy of the amplified pulses is displayed, for different pump power levels, in the left diagram of figure 6.1.7 as a function of the repetition rate. The pulse energy increased linearly with pump power and depended only weakly on repetition rate. The maximum pulse energies of 1.1 nJ (987 kHz) to 2.0 nJ (49 kHz) correspond to an amplifier gain of 21.9 dB to 24.7 dB. This gain values were calculated from the input pulse energy of 7.7 pJ and the output pulse energies and included therefore the attenuation of the second modulator. The low influence of

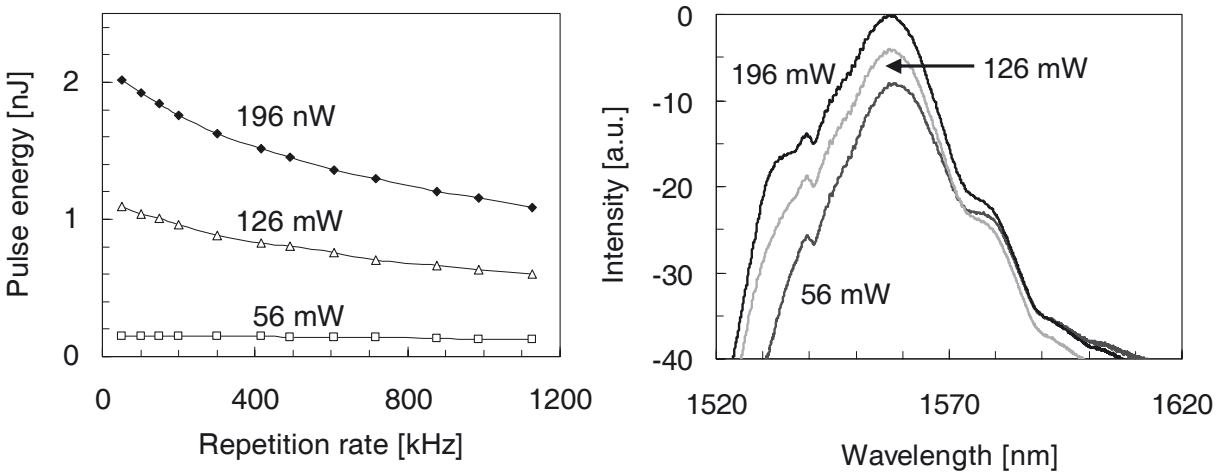

Fig. 6.1.7 *Left diagram: Pulse energy after the second modulator as a function of the repetition rate and the pump power of the preamplifier. Output spectra after the second modulator at a repetition rate of 200 kHz for preamplifier pump powers between 56 mW to 196 mW. (An artificial offset is introduced on the intensity of the spectra for an improved visibility).*

the repetition rate on the pulse energy is attributable to some extent to the unpicked pulses in the input signal, as this contribution extracted energy from the amplifier, but did not pass the second modulator. Nevertheless, calculations showed that the generated output power increased with increasing repetition rate, even if the contribution of the suppressed pulses was taken into account. Hence, the preamplifier was not saturated.

The evolution of the signal spectrum with preamplifier pump power and repetition rate can be seen in the right diagram of figure 6.2.7 and in figure 6.2.8. The spectral bandwidth (FWHM) was much smaller than the input signal and decreased from 11.0 nm to 9.9 nm as the pump power was increased from 56 mW to 196 mW. This reduction of the spectral bandwidth is attributable to the Er^{3+}-gain spectrum and the resulting gain narrowing. The signal spectrum depended only weakly on repetition rate; however, the average signal wavelength decreased

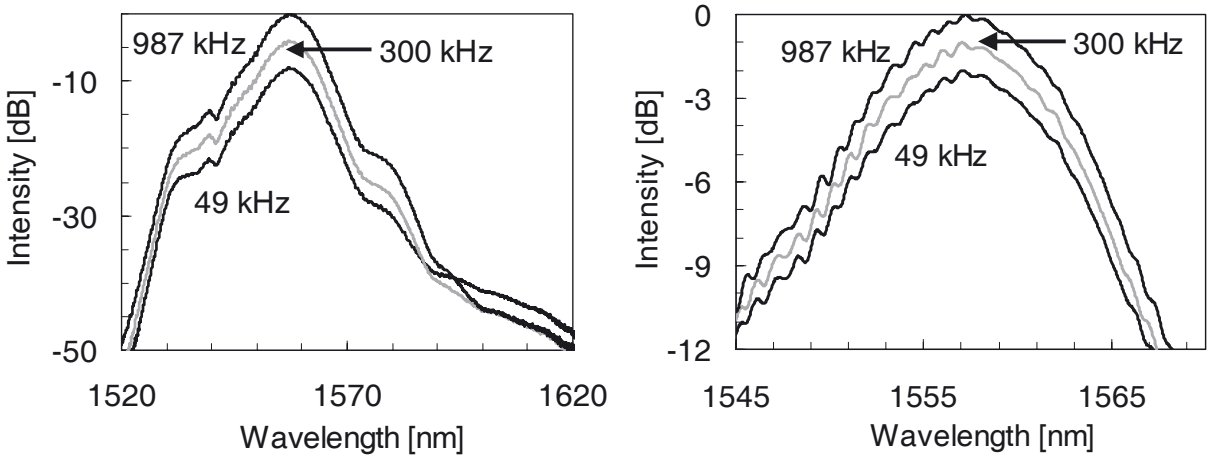

Fig.6.1.8 *Output spectra for repetition rates of 49 – 987 kHz in combination with a preamplifier pump power of 196 mW. The right diagram shows these spectra in more detail. (An artificial offset is introduced on the intensity of the spectra for an improved visibility).*

from 1558.5 nm (0.12 nJ) to 1556.9 nm (2 nJ) with increasing pulse energy. This wavelength shift is a result of the decreasing signal reabsorption in the Er^{3+}-fiber with increasing inversion (section 2.4.2).

Additionally, in all measured spectra the intensity at the 1534 nm Er^{3+}-gain peak was at least 15 dB below the spectral intensity at the maximum at about 1557 nm. However, further experiments showed that the 1534 nm gain peak increased and became even dominant if the gain fiber length was reduced. Finally it should be mentioned, that the signal spectra showed slight modulations with a period of about 1.0 nm. These modulations are described in more detail in section 6.3.1.

6.1.5 Power-amplifier

After the preamplifier and the second modulator, the pulses were amplified to pulse energies in the µJ range by a two-stage fiber power-amplifier. The detailed set-up of this amplifier is shown in figure 6.1.9. Similar to the preamplifier, each stage consists mainly of an Er^{3+}-fiber, a 1480/1550 nm WDM-coupler and an optical fiber isolator. The two amplifier stages EDFA 2 and EDFA 3 were pumped in backward direction, as for such a pumping arrangement a higher efficiency and smaller four-wave-mixing effects were experimentally observed. The 1480 nm pump light was provided by a commercial Raman shifted Yb^{3+}-fiber laser [OFS03b]. In combination with a fiber-coupled 975 nm laser diode with a maximum output power of 17.5 W, the Raman-shifted laser provided up to 4 W output power at 1480 nm from a single-mode fiber. The 1480 nm pump light was distributed to the two power-amplifier stages by a fiber coupler with a coupling ratio of 1:22. For minimum polarization dispersion isolators were used, which transmitted only one polarization mode. For that reason, the polari-

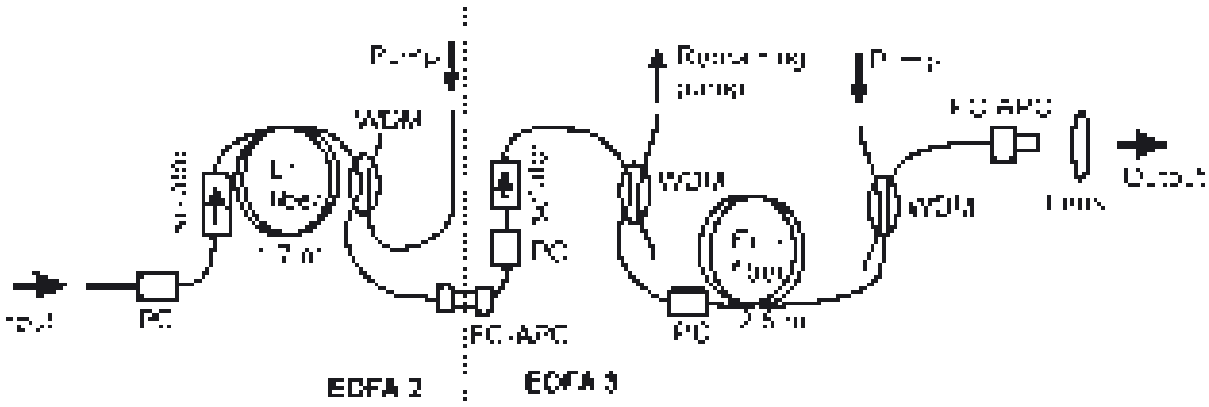

Fig. 6.1.9 *Set-up of the two stage Er^{3+}-fiber power-amplifier. The first power-amplifier stage (EDFA 2) is located left of the vertical dashed line, while the components on the right side of this line belong to the second stage of the power-amplifier (EDFA 3). PC: Polarization controller, WDM: 1480/1550 nm WDM-coupler, FC-APC: FC-APC fiber connector.*

zation was adjusted before each isolator by a fiber optical polarization controller. Furthermore, an additional WDM-coupler was inserted before the isolator in the second power-amplifier stage, to protect this isolator from potentially high pump power levels after the Er^{3+}-fiber.

In order to avoid modulation instabilities, only fiber optic components with normal dispersion were employed. For the two amplifier stages, the same gain fiber with high doping concentration was used as in the oscillator. The corresponding fiber lengths were 1.7 m and 2.6 m, respectively, for EDFA 2 and EDFA 3. The fibers in the WDM-couplers had a mode field area of about 44 µm² and a dispersion of about -2 ps/(nm·m) at 1550 nm, which was calculated from the specified refractive index structure. For the other fiber components a telecommunication fiber with a mode field area of about 50 µm² and a dispersion of -7 ps/(nm·m) was employed.

Owing to the high signal intensity, the optical Kerr-effect caused significant intensity dependent polarization rotation in the Er^{3+}-fiber of EDFA 3, if the light was elliptically polarized (section 2.5.2). Thus, birefringence was induced by coiling the Er^{3+}-fiber (∅ 6 cm) of this amplifier stage [KGM00][URE80]. By this way, the fiber became polarization maintaining. A fiber optical polarization controller before the fiber coil enabled an adjustment of the signal polarization to the fiber polarization modes.

The operation of the two-stage power-amplifier was investigated in detail by analyzing the signal after the first power-amplifier stage and the power-amplifier output port. In this section, only the operation of the first power-amplifier stage is described. The signal after the second power-amplifier stage is described in the next section, as the performance of the complete oscillator-amplifier system is largely determined by the properties of this signal.

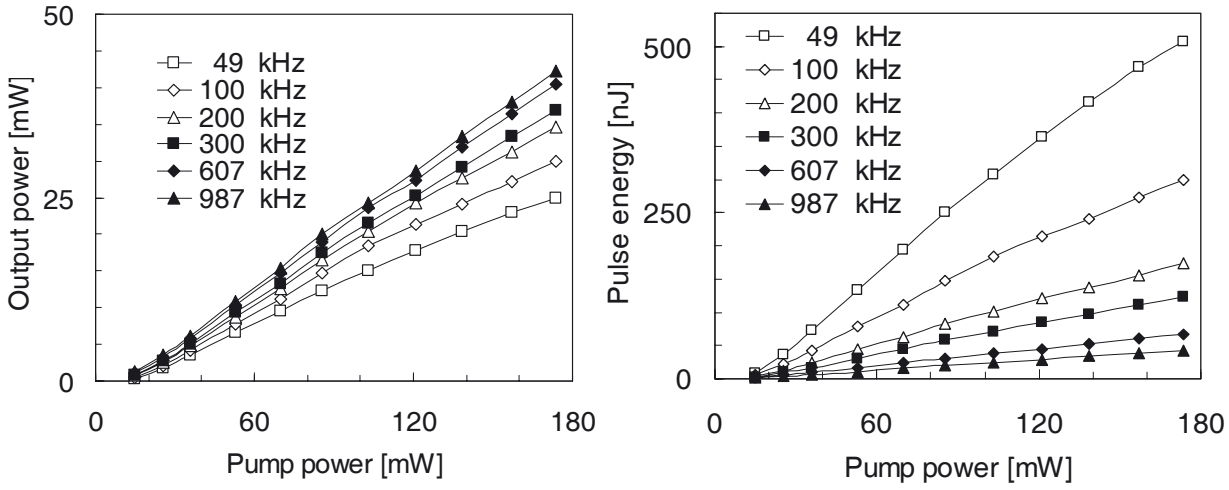

Fig.6.1.10 *Left diagram: Signal power after the first power-amplifier stage as a function of the pump power and the repetition rate. Right diagram: Corresponding pulse energy as function of the pump power and the repetition rate.*

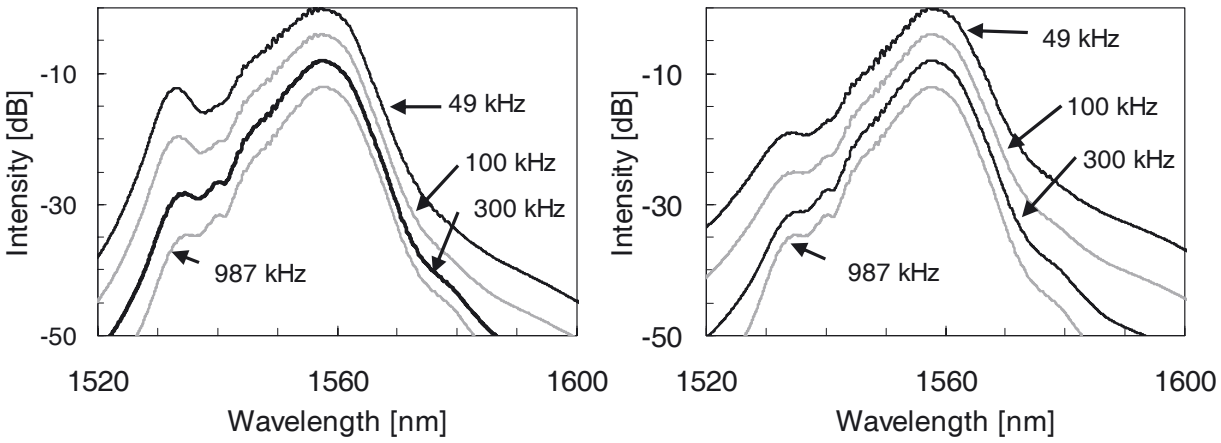

Fig. 6.1.11 *Output spectra after the first power-amplifier stage for repetition rates between 49 kHz and 987 kHz. Left diagram: Amplifier was pumped with 173 mW for all repetition rates. Right diagram: For each repetition rate, the pump power was adjusted for an output pulse energy of about 44 nJ. (An artificial offset is introduced on the intensity of the spectra for an improved visibility).*

The output power of the first power-amplifier stage increased linearly with pump power above the threshold (12 mW) to up to 42 mW at 173 mW pump power (fig. 6.1.10). Furthermore, it decreased by about 40% as the repetition rate was reduced from 987 kHz to 49 kHz. The later indicated that the amplifier was largely saturated, since the reduction of the repetition rate corresponded to a decrease of the input power by a factor of 23.

The maximum pulse energy increased from 42 nJ (987 kHz) to 508 nJ (49 kHz) as the repetition rate was reduced (fig. 6.1.10). These pulse energies correspond to an amplifier gain of 15.7 dB at 987 kHz and up to 23.9 dB at 49 kHz. It should be noted, that additional experiments showed that at high repetition rates the pulse energy was only limited by the available pump power. However, at low repetition rates the gain peak at 1534 nm became dominant if the pump power was further increased and, besides, the suppression of laser bursts at 1.53 µm and 1.55 µm became increasingly difficult.

Spectral bandwidths (FWHM) between 8.5 nm and 9.0 nm were measured for the output signal. Hence, the bandwidth of the input signal (~ 10 nm) was further reduced by the gain spectrum. Like in the preamplifier, the average wavelength decreased with increasing pulse energy from 1559.9 nm (1.3 nJ) to 1556.2 nm (0.5 µJ).

In the output spectra, the relative signal intensity of the gain peak at 1534 nm and for wavelengths above about 1570 nm increased with decreasing repetition rate (Fig. 6.1.11). Such a spectral evolution was observed in combination with constant pump power and, to a smaller extent, for constant output pulse energy. For constant pump power, an increase of the 1534 nm peak with decreasing repetition rate was expected, as this resulted in an increase of the amplifier gain and the Er^{3+}-inversion and therefore in a lower signal reabsorption.

For constant output pulse energy, the gain and therefore the inversion were independent of the repetition rate. Thus, the observed increase of the relative spectral intensity at 1534 nm was not attributable to variations of the gain spectrum. However, the contribution of the ASE increases with decreasing repetition rate. This is attributable to the fact that the ASE power depends only on the inversion, while the signal power is proportional to the repetition rate.
It can be seen from the measured spectra, that a repetition rate reduction from 987 kHz to 49 kHz resulted in an 3.8 dB increase of the spectral intensity at 1534 nm. Based on this data and the previous described relation, it was determined that the ASE signal contributes between 7% at 987 kHz and 61% at 49 kHz to the spectral intensity at 1534 nm. Furthermore, for wavelengths above 1590 nm the corresponding increase of more than 12 dB indicates that at these wavelengths the spectral intensity is mainly attributable to ASE.
During the previous described measurements, a pump power of 196 mW was applied to the preamplifier. Additional experiments showed, that the spectral bandwidth after the first power-amplifier stage decreased by 0.1 - 0.2 nm and the output power by 9% - 19%, if the preamplifier pump power was reduced by 35%.

6.1.6 Grating compressor

A dispersive grating compressor behind the power amplifier was used for temporal recompression of the chirped amplified signal. For maximum compressor transmission, the polarization of the incident beam was adjusted by a λ/2- and a λ/4-wave plate. Such an adjustment was required as the diffraction efficiency of the gold-coated holographic gratings with a line spacing of 1100 l/mm was more than 90% for s-polarization, but below 10% for p-polarization. The detailed set-up of the grating compressor is shown in fig. 6.1.12. This double-pass grating compressor set-up was principally the same as described in section 2.6. However, a retro-reflecting 90° mirror pair was employed between the two gratings. By this way, the grating distance and therefore the dispersion of the compressor could be adjusted by a translation of this retro-reflector. In addition, this arrangement enabled a more compact compressor set-up. For an adjustment of the dispersion slope of the compressor to the fiber stretcher, the two gratings could be simultaneously rotated relative to the incident beam (eqs. 2.6.3).
Based on the specified dispersion slope of the fiber stretcher, an incident angle of 53° was calculated for the first grating. Hence, an optical path length between the two gratings of about 0.9 m was required for compensation of the stretcher GVD (eqs. 2.6.2). As the diffraction angle at the first grating depended on wavelength, the width of the second grating limited the

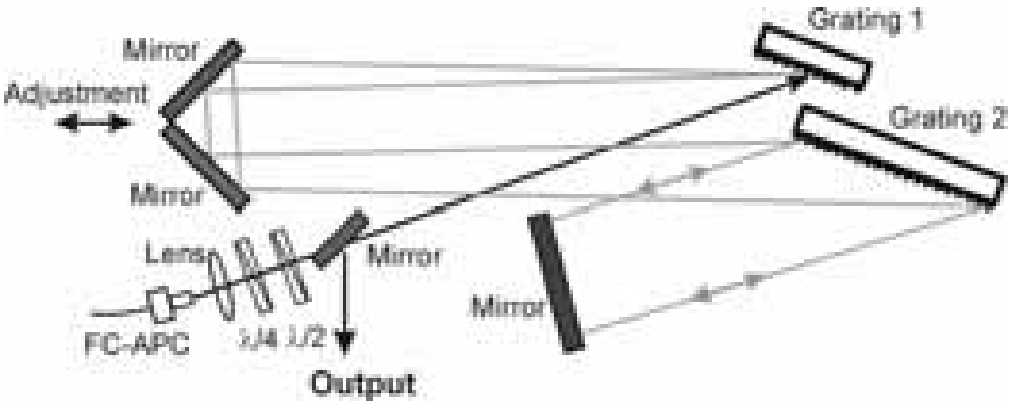

Fig 6.1.13 *Arrangement of the grating compressor. The compressor length was adjusted by moving the mirror pair in 90° arrangement.*

transmission bandwidth of the compressor. Calculation of the resulting beam propagation showed that the 96 mm wide ruled area of grating 2 limited the compressor transmission bandwidth to about 15 mm. It should be mentioned, that the diameter of the input beam was neglected in this calculation.

The grating compressor was adjusted for maximum transmission at a repetition rate of 200 kHz and maximum output pulse energy of the power amplifier. This resulted in a transmission window that extended from 1553 nm to 1565 nm. Within this transmission window a compressor efficiency of more than 70% was observed, if the polarization controller before the coiled gain fiber and the waveplates were adjusted for maximum transmission.

It should be noted, that after the compressor an influence of the detection fiber position and the focusing on the measured spectrum was noticed, although no clear relation between position and detected spectrum could be derived. This strongly indicated that the various frequencies showed a slightly different spatial distribution after the compressor. This is most likely caused by some curvatures of the mirrors and deviations for the grating and the mirror orientation. Curvatures of the mirror surfaces can be caused by tension due to the dielectric reflective coating. Such tensions were indicated by the fact, that the dielectric coatings of several mirrors of the coating charge showed tension cracks. Furthermore, in this set-up the relative orientation of the two gratings could only be determined with an accuracy of about 0.05°, even though the adjustment elements enabled a much more precise positioning of the individual elements. Calculations showed that a deviation of 0.05° from the desired parallel grating mounting resulted in a displacement by about 0.9 mm over the transmission bandwidth of the compressor (12 nm). Variations of the angle between the retro-reflecting mirror pair had a similar effect. Hence, most likely the limited accuracy of the adjustment and curvatures of the mirrors may have caused the previous described effects.

6.2 Experimental results for the oscillator-amplifier system

The amplification in the fiber amplifiers and the transmission properties of the grating compressor determine the spectrum and the pulse energy of the emitted pulses. Furthermore, in addition to the output spectrum the combined influence of the fiber amplifier system and the grating compressor determine the temporal shape of the output signal.

In order to reveal the various influences on the output signal of the oscillator-amplifier-system, measurements of the output powers and spectra after the fiber amplifier and behind the grating compressor were required. The corresponding results are described in the following subsections. Furthermore, the temporal shape of the output signal was measured behind the compressor as a function of the repetition rate and the power-amplifier pump power. This enabled also a determination of the dispersive effects of the fiber-amplifier chain, as the dispersion of the grating compressor can be determined from the geometrical set-up.

6.2.1 Output signal of the fiber amplifier

In the left diagram of figure 6.2.1, the measured output power of the fiber amplifier-chain is plotted versus power-amplifier pump power for repetition rates between 49 kHz and 987 kHz. Furthermore, the output pulse energies, calculated from the measured output powers and the repetition rates, are plotted in the right diagram of figure 6.2.1 versus pump power for the various repetition rates. It can be seen that for repetition rates above 200 kHz the output power increased almost linearly with a slope efficiency of about 40% over the hole pump power range, resulting in an maximum output power of 1.41 W at a maximum pump power

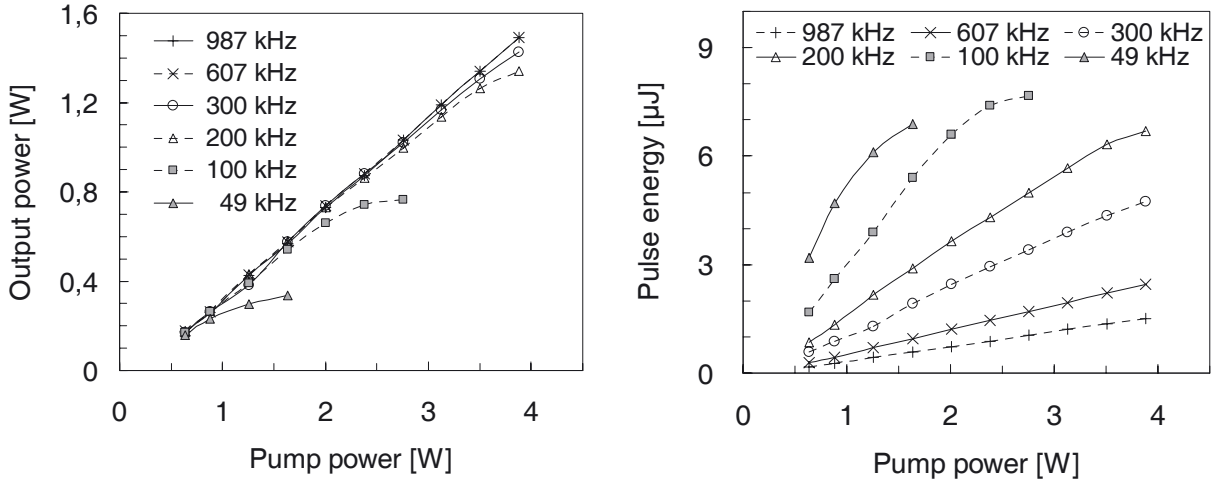

Fig. 6.2.1 *Left diagram: Output power of the fiber amplifier chain versus power-amplifier pump power for repetition rates between 49 kHz and 987 kHz. Right diagram: Corresponding pulse energy as function of the pump power and the repetition rate.*

of 3.9 W. On the contrary, the slope decreased at high pump powers for lower repetition rates. For pulse repetition rates of 49 kHz and 100 kHz even a decrease of the output power was detected, if the pump power was raised above the maximum values plotted in figure 6.2.1 (see section 6.3.4). The pulse energy curves in the right diagram of figure 6.2.1 show that these deviations from a linear slope were observed for output pulse energies above about 6 µJ and that the pulse energy was limited to about 7 µJ. This limitation and the corresponding physical mechanism are described in chapter 6.3.4 in more detail. For repetition rates above 200 kHz such a limitation was not observed, as the pulse energy was limited to lower values by the available pump power.

The output spectra of the fiber power-amplifier are shown in figure 6.2.2 for pulse energies between 1.33 µJ and 6.7 µJ and a repetition rate of 200 kHz. It is most noticeable that the output spectra show spectral modulations with a period of about 1 nm, whose amplitude strongly increased with pulse energy. These spectral modulations are described in more detail in section 6.3.1. The output spectra had spectral bandwidths (FWHM) slightly above 7 nm for pulse energies up to about 1.5 µJ. For higher pulse energies, the spectral bandwidth could not adequately be described by the FWHM definitions, because of the modulations on the spectrum. However, if the spectral modulations were neglected, the output spectra had similar spectral bandwidths at higher pulse energies. Furthermore, similar to the intermediate amplifier stages, the relative spectral intensity at the Er^{3+}-gain peak at 1534 nm increased with pulse energy, which is attributable to a reduced signal reabsorption in the Er^{3+}-fiber with increasing gain and the corresponding shift of the gain spectrum to shorter wavelengths. For pulse energies above about 4 µJ, the spectrum showed in the logarithmic plot a linear shape on the long wavelength side of the spectral maximum. Nonlinear effects

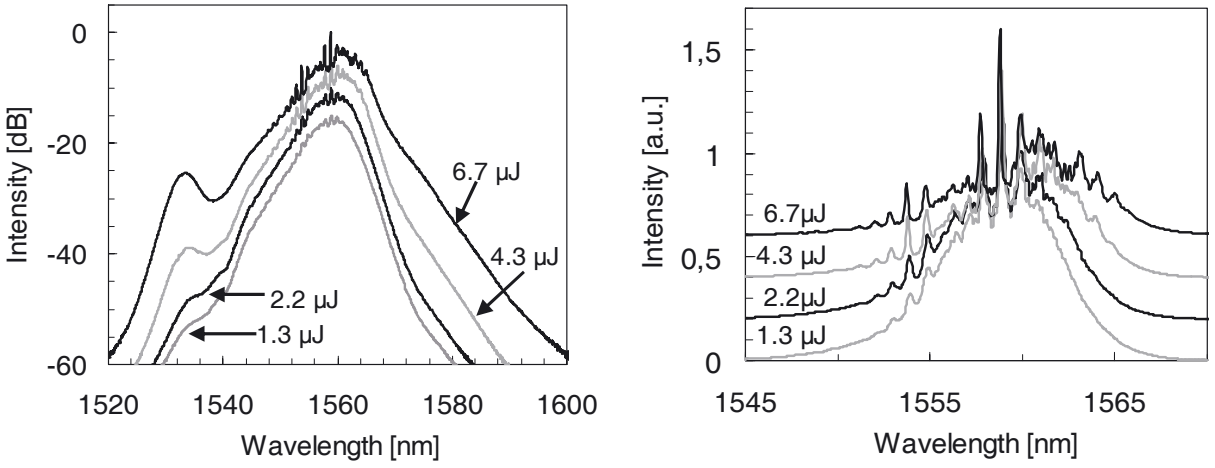

Fig.6.2.2 *Output spectra of the fiber amplifier chain at a repetition rate of 200 kHz and for output pulse energies between 1.33 µJ and 6.7 µJ. These spectra are plotted on a logarithmic scale in the left diagram. The right diagram shows the central part of these spectra in more detail on a linear scale. (An artificial offset is introduced on the intensity of the spectra for an improved visibility)*

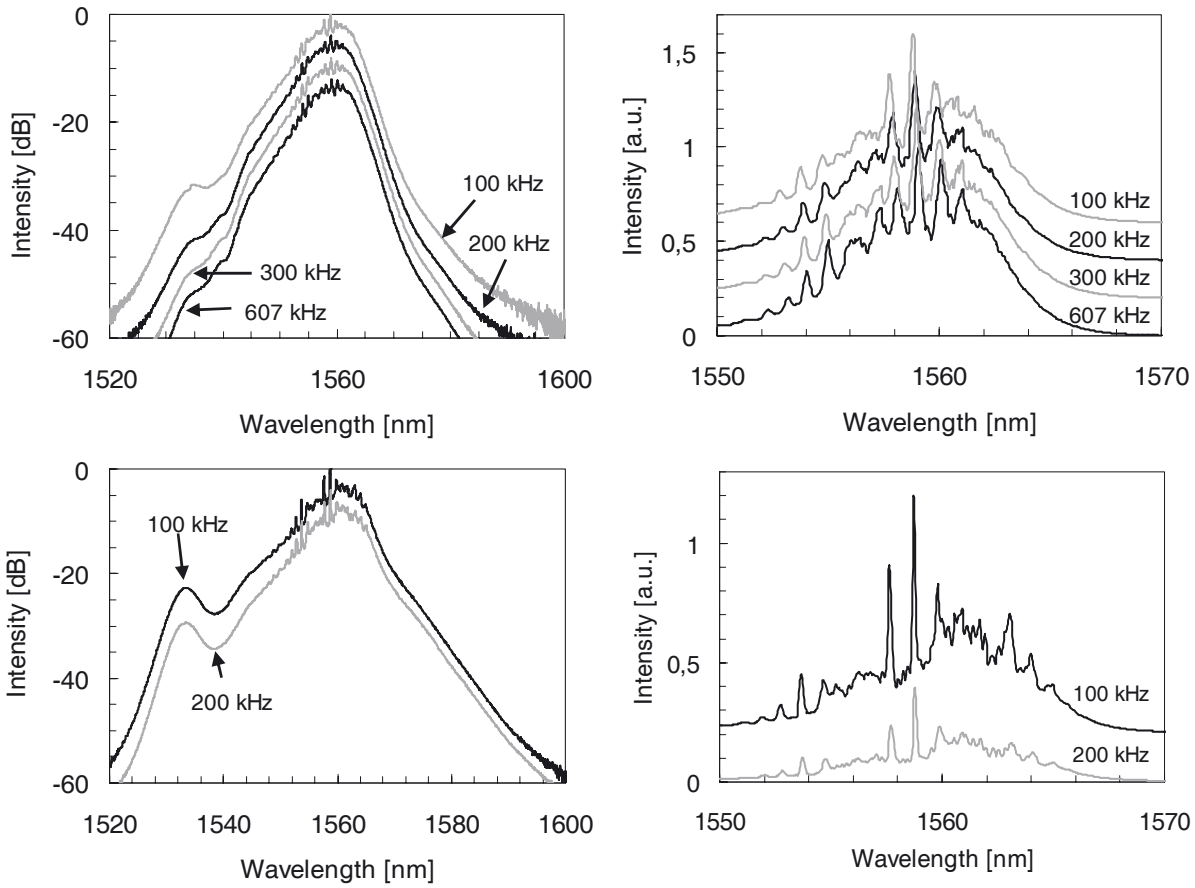

Fig.6.2.3 *Output spectra behind the fiber amplifier chain for pulse energies of 2.5 µJ (upper diagrams) and 6.6 µJ (lower diagrams). The left diagrams show the spectra on a logarithmic scale, while the right diagrams show the central part of these spectra in more detail on a linear scale. (An artificial offset is introduced on the intensity of the spectra for an improved visibility)*

must cause this power dependent spectral shape as it deviates from the gain spectrum of the Er^{3+}-ions. A more detailed description of this spectral feature can be found in section 6.3.1.

Figure 6.2.3 shows the influence of the repetition rate on the output spectra for output pulse energies of 2.5 µJ and 6.6 µJ. It can be seen that the output spectra were nearly independent of the repetition rate. Like after the first power amplifier stage, only the relative spectral intensity at the 1534 nm Er^{3+}-gain peak and above about 1580 nm increased with decreasing repetition rate. This spectral evolution was due to the contribution of the ASE to the output signal, which is described for the first power amplifier stage in more detail in section 6.1.5.

Figure 6.2.4 shows that for pulse energies up to 6.5 µJ the average wavelength of the signal increased with increasing output pulse energy. This shift of the output spectrum to longer wavelengths can also be noticed from the linear spectra in figure 6.2.2. Conversely, a decrease of the average wavelength with increasing output pulse energy can be expected, as the Er^{3+}-gain spectrum is shifted to shorter wavelengths with increasing gain as signal reabsorption becomes smaller (section 2.4.2). Such a decrease of the average wavelength with increasing pulse energy was also observed for the intermediate amplifier stages (section 6.1.4-5). How-

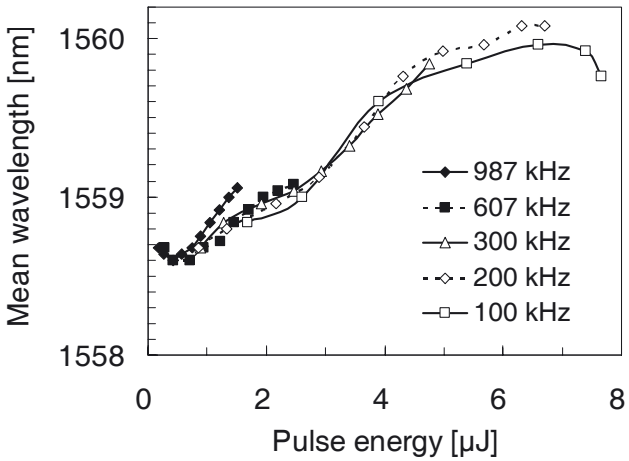

Fig. 6.2.4 *Average wavelength of the output signal versus pulse energy for repetition rates between 100 kHz and 987 kHz.*

ever, the energy extraction during pulse amplification results in a decrease of the Er^{3+}-inversion along the pulse. This gain saturation during pulse amplification shifts the effective Er^{3+}-gain to longer wavelengths with increasing pulse energy, since the carrier wavelength of the chirped signal pulses decrease along the pulse. Hence, the decrease of the average wavelength with increasing pulse energy shows that in the power-amplifier the gain saturation dominates over the gain shift due to the increased inversion.

A slight decrease of the average wavelength with increasing pulse energy was observed above 6.5 µJ pulse energy at a repetition rate of 100 kHz. A detailed analysis of the output spectra pointed out that this wavelength decrease was solely caused by to an increase of the spectral intensity at 1534 nm gain peak. Moreover, at this repetition rate the spectral intensity at 1534 nm is mainly attributable to the ASE (section 6.1.5). Thus, this average wavelength decrease is a result of the increased ASE contribution.

6.2.2 Transmission properties of the grating compressor

The output power behind the grating compressor is plotted versus the power-amplifier pump power in the left diagram of figure 6.2.5 for repetition rates between 49 kHz and 987 kHz. It can be seen that the curves were similar shaped as those that were measured before the compressor (see figure 6.2.1). However, due to the compressor loss the maximum output power was about 35% lower. The plot of the corresponding pulse energies in the right diagram of figure 6.2.5 shows that this system delivered pulse energies of more than 4 µJ after recompression for repetition rates of up to 200 kHz. The maximum pulse energy decreased almost linearly as the repetition rate was further increased to about 1 µJ at 987 kHz.

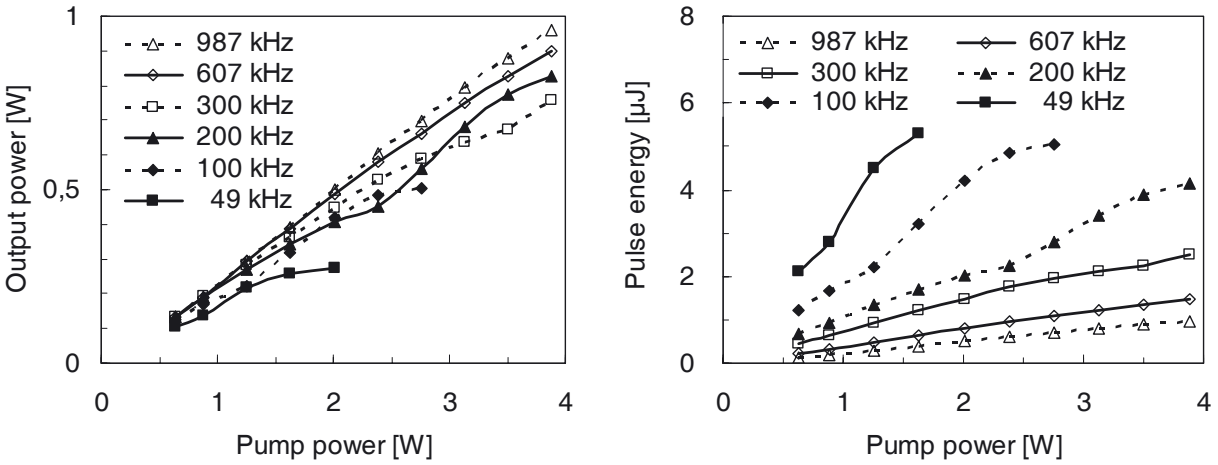

Fig. 6.2.5 *Left diagram: Output power behind the grating compressor as a function of the power-amplifier pump power and the repetition rate. Right diagram: Corresponding pulse energy behind the compressor as a function of the power-amplifier pump power and the repetition rate.*

The waveplates and the polarization controller before the coiled gain fiber were adjusted for maximum output signal at 200 kHz repetition rate and maximum pump power. The settings were adjusted to this operation mode in order to enable high output pulse energies without an individual readjustment. During adjustment of the polarization elements, a complex interaction between the settings of the polarization controller and waveplates and the compressor transmission was noticed. Maximum compressor transmission was not achieved if these settings were only iteratively adjusted for maximum output signal. For that reason the settings of the polarization controller were initially varied randomly and the waveplate settings were than readjusted for maximum transmitted power. Afterwards, the polarization controller settings were chosen that enabled the highest signal transmission in the compressor.

The complexity of this adjustment is attributable to the interaction of nonlinear polarization effects and the fiber birefringence. In order to avoid nonlinear polarization rotation, the signal polarization must be adjusted to one of the polarization axis of the fiber (section 2.4.2). In addition, if the input signal is polarized close to the fast axis, the intrinsic birefringence of the fiber can be canceled by the nonlinear birefringence [AGR95]. Consequently, the polarization must be adjusted to the slow axis of the fiber, since a signal polarization parallel to the fast axis becomes also instable at high intensities. However, the adjustment of the polarization relative to the fiber axis cannot directly be determined from the output signal and is made even more difficult by fiber bends before and after the coiled gain-fiber.

The left diagram of figure 6.2.6 shows for the previous set-up the relation between the output pulse energy and the compressor transmission for various repetition rates. The displayed transmission data were calculated from the transmitted signal power and the input power multiplied with the power fraction within the transmission window. The later was computed

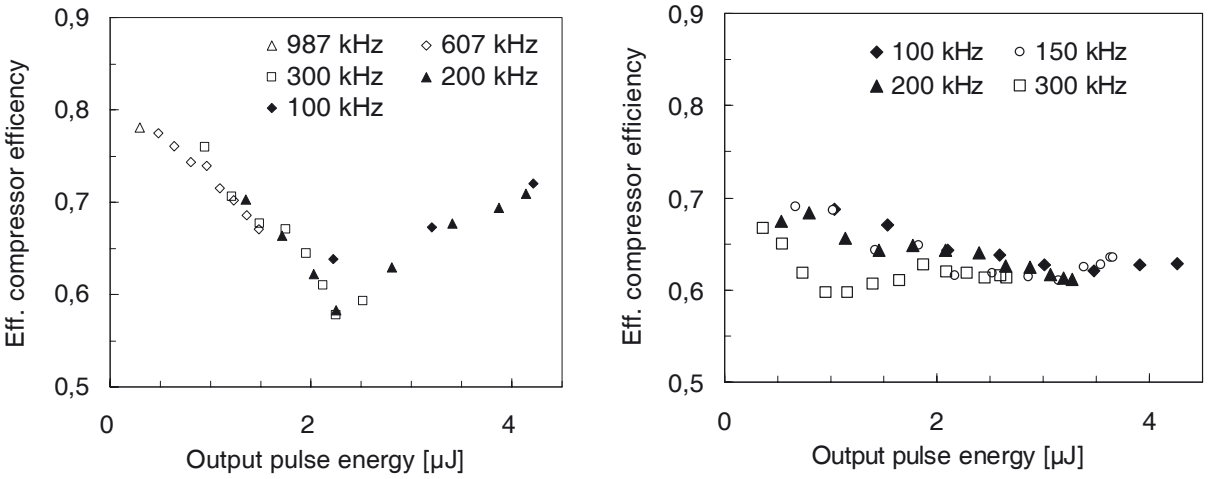

Fig. 6.2.6 *Effective compressor transmission versus output pulse energy. The effective transmission was calculated from the measured transmitted power and the input power within the transmission window between 1553 nm and 1565 nm. Left diagram: Polarization controller before the fiber coil and the waveplates were adjusted for maximum grating transmission at 200 kHz repetition rate and amplifier pump power. Right diagram: Waveplates and polarization controller settings were individually adjusted for maximum compressor transmission. During these measurements, mirrors with a lower reflectivity were incorporated into the compressor than for the measurements shown in the left diagram. Furthermore, the set-up of the power-amplifier was slightly different (gain fiber length slightly shorter, EDFA2 codirectional pumped).*

from the amplifier output spectra (between 83% and 89%), while the transmission window (1553 nm to 1565 nm) was determined from the transmitted signal spectra.

A compressor transmission of up to 78%, corresponding to a grating efficiency of about 94%, was observed at low pulse energies. With increasing pulse energy, the efficiency decreased down to 58%, corresponding to an output pulse energy of 2.3 µJ. As the pulse energy was further raised, the efficiency increased again up to 72% for an output pulse energy of 4.2 µJ. It is worth to mention, that the maximum for high pulse energies corresponds to the input pulse parameters, which were used for the adjustment of the polarization controller and the waveplates for maximum compressor transmission.

It can be seen in the right diagram of figure 6.2.6 that the compressor transmission was nearly independent of the pulse energy, if the polarizing elements were individually adjusted for maximum compressor transmission for each amplifier setting. This shows that the variation of the compressor transmission with pulse energy is attributable to the nonlinear polarization evolution in the fiber amplifier. It should be noted, that during the experiments shown in the right diagram of figure 6.2.6, the retro reflector consisted of metal-coated mirrors, while dielectric mirrors were employed for the measurements shown in the left diagram. Thus, the lower transmission maximum in the right diagram is most likely attributable to the higher loss of the metal-coated mirrors.

6.2.3 Temporal pulse recompression

Initially, in order to adjust the grating separation of the compressor for minimum output pulse duration, the temporal pulse shape was measured as a function of the grating separation by an interferometric autocorrelator [DFM85]. During these experiments it was discovered, that the grating distance for minimum pulse duration decreased with increasing pulse energy. The same relation between pulse energy and grating separation was observed, if the output signal was focused into a beta-barium-borate (BBO) crystal and the compressor was adjusted for maximum second harmonic generation (SHG) in the BBO crystal. The efficiency of the SHG generation rises with increasing signal intensity [KOE99] and the signal intensity increases with decreasing pulse duration. Therefore, this observation also shows that the required compressor dispersion for minimum output pulse duration depended on the amplifier output pulse energy.

Based on these initial observations, the influence of the amplifier output pulse energy and the repetition rate on the temporal recompression of the signal was investigated in detail. This was accomplished by adjusting the grating separation for each amplifier setting for maximum SHG signal. In order to achieve additionally a compensation of the third order dispersion (TOD), the dispersion slope of the compressor (TOD/GVD) was varied between -31.1 fs and -24.2 fs (at 1558 nm), as a slope of about -27 fs was specified for the stretcher (section 6.1.2). This was done by varying the incident angle on the first compressor grating between 51.7° and 53.8° (eqs. 2.6.3) .

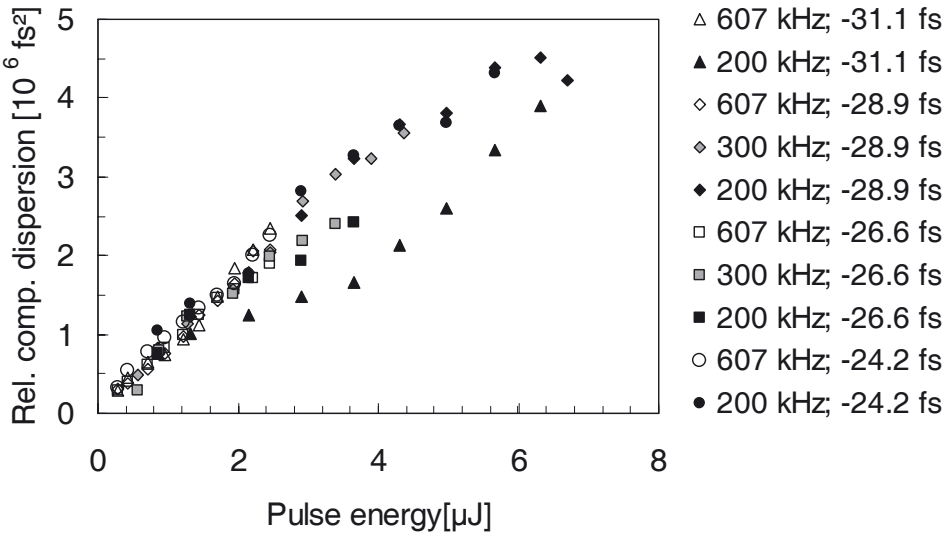

Fig. 6.2.7 *Change of the compressor dispersion with input pulse energy for various repetition rates and different dispersion slopes (TOD/GVD) of the compressor. During these measurements, the compressor was adjusted for maximum SHG efficiency of the output signal. The repetition rate and the dispersion slope are mentioned for each measurement series in the legend. The relative dispersion was calculated according to eqs. 2.6.2 from the variations of the grating separations.*

The resulting variation of the compressor GVD optimum with input pulse energy is plotted in figure 6.2.7 for various repetition rates and compressor dispersion slopes. It can be seen, that the GVD of the compressor increased nearly linearly with increasing pulse energy. As the compressor has a negative GVD (eqs. 2.6.2), this increase corresponds to a reduction of the grating separation and the absolute value of the compressor dispersion. Hence, the chirp of the amplified pulses must decrease with increasing pulse energy. This intensity dependent dispersion effect is described in more detail in section 6.3.2.

During these experiments, the interferometric autocorrelation functions showing that the lowest pulse distortions were observed in combination with a compressor dispersion slope of -28.9 fs at 1558 nm. The latter corresponded to an incident angle of 52.3° at the first compressor grating. This pointed out that the best TOD compensation was achieved for a TOD/GVD ratio of -28.9 fs. For the other dispersion slope values larger pulse chirps were indicated, which could not be compensated by an adjustment of the grating separation. Variations of the grating separations also confirmed, that the compressor adjustment for maximum SHG efficiency corresponded to the shortest output pulse durations.

The measured autocorrelation functions (ACF) depended only on the pulse energy and not on

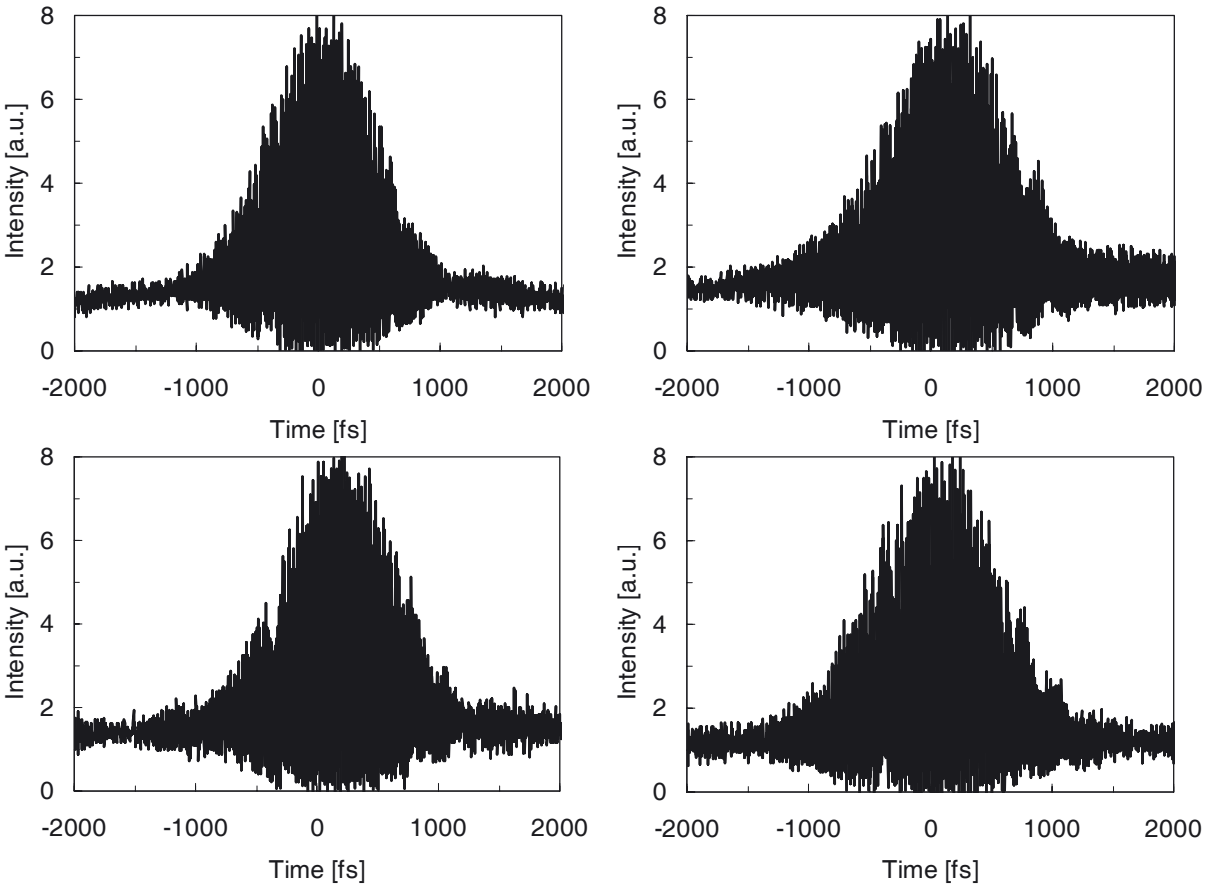

Fig. 6.2.8 *Autocorrelation traces of the output signal measured at a repetition rate of 200 kHz. The four traces correspond to pulse energies of 0.9 µJ, 2.0 µJ, 2.8 µJ and 4.1 µJ (starting fro left to right) behind the compressor.*

the repetition rate. The same relation was previously described for the output spectra (section 6.2.1). This strongly indicated that the optical properties of the fiber amplifier depended only on the gain and the pulse energy and not on the repetition rate or the average output power.

Figure 6.2.8 shows the relation between output pulse energy and the measured autocorrelation functions (ACF) for output (input) pulse energies between 0.9 µJ (1.3 µJ) and 4.1 µJ (6.7 µJ). With increasing pulse energy, the width (FWHM) of the ACF increased from about 1140 fs below 1 µJ pulse energy to 1350 fs at 4.1 µJ. This corresponds to pulse widths (FWHM) between 810 fs and 960 fs, assuming a Gaussian pulse shape [DFM85]. The increase of the pulse width with increasing pulse energy can also be seen in the left diagram of figure 6.2.9, where the pulse width, determined from the ACF, is plotted versus the output pulse energy. Conversely, the bandwidth limited pulse width, calculated from the amplifier output spectra and the transmission bandwidth of the compressor, was roughly independent of the output pulse energy.

With growing pulse energy, the slight fluctuations in the wings of the ACF increased. Moreover, for output pulse energies above about 2 µJ, the ACF showed an additional peak at a time distance of about 6.5 ps relative to the main autocorrelation peak (right diagram in figure 6.2.9), which amplitude raised with increasing pulse energy. The time distance of this side peak to the main peak of about 6.5 ps correspond roughly to the modulation period of about 130 GHz (≈ 1 nm) which was observed in the amplifier output spectrum (section 6.2.1). Moreover, the spectral modulations as well as the mentioned side peak increased with growing pulse energy. These facts indicate that the side peak in the ACF, which corresponds to a satellite pulse, is a direct result of the spectral modulations.

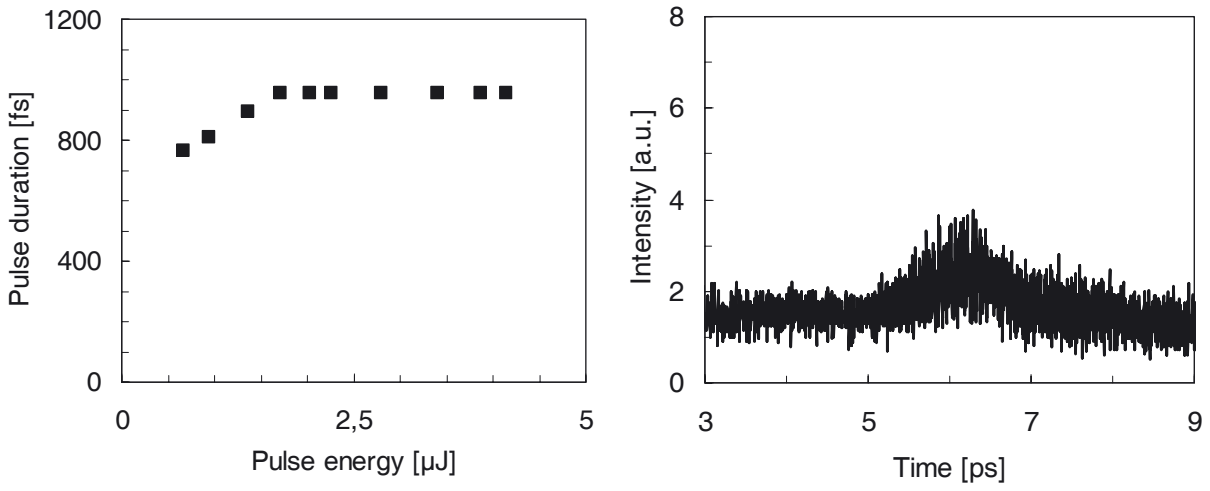

Fig. 6.2.9 *Left diagram: Pulse duration (FWHM) of the output pulses versus output pulse energy. The pulse durations were calculated from the measured autocorrelation widths assuming a Gaussian pulse shape. Right diagram: Side peak in the autocorrelation function measured for an output pulse energy of 4.1 µJ.*

Thus, increasing phase distortions with increasing pulse energy were indicated by the fluctuations in the ACF pulse wings, the increasing pulse width and the previous described side peak. However, the autocorrelation measurements gave no detailed information about the phase distribution inside the recompressed pulse. A detailed analysis of this effect requires therefore more sophisticated pulse measurement techniques like frequency resolved optical gating [AKO03], which were not available during these experiments.

By Fourier-transform calculations, the bandwidth-limited pulse durations were determined from the amplifier output spectra and the transmission window of the compressor. These computations resulted in pulse durations of about 670 fs, which were nearly independent of the pulse energy. Hence, the measured pulse durations were between 21% and 43% above the bandwidth limit. In these calculations, the pulse width was defined as the time interval that contains 77% of the pulse energy, which is equal to the FWHM pulse width for a Gaussian pulse. By this definition, the influence of the exact pulse shape on the pulse width was reduced.

Further calculation showed that the bandwidth limited pulse duration was mainly determined by the spectral filtering of the grating line. This can be seen in figure 6.2.10, where the bandwidth limited pulse duration (77% definition) is plotted versus the transmission bandwidth of the compressor. It can be noticed from this plot that the bandwidth limit for the pulse duration can be reduced by about 30%, if the transmission bandwidth of the gratings is increased from 12 nm to 20 nm. This can be realized installing a 16 cm broad grating in the compressor, instead of the employed second grating with a 9.6 cm broad ruled area.

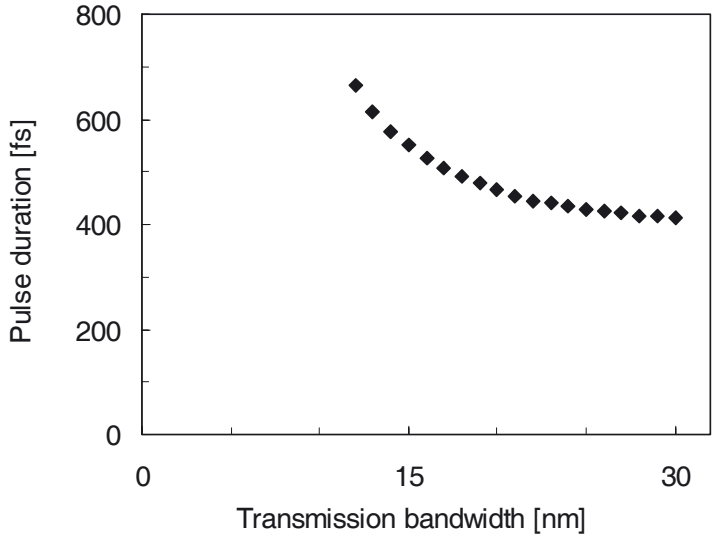

Fig. 6.2.10 *Bandwidth limited pulse duration (77% definition) versus transmission bandwidth of the grating compressor. The amplifier output spectrum which was used for this calculations were measured for an amplifier output pulse energy of 4.7 µJ. The transmission bandwidth was centered at 1559 nm, since this center wavelength resulted in the shortest pulse durations during these calculations.*

6.3 Nonlinear effects in the fiber amplifier

During the previous described experiments it was observed, that the amplifier efficiency and the spectral and temporal properties of the output signal, such as the modulations of the spectrum or the signal chirp, depended on the output pulse energy. This indicated that the signal was significantly influenced by nonlinear effects during amplification. Moreover, nonlinear effects were strongly favored in the gain-fiber by the high signal intensity of up to 87 GW/cm² and the large energy extraction. This peak intensity in the gain fiber, with a mode field area of 16 µm², was calculated for an output pulse energy of 7 µJ and a pulse duration of 0.5 ns. The latter was determined from the spectral bandwidth of the output signal (~ 7.5 nm), by taking the dispersive pulse stretching of -70 ps/nm into account.
For that reasons, the observed nonlinear effects in the fiber amplifier and the influence on the amplifier operation were described in detail in the following sections. Moreover, the resulting limitations were discussed and it is pointed out how these limitations can be reduced.

6.3.1 Spectral modulations

It was described in section 6.2.1, that the amplitude of the spectral modulations in the output signal increased with pulse energy. Nevertheless, no influence of the pulse energy on the modulation period (~ 1 nm) and the position of the resulting maxima were observed (fig.6.2.2). Furthermore, slight spectral modulations were already observed after the fiber stretcher (fig. 6.1.5), which were caused by SPM in the stretcher-fiber. However, the modulations in the output spectra were not attributable to the fiber stretcher, since the modulations in the output spectra and in the spectra after the fiber-stretcher had different modulation periods (left diagram in figure 6.3.1).
Potentially, such modulations with a period of 1 nm can be generated or initiated by an etalon with an optical length of about 1.2 mm in the amplifier set-up. However, for the modulators and the optical isolators an optical return loss of more than 40 dB was specified and a replacement of these components showed no influence on these modulations. Thus, the modulations were not attributable to etalon effects in these elements. The remaining amplifier set-up included no (sub-) elements or spacings with an optical length of about 1.2 mm and replacements of the various other fiber optic components (gain fiber, WDM-coupler, FC-APC connectors) showed also no influence on the modulations. Therefore, the spectral modulations were not attributable to an etalon in the amplifier set-up.

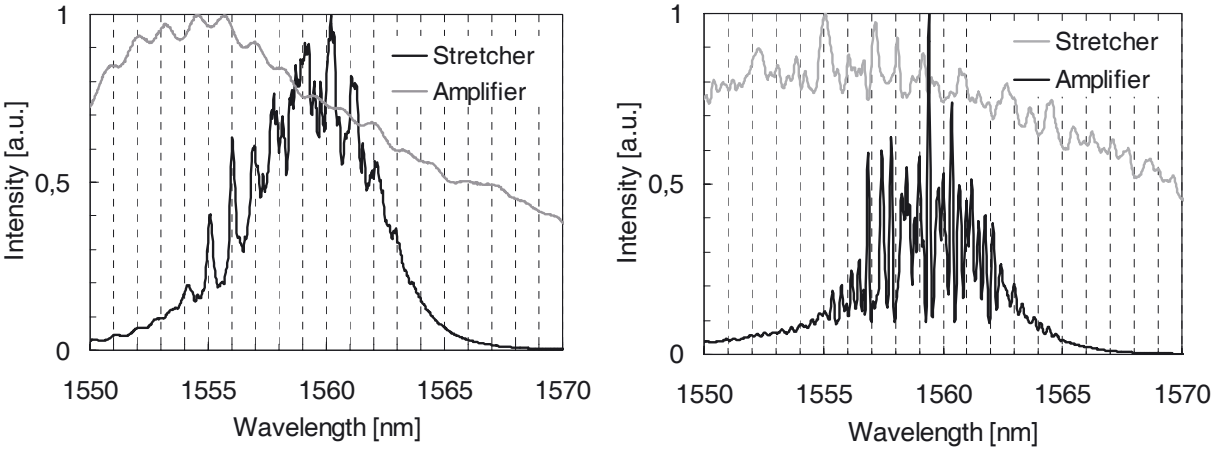

Fig. 6.3.1 *Spectra after the stretcher and after the power amplifier for 2.9 µJ pulse energy at 200 kHz. Left diagram: Stretcher dispersion: -70 ps/nm. Right diagram: Stretcher dispersion: -160 ps/nm.*

The spectral modulations were also not caused by mode beating between the two polarizations modes in the coiled gain-fiber, as the positions of the maxima in the spectra were not influenced by the polarization controller before the coiled fiber. Moreover, calculations showed that this would require a birefringence of about $2.9 \cdot 10^{-4}$, even if the total gain-fiber length of 8.3 m were taken into account. This value is about two orders of magnitude larger than the birefringence of the gain-fiber, even if the fiber core is elliptically shaped (which is likely due to the high doping concentration) and if the coiling of the gain-fiber is taken into account [AGR95][URE80]. Furthermore, a replacement of the Er^{3+}-fibers in the three amplifier stages by other fibers with different core parameters showed also no significant influence on the position of the peaks. Thus, these modulations were not influenced by the specific core-structure of the Er^{3+}-fiber.

In order to determine the influence of the pulse stretching on these modulations, the dispersive fiber in the stretcher was replayed by another normal dispersive fiber. By this way, the dispersive pulse stretching for the double pass arrangement was increased from -70 ps/nm to -160 ps/nm. For both set-ups, the spectra after the stretcher and behind the power-amplifier are shown in the right diagram of figure 6.3.1. It can be seen, that after the stretcher the modulation period remained nearly constant, although the modulation amplitude was larger for the -160 ps/nm stretcher. Conversely, the increase of the pulse stretching by a factor of 2.3 resulted in a similar decrease of the modulation period in the amplifier output spectrum. Thus, independent of the dispersive pulse stretching, the time separation between the spectral peaks on the chirped pulse was about 70 ps, which can be calculated from the modulation period and the dispersive pulse stretching (e.g. ~ 1 nm period for the -70 ps/nm stretcher).

Furthermore, it is noticeable from the output spectra, as well as from the spectra of the intermediate amplifier stages, that the amplitude of the spectral modulations increased with de-

creasing wavelength over the spectral bandwidth of the signal (e.g. fig. 6.1.8, 6.2.2, 6.2.3, 6.3.1). In combination with the previous mentioned results, this indicates that these modulations are attributable to some resonance effect with a frequency of about 14 GHz (≈ 70 ps) in the amplifier-chain, which is stimulated by the optical pulse.

Probably, such a resonance is not due to the passive fiber material, as silica fibers were excessively investigated and no report of such a resonance was found in the literature. Nevertheless, it should be noted, the resonance frequency of about 14 GHz corresponds roughly to the frequency shift of the SBS in silica fiber. Moreover, the delayed response of the SRS is roughly the inverse of the SRS frequency shift [AGR95]. For that reason, a nonlinear response due to the SBS, which is delayed roughly by the inverse of the SBS frequency shift, can be supposed. Principally, the influence of the SBS on the refractive index can be calculated based on the SBS gain spectrum by using the Kramers-Kronig relation. A Fourier-transformation of the resulting function provides then the temporal response function of the SBS.

The $LiNO_3$ based Mach-Zehnder was only specified for frequencies of up to 2.5 GHz. Additionally, the operation characteristics of this element were most likely not tested for the high peak intensities in this amplifier system (~ 10 W after the preamplifier), as the modulator was designed for telecommunication application. Consequently, the modulators were a potential source for the spectral modulations. However, the observed modulations after the first modulator were similar to the modulations after the fiber stretcher. Additionally, the second modulator showed no influence on the positions of the maxima in the spectrum, which was confirmed by spectral measurements before and after the second modulator. Moreover, similar spectral modulations were previously observed in an Yb^{3+}-fiber-CPA-system, where the repetition rate was reduced by two acousto-optic modulators [LLZ01]. However, the origin of these modulations was not described in this publication. Nevertheless, this result is a further indication that the modulations were not caused by the $LiNO_3$ based Mach-Zehnder modulators.

A potential source for the spectral modulations is the gain material. The gain and the refractive index are strongly influenced by the population distribution over the various sub-levels of the laser levels, as they correspond to optical resonances close to the signal wavelengths. Moreover, transitions between the various sub-levels were initiated by the energy extraction during pulse amplification. Eventually, the transitions between the different sub-levels have the same time scale as the observed modulations (70 ps for the Er^{3+}-CPA-system). However, additional investigations and experiments are required for an identification of the detailed mechanism for the observed spectral modulations and possible countermeasures.

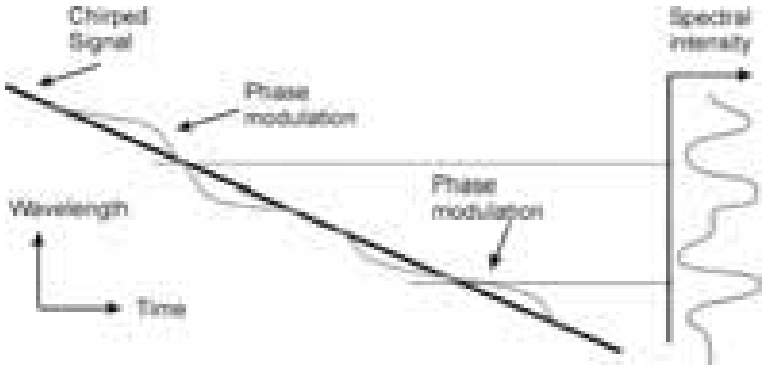

Fig. 6.3.2 *Influence of a phase modulation on the signal spectrum of a chirped pulse. The black line shows the initial pulse while the grey line shows the phase-modulated signal. At the right, the resulting pulse spectrum is plotted, assuming constant intensity along the chirped pulse.*

The observed spectral modulations in the output signal can be generated by amplitude modulations or by phase modulations along the chirped pulse. While the effect of an amplitude modulation on the output spectrum is quite obvious, the influence of a phase modulation on the output spectrum of the highly stretched pulse is illustrated in figure 6.3.2. It can be seen, that it causes variations of pulse chirp and this results in intensity variations in the pulse spectrum, even if the intensity distribution along the chirped pulse remains constant. Additionally, initial amplitude modulations result also in variations of the initial chirp due to the SPM in the fiber (section 2.2.2).

Moreover it should be mentioned, that initial phase or amplitude fluctuations could evolve into grey or even black solitons, due to the high signal intensity of the amplified pulse in the normal dispersive fiber [AGR95]. Such solitons correspond to an intensity dip in an uniform background and have the inverse shape of a conventional soliton, as the opposite dispersion is compensated by an inverse intensity distribution. In combination with the high intensities in the gain fiber it can be expected, that initial disturbances evolve into grey or dark solitons. Furthermore, it is worth to mention, that the spectral wings of a (positive or negative) sech^2 shaped pulse show a nearly linear shape in a logarithmic plot of the spectrum. Such a linear shape was observed at high pulse energies on the long wavelength side of the output spectrum and was not attributable to the Er^{3+}-gain spectrum. Hence, this indicates, that the pulse dynamics in the amplifier is affected by such dark soliton effects under these operation conditions. The increase of the spectral modulations with pulse energy may be also attributable to such effects. In order to reduce these soliton effects in the last amplifier stage a fiber with a large mode field diameter and a short fiber length should be preferred.

6.3.2 Nonlinear dispersion

The autocorrelation measurements showed that the required anomalous compressor dispersion changed by up to $-4 \cdot 10^6$ fs² as the output pulse energy of the amplifier was increased by about 6 µJ (fig. 6.2.7). Calculation showed that this effect could not be attributable to the increase of the average wavelength with increasing pulse energy, as this would require an uncompensated TOD of about $3 \cdot 10^9$ fs^3. Such a large uncompensated TOD could be excluded from the system set-up as well as from the measured autocorrelation traces. The variation of the required compressor dispersion with increasing pulse energy indicated that the normal chirp of the amplified pulse was decreased by nonlinear effects. This could not be caused by SPM, as SPM generates an additional positive chirp (section 2.2.2).

The refractive index and the dispersion of Er^{3+}-doped fibers depend significantly on the inversion, as the Er^{3+}-ions have optical transitions close to the signal wavelength (section 2.4.2). Thus, the decrease of the Er^{3+}-inversion during pulse amplification results in a change of the refractive index and the GVD of the gain fiber. Both effects influence the pulse chirp as they influence the relative propagation velocity along the chirped pulse. It was calculated, that for a 6 µJ output pulse the observed pulse energy dependent dispersion effect would correspond to a nonlinear GVD of about 1000 fs/(nm·m) or a decrease of the refractive index by about $3 \cdot 10^{-4}$/nm at the signal wavelength during pulse amplification.

Computations of these effects for the used Er^{3+}-fiber, according to reference [HBU96], resulted in a decrease of the refractive index by about $5 \cdot 10^{-6}$ per nm along the central pulse and a change of the GVD by -0.6 fs/(nm·m) for a 6 µJ pulse. The energy extraction of such an output pulse correspond to stimulated emissions of about 3% of the Er^{3+}-ions in the second power-amplifier stage. Hence, the calculated nonlinear dispersion due to the refractive index change is about one order magnitude and the calculated GVD effect is about three orders of magnitude below the observed effect. Besides, a nonlinear anomalous GVD which is much higher than the normal GVD of the fiber (-22 fs/(nm·m)) would result in modulation instabilities in combination with the high signal intensities in the gain-fiber. However, such modulation instabilities were not indicated by the output spectrum. Thus, the nonlinear dispersion is most likely not attributable to GVD changes during pulse amplification. This leads to the conclusion, that the nonlinear refractive index change in the Er^{3+}-fiber was much higher than calculated.

The above used equations from reference [HBU96] made implicitly the assumption that the population distribution within each laser level is in thermal equilibrium. However, the large

energy extraction of the about 0.5 ns long pulse may cause large deviations from the thermal equilibrium within the energy levels. Furthermore, laser emission at the signal wavelength of about 1.56 µm terminates above the lowest energy level of the ground state. Hence, the energy extraction may result in a large overpopulation of this sublevel during pulse amplification, relative to the thermal equilibrium. In addition, the previous mentioned equations showed a much larger influence of the Er^{3+}-inversion on the refractive index at about 1.53 µm, which corresponds to absorption or emission from or to the lowest ground state sublevel (section 2.4.2; fig.2.4.6). This resonance must occur at longer wavelengths if the sublevel above the lowest ground state becomes populated. Thus, deviations of the population distribution within each laser level from thermal equilibrium may cause a much larger refractive index change during pulse amplification than previously calculated.

Besides that, due to the high signal intensity and the high doping concentration of the gain fiber, exited state absorption, two-photon absorption and cooperative upconversion effects can potentially result in a population of higher Er^{3+} energy levels. A population of energy levels above the upper pump level was indicated by a green fluorescence of the fiber. As the power-amplifier showed an efficiency of about 40%, the energy of about 50% of the pump photons can potentially be transferred, directly or indirectly, to higher energy levels. The influence of these energy levels on the refractive index was also not included in previous calculations, although even small populations of higher energy levels can significantly influence the refractive index [AES03][AEA98]. Hence, the detailed mechanism, which causes the large nonlinear dispersion, and the contribution of the previous mentioned effects, must be cleared up by additional experiments.

For optimal pulse compression, the amplifier system must be operated at constant pulse power level, because of the described nonlinear dispersion effect. Alternatively, variations of the output pulse energy of the amplifier require a simultaneous adaptation of the compressor length. Thus, it may be advantageous to operate the amplifier at the maximum required output pulse energy level and to realize lower pulse energies by attenuation of the output signal.

6.3.3 Four-wave mixing

During initial experiments, the two power amplifier stages were pumped in the forward direction in order to achieve minimum amplifier noise. However, in combination with higher output pulse energies the build up of additional peaks at about 1534 nm and 1584 nm were observed in the output spectrum of both power-amplifier stages. The build up of these peaks with increasing pulse energy is shown in the left diagram of figure 6.3.3 for the output signal

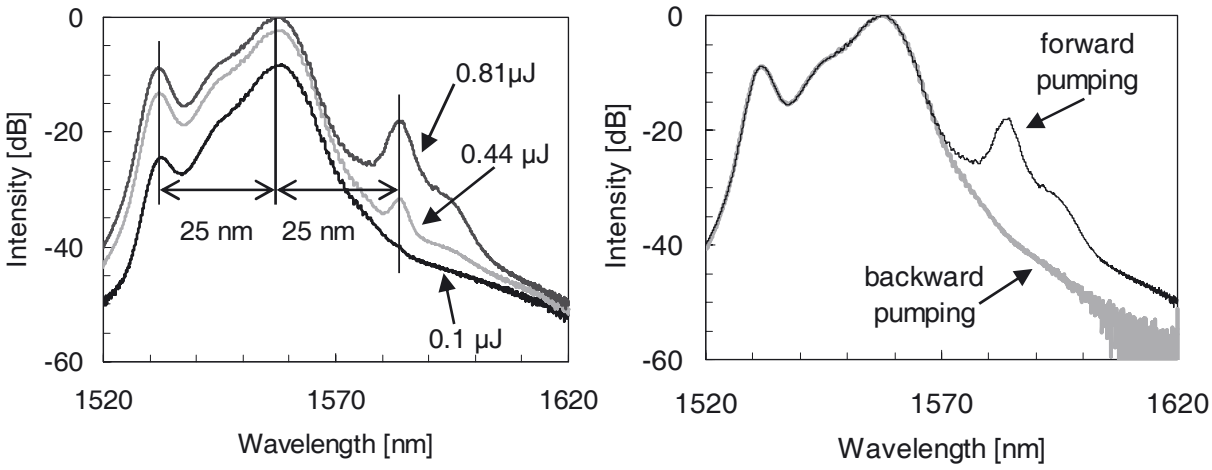

Fig. 6.3.3 *Influence of the pump direction on four-wave-mixing effects. Left diagram: Output spectra of the first power-amplifier stage, pumped in forward direction, for pulse energies between 0.1 µJ and 0.81 µJ .The four-wave mixing is indicated by the vertical lines and the two horizontal arrows. Right diagram: Influence of the pump direction on the output spectra of the first power-amplifier stage measured for an output pulse energy of 0.8 µJ. All spectra were measured at a repetition rate of 100 kHz.*

of the first power amplifier stage. The gain peak at 1534 nm is characteristic for highly inverted fiber and decreased due to signal reabsorption if the gain fiber length was increased. Variations of the input spectrum from the preamplifier showed, that for constant output pulse energy, a higher 1534 nm peak resulted also in an increase of the 1584 nm peak. Both peaks were symmetrically located relative to the center wavelength of the output pulses. Furthermore, the 1584 nm signal peak cannot be attributed to the Er^{3+}-gain spectrum. Therefore the experimental results strongly indicated that the peak at 1584 nm was generated by four-wave-mixing (FWM) between the main signal and the signal intensity at 1534 nm.

Further experiments showed, that the 1584 nm peak and therefore FWM were strongly reduced, if the amplifier was pumped in the backward direction. This can be seen in the right diagram of figure 6.3.3, where the output spectra of the first power-amplifier stage are shown for both pump directions. Both spectra were measured for an output pulse energy of 0.8 µJ and with the same amplifier components. The observed strong reduction of FWM for backward pumping was despite of the fact that for this set-up the amplified signal had to pass the fiber sections in the WDM-coupler. Measurements of the transmission curve of the 1480/1550 nm WDM-coupler additionally confirmed that the suppression of the 1584 nm peak was not attributable to this coupler.

Furthermore, by variation of the gain fiber length in the preamplifier, the relative signal intensity of the 1534 nm gain peak in the input signal was changed. These experiments showed that FWM results in the build up of a long wavelength signal peak even for backward pumping, if the signal intensity at 1534 nm in the input signal was not sufficiently suppressed.

It should be noted, that during these initial experiments a 1.6 m long Er^{3+}-fiber with a mode field diameter of 5.5 µm (at 1550 nm), an absorption of 77.5 dB/m (at 1530 nm) and a calculated dispersion of about -10 fs/(nm·m) was employed [LIE03d]. For this fiber, a FWM coherence length of about 50 m was calculated (eqs. 2.2.8). Thus, FWM phase matching remains nearly unchanged along the power-amplifier. For the gain fiber in the final power-amplifier set-up, with a dispersion of -22 fs/(nm·m) (section 6.1.5), a FWM coherence length of 23 m was calculated for the previous mentioned FWM process. Thus, also for this gain fiber the FWM phase matching remains nearly constant along the power-amplifier.

FWM cannot occur between the intensity of the signal pulses at 1534 nm and 1559 nm, since these pulses were highly chirped. Hence, the observed FWM must occur between the main signal and the amplified spontaneous emission of the Er^{3+}-gain fibers at 1534 nm. Furthermore, measurements of the output spectra as a function of the repetition rate for constant pulse energy had shown that the ASE made a significant contribution to the signal intensity as 1534 nm (section 6.1.5). Consequently, the two side peaks are not phase matched relative to the chirp of the initial pulse and suppression of the FWM is highly desirable.

The mechanism, which caused the observed influence of the pump direction on FWM, was further investigated by calculating the signal amplification along the gain-fiber. These calculations were carried out by means of the commercial OASIX software, which was developed for telecommunication Er^{3+}-amplifier [LUE99]. By this way, the evolution of the main signal at 1557 nm as well as of the short wavelength peak at 1532 nm along an Er^{3+}-gain fiber was simulated for both pump directions. It should be mentioned, that in these simulations the short wavelength peak was located at 1532 nm, while it was observed at 1534 nm in the employed gain fiber.

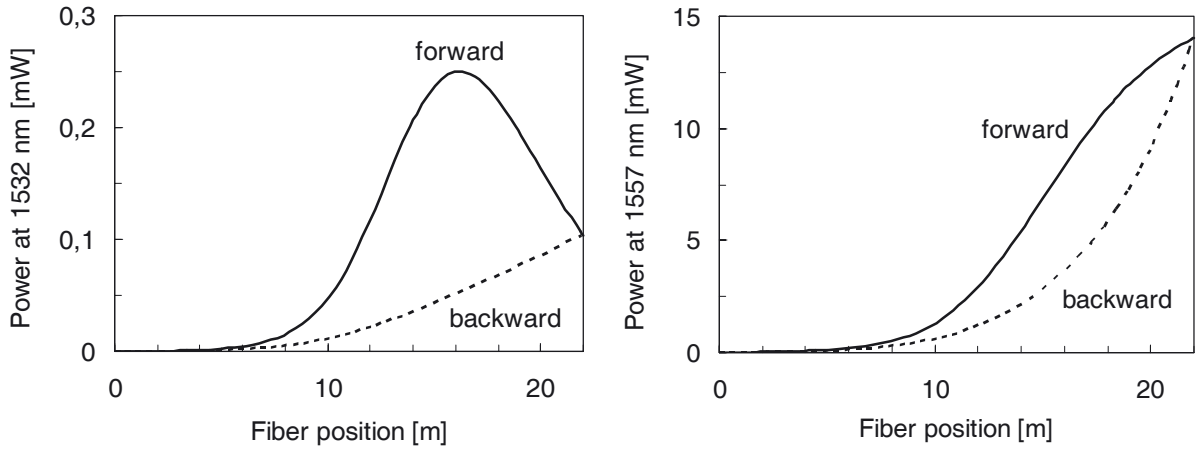

Fig. 6.3.4 *Calculated evolution of the signal power at 1532 nm and 1557 nm along the OFS Er^{3+}-gain fiber MP980 [OFS03c] for forward and backward pumping at 1480 nm. For these calculations, based on the OASIX 3.1 software [LUC99], input powers of 0.1 µW at 1532 nm and 10 µW at 1557 nm were assumed. A fiber length of 22 m was chosen, as the specified absorption was about 13 times lower than the gain fiber in the power-amplifier. For both pump directions, the pump power was adjusted for a gain of 31.5 dB at 1557 nm.*

For both wavelengths, the computed signal evolution is displayed in figure 6.3.4 for forward and for backward pumping. It can be seen that inside the Er^{3+}-fiber the signal power of the 1532 nm signal becomes much higher for forward pumping, even if the output signal power was the same as for backward pumping. As the coherence length for FWM is much longer than the gain fiber length, the FWM efficiency is proportional to the intensity at the signal wavelength and the short wavelength gain peak, integrated over the gain-fiber length. Since for backward pumping the signal intensity at 1534 nm is lower along the gain fiber than for backward pumping, the FWM efficiency is also much lower for forward pumping. Furthermore, due to the previous mentioned relation, the influence of the FWM on the signal becomes larger, even for constant output pulse energy, as the signal intensity at 1534 nm increases. This agrees with the observed FWM effects even for the backward pumping scheme in combination with a high input signal intensity at 1534 nm.

Based on the previous described results, the backward pumping scheme was used in the power-amplifier. Moreover, the Er^{3+}-fiber lengths, especially in the preamplifier, were adjusted for a suppression of the signal build up at 1534 nm. However, an increase of the gain fiber length improves the suppression of the 1534 nm gain peak, but reduces also the gain bandwidth due to the increased signal reabsorption. Additionally, the FWM increases also with the gain fiber length, as the FWM coherence length is much larger than the gain-fiber length. Thus, for the fiber amplifiers the shortest gain-fiber lengths were chosen, which enabled a sufficient suppression of the 1534 nm signal intensity. In addition, the threshold for significant FWM can be further increased by increasing the effective area of the (gain) fibers and by suppression the short wavelength gain peak with additional spectral selective elements (coupler, absorber, filter).

6.3.4 Gain saturation

Previous described measurements indicated that the output pulse energy of the oscillator-amplifier system was limited to about 7 µJ by nonlinear effects (fig. 6.2.1). The limiting mechanism was further investigated by increasing the dispersive pulse stretching of the stretcher from -70 ps/nm to -160 ps/nm (see section 6.3.1). By this way, the pulse duration was increased and consequently, the signal intensity in the fiber was reduced. Nevertheless, the same limitation for the output pulse energy was observed (fig. 6.3.5). This pointed out, that the nonlinear pulse energy limitation was not attributable to the high signal intensity in the gain-fiber.

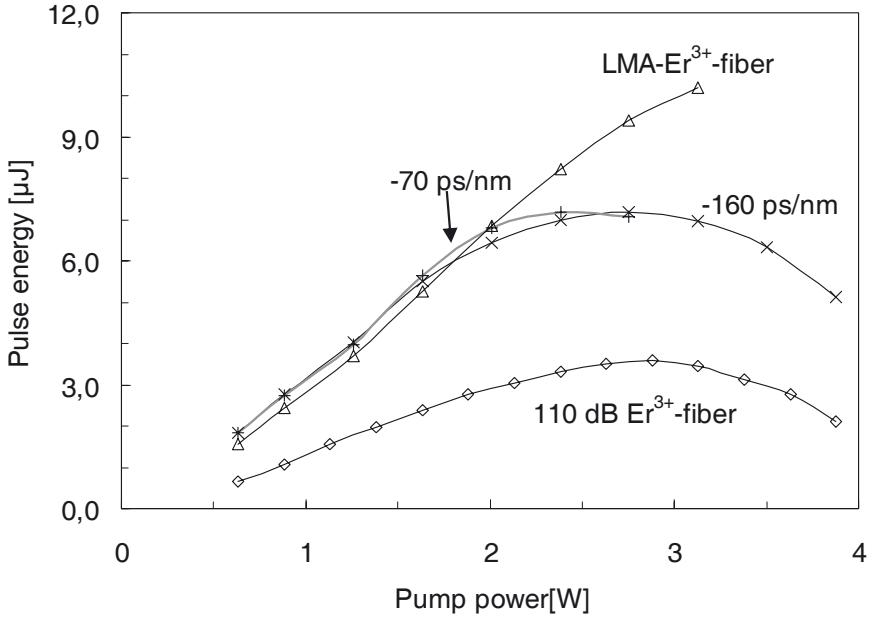

Fig. 6.3.5 *Pulse energies after the power amplifier versus amplifier pump power. The diagram shows these data for the power amplifier set-up described in section 6.1.5 in combination with a -70 ps/nm and a -160 ps/nm fiber stretcher. In addition the output pulse energies were displayed which incorporated an 1.3 m long highly doped Er^{3+}-fiber (peak absorption: 110 dB at1530 nm) [LIE03c] or a combination of 2.5 m long large-mode-area Er^{3+}-fiber and 1.5 m conventional Er^{3+}-fiber in the power-amplifier (fiber stretcher: -70 ps/nm). These pulse energies were measured at a repetition rate of 100 kHz, except for the 110 dB-fiber, where a repetition rate of 300 kHz was applied because of the lower pulse energy limit.*

Furthermore, the gain-fiber in the final power amplifier stage was replaced by a 1.3 m long highly doped Er^{3+}-fiber (1300 ppm mol Er_2O_3) with a mode field diameter of 5.4 µm and a peak absorption of 110 dB (1530 nm) [LIE03c]. The length of this gain fiber was adjusted for similar output spectra (1534 nm gain peak) as for the conventional power-amplifier set-up. Despite of the about larger 80% larger mode field area of this fiber, the output pulse energy was limited to 3.6 µJ (pulse stretching: -70 ps/nm), which was about two times lower than for the standard power-amplifier set-up.

Based on the specifications, a total Er^{3+}-ion number of $1.9 \cdot 10^{15}$ and $7.2 \cdot 10^{14}$, respectively, were calculated for the conventional and the 110 dB gain fiber in the power-amplifier. This indicated that the pulse energy limitation was caused by gain saturation effects, as the maximum output pulse energy was roughly proportional to the number of Er^{3+}-ion in the gain-fiber. For both Er^{3+}-fibers, the maximum output pulse energies corresponded to stimulated emissions of about 3% of the Er^{3+}-ions. However, the actual emission rate could be higher than calculated, as fiber losses and signal reabsorption were neglected in these calculations. It is also worth to mention, that an energy extraction from about 10% of the Er^{3+}-ions during pulse amplification where previously reported for an Er^{3+}-doped fiber amplifier with 1 ns output pulses [TRD97]. However, this amplifier was pumped at 980 nm, which enabled a

higher inversion, and operated at the narrow gain peak at 1.53 µm, where the Er^{3+}-ions have a larger emission-cross section.

In order to overcome the pulse energy limitation, a new Er^{3+}-fiber was also designed with an increased mode field diameter of about 26 µm², but with roughly the same fiber dispersion and active core as the initial used Er^{3+}-fiber. A larger mode field-diameter was preferred as nonlinear effects in the gain fiber (e.g. SPM, FWM) were reduced with increasing mode field diameter. This new fiber structure, with an additional passive refractive index structure around the active core, was developed based on the computation scheme described in appendix A.

This large-mode-area fiber showed a much lower pump absorption due to the reduced overlap between the active core and the pump light distribution. For that reason, a combination of 2.5 m of this large-mode-area (LMA) fiber and 1.5 m of the initial Er^{3+}-fiber were spliced into the second stage of the power amplifier. The LMA fiber was orientated to the output, in order to minimize nonlinear effects. Since both fibers had the same active core structure, the Er^{3+}-ion number was increased by about 50%, compared to the initial set-up.

This modified amplifier set-up showed a similar slope efficiency as for the conventional gain fiber and emitted output pulse energies of up to 10 µJ, without significant gain saturation effects were (fig. 6.3.5). A further increase of the output pulse energy was avoided by end facet destructions at the power-amplifier output (see section 6.3.5). Additionally, an optimization and a reliable rearrangement of this new fiber set-up was not possible, since, due to a fabrication defect, the LMA-fiber had a large eccentric core (~ 5 µm), which resulted typically in large splicing losses (> 3 dB). Nevertheless, these results show that the pulse energy limitations can largely be overcome by specially designed gain fibers and adopted amplifier set-ups, which enable a higher Er^{3+}-ion number in the final amplifier stage.

Qualitatively, the previous described saturation of the output pulse energy was predicted by standard amplifier theory [AGR95]. However, it was not predicted by this theory and therefore completely unexpected, that a further increase of the pump power resulted in a decrease of the amplifier output power and the output pulse energy. In this pump power range, above the maximum output pulse energy, it was noticed from the output spectra, that the ASE intensity at 1534 nm increased with pump power. Furthermore, measurements of the remaining pump power after the gain-fiber showed that the pump power absorption decreased with increasing pump power. Occasionally, even laser emission at 1534 nm was observed in this pump power range. These observations pointed out, that the inversion and therefore the also

the amplification at the signal wavelength increased further with growing pump power [MNC97].

The observed decrease was not attributable to two-photon absorption, as it was not influenced by the fiber stretching and the peak signal intensity, respectively. It was also not caused by homogeneous upconversion, as the influence of this effect on the output signal decreases with growing pump and signal power [NHA03]. However, the decrease of the output power with growing pump power must be related to high pulse energies or a high inversion, since it was not observed at higher repetition rates with lower output pulse energies or for a cw input signal.

One possible mechanism for this output power decrease is an increased signal absorption due to a growing population of exited states, above the upper laser level. It is well known, that Er^{3+}-ions can be exited from the upper laser level $^4I_{13/2}$ to the $^4I_{9/2}$ level by pair induced up-conversion [MIN91] (see fig. 2.4.4). As the energy gap for this transition corresponds roughly to the photon energy of the laser signal, such transitions may be also initiated by high intensity signals. Additionally, calculations pointed out, that the energy difference between $^4I_{9/2}$ level and the $^4S_{3/2}$ level is quite similar to the photon energy of the signal. Therefore, a population of the $^4I_{9/2}$ may result in a strong exited state absorption (ESA) at the signal wavelength. A strong indication for such transition is the relatively bright green fluorescence of the Er^{3+}-fiber that was observed for high output pulse energies and indicated a population of the $^4S_{3/2}$ level. Normally ESA from the $^4I_{9/2}$ level can be neglected, because in silica fibers the population of this energy level is quite low, due to the short nonradiative lifetime of about 20 ns (eqs. 2.4.1; fig. 2.4.4). However, the duration of the amplified pulses is much smaller than this nonradiative decay time. For that reason, the population of this level, generated by exited state absorption, is accumulated over the pulse duration, which can result in additional exited state absorption effects.

The previous described mechanism would explain the observed output power decrease at high pump power levels in combination with high pulse energies. However, it must be further investigated experimentally and theoretically, if the observed effects are actually attributable to the proposed mechanism.

6.3.5 Fiber surface damages

For pulse energies above about 10 µJ in combination with a repetition rate of 100 kHz, a destruction of the end facet of the FC/APC connector at the output of the power amplifier was observed. Such a destructed end facet is shown in figure 6.3.6. Experimentally, this end facet

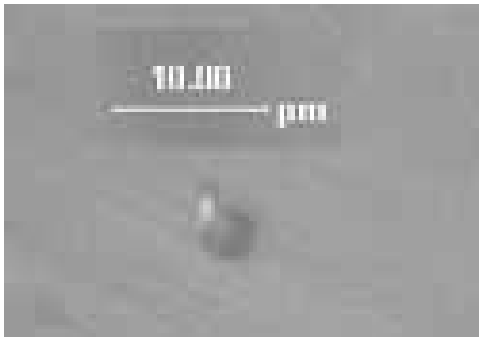

Fig.6.3.6 *End faced of the FC/APC connector of the power amplifier output after transmission of 10 µJ pulses. The damaged area in the center of the fiber core had a diameter of about 3 µm and was therefore significantly smaller than the mode field diameter of 8 µm.*

destruction was indicated by a drop of the output power behind the collimating lens by about 18%. This power drop occurred after about one minute operation with the above mentioned parameters. This damaged end facet showed a circular hole of about 3 µm diameter in the center of the core area with an extension at one side. The lower depth of this extension is an indication that it is a secondary effect of the initial hole formation. In the fiber, the signal intensity usually decreases from the center of the core to the cladding because of the mode field distribution (fig. 2.1.2). Hence, the hole diameter of 3 µm, which was much smaller than the mode field diameter of about 8 µm, indicates, that only in the central core area the signal intensity was above the damage threshold of the fiber surface.

A pulse energy of 10 µJ results in a pulse energy density 20 J/cm² at the output facet of this fiber with a mode field diameter of 50 µm². In the center of this single-mode fiber the energy density is even higher, due to the mode field distribution (fig. 2.1.2). Furthermore, the output pulses were about 0.5 ns long, as they were initially stretched by -70 ps/nm and had a spectral bandwidth of 7 - 8 nm. Thus, the output pulse energies were roughly at the damage threshold for silica glass, since a damage threshold of about 50 J/cm² is mentioned in the literature for this material [RWD97]. The latter was determined for 15 ns pulses at 1064 nm. Therefore, the lower observed damage threshold may be attributable to the shorter pulse duration. To some extent the damage threshold is also influenced by the surface quality of the fiber end, since in general surface damage formation starts from surface defects [GNA02][DSK02][RWD97]. Inspections by a microscope showed, that machine polishing resulted in a better surface quality than the previous used hand polishing. Thus, machine polishing may slightly increase the damage threshold. However, this requires further statistical investigations.

By splicing a short length of a coreless fiber onto the fiber end, the limitations by the surface damage threshold can be largely overcome, as the resulting beam width expansion in the coreless fiber reduces the intensity at the end surface.

6.4 Conclusion and outlook

The experiments showed, that femtosecond pulses with several µJ pulse energy and with variable repetition rates of several 100 kHz could be generated by a modular chirped-pulse Er^{3+}-fiber oscillator-amplifier system.

It was detected, that nonlinear polarization effects affected the signal polarization in the power amplifier. These were reduced by a coiling of the gain-fiber in combination with a polarization adjustment. However, these effects can be eliminated by polarization maintaining fibers. Therefore, the use of such fiber components is highly preferable, especially in the power amplifier. This would also simplify the adjustment of the amplifier system.

Fourier-transformations of the output spectra revealed that the output pulse duration was limited by the transmission bandwidth of the grating compressor. These computations also indicated that the minimum pulse duration could be reduced by about 35%, if the compressor transmission bandwidth is increased from 12 nm to 20 nm. This can be accomplished by incorporating a larger grating into the compressor. Furthermore, the use of a single grating in combination with retro-reflecting prism would simplify the compressor adjustment and avoid a spatial chirp on the compressed output signal.

Alternatively, the grating compressor can eventually be replaced by an air-guiding photonic bandgap fiber [MTH03][LSN03]. This would enable an extremely compact compressor set-up with no free beam alignment in combination with a large transmission bandwidth. However, it must be investigated, if the high peak power of compressed µJ pulses causes large nonlinear effects in these fibers. Furthermore, for (nearly) bandwidth limited output pulses, in such a modified set-up an adoption of the dispersion slope of the fiber stretcher to the bandgap fiber in the compressor is required. Such an adoption can be achieved by combining different fibers in the fiber stretcher or by specially adopted refractive index structures for the stretcher fiber.

The output signal had only a bandwidth of about 8 nm due to the gain narrowing by the Er^{3+}-fiber amplifiers. On the other hand, much broader gain bandwidths were demonstrated for Er^{3+}-amplifiers. However, the required suppression of the narrow gain peak at 1534 nm determined largely the Er^{3+}-fiber lengths and consequently the gain spectrum of these active fibers. Hence, a suppression of the 1534 nm gain peak by additional elements would enable an optimization of the gain-fiber length for larger gain bandwidths and therefore a reduction of the gain narrowing in the Er^{3+}-fibers. Such a suppression of the 1534 nm signal can be achieved even without additional elements by replacing the 1480/1550 nm WDM-couplers, for insertion of the pump light, by WDM-couplers with a transmission period of about 54 nm

(maximum coupling at 1480 nm and 1534 nm). Moreover, the gain bandwidth can be further increased by incorporating additional gain flattening filters into the fiber amplifier [YOO98]. By this way, the spectral bandwidth of the output signal can be increased, which enables even shorter pulse widths. A broader spectral bandwidth would also reduce the signal intensity in the fiber and therefore reduce nonlinear effects due to the dispersive pulse stretching.

Initial experiments had shown that the maximum pulse energy could be further increased by special adopted fiber designs. Moreover, numerical simulations based on the calculation scheme described in appendix A pointed out, that the mode field area of the gain fiber could be increased at least by a factor of three, while maintaining single-mode operation and normal dispersion at the signal wavelengths. The resulting refractive index structures consisted of a high index core and a high index ring, which were separated by a ring with a lower refractive index. Furthermore, these simulations pointed out, that by doping the inner core, the high refractive index ring with Er^{3+}-ions, a good overlap between signal mode and doping distribution could be achieved. Simultaneously the Er^{3+}-ion number per fiber length can be increased several times. Hence, a corresponding further increase of the maximum output pulse energy can be expected in combination with such gain-fibers, as the pulse energy limitation was attributable to the limited Er^{3+}-ion number and to nonlinear effects in the gain fiber.

Finally, it should be mentioned, that in combination with a nonlinear crystal the output wavelength of this oscillator-amplifier system would match the signal wavelength of conventional Ti:sapphire lasers. Therefore, the incorporation of such a nonlinear crystal into the set-up is advantageous for numerous applications.

7 Summary and outlook

Rare-earth-doped silica fibers are well suited for the generation and amplification of pulsed laser radiation, as their broad gain bandwidth enables the generation of ultrashort pulses as well as broadband and widely tunable laser emission. However, the large variety of applications requires an adaptation of laser parameters like spectral bandwidth, pulse duration and pulse energy. Therefore, the objective of this work was to develop and investigate the variety of laser parameters, which can be realized by pulsed fiber-lasers. For that reason, three different basic set-ups were realized and characterized: a wavelength tunable Q-switched Ytterbium fiber laser for the generation of narrow-linewidth microsecond pulses, a mode-locked Ytterbium fiber laser for generation of broad bandwidth signals and an oscillator-amplifier system based on Erbium doped fibers which was capable to generate ultrashort pulses with high pulse energies.

In this work, Q-switching of a Ytterbium double-clad fiber laser by Thulium codoping was demonstrated for the first time. The Thulium-codoping acted as a saturable absorber, and initiated and supported thus pulsed laser operation. Furthermore, it was noticed, that the repetition rate and the temporal dynamics were determined by relaxation oscillations, which were maintained by the saturable absorption of the Thulium ions. Based on the corresponding equations, the laser set-up could be precisely optimized to the specific requirements on pulse duration and repetition rate of various applications.

The realized fiber laser system showed a maximum output power of 2.4 W, a maximum repetition rate of 140 kHz, a maximum pulse energy of 21.8 µJ and a minimum pulse duration of 1.1 µs. Tunable (1055 nm – 1090 nm) and narrow linewidth (0.17 GHz – 4 GHz) operation was realized by inserting a grating pair in Littman-Littrow configuration into the ring-cavity. The spectral linewidth increased with fiber length and pulse energy and it was revealed that this broadening was attributable to four-wave-mixing in the optical fiber. Hence, the laser linewidth can be further reduced by the use of short fibers with high doping concentrations and a large mode field diameter. Based on the observed power dependence of the laser linewidth and the dominant broadening in the gain fiber by the FWM, it could be predicted, that the laser linewidth of high energy pulses can be minimized by reducing the intra-cavity intensity and using a fiber power-amplifier at the output. Such a set-up should enable additionally an independent variation of the repetition rate and the pulse energy.

The laser source is especially promising for the pumping of optical parametric oscillator for the generation of mid-infrared radiation. Due to the narrow linewidth and the wavelength tunability of this pump source, the generated mid-infrared radiation is well suited for chemical and environmental sensing. Additionally, this laser system provides the required peak power for the nonlinear frequency conversion due to the pulsed operation.

A mode-locked Ytterbium fiber laser was developed, since this pulse generation mechanism enables much shorter pulse durations and much broader spectral bandwidths than Q-switched laser set-ups. Up to now the output power of such laser systems was rather limited, because of direct pumping into the active core. Therefore, a mode-locked fiber laser with a long cladding-pumped Ytterbium fiber in the cavity was shown for the first time, in this work. It was passively mode-locked by nonlinear polarization rotation and emitted pulses with up to 9.5 nJ pulse energy and 40 nm spectral bandwidth at a repetition rate of 7.6 MHz in combination with a single mode beam quality. There was an upper pulse energy limit that was attributable to the mode-locking mechanism. Therefore, at higher pump powers, multiple closely spaced pulses were circulating in the cavity. Compensation of the normal fiber dispersion was enabled by a dispersive grating pair in the cavity. The influence of the grating dispersion on laser operation was investigated in detail. It was shown that laser operation was quite insensitive to the overall cavity dispersion, while temporal compression of the output pulses was limited by the large uncompensated third order dispersion in the cavity.

Because of new progress in fiber technology, highly doped double-clad Yb^{3+}-fibers with large active core diameters and low numerical apertures have become available. Hence, even in combination with cladding pumping, the cavity length and consequently the uncompensated TOD can be strongly reduced, since the increased active-core diameter strongly improves the pump light absorption (up to 11 dB/m at 975 nm, e.g. [LIE03][NUF03]). For such a modified set-up, much shorter output pulses can be expected in combination with standard compression schemes, as the temporal compression was strongly limited by the large uncompensated TOD in the cavity. Moreover, the much larger mode field area of these fibers strongly reduces nonlinear effects. Thus, a further increase of the maximum output pulse energy can be expected. Additionally, the use of such short gain fibers shifts the gain maximum from about 1.1 µm to shorter wavelengths. Such a wavelength shift is required for seeding of Yb^{3+}:YAG based amplifiers, which provide gain at about 1.035 µm.

Furthermore, photonic crystal fibers (PCF) with anomalous dispersion at 1 µm are now commercially available [BMK99][THO03]. By incorporating such fibers in the cavity instead

of the dispersive grating pair, the GVD and the TOD in the cavity can be simultaneously compensated, as the dispersion slope of such PCF can be adapted to the gain fiber [ILI03]. Eventually, the dispersion compensation can even be realized by anomalous dispersion air-core photonic bandgap PCF, which show very low nonlinearity like dispersive grating pairs, as most of the signal power is propagating inside the air core [MTH03].

For the first time a large spectral broadening of a mode-locked Ytterbium fiber laser, by intra-cavity spectral filtering was demonstrated. The suppression of the long wavelength components in the dispersive delay line resulted in a large spectral broadening on the long wavelength side of the output spectrum. This effect resulted in a spectral bandwidth of up to 118 nm, which was several times larger than previous Ytterbium fiber laser systems, in combination with an output power of 1.3 W. Furthermore, excellent beam quality was guaranteed due to the single-mode gain fiber. For this laser, the relation between spectral filtering and spectral broadening was further examined. It was identified, that the observed broadening was attributable to nonlinear effects in the gain fiber. Because of the large spectral bandwidth, the high output power and the excellent beam quality, this laser system is well suited for optical measurement techniques like optical coherence tomography, which need large spectral bandwidths for high-resolution measurements.

In the realized Ytterbium based laser set-ups, the pump light was coupled into the double-clad fiber by free-space bulk optics. Therefore, the adjustment of these set-ups was sensitive to thermal effects caused by the free space pump light coupling. These set-ups can therefore be strongly simplified by employing transversal coupling schemes for the pump light, which are now commercial available [OFS03][ITF03]. In combination with fiber based dispersion compensation schemes and spectral filtering elements (e.g. Bragg-gratings), this enables compact all-fiber laser set-ups.

As the third set-up, a chirped pulse oscillator-amplifier system, based on Erbium doped fibers, was realized for the generation of high pulse energies in combination with pulse durations in the femtosecond range. Generation of output pulses with more than 4 µJ pulse energy in combination with pulse durations between 810 fs and 960 fs were demonstrated. The repetition rate of this system was continuously tunable at least between 50 kHz and 1 MHz and the pulse emission could be triggered by an external source.

This modular system consisted of an all-fiber oscillator-amplifier set-up and a diffractive grating compressor. For this system, the signal evolution during propagation and amplifica-

tion in the various system modules was investigated in detail. By this way, the influence of various linear and nonlinear effects on the output signal was analyzed. It was discovered that in combination with the Er^{3+}-gain structure, four-wave-mixing was largely suppressed by backward pumping. Simulations revealed that the pump arrangement strongly influenced the gain spectrum along the fiber. By this way, the power evolution of the various wavelengths along the fiber and therefore the four-wave-mixing was influenced. Additionally, it was observed that the chirp of the amplified pulses decreased with increasing pulse energy. Thus, the compressor dispersion for minimum output pulse duration depended strongly on the energy of the amplified pulses. This effect must be attributable to resonant dispersion effects of the gain fibers and was about one order of magnitude larger than described in the literature [HBU96]. A detailed analysis of the basic mechanism of this effect was however outside the scope of this work and should be therefore the subject of future research work.

Fourier-transform calculations of the output spectra revealed, that the limited transmission bandwidth of the grating compressor was the dominating limitation for the duration of the compressed output pulses. Furthermore, these computations indicated that by increasing the transmission bandwidth of the grating compressor from 12 nm to 20 nm the pulse duration could be reduced by about 35%. This can be accomplished by incorporating a larger grating into the compressor. Besides, the spectral bandwidth of the output signal can be increased by incorporating additional gain flattening filters into the fiber amplifier [YOO98]. This would enable a further reduction of the output pulse duration.

The output pulse energy was limited to about 7 µJ before the grating compressor by saturation effects in the gain fiber. By further experiments in combination with a specially designed gain fiber, pulse energies of more than 10 µJ were demonstrated, showing that the limitation due to saturation effects in the gain fiber can be overcome by this way. Further computations revealed that by gain fibers with a modified doping distribution refractive index profile the maximum pulse energy can be increased at least by a factor of three. In this computed fiber structure with two additional cladding layers the active doping is located in the central core and the outer cladding layer.

For that system, a high reliability can be expected, since it was nearly completely based on telecommunication grade components. In combination with a nonlinear crystal, the output wavelength of this laser system can be matched to the signal wavelength of conventional Ti:sapphire lasers. By this way, this high-repetition fiber based system can replace these bulk lasers in many applications.

Appendix

A Calculation of optical fiber properties

A.1 Numerical approximation of the field distribution in an optical fiber

Operation of short pulse fiber lasers and amplifiers are determined to a large extend by the mode field area and the dispersion of the optical fibers in the set-up. Since nonlinear effects scale inversely to the mode field area and the fiber dispersion influences phase sensitive nonlinear effects (e.g. FWM) the interaction between linear and nonlinear effects in the fiber. In particular, modulation instabilities disturb high-energy pulses if they propagate in fibers with anomalous dispersion [AGR95]. The resulting limitation for the peak power is usually far below the limits of other nonlinear effects. For silica glass, the material dispersion becomes anomalous above 1.3 µm. Hence, for amplification and transmission of high pulse energies at longer wavelengths (e.g. 1.55 µm), sophisticated fiber designs are required, which enable simultaneously a large mode field diameter (MFD) and normal fiber dispersion. Especially for active fibers, the fiber design had to take into account the constraints of the production process. Consequently for optimization of fiber designs numerical calculation schemes for the field distribution and the waveguide dispersion are required, which are suitable for arbitrary radial refractive index profiles.

As described section 2.1.1 the radial field distribution in each sector were determined by a differential equation for Bessel functions (eqs. 2.2 – 2.4). The corresponding general solution for each layer with constant n is a linear combination of the Bessel functions J_m and Y_m or K_m and I_m (eqs. A.1 – A.4) [BSE91].

$$F(\rho) = A\,J_m(\kappa\rho) + B\,Y_m(\kappa\rho) \quad : \quad n \geq \beta / k_0 \tag{A.1}$$

$$F(\rho) = C\,K_m(\gamma\rho) + D\,I_m(\gamma\rho) \quad : \quad n < \beta / k_0 \tag{A.2}$$

$$\kappa^2 = n^2 k_0^2 - \beta_2 \quad : \quad n \geq \beta / k_0 \tag{A.3}$$

$$\gamma^2 = \beta_2 - n^2 k_0^2 \quad : \quad n < \beta / k_0 \tag{A.4}$$

The constants A, B, C and D must be determined from the boundary condition, that at each layer boundary the electric field and its first derivative must be continuous [TJK00]. In addition, the field should decay roughly exponential for large ρ and must be finite at ρ = 0. These conditions determine only the relative values of these constants. For determination of the absolute values of these constants, the signal power must be taken into account. Each

solution of β and m, for which the above-mentioned boundary conditions can be fulfilled, describes an optical mode.

In order to ensure an excellent beam quality and to avoid mode-dispersion, single-mode fibers are highly preferable for pulsed fiber lasers. These fibers support only the fundamental mode, which exists in every guiding optical fiber. Hence, the calculations were focused on the fundamental mode and all of the following discussions and calculations refer to this mode, except mentioned otherwise. It should be noted that for the fundamental mode the index m is equal 0. In addition, if there exist multiple solutions for β_m, it has the highest value for β.

Equations A.5 – A.8 give the general solution for the fundamental mode in each layer and its first derivative [BSE91]. In addition, the first derivative is mentioned, because of the above-described boundary condition. The corresponding Bessel functions $J_0(x)$, $J_1(x)$, $Y_0(x)$, $Y_1(x)$ and modified Bessel functions $I_0(x)$, $I_1(x)$, $K_0(x)$ and $K_1(x)$ are shown in figure A1. For numerical calculation of the field distribution, rational approximations of these functions were used [PTV92].

$$F(\rho) = A J_0(\kappa\rho) + B Y_0(\kappa\rho) \quad : \quad n \geq \beta / k_0 \qquad (A.5)$$

$$F'(\rho) = -\kappa A J_1(\kappa\rho) - \kappa B Y_1(\kappa\rho) \quad : \quad n \geq \beta / k_0 \qquad (A.6)$$

$$F(\rho) = C K_0(\gamma\rho) + D I_0(\gamma\rho) \quad : \quad n < \beta / k_0 \qquad (A.7)$$

$$F'(\rho) = -\gamma C K_m(\gamma\rho) + \gamma D I_m(\gamma\rho) \quad : \quad n < \beta / k_0 \qquad (A.8)$$

β can be determined by simultaneous solving the equations A.5-A.8 for each layer with respect to the boundary conditions. However, solving this eigenvalue problem is relatively complex. Therefore, an alternative method was chosen for solving this eigenvalue problem.

Since the field must be finite at ρ = 0, the constants B and C are zero at this point. Therefore, the field distribution in the center of the fiber, and the adjoining region with the same refractive index, is described by the function $J_0(\kappa\rho)$ or $I_0(\gamma\rho)$. In the surrounding cladding with con-

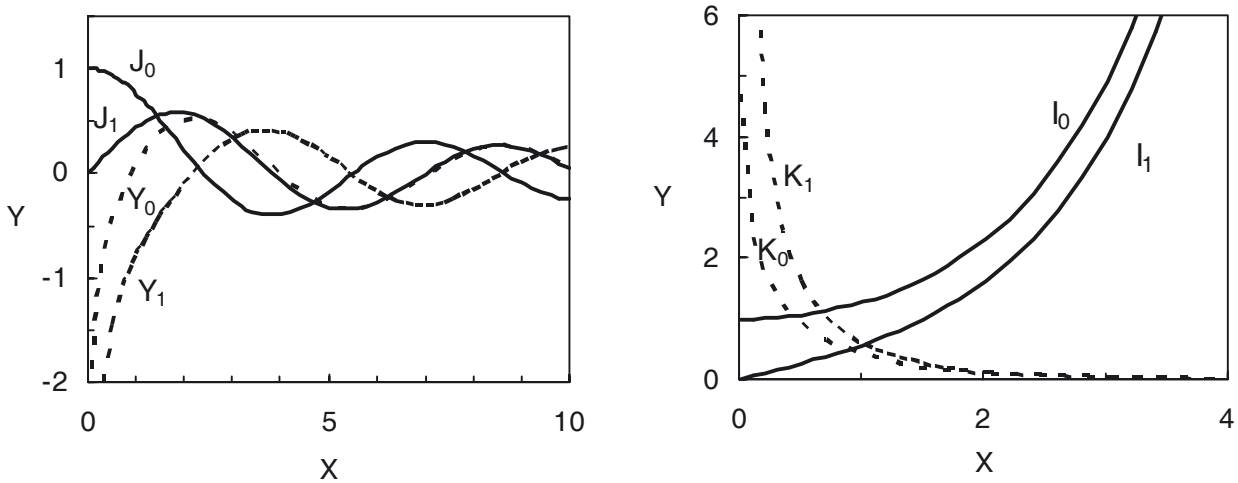

Fig. A.1 Bessel functions $J_0(x)$, $J_1(x)$, $Y_0(x)$, $Y_1(x)$ and modified Bessel functions $I_0(x)$, $I_1(x)$, $K_0(x)$ and $K_1(x)$.

stant refractive index, the field is described by $K_0(\gamma\rho)$ since the field must decay exponentially for large ρ. Furthermore, it can be easily derived from the above mentioned equations that the effective refractive index of a guided mode must be higher than the surrounding cladding and lower than the highest index in the core. Based on this, a rough estimate for β can be made according to equation 2.1.7. Using this value for β, the field distribution was calculated starting at $p = 0$ with $A = 1$; $D = 0$ ($n_{eff} \geq n(\rho = 0)$) or $A = 0$; $D = 1$ ($n_{eff} < n(\rho = 0)$). At each layer boundary, the coefficients for the adjoined function were calculated from the boundary condition. By this way, the field distribution is calculated up to the cladding region.

In the cladding region with constant refractive index the exponentially decaying field is described solely by $K_0(\gamma\rho)$. Since $D = 0$ in this region, the coefficient C was determined based from the continuity of the electric field at this boundary. Subsequently, at this boundary the first derivatives of both functions were calculated. If the β value, used in the calculations, is an eigenvalue and corresponds to a fiber mode, the derivatives of both functions have the same value at this boundary. If the derivatives of both functions have different values, the quotient of both values is used as error signal and β is iteratively approximated by this way.

Worth to mention is, that there can exist several eigenvalues for β even for $m = 0$, if the fiber is not single mode. In this case β and the field distribution of the fundamental mode can be calculated based on the fact that that this mode corresponds to the highest eigenvalue for β. Hence, for such refractive profiles the first estimation for n_{eff} should be close to the highest refractive index in the fiber core. In addition, the iterative approximation for β must start with relatively small correction steps. Furthermore, the electric field distribution of higher order modes becomes zero at least at one point for $\rho < \infty$. Hence, it can be noticed from the electric field distribution, if an eigenvalue corresponds not to the fundamental mode.

The intensity distribution inside the fiber is then determined from the electric field distribution. The signal power for this intensity distribution is computed by integrating the light intensity over the fiber cross section. Based on this data the intensity and electric field distribution is finally rescaled, so that it corresponds to the power level of the signal.

This approximation method can be easily adopted for higher order modes by taking the appropriate boundary condition at $\rho = 0$ into account and by using the functions A.1 and A.2 with the corresponding m-value. However, the number of fiber modes is limited. So no solution for β can be found, if the mode is not supported by the fiber.

According to the previous description β is the solution of an eigenvalue equation, which corresponds to a fiber mode. The corresponding effective index n_{eff} can be calculated by using

equation 2.1.7. However, the effective index can also be derived from the field distribution by taking the phase effects of the refractive index profile on the propagating electric field into account. Based on this more intuitive approach, the fundamental mode field distribution and the effective index can also be calculated for a given fiber index profile. This alternative approach should be described in the following section.

The refractive index profile of the fiber causes a phase delay of the electric field at each point, which is proportional to the local refractive index. Nevertheless, for a fiber mode the phase distribution remains constant during propagation. Therefore, the interference between the local electric field components and the local phase delay by the refractive index profile result in an equilibrium. Hence, the effective index can be calculated by taking the interference of the local electric fields into account.

Equations A.9 and A.10 describe the addition of two electric fields, E_1 and E_2, with different phases ϕ_1 and ϕ_2 [GUE90]. The variation of the refractive index causes only small phase differences between the local electric fields, if they were calculated for an (quasi) infinitesimal small propagation distance. This (quasi) infinitesimal approach is especially adapted to this problem, as the resulting phase distribution of a mode remains constant during propagation. For small phase differences, equations A.9 and A.10 can be simplified to equation A.11 and A.12. The local phase delay of the electric field is proportional to the refractive index at this fiber position. Hence, for the combined electric field, from two fiber segments, the effective index can be calculated according to equation A.17.

$$E^2 = (E_1 \cos\phi_1 + E_2 \cos\phi_2)^2 + (E_1 \sin\phi_1 + E_2 \sin\phi_2)^2 \qquad (A.9)$$

$$\tan\phi = \frac{E_1 \sin\phi_1 + E_2 \sin\phi_2}{E_1 \cos\phi_1 + E_2 \cos\phi_2} \qquad (A.10)$$

$$E \cong E_1 + E_2 \qquad (A.11)$$

$$\phi \cong \frac{E_1\ \phi_1 + E_2\ \phi_2}{E_1 + E_2} \qquad (A.12)$$

$$n \cong \frac{E_1\ n_1 + E_2\ n_2}{E_1 + E_2} \qquad (A.13)$$

By integrating the electric field over the area of each ring segment with constant refractive index, the corresponding total electric field amplitude can be calculated. The electric fields from the various ring segments were then be added by using equations A.11 and A.12. By this way, the effective refractive index can be calculated according to A.13, if the electric field distribution and the refractive index profile are known[7]. These numerical calculations result in

the same value for the effective refractive index as the determination from the eigenvalue β.
For approximation of the mode field distribution by this approach a rough estimate for n_{eff}, and β (eqs. 2.7), is calculated in the first step. This is done by using a coarse approximation for the mode field distribution, for e.g. a Gaussian field distribution with a mode field diameter comparable to the core diameter. The resulting value of n_{eff}, or respectively β, is then used for calculating a new field distribution as described for the previous numerical method. For this new field distribution, the effective refractive index is then calculated.
For a more accurate approximation, the average of the previous and the new value for n_{eff} is then calculated. By this way, the accuracy of this approximation for n_{eff} and the field distribution can be successively improved. The convergence of this method can be made more stable, if the mean of the previous and the new value for n_{eff} is replaced by a weighted average, which is closer to the previous value n_{eff}.
In order to compare the two approximation methods, the quotient of the slopes at the core cladding boundary was calculated for the computed field distribution by the second approximation method. Calculations for many refractive index profiles showed, that the deviation of this quotient from the theoretical value of 1 was always below 0.5%. This small deviation is most likely a result the limited accuracy of the numeric calculation. (e.g. in these calculations the electric fields of each ring segments (10 nm width), was approximated by the value in the middle of the ring). Typically, calculations that use the quotient of the slopes as an error signal were slightly more accurate than these based on n_{eff}. However, for complex index profiles, the first method showed quite often no convergence (this is influenced also by the first estimate for β). For such index profiles, the convergence of the second method showed to be more stable.

A.2 Calculation of the waveguide dispersion of an optical fiber

The relation between the group velocity dispersion and the effective index in an optical fiber is given by equation A.14 or A.15 [AGR95]. The dependence of the refractive index n on wavelength, and therefore the dispersion, is the sum of a material contribution and the variation of the effective index attributable to waveguide effects. The latter is directly related to the variation of field distribution with wavelength. Usually, the effect of the material dispersion on the mode field distribution is negligible small. Thus, these two contributions to the dispersion can be separated. The material dispersion depends on fiber composition and is for that reason fixed in most cases. Therefore, the fiber dispersion can only be adjusted by

designing a waveguide structure with the required waveguide dispersion. Hence, following discussion focuses on waveguide dispersion.

$$\beta_2 = \left(\frac{d^2\beta}{d\omega^2}\right) \cong \frac{\lambda^3}{2\pi c^2}\frac{d^2n}{d\lambda^2} \tag{A.14}$$

$$D \cong -\frac{2\pi c}{\lambda^2}\beta_2 \cong -\frac{\lambda}{c}\frac{d^2n}{d\lambda^2} = -\frac{\lambda}{c}\frac{d}{d\lambda}\left(\frac{d\ n}{d\lambda}\right) \tag{A.15}$$

$$n(\lambda) = n(\lambda)_{material} + n(\lambda)_{waveguide} \tag{A.16}$$

For numerical calculation of the waveguide dispersion, the differentials in A.15 must be replaced by differences, which lead to equation A.17. For a high accuracy of this calculation, the differences in these equations must be much larger than the variations of the calculated $n_{eff}(\lambda)$ attributable to numerical errors of the approximation. However, the wavelength difference should also be small in order to minimize averaging effects, since these differences replace differentials. For that reasons the waveguide dispersion should be calculated for different values for $\Delta\lambda$ (e.g. 15 nm, 30 nm and 50 nm). By this way significant errors caused by the numeric were usually indicated by large variations between the calculated values for the waveguide dispersion $D_{WG}(\lambda)$.

In a similar way the dispersion slope of the waveguide dispersion, which is the derivative of the waveguide dispersion (d/dλ or d/dω), can be determined.

$$\begin{aligned} D_{WG} &\cong -\frac{\lambda}{c}\frac{\left(\frac{d\ n_{eff}}{d\lambda}\right)_{\lambda+\Delta\lambda/2} - \left(\frac{d\ n_{eff}}{d\lambda}\right)_{\lambda-\Delta\lambda/2}}{\Delta\lambda} \\ &\cong -\frac{\lambda}{c}\frac{\left[n_{eff}(\lambda+\Delta\lambda) - n_{eff}(\lambda)\right]}{\Delta\lambda^2} - \frac{\left[n_{eff}(\lambda) - n_{eff}(\lambda-\Delta\lambda)\right]}{\Delta\lambda^2} \end{aligned} \tag{A.17}$$

B Units in fiber optic telecommunication and laser physics

In laser physics, the optical power is typically measured in Watts. Conversely, telecommunication engineers usually use the logarithmic dBm units for power levels. The latter can be attributed to the fact that dBm units are better adapted to the logarithmic dB scale, which is used for characterizing of amplification or loss of fiber optic components and transmission lines. The relation between Watts and dBm scale on the one side and the linear loss factor L_{lin} and dB scale on the other side were described by equations B.1 and B.2.

$$P[mW] = 1mW \cdot 10^{P[dBm]/10} \qquad (B.1)$$

$$L_{lin} = 10^{-L[dB]/10} \qquad (B.2)$$

The second and the third order dispersion are usually characterized in laser physics by the parameters β_2/[fs²] and β_3[fs³] (section 2.1.2). However, the second order dispersion of optical fibers per unit length is usually described in terms of the dispersion parameter D [ps/(nm·km)]. Furthermore, the third order dispersion is characterized by the ratio between the second order dispersion and the dispersion slope. The corresponding parameters, which were commonly used, are κ or C/C'.

Equations B.3 and B.4 describe the conversion between these different dispersion parameters for a fiber of length l. The last numerical factor in { } brackets in these equations is due to the different prefixes of the mentioned units. If this prefixes were taken into account, this numerical factors must set equal 1. Finally, it should be noted, that if units were not explicitly mentioned in brackets, the corresponding SI-units with no prefixes must be used.

$$D\left[\frac{ps}{nm \cdot km}\right] = -\frac{2\pi c}{\lambda^2 \cdot l}\beta_2\left[fs^2\right]\cdot\{10^{-24}\} \qquad (B.3)$$

$$\kappa[nm] = \frac{1}{\frac{C}{C'}\left[nm^{-1}\right]} = \frac{D}{\frac{dD}{d\lambda}} \cong \frac{-\lambda^2 \cdot \beta_2[fs^2]}{2\pi c \cdot \beta_3[fs^3]}\cdot\{10^{24}\} \qquad (B.4)$$

C Doping concentrations in silica fibers

In the literature and in manufacturer data sheets the doping concentration of rare earth (Re) doped fibers were specified by the molar concentration (mol%), the parts per million mol Re_2O_3 concentration (ppm mol Re_2O_3), the part per million weight concentration (ppm wt) of Re^{3+} or Re_2O_3, or by the numbers of Re^{3+}-ions per volume (ions/m³).

The definitions of the molar concentrations and the conversion between mol% and ppm mol were described by equations C.1 – C.5. In these equations n(X) denotes the concentration of molecule X in the host material. It is assumed, that the host material is pure silica and that the doping concentrations are much smaller than the SiO_2 concentration of the host. For other glass compositions or high doping concentrations, the SiO_2 concentration must be replaced by the concentration of the glass forming material.

The conversion between the molar and the weight concentrations were described by equations C.6 – C.8, where W(X) denotes the molecular weight of molecule or ion X In these equations the molecular mass of SiO_2 must be replaced by the average molecular mass of the glass forming material, if the glass composition deviates significantly from pure silica glass.

$$c(\mathrm{Re}_2O_3)[ppm\,mol] = 10^6 \frac{n(\mathrm{Re}_2O_3)}{n(SiO_2)} \quad (C.1)$$

$$c(\mathrm{Re}^{3+})[ppm\,mol] = 2 \cdot c(\mathrm{Re}_2O_3)[ppm\,mol] = 10^6 \frac{n(\mathrm{Re}^{3+})}{n(SiO_2)} \quad (C.2)$$

$$c(\mathrm{Re}_2O_3)[mol\,\%] = 100 \frac{n(\mathrm{Re}_2O_3)}{n(SiO_2)} \quad (C.3)$$

$$c(\mathrm{Re}^{3+})[mol\,\%] = 2 \cdot c(\mathrm{Re}_2O_3)[mol\,\%] = 100 \frac{n(\mathrm{Re}^{3+})}{n(SiO_2)} \quad (C.4)$$

$$c(X)[ppm\,mol] = 10\,000 \cdot c(X)[mol\,\%] \quad (C.5)$$

$$c(\mathrm{Re}_2O_3)[wt\,\%] = \frac{c((\mathrm{Re}_2O_3)[mol\,\%] \cdot W(\mathrm{Re}_2O_3)}{\cdot W(SiO_2)} \quad (C.6)$$

$$c(\mathrm{Re}^{3+})[wt\,\%] = \frac{2 \cdot W(\mathrm{Re}^{3+})}{W(\mathrm{Re}_2O_3)} c(\mathrm{Re}_2O_3) \quad (C.7)$$

$$c(x)[ppm\,wt] = 10\,000 \cdot c(x)[wt\,\%] \quad (C.8)$$

The relation between the molar concentration and the number of ions per volume is given by equations C.9, where D is the density of the host glass and NA is the Avogadro number ($6.02 \cdot 10^{23}$).

$$\rho(\mathrm{Re}^{3+})[cm^{-3}] = \frac{D[g/cm^{-3}] \cdot NA}{W(SiO_2)} \cdot c(\mathrm{Re}^{3+})[ppmmol] \cdot 10^{-6} \quad (C.9)$$

Based on the previous mentioned equations two examples for the different doping concentration definitions are shown in equations C.10 and C.11. The corresponding molecular masses are 60.1 g/mol (SiO_2), 382 g/mol (Er_2O_3), 167 g/mol (Er^{3+}), 394 g/mol(Yb_2O_3) and 173 g/mol (Yb^{3+}). Furthermore, the density of silica glass is 2.86 g/cm³.

$$1000\,ppm\,mol\,(Er_2O_3) = 0.1\,mol\,\%\,(Er_2O_3) = 0.637\,wt\,\%\,(Er_2O_3) = \\ = 0.557\,wt\,\%\,(Er^{3+}) = 5.74 \cdot 10^{19}\,cm^{-3}\,(Er^{3+}) \quad (C.10)$$

$$1000\,ppm\,mol\,(Yb_2O_3) = 0.1\,mol\,\%\,(Yb_2O_3) = 0.657\,wt\,\%\,(Yb_2O_3) = \\ = 0.577\,wt\,\%\,(Yb^{3+}) = 5.74 \cdot 10^{19}\,cm^{-3}\,(Yb^{3+}) \quad (C.11)$$

D Abbreviations

ACF: Autocorrelation function
ASE: Amplified spontaneous emission
CPA: Chirped pulse amplification
CW: Continuous wave
DCF: Double clad fiber
EDFA: Erbium doped fiber amplifier
ESA: Excited state absorption
FR: Faraday rotator
FWHM: Full width half maximum
FWM: Four-wave-mixing
GVD: Group velocity dispersion
HWP: Half wave plate
NLPR: Nonlinear polarization rotation
OCT: Optical coherence tomography
PBS: Polarization beam splitter
PC: Polarization controller
PCF: Photonic crystal fiber
PM: Polarization maintaining (fiber)
PMD: Polarization mode dispersion
QWP : Quarter wave plate
SHG: Second harmonic generation
SM: Single mode (fiber)
SPM: Self phase modulation
SBS: Stimulated Brillouin scattering
SRS: Stimulated Raman scattering
TOD: Third order dispersion
WDM: Wavelength-division-multiplexer
XPM: Cross phase modulation

References

[AAF01] P. Adel, M. Auerbach, C. Fallnich, H. Welling, "Super-Stretched mode-locked Yb^{3+}-fiber laser with 33 nm bandwidth and 56 nJ pulse energy", OSA Trends in optics and Photonics Vol. **50**, Advanced Solid State Lasers, 359 – 361 (2001)

[AAW02] M. Auerbach, P. Adel, D. Wandt, C. Fallnich, S. Unger, S. Jetschke, H.-R. Müller, "10 W widely tunable narrow linewidth double-clad fiber ring laser," Opt. Express **10**, 139 - 144 (2002)

[AAY00] O. Aso, S. Arai, T. Yagi, M. Tadakuma, Y. Suzuki, S. Namiki, "Broadband four-wave mixing generation in short optical fibers," Electronic Letters **36**, 709 – 711 (2000)

[AEA98] J. W. Arkwright, P. Elango, G. R. Atkins, T. Whitbread, M. J. F. Digonnet, "Experimental and Theoretical Analysis of the Resonant Nonlinearity in Ytterbium-doped Fiber," J. of Lightwave Technology **16**, 798 – 806 (1998)

[AES03] O. L. Antipov, O.N. Eremeykin, A. P.Savikin, V. A. Vorob'ev, D. V. Bredikhin, M.S. Kuznetsov, "Electronic Changes of Refractive Index in Intensively Pumped Nd:YAG Laser Crystals," IEEE J. of Quantum Electron. **39**, 910 – 917 (2003)

[AFF96] M. A. Arbore, M. M. Fejer, M. E. Fermann, A. Hariharan, A. Galvanauskas, D. Harter, "Frequency doubling of femtosecond erbium-fiber soliton lasers in periodically poled lithium niobate," Opt. Lett. **22**, 13 – 15 (1997)

[AGR95] G. P. Agrawal, Nonlinear Fiber Optics, Academic Press, San Diego, Second Edition (1995)

[AGR97] G. P. Agrawal, Fiber-Optic Communication Systems, Wiley, New York , Second edition (1997)

[AKH92] S. A. Akhmanov, V. A. Vysloukh, A. S. Chirkin, Optics of Femtosecond Laser Pulses, American Institute of Physics (1992)

[AKO03] S. Akturk, M. Kimmel, P. O'Shea, R. Trebino, "Measuring spatial chirp in ultrashort pulses using single-shot Frequency-Resolved Optical Gating," Opt. Express 11,68 – 78 (2003)

[APL98] H. L. An, E. Y. Pun, H. D. Liu, X. Z. Lin, "Effects of ion clusters on the performance of a heavily doped erbium-doped fiber laser," Opt. Lett. **23**, 1197 – 1199 (1998)

[ATT97] D. Artigas, L. Torner, J. P. Torres, N. N. Akhmediev, "Asymmetrical splitting of higher-order optical solitons induced by qunintic nonlinearity," Opt. Commun. **143**, 322 – 328 (1997)

[BBU98] R. W. Boyed, E. L. Buckland, "Nonlinear Optical Interactions in Optical Fibers," J. of Nonlinear Optical Physics & Materials **7**, 105 – 112 (1998)

[BKR02] A. Ortigosa-Blanch, J. C. Knight, P. St. J. Russell, "Pulse breaking and supercontinuum generation with 200-fs pump pulses in photonic crystal fibers," Opt. Soc. Am. B. **19**, 2567 – 2572 (2002)

[BLA01] N. A. Brilliant, K. Lagonik, "Thermal effects in dual-clad ytterbium fiber laser," Opt. Lett. **26**, 1669 – 1671 (2001)

[BMK99] T. A. Birks, D. Mogilevtsev, J. C. Knight, P. St. J.Russell, "Dispersion Compensation Using Single-Material Fibers," IEEE Photonics Technology Lett. **11**, 674 – 676 (1999)

[BOE99] M. Böhm, Department of Physics, Universität Rostock, personal communication (1999)

[BRA86] R. N. Bracewell, The Fourier Transform and its applications, McGraw-Hill, New York (1986)

[BRE98] A. Bertoni, G. C. Reali, "A model for the optimisation of double-clad fiber laser operation," Appl. Phys. B **66**, 547 – 554 (1998)

[BSC93] Bergmann, Schaefer, Lehrbuch der Experimentalphysik Band 3, Walter de Gruyter, Berlin, 9. Auflage (1993)

[BSE91] I. N. Bronstein, K. A. Semendjajew, Taschenbuch der Mathematik, Deutsch, Frankfurt, 25. Auflage (1991)

[CCB96] S. Colin, E. Contesse, P. Le Boudec, G. Stephan, F. Sanchez, "Evidence of a saturable-absorption effect in heavily erbium-doped fibers," Opt. Lett. **21**, 1987 - 1989 (1996)

[CCL02] S. Coen, A. H. L. Chau, R. Leonhardt, J. D. Harvey, J. C. Knight, W. J. Wadsworth, P. S. J. Russel, "Supercontinuum generation by stimulated Raman scattering and parametric four-wave mixing in photonic crystal fibers," J. Opt. Soc. Am. B **19**, 753 – 764 (2002)

[CGP98] Z. Y. Chen, A. B. Grudinin, J. Porta, J. D. Minelly, "Enhanced Q switching in double-clad fiber lasers," Opt. Lett. **23**, 454 - 456 (1998)

[CLG02] D. Cote, N. Laman, H. M. van Driel, "Rectification and shift currents in GaAs," Appl. Phys. Lett. **80**, 905 – 907 (2002)

[COR03] Corning Inc., LEAF –DCF modules, www.corning.com

[CRP97] V. Cautaerts, D. J. Richardson, R. Paschotta, D. C. Hanna, "Stretched pulse Yb^{3+}:silica fiber laser", Opt. Lett. **22**, 316 (1997)

[CZT97] S. V. Chernikov, Y. Zhu, J. R. Taylor, V. P. Gaponsev, "Supercontinuum self-Q-switched ytterbium fiber laser," Opt. Lett. **22**, 298 –300 (1997)

[DCH99] J.-C. Dung, S. Chi, "Dispersion compensation and gain flattened for a wavelength division multiplexing system by using chirped fiber gratings in an erbium-doped fiber amplifier," Opt. Commun. **162**, 219 – 222 (1999)

[DDU94] M. L. Dennis, I. N. Duling III, "Third-order dispersion in femtosecond fiber lasers," Optics Letters **19**, 1750 – 1752 (1994)

[DES94] E. Desurvire, Erbium-Doped Fiber Amplifiers, Wiley, New York (1994)

[DFM85] J. C. M. Diels, J. J. Fontaine, I. C. McMichael, F. Simoni, "Control and measurement of ultrashort pulse shapes (in amplitude and phase) with femtosecond accuracy," Appl. Opt. **24**, 1270 – 1282 (1985)

[DHV92] T. Dresel, G. Häusler, and H. Venzke, "Three-dimensional sensing of rough surfaces by coherence radar," Appl. Opt. **31**, 919 - 925 (1992)

[DIE95] J. Diels, Ultrashort laser pulse phenomena, Academic Press, San Diego (1995)

[DLF01] V. Doya, O. Legrand, F. Mortessagne, “Optimized absorption in a chaotic double-clad fiber amplifier,” Opt. Lett. **26**, 872 – 874 (2001)

[DPG02] J. M. Dudley, L. Provino, N. Grossard, H. Maillotte, R. S. Windeler, B. J. Eggelton, S. Coen, “Supercontinuum generation in air-silica microstructured fibers with nanosecond and femtosecond pulse pumping,” J. Opt. Soc. Am. B **19**, 765 – 771 (2002)

[DSK02] S.G. Demos, M. Staggs, K. Minoshima, J. Fujimoto, “Characterization of laser induced damage sites in optical components,” Optics Express **10**, 1444 – 1450 (2002)

[FWA98] A. Fellegara, S. Wabnitz, “Electrostrictive cross-phase modulation of periodic pulse trains in optical fibers,” Opt. Lett. **23**, 1357 – 1359 (1998)

[GKE00] L. Grüner-Nielsen, S. N. Knudsen, B. Edvold, T. Veng, D. Magnussen, C. C. Larsen, H. Damsgaard, “Dispersion Compensating Fibers,” Optical Fiber Technology **6**, 164 – 180 (2000)

[GLL02] G. Genty, M. Lehtonen, H. Ludvigsen, J. Broeng, M. Kaivola, “Spectral broadening of femtosecond pulses into continuum radiation in microstructured fibers,” Opt. Express **10**, 1083 – 1098 (2002)

[GSB01] A. Galvanauskas, Z. Sartania, M. Bischoff, “Millijoule femtosecond fiber CPA system,” OSA Trends in optics and Photonics Vol. **50**, Advanced Solid State Lasers, 679 – 681 (2001)

[GUE90] R. D. Guenther, Modern Optics, Wiley, New York (1990)

[GGZ98] H. Guerrero, G. V. Guinea, J. Zoido, “Mechanical Properties of Polycarbonate Optical Fibers,” Fiber and Integrated Optics **17**, 231 – 242 (1998)

[GKE00] L. Grüner-Nielsen, S. N. Knudsen, B. Edvold, T. Veng, D. Magnussen, C. C. Larsen, H. Damsgaard, “Dispersion Compensating Fibers,“ Optical Fiber Technology **6**, 164 – 180 (2000)

[GNA02] L. Gallais, J. Y. Natoli, C. Amra, “Statistical study of single and multiple pulse laser-induced damage in glasses,” Optics Express **10**, 1465 – 1474 (2002)

[HBU96] M. B. Hoffmann, J. A. Buck, “Erbium resonance-based dispersion effects on subpicosecond pulse propagation in fiber amplifiers: analytical studies,” J. Opt. Soc. Am. B **13**, 2012 – 2016 (1996)

[HFH91] M. Hofer, M. E. Fermann, F. Haberl, M. H. Ober, A. J. Schmidt, ”Mode-locking with cross-phase and self-phase modulation,” Opt. Letters **16**, 502 – 504 (1991)

[HHR99] R. Hofer, M. Hofer, G. A. Reider, “High energy, sub-picosecond pulses from a Nd-doped double-clad fiber laser,” Opt. Commun. **169**, 135 (1999)

[HML03] A. Heisterkamp, T. Mamom, H. Lubatschowski, W. Drommer, O. Kermani, H. Welling, W. Ertmer, “Application of Ultrashort Laser Pulses in Living Animals,” Graefe's Arch. Clin. Exp. Opthal., **241**, 511 – 517 (2003)

[HSI97] M. Horowitz, Y. Silberberg, “Nonlinear filtering by use of intensity-dependent polarization rotation in birefringent fibers,” Opt. Lett. **22**, 1760 – 1762 (1997)

[HZC01] Z. Hong, H. Zheng, J. Chen, J. Ge, "Laser-diode-pumped Cr^{4+}, Nd^{3+}:YAG self-Q-switched laser with high repetition rate and high stability," Appl. Phys. B **73**, 205-207 (2001)

[ILI03] R. Iliew, Institut fuer Festkoerpertheorie und Theoretische Optik, Friedrich-Schiller-Universitaet Jena, Germany, personal communication (2003)

[ITF03] ITF data sheet for multimode couplers PSP class, power performer series. www.itfoptical.com

[JAL97] S. Jarabo, J. M. Álvarez, "Experimental cross sections of erbium-doped silica fibers pumped at 1480 nm," Appl. Opt. **37**, 2288 – 2295 (1997)

[JDS03] JDS Uniphase, datasheet for 2.5 GHz/s Bias ready modulator. www.jdsuniphase.com

[JHN98] D. J. Jones, H. A. Haus, L. E. Nelson, E. P. Ippen, "Stretched-Pulse Generation and Propagation," IEICE Trans. Eletron. **E81-C**, 180 – 187 (1998)

[JKI99] S. D. Jackson, T. A. King, "Dynamics of the output of heavily Tm-doped double clad silica fiber lasers," J. Opt. Soc. Am. B **16**, 2178 – 2188 (1999)

[KAA03] M. E. Klein, P. Adel, M. Auerbach, C. Fallnich, P. Groß, K.-J. Boller, "Microsecond pulsed optical parametric oscillator pumped by Q-switched fiber lasers," Opt. Lett. **28**, 2222 - 2224 (2003)

[KAM81] A. A. Kaminskii, Laser Crystals, Vol. 14, Springer, Berlin (1981)

[KAS02] R. Caspary "Applied Rare-Earth Spectroscopy for Fiber Laser Optimization," Shaker, Aachen (2002)

[KGO93] W. H. Knox, J. G. Gordon, "Frequency domain dispersion measurements in tunable mode-locked lasers," Opt. Soc. Am. B **10**, 2071 – 2079 (1993)

[KGM00] J. P. Koplow, L. Goldberg, R. P. Moeller, D. A. V. Kliner, "Polarization-maintaining double-clad fiber amplifier employing externally applied stress-induced birefringence," Opt. Lett. **25**, 387 - 389 (2000)

[KJG01] D. A. V. Kliner, J. P. Kopolow, L. Goldberg, A. L. G. Carter, J. A. Digweed, "Polarization-maintaining amplifier employing double-clad bow-tie fiber," Opt. Lett. **26**, 184 – 186 (2001)

[KKG00] J. P. Koplow, D. A. V. Kliner, L. Goldberg, "Single-mode operation of a coiled multimode fiber amplifier," Opt. Lett. **25**, 442 – 444 (2000)

[KKR02] K. König, O. Krauss, I. Riemann, "Intratissue surgery with 80 Mhz nanojoule femtosecond laser pulses in the near infrared," Opt. Express **10**, 171 – 176 (2002)

[KLJ99] B. K. Kim, J. C. Lee, Y. M. Jhon, M.-W. Kim, S. K. Kim, S. S. Choi, M. S. Oh, "Characteristics of the intracavity dispersion in erbium-doped fiber laser," Opt. Lett. **24**, 391 – 393 (1999)

[KOE99] W.Köchner, Solid-State Laser Engineering, Springer, Berlin, 5. Auflage (1999)

[LFM89] R. I. Laming, M. C. Farries, P. R. Morkel, L. Reekie, D. N. Payne, "Efficient pump wavelengths of erbium-doped fibre optical amplifier," Electron. Lett. **25**, 12 – 14 (1989)

[LIE03] Liekki Oy, data sheet for the LF 6200 fiber, www.liekki.com

[LIE03b] Liekki Oy, data sheet for the LF 2400 fiber, www.liekki.com

[LIE03c] Liekki Oy, Experimental high Er doped fiber 110 dB/m, www.liekki.com

[LIE03d] Liekki Oy, Experimental high Er doped fiber 80 dB/m, www.liekki.com

[LLZ01] A. Liem, J. Limpert, H. Zellmer, A. Tünnermann, D. Nickel, U. Griebner, G. Korn, S. Unger, "High Energy Ultrafast Fiber-CPA System," OSA Trends in optics and Photonics Vol. **50**, Advanced Solid State Lasers, 111 - 113 (2001)

[LML02] S. Longhi, M. Marcello, P. Laporta, O. Svelto, M. Belmonte, "Propagation, manipulation, and control of picosecond optical pulses at 1.5 µm in fiber Bragg gratings," J. Opt. Soc. Am. B **19**, 2742 – 2757 (2002)

[LSM03] J. Limpert, T. Schreiber, S. Nolte, H. Zellmer, A. Tünnermann, "All fiber chirped-pulse amplification system based on compression in air-guiding photonic bandgap fiber," Opt. Express 24, 3332 – 3337 (2003)

[LUC99] OASIX 3.1. Optical amplifier simulation program. Copyright: Lucent Technologies 1999.

[LUE96] A. Liu, K. Ueda, "The Absorption Characteristics of Rare Earth Doped Circular Double-Clad Fibers," Optical Review **3**, 276 – 281 (1996)

[MEN93] C. R. Menyuk, "Soliton robustness in optical fibers," J. Opt. Soc. Am. B **10**, 1585 – 1591 (1993)

[MIN91] W. J. Miniscalco, "Erbium-Doped Glasses for Fiber Amplifiers at 1500 nm," J. of Lightwave Technology **9**, 234 – 250 (1991)

[MKC99] U. Morgner, F.X. Kaertner, S.H. Cho, Y. Chen, H.A. Haus, J.G. Fujimoto, E.P. Ippen, V. Scheuer, G. Angelow, T. Tschudi, "Sub-two-cycle pulses from a Kerr-lens mode-locked Ti:sapphire laser," Opt. Lett. **24**, 411 - 413 (1999)

[MLE82] C.A. Morrison, R. P. Leavitt, 46. Spectroscopic Properties of Triply Ionized Lanthanides in Transparent Host Crystals, Handbook on the Chemistry and Physics of Rare Earths, Edited by K. A. Gschneider, Jr., North-Holland Publishing (1982)

[MMF99] A. Melloni, M. Martinelli, A. Fellegara, "Frequency characterization of the Nonlinear Refractive Index in Optical Fiber," Fiber and Integrated Optics **18**, 1 - 13 (1999)

[MMO86] F. M. Mitschke, L. F. Mollenauer, "Discovery of the solitons self-frequency shift," Opt. Lett. **11**, 659 – 661 (1986)

[MNC97] P. Myslinski, D. Nguyen, J. Chrostowski, "Effects of Concentration on the Performance of Erbium-Doped Fiber Amplifiers," J. of Lightwave Technology **15**, 112 - 120 (1997)

[MSA98] S. K. Mondal, S. N. Sarkar, "Interesting effect of optical Kerr nonlinearity in expanding single-mode regime of optical fibers using dispersion –flattened profiles," Opt. Comm. **150**, 81 – 84 (1998)

[MSB99] E. B. Mejia, A. N. Starodumov, Y. O. Barmenkov, "Blue and infrared up-conversion in Tm^{3+}-doped fluorozirconate fiber pumped at 1.06, 1.117 and 1.18 µm," Appl. Phys. Lett. **74**, 1540 – 1554 (1999)

[MTH03] C. J. S. de Matros, J. R. Taylor, T. P. Hansen, K. P. Hansen, J. Broeng, "All-fiber chirped pulse amplification using highly-dispersive air-core photonic bandgap fiber," Opt. Express **11**, 2832 - 2837 (2003)

[NAH03] I. Nusinsky, A. A. Hardy, "Analysis of the Effect of Upconversion on Signal Amplification in Erbium-Doped Fiber Amplifiers (EDFAs)," IEEE J. of Quantum Electron. **39**, 548 – 554 (2003)

[NAS01] Y. Nagasawa, K. Aikawa, N. Shamoto, A. Wada, Y. Sugimasa, I. Suzuki, Y. Kikuchi, "High Performance Dispersion Compensating Fiber Module," Fujikura Technical Review 2001

[NJT97] L. E. Nelson, D. J. Jones, K. Tamura, H. A. Haus, E. P. Ippen, "Ultrashort-pulse fiber ring laser, " Appl. Phys. B **65**, 277 – 294 (1997)

[NMP98] J. Nilson, J. D. Minelly, R. Paschotta, A. C. Tropper, D. C. Hanna, "Ring-doped cladding-pumped single-mode three-level fiber laser," Opt. Lett. **23**, 355 – 357 (1998)

[NUF03] Nufern, data sheets forYb^{3+} double clad fibers. www.nufern.com

[OFS03] OFS, data sheet for tapered fiber bundle. www.ofsoptics.com

[OFS03b] OFS, Cladding pumped Fiber Laser cavity with integrated Cascaded Raman Resonator. www.ofsoptics.com

[OFS03c] OFS, data sheet for the MP 980 nm Er^{3+}-doped fiber. www.ofsoptics.com

[OPR98] H. L. Offenhaus, N. G. Brodewick, D. J. Richardson, R. Sammut, J. Caplen, L. Dong, "High-energy single-transverse-mode Q-switched fiber laser based on a multimode large-mode-area erbium-doped fiber," Opt. Lett. **23**, 1683 – 1685 (1998)

[PBH02] B. Povazay, K. Bizhea, B. Herrmann, A. Unterhuber, H. Sattmann, A. F. Fercher, W. Drexler, C. Schubert, P. K. Ahnelt, M. Mei, R. Holzwarth, W. J. Wadsworth, J. C. Kneight, P. St. J. Russel, "Enhanced visualization of choroidal vessels using ultrahigh resolution ophthalmic OCT at 1050 nm," Opt. Express 11, 1980 – 1986 (2003)

[PCH95] H. M. Pask, R. J. Carman, D. C. Hanna, A. C. Tropper, C. J. Mackechnie, P. R. Barber, J. M. Dawes, "Ytterbium-Doped silica Fiber Lasers: Versatile Sources for the 1-1.2 µm Region," IEEE J. of selected Topics in Quantum Electronics **1**, 2 - 13 (1995)

[PNT97] R. Paschotta, J. Nilson, A. C. Tropper, D. C. Hanna, "Ytterbium-Doped Fiber Amplifiers," IEEE J. of Quantum Electronics **33**, 1049 – 1056 (1997)

[PTV92] W. H. Press, S. A. Teukolsky, W. T. Vetterling, B. P. Flannery, Numerical Recipes in C, Cambridge, Second edition (1992)

[RGB97] J. K. Ranka, A. L. Gaeta, A. Baltuska, M. S. Pshenichnikov, D. A. Wiersma, "Autocorrelation measurement of 6-fs pulses based on the two-photon-induced photocurrent in a GaAsP photodiode," Opt. Lett. **22**, 1344 -1346 (1997)

[RMO97] R. Rangel-Rojo, M. Mohebi, "Study of the onset of self-pulsing behaviour in an Er-doped fibre laser," Opt. Commun. **137**, 98 – 102 (1997)

[RPN02] F. Rotermund, V. Petrov, F. Noack, V. Pasiskevicius, J. Hellström, F. Laurell, H. Hundertmark, P. Adel, C. Fallnich, "Compact all-diode-pumped femtosecond laser source based on chirped pulse optical parametric amplifiaction in periodically poled $KTiOPO_4$," Electron. Lett. **38**, 561 (2002)

[RWD97] W. Riede, U. Willamowski, M. Dieckmann, D. Ristau, U. Broulik, B. Steiger, "Laser induced damage measurements according to ISO/DIS 11254-1: results of a national round robin experiment on Nd:YAG optics," in Laser Induced Damage in Optical Materials: 1997, G.J. Exharos, M. R. Kozlowski, A. H. Guenther, M. J. Soileau, editors, Proc. SPIE **3244**, 96 – 105 (1997)

[SBG01] C. Schaffer, A. Brodeur, J. F. García, E. Mazur, "Micromachining bulk glass by use of femtosecond laser pulses with nanojoule energy," Opt. Lett. **26**, 93 – 95 (2001)

[SCB94] C. Spielmann, P. F. Curley, T. Brabec, F. Krausz, "Ultrabroadband Femtosecond Lasers," IEEE J. of Quantum Electron. **30**, 1100 (1994)

[SDS98] B. N. Samson, L. Dong, J. P. de Sandro, J. E. Caplen, "1.2 dB/cm gain in erbium :luthecium co-doped Al/P silica fibre," Electron. Lett. **34**, 111 – 113 (1998)

[SIG86] Siegman, Lasers, University Science Books, Sausalito (1986)

[SKK98] P. C. So, H. Kim, I. E. Kochevar, "Two-photon deep tissue ex vivo imaging of mouse dermal and subsutaneous structures," Opt. Express **16**, 339 - 350 (1998)

[SPA02] J. Subías, J. Pelayo, R. Alonso, F. Villuendas, C. Heras, "Electrostriction-free measurement in single mode optical fibers based on nonlinear-polarization evolution," J. Opt. Soc. Am. B **19**, 390 - 394 (2002)

[SPH88] E. Snitzer, H. Po, F. Hakimi, R. Tumminelli, B.C. McCollum, "Double Clad, Offset Core Nd Fiber Laser," Optical Fiber Sensors Conference, New Orleans, PD5 (1988)

[STO80] R. H. Stolen, "Nonlinearity in Fiber Transmission," Proc. of the IEEE **68**, 1232 – 1236 (1980)

[SZE97] A. K. Srivastava, J. L. Zyskind, J. D. Evankow, J. W. Sulhoff, Y.Sun, M. A. Mills, "Very flat Gain Erbium-Doped Fiber Amplifier Using Samarium-Doped Fiber," IEEE Photonics Technology Lett. **9**, 1576 – 1578 (1997)

[SZS97] Y. Sun, J. L. Zyskind, A. K. Srivastava, "Average Inversion Level, Modeling, and Physics of Erbium-Doped Fiber Amplifiers," IEEE J. of selected Topics in Quantum Electronics **3**, 991 – 1007 (1997)

[TAM94] K. Tamura, "Additive Pulse Mode-Locked Erbium-doped Fiber Lasers," Ph. D. Thesis, MIT, (1994)

[TDD03] L. Tordella, H. Djellout, B. Dussardier, A. Saissy, G. Monnom, "High repetition rate passively Q-switched Nd^{3+}:Cr^{4+} all fibre laser," Electron. Lett. **39**, 1307 – 1308 (2003)

[TDN94] K. Tamura, C. R. Doerr, L. E. Nelson, H. A. Haus, E. P. Ippen, "Technique for obtaining high-energy ultrashort pulses from an additive-pulse mode-locked erbium-doped fiber ring laser," Opt. Lett. **19**, 46 - 48 (1994)

[THR03] Thorlabs Inc, Catalog 2003, www.thorlabs.com

[TKA00] K. Thyagarajan, J. Knaur, "A novel design of an intrinsically gain flattened erbium doped fiber," Opt. Commun. **183,** 407 – 413 (2000).

[TKS02] S. Tammela, P. Kiiveri, S. Särkilahti, M. Hotoleanu, H. Valkonen, M. Rajala, J. Kurki, K. Janka, "Direct Nanoparticle Deposition Process for manufacturing very short high gain Er-doped silica glass fibers," ECOC 2002 Proceedings **4**, 9.4.2 (2002)

[TLM02] K. Takaichi, J. Lu, T. Murai, T. Uematsu, A. Shirakawa, K. Ueda, H. Yagi, T. Yanagitani, A. Kaminskii, "Chromium Doped $Y_3Al_5O_{12}$ Ceramics – a Novel Saturable Absorber for Passively Self-Q-switched One-Micron Solid State Lasers," Jpn. J. Appl. Phys. **41**, L96-L98 (2002)

[TNH94] K. Tamura, L. E. Nelson, H. A. Haus, E. P. Ippen, "Soliton versus nonsoliton operation of fiber ring lasers," Appl. Phys. Lett. **64**, 149 – 151 (1994)

[TRD97] D. Taverner, D. J. Richardson, L. Dong, J. E. Caplen, K. Williams, R. V. Penty, "158-µJ pulses from a single-transverse-mode,large-mode-area erbium-doped fiber amplifier," Opt. Lett. **22**, 378 – 380 (1997)

[TRE69] E. B. Treacy, "Optical Pulse Compression with Diffraction Grating," IEEE Journal of Quantum Electronics, **QE-5**, 454 – 458 (1969)

[UNG03] S. Unger, Institut fuer physikalische Hochtechnologie in Jena (IPHT), Germany, personal communication (2003)

[URE80] R. Ulrich, S. C. Rashleigh, W. Eickhoff, "Bending-induced birefringence in single-mode fibers," Opt. Lett. **5**, 273 – 275 (1980)

[USI79] R. Ulrich, A. Simon, "Polarization optics of twisted single-mode fibers," Applied Optics **18**, 2241 - 2251 (1979)

[VPA00] M. V. D. Vermelho, U. Peschel, J. S. Aitchison, "Simple and Accurate Procedure for Modeling Erbium-doped Waveguide Amplifiers with High Concentrations," J. of Lightwave Technology **18**, 401 – 408 (2000)

[WAF02] P. Wessels, M. Auerbach, C. Fallnich, "Narrow-linewidth master oscillator power amplifier system with very low amplified spontaneous emission," Opt. Commun. **205**, 215- 219 (2002)

[WFA03] P. Wessels, C. Fallnich, "Polarization dependent gain in neodymium and ytterbium doped fiber amplifiers," Opt. Express **11**, 530 - 534 (2003)

[WLT97] D. Wandt, M. Lascheck, A. Tünnermann, H. Welling, "Continously tunable external-cavity diode laser with a double-grating arrangement," Opt. Lett. **22**, 390- 392 (1997)

[WNC02] M. Will, S. Nolte, B. N. Chichkov, A. Tünnermann, "Optical properties of waveguides fabricated in fused silica by femtosecond laser pulses," Appl. Opt. **41**, 4360 - 4364 (2002)

[WNC03] Y. Wang, J. S. Nelson, Z. Chen, B. J. Reiser, R. S. Chuck, R. S. Windeler, "Optimal wavelength for ultrahigh-resolution optical coherence tomography," Opt. Express **11**, 1411 – 1417 (2003)

[YEH89] C. Yeh, Handbook of Fiber Optics, Academic Press, San Diego (1989)

[YOO98] M. Yamada, H. Ono, Y. Ohishi, “Gain-flattened broadband Er3+-doped silica fibre amplifier with low noise characteristics,” Electron. Lett., **34**, 1747 -1748 (1998)

[YPO02] J. W. Yu, Y. Park, K. Oh, I. B. Kwon, “Brillouin frequency shifts in silica optical fiber with the double cladding structure,” Opt. Express, **10**, 996-1002 (2002)

[ZEN93] L. Zenteno, “High-Power Double-clad Fiber Lasers,” Journal of Lightwave Technology **11**, 1435-1446 (1993)

[ZTW97] H. Zellmer, A. Tünnermann, H. Welling, V. Reichel, “Double-clad Fiber Laser with 30 W Output Power,“ Optical Amplifier and their Applications,” Technical Digest (Optical Society of America Washington, DC 1997), 251 (1997)

Publications

Journal articles

P. Adel, M. Auerbach, C. Fallnich, S. Unger, H.-R. Müller, J. Kirchhof, "Passive Q-switching by Tm^{3+}-codoping of a Yb^{3+}-fiber laser," Optics Express **11**, 2730 – 2735 (2003)

M. E. Klein, P. Adel, M. Auerbach, C. Fallnich, P. Groß, K.-J. Boller, "Microsecond pulsed optical parametric oscillator pumped by a Q-switched fiber laser," Optics Letters **28**, 2222 - 2224 (2003)

V. Petrov, F. Noack, F.Rotemund, V. Pasiskevicius, A. Fragemann, F. Laurell, H. Hundertmark, P. Adel, C. Fallnich, "Efficient All-Diode-Pumped Double Stage Femtosecond Optical Parametric Chirped Pulse Amplification at 1-kHz with Periodically Poled $KTiOPO_4$," Jpn. J. Appl. Phys. **42**, L1327 – L1329 (2003)

P. Adel, C. Fallnich, "High power ultra-broadband mode-locked Yb^{3+}-fiber laser with 118 nm bandwidth," Optics Express 10, 622 – 627 (2002)

F. Rotermund, V. Petrov, F. Noack, V. Pasiskevicius, J. Hellström, F. Laurell, H. Hundertmark, P. Adel, C. Fallnich, "Compact all-diode-pumped femtosecond laser source based on chirped pulse optical parametric amplification in periodically poled $KTiOPO_4$," Electron. Lett. **38**, 561 -563 (2002)

M. Auerbach, P. Adel, D. Wandt, C. Fallnich, S. Unger, S. Jetschke, H. R. Mueller, "10 W widely tunable narrow linewidth double clad fiber ring laser," Optics Express **10**, 139 -144 (2002)

P. Adel, M. Auerbach, C. Fallnich, S. Unger, H.-R. Mueller, "Super-stretched mode-locked Yb^{3+}-fiber ring laser with 40 nm bandwidth, 9.5 nJ pulse energy and 630 mW output power," Opt. Commun. **211**, 283 - 287 (2002)

International conferences

P. Adel, M. Engelbrecht, C. Fallnich, "Modular high repetition rate ultrafast all-fiber Er^{3+} oscillator-amplifier system with µJ pulse energy," Advanced Solid State Photonics 2004,TuB5 (2004), Santa Fe

P. Weßels, P. Adel, M. Auerbach, D. Wandt and C. Fallnich, “Suppression of Brillouin scattering in a single-mode Neodymium-doped fiber amplifier,” CLEO 2004, CWA (2004), San Francisco

P. Adel, M. Auerbach, C. Fallnich, S. Unger, H.-R. Mueller, “Wavelength tunable narrow linewidth Yb^{3+}-fiber laser with passive Q-switching based on Tm^{3+}-codoping” CLEO 2003, CMK1, Baltimore.

P. Adel, C. Fallnich, “Extremely broadband Yb^{3+}-fiber laser with high output power,” OSA Annual Meeting 2002, MG, Orlando

M. Auerbach, P. Adel, D. Wandt, C. Fallnich, S. Unger, S. Jetschke, H.-R. Mueller, “10 W widely tunable narrow linewidth double-double clad fiber ring laser,” CLEO 2002, CTHX2, Long Beach

F. Rotermund, V. Petrov, F. Noack, V. Pasiskevicius, J. Hellström, F. Laurell, H. Hundertmark, P. Adel, C. Fallnich, “Compact all-diode-pumped femtosecond laser source based on chirped pulse optical parametric amplification in periodically poled $KTiOPO_4$,” CLEO 2002, CTuO1, Long Beach

P. Adel, M. Auerbach, C. Fallnich, H. Welling, “Super-Stretched mode-locked Yb^{3+}-fiber laser with 33 nm bandwidth and 56 nJ pulse energy”, OSA Trends in optics and Photonics Vol. 50, Advanced Solid State Lasers, 359 – 361 (2001)

P. Adel, H. Hundertmark, M. Auerbach, C. Fallnich, “Stretched-pulse additive pulse mode locked fiber laser enable up to 77 nJ pulse energy,” EPS Conference on Lasers and Electro-Optics/Europe (CLEO/Europe 2001), Progress in Solid-State Lasers (European Physical Society, Munich 2001), C-PSL 152, 122 (2001)

P. Wessels, M. Auerbach, P. Adel, C. Fallnich, “High power fiber-based laser systems with narrow linewidth,” EPS Conference on Lasers and Electro-Optics/Europe (CLEO/Europe 2001), Progress in Solid-State Lasers (European Physical Society, Munich 2001), 61 (2001)

A. Isemann, P. Adel, T. Groß, C. Fallnich, “First Cr3+: LiCAF diode-pumped regenerative amplifier seeded by a frequency doubled mode-locked Er3+-fiber-laser” In: OSA Trends in

Optics and Photonics TOPS, Vol. 56, Conference on Lasers and Electro-Optics (CLEO 2001),Technical Digest, Postconference Edition (Optical Society of America, Washington DC, 2001), 502 (2001)

National conferences

P. Adel, M. Auerbach, C. Fallnich, "Passiv guetegeschaltete Yb^{3+}-Tm^{3+}-Faserlaser," DPG-Tagung 2003, Hannover (Germany) Q 17.1

H. Hundertmark, P. Adel, C. Fallnich, "Quasi-all-fiber modengekoppelter Erbium-Faserlaser," DPG-Tagung 2000, Bonn (Germany), Q 9.1

O. Thiele, P. Adel, C. Fallnich, H. Welling, "Passiv modengekoppelter Erbium-Faserlaser," DPG-Tagung 1999, Heidelberg (Germany), Q 45.2

Curriculum vitae

Name:	Peter Wolfgang Adel
Date of birth:	25.07.1969
Place of birth:	Nürnberg
Parents:	Hans Adel,
	Luise Adel, née Lang
Marital status:	married

Education:

School education	1976 - 80	Grundschule Stein, Mittelfranken
	1980 - 90	Gymnasium Stein, Mittelfranken
		Abitur: June 1990
Military service	1990 - 91	Nachschubkompanie 120, Amberg
University education	1991 - 97	Student of physics, Universität Erlangen Diploma thesis: “Mode locked Erbium fiber laser”
	1993 – 94	Study abroad at the Imperial College London (Great Britain)

Employment:

08.1997 – 12.1997	Auxiliary scientific employee at the Lehrstuhl für Optik,
	Universität Erlangen
since 1.2.1998	Scientific employee at the Laser Zentrum Hannover e. V.

Danksagung

An dieser Stelle möchte ich mich bei allen bedanken, die direkt oder indirekt zum Gelingen dieser Arbeit beigetragen haben.

Zu allererst danke ich meinen *lieben Eltern*, die mir das Studium ermöglicht haben und mir stets mir Rat und Tat zur Seite standen. Ohne deren Unterstützung und Rückhalt wäre diese Arbeit niemals möglich gewesen. Mein herzlicher Dank gilt auch *meinen Geschwistern*, die mir in der ganzen Zeit mit viel Verständnis und Geduld entgegen gekommen sind.

Mein ganz besonderer Dank gilt meiner lieben Frau *Dr. Susanna Adel* für ihr Verständnis und ihre Unterstützung. Sie hat mir den Rückhalt gegeben, um die stressigen Tage der Promotion durchzustehen.

Für die Überlassung dieses interessanten Themas und die Möglichkeit diese Arbeit am Laser Zentrum Hannover e.V. durchzuführen, möchte ich mich bei meinem Doktorvater *Prof. Dr. H. Welling*, sowie bei *Dr. Carsten Fallnich* und *Prof. Dr. A. Tünnermann* bedanken. Außerdem möchte ich mich bei *Dr. Carsten Fallnich* für die stete Diskussionsbereitschaft und die vielen Anregungen bedanken. Danken möchte ich *Prof. Dr. A. Tünnermann* auch für die bereitwillige Übernahme des Korreferates. Mein besonderer Dank gilt auch *Prof. Dr. M. Kock* für die Übernahme des Prüfungsvorsitzes.

Dr. Dieter Wandt möchte ich für seine Diskussionsbereitschaft, seine Anregungen, seine stete Hilfsbereitschaft, die angenehme Büroatmosphäre und nicht zuletzt für seine Korrekturhinweise zu dieser Arbeit danken.

Meinen Kollegen *Dipl. Phys. Holger Hundertmark, Dr. Mario Auerbach*, *Dipl. Phys. Martin Engelbrecht*, *Dr. Peter Wessels*, *Dr. Andreas Isemann* und *Dr. Dietmar Kracht* danke ich für ihre Unterstützung, für viele Diskussionen im wissenschaftlichen und alltäglichen Leben und das angenehme Arbeitsklima in der Gruppe „Faserlaser“. Weiterhin möchte ich mich bei *Dipl. Phys. Sebastian Bartel* bedanken für seine Unterstützung bei den Messungen mit der Streakkamera.

Für die Herstellung der benötigten aktiven Fasern möchte ich mich bei den Kollegen des IPHT in Jena im Bereich „Optik“ bedanken. Ohne diese Unterstützung hätten große Teile dieser Arbeit nicht durchgeführt werden können. Besonders hervorheben möchte ich dabei die

Bereitschaft von Frau *Dr. Sonja Unger*, auf meine Wünsche bei dem Faserdesign einzugehen. Sehr zu schätzen weis ich auch die Diskussionen mit *Dr. Ulrich Röpke* bezüglich der theoretischen Modellierung von aktiven Fasern.

Schließlich möchte ich noch die Zusammenarbeit mit *Dr. Marvin Klein* und seinen Kollegen nicht unerwähnt lassen. Sie trug entscheidend dazu bei, das Anwendungspotential von schmalbandigen gütegeschalteten Faserlasern mit abstimmbarer Wellenlänge nachzuweisen.